Universidad Autónoma de Madrid
Facultad de Ciencias

Nanoscale Engineered Electrode Materials for High Performance Lithium-Ion Batteries

TESIS DOCTORAL

Venkata Sai Avvaru

Advanced Materials and Nanotechnology

Madrid, 2021

Universidad Autónoma de Madrid
Facultad de Ciencias
Materiales Avanzados y Nanotecnología

Materiales Nanodisenados Para Electrodos De Baterias De Iones De Litio De Alto Rendimiento

TESIS DOCTORAL

Venkata Sai Avvaru
Advanced Materials and Nanotechnology

Directores de Tesis

Dr. Vinodkumar Etacheri

Madrid, 2021

This PhD thesis was elaborated in the period working from September 2017 to July 2021 at IMDEA Materials Institute and the Department of Advanced Materials and Nanotechnology of the Universidad Autónoma de Madrid (UAM), under the supervision of Dr. Vinodkumar Etacheri and the tutoring of Prof. Carmen Morant Zacares.

El presente trabajo se elaboró en el período comprendido entre septiembre de 2017 y julio de 2021 en el Instituto IMDEA Materiales y el departamento de Materiales Avanzados y Nanotecnologia de la Universidad Autónoma de Madrid (UAM), bajo la supervisión del Dr. Vinodkumar Etacheri y la tutoría de la Profesora Carmen Morant Zacares.

institute imdea materials

EXCELLENCE
MARÍA
DE MAEZTU

UAM
Universidad Autónoma
de Madrid

Dedicated to my family

Acknowledgement

I would like to express my sincere gratitude to my supervisor, Dr. Vinodkumar Etacheri, for seeing me fit as doctoral student in his electrochemistry group and for patiently discussing, encouraging and correcting my works. I came across a number of people whose contributions in various ways helped in my field of work.

Special thanks to my tutor Prof. Carmen Morant Zacarés for continuous encouragement and support.

I would like to thank Spanish ministry for funding, which enable me to stay in Spain and finish this study.

It is an honour for me to thank Dr. Tata Narasinga Rao, Ms. J. Revathi and Dr. Mani Karthik, who directed me to the PhD research in nanomaterials.

I am heartily thankful to IMDEA Materials Institute for providing conveniently accessible facilities and a comfortable working environment. I would like to thank Rosa María Bazán, Mariana Huerta, and Ainhoa Zapatero, for their administrative assistance and Raul for IT support during this study. I thank the experimental supports particularly from Dr. Miguel Castillo for HRTEM studies, and Dr. Javier Garcia for XRD measurements.

It is pleasure to thank Dr. Steven J. Hinder, University of surrey for XPS analysis.

I would like to extent my thanks to all my electrochemistry group researchers, Rudi Ruben Maça, Alvaro Doñoro, Wenliang Feng, Mewin Vincent and Dr. Daniel Cíntora for their experimental support, suggestions and academic knowledge.

I am thankful to all my collaborators, Dr. Juan Jose, Dr. Deyi Wang, Dr. Moumita Rana, Abdulmalik Yusuf, Dr. Jing Zhang from IMDEA materials for their help and fruitful discussions

It is a pleasure to thank all my research friends in IMDEA and abroad, particularly Chandrashekhar Pilgar, Shruti Banait, Dr. Xiaolin, Dr. Cleis Santos, Venkatesh Sivagnana, Harish, Suresh, Riya Davis, Joseph, Pradeep etc. for their friendship and critical comments on my research work.

Additionally, it has been a great experience to get to know new people and new cultures to widen my point-of-view which is also helpful to keep an open mind for personal and social development. So, I would like to thank all my colleagues that supported me and facilitated my research and studies.

At last, but not the least, I am grateful to thank my family. This thesis would not have been possible without their support and constant encouragement.

Thank you
Venkata Sai Avvaru

Abstract

Rechargeable batteries are one of the most prominent energy storage devices for portable electronics, medical applications, electric vehicles and power grids. Secondary lithium-ion batteries (LIBs) have been a subject of intense research due to their high energy density, good cycle life and efficiency compared to Pb-acid, Ni-MH and Ni-Cd batteries. However, energy (100-300 Wh kg^{-1}) and power density (250-400 W kg^{-1}) of current generation Li-ion batteries are inadequate for several applications including long-range electric vehicles. One of the main reasons for this is the implementation of low specific capacity graphite anodes possessing sluggish Li-ion diffusion kinetics. Consequently, numerous efforts have been focused on the development of high specific capacity anodes capable of delivering high energy density and fast charging with long-cycle life. This thesis is focused on pseudocapacitive storage of high-capacity anodes based on transition metal-oxides (TMO) for next generation lithium-ion batteries as a substitute for conventional anodes.

We demonstrated a high energy (400 Wh kg^{-1}) and power density (1 kW kg^{-1}) Li-ion batteries based on extremely pseudocapacitive interface engineered ultrafine CoO nanoparticles (~10 nm) chemically bonded to three-dimensional nitrogen-doped reduced graphene-oxide (CoO@3D-NRGO) hybrid anodes. This hybrid anode demonstrated excellent pseudocapacitance (~92%), specific capacity (1429 mAh g^{-1} @ 25 mA g^{-1}), rate performance (906 mAh g^{-1} @ 5 A g^{-1}), and cycling stability (990 mAh g^{-1} after 7500 cycles @ 5 A g^{-1}). Outstanding electrochemical performance of CoO@3D-NRGO‖$LiNiMnCoO_2$ full-cells is credited to the extreme pseudocapacitance of CoO@3D-NRGO anode resulting from Li_2O/Co/NRGO nanointerfaces and Co-O-C bonds.

Nanograin-boundary rich hierarchical Co_3O_4 nanorods resulted in high energy (480 Wh kg^{-1}) and power density (980 W kg^{-1}) lithium-ion batteries. These defective anodes exhibited extreme pseudocapacitance (up to 81%), reversible capacity (1593 mAh g^{-1} @ 50 mA g^{-1}), rate performance (800 mAh g^{-1}@ 30 A g^{-1}), cycling stability (~60% after 1000 cycles @ 1 A g^{-1}), coulombic efficiency (~100%) and ultrafast-charging (~35 secs @ 30 A g^{-1}). Li-ion storage performances presented in this case are significantly superior to the previously reported conversion type anodes. A Li-ion full-cell composed of Co_3O_4 nanorod anode and $LiNiMnCoO_2$ cathode demonstrated excellent cycling stability (~80% after 200 cycles @ 1 A g^{-1}). Mechanistic studies including *in-situ* XRD and EELS mapping illustrated unique Li-ion storage at grain boundaries. Outstanding performance of Co_3O_4 nanorods anode is credited to the synergy between conversion mechanism of Co_3O_4 and pseudocapacitive Li-ion storage at numerous Li_2O/Co/$Li_{1.47}Co_3O_{3.72}$ nanointerfaces.

Oxygen deficient rutile TiO_2 nanowires are demonstrated as highly pseudocapacitive anodes for high energy (350 Wh kg^{-1}) and power density (2 kW kg^{-1}) Li-ion batteries. Rutile $TiO_{1.7}$ nanowires presented in this case exhibited excellent pseudocapacitance (up to 97%), specific capacities (430 mAh g^{-1} @ 25 mA g^{-1}), rate capability (66 mAh g^{-1} @100 A g^{-1}), cycling stability (74% after 30000 cycles @ 50 A g^{-1}), coulombic efficiency (~100%) and ultrafast charging (~7 secs @ 100 A g^{-1}). These results are vastly superior to the previously reported values for TiO_2 based Li-battery anodes. Lithium-ion full-cell composed of oxygen vacant rutile TiO_2 nanowire anode and $LiNiMnCoO_2$ cathode verified excellent cycling stability (80% after 2500 cycles @ 1 A g^{-1}). Mechanistic studies proved oxygen vacancy induced crystalline to amorphous transition of rutile TiO_2 nanowires. Outstanding performance of rutile $TiO_{1.7}$ nanowires anode is credited to the Li-ion intercalation pseudocapacitance resulting from oxygen vacancies.

High-performance lithium-ion batteries based on extremely pseudocapacitive defect engineered Co_3O_4 nanosheets anodes are demonstrated. Defective Co_3O_4 nanosheet anode presented here composed of vacancies, dislocations and grain boundaries. Unique 2D holey framework enabled efficient charge transport as well as accommodation of volume changes during charge-discharge process. These anodes exhibited excellent pseudocapacitance (up to 87%), specific capacity (1490 mAh g^{-1} @ 25 mA g^{-1}), rate performance (592 mAh g^{-1} @ 30 A g^{-1}), cycling stability (85% after 500 cycles @ 1 A g^{-1}) and columbic efficiency (~100%). Outstanding electrochemical performance of Co_3O_4 nanosheets is credited to the pseudocapacitive nature of conversion reaction resulting from ultrafast Li-ion diffusion through crystal defects.

Above demonstrated strategies of defect induced pseudocapacitance can be easily extended for various environmental friendly/ inexpensive transition metal-oxide anodes (Fe_2O_3, MnO_2 etc.) for next-generation high energy/power density and ultra-long-life rechargeable batteries.

Resumen

Las baterías recargables son uno de los dispositivos de almacenamiento de energía más destacados para electrónica portátil, aplicaciones médicas, vehículos eléctricos y redes eléctricas. Las baterías secundarias de iones de litio (LIBs) han sido objeto de intensas investigaciones debido a su alta densidad de energía, buena vida útil del ciclado y eficiencia en comparación con las baterías de Pb-ácido, Ni-MH y Ni-Cd. Sin embargo, la densidad de energía (100-300 Wh kg^{-1}) y de potencia (250-400 W kg^{-1}) de la generación actual de baterías de iones de litio son inadecuadas para varias aplicaciones, incluyendo los vehículos eléctricos de largo recorrido. Una de las principales razones de esto es la implementación de ánodos de grafito de baja capacidad específica, que poseen una lenta cinética de difusión de iones de Li. En consecuencia, numerosos esfuerzos se han centrado en el desarrollo de ánodos de alta capacidad específica, capaces de ofrecer alta densidad de energía y carga rápida con una gran vida útil de ciclado. Esta tesis se centra en el almacenamiento pseudocapacitivo de ánodos de alta capacidad basados en óxidos de metales de transición (TMO) para la próxima generación de baterías de iones de litio, como sustituto de los ánodos convencionales.

Mostramos baterías de iones de litio, con alta densidad de energía (400 Wh kg^{-1}) y de potencia (1 kW kg^{-1}), basadas en ánodos híbridos de nanopartículas ultrafinas de CoO (~10 nm) químicamente unidas a óxido de grafeno reducido tridimensional dopado con nitrógeno (CoO@3D-NRGO), diseñados con una interfaz extremadamente pseudocapacitiva. Este ánodo híbrido demostró una excelente pseudocapacitancia (~92%), capacidad específica (1429 mAh g^{-1} @ 25 mA g^{-1}), capacidad de ciclado (906 mAh g^{-1} @ 5 A g^{-1}) y estabilidad de ciclado (990 mAh g^{-1} después de 7500 ciclos @ 5 A g^{-1}). El excepcional rendimiento electroquímico de las celdas

completas CoO@3D-NRGO‖LiNiMnCoO$_2$ se atribuye a la extrema pseudocapacitancia del ánodo de CoO@3D-NRGO resultante de las nanointerfases Li$_2$O/Co/NRGO y enlaces Co-O-C.

Las nanovarillas jerárquizadas de Co$_3$O$_4$, consistentes en bordes de nanograno, dieron lugar a una batería de litio-ion de alta densidad de energía (480 Wh kg^{-1}) y de potencia (980 W kg^{-1}). Estos ánodos, basados en defectos, exhibieron pseudocapacitancia extrema (hasta 81%), capacidad reversible (1593 mAh g^{-1} @ 50 mA g^{-1}), capacidad de ciclado (800 mAh g^{-1}@ 30 A g^{-1}), estabilidad de ciclado (~ 60% después de 1000 ciclos @ 1 A g^{-1}), eficiencia culómbica (~ 100%) y carga ultrarrápida (~ 35 segundos @ 30 A g^{-1}). Los rendimientos de almacenamiento de iones de Li presentados en este caso son significativamente superiores a los ánodos de tipo conversión reportados anteriormente. Una celda completa de Li-ion, compuesta de un ánodo de nanovarillas de Co$_3$O$_4$ y un cátodo de LiNiMnCoO$_2$, demostró una excelente estabilidad de ciclado (~80% después de 200 ciclos @ 1 A g^{-1}). Los estudios mecanísticos, incluido el mapeo in situ mediante XRD y EELS, ilustraron el proceso único de almacenamiento de iones de Li en los bordes de grano. El excepcional rendimiento del ánodo de nanovarillas de Co$_3$O$_4$ se atribuye a la sinergia entre el mecanismo de conversión de Co$_3$O$_4$ y el almacenamiento pseudocapacitivo de iones de Li en numerosas nanointerfases Li$_2$O/Co/Li$_{1.47}$Co$_3$O$_{3.72}$.

Los nanocables de TiO$_2$ rutilo, con vacantes de oxígeno, como ánodo altamente pseudocapacitativos para baterías de iones de litio de una alta densidad de energía (350 Wh kg^{-1}) y de potencia (2 kW kg^{-1}). Los nanocables de TiO$_{1.7}$ rutilo presentados en este caso exhibieron una excelente pseudocapacitancia (hasta 97%), capacidad específica (430 mAh g^{-1} @ 25 mA g^{-1}), capacidad de ciclado (66 mAh g^{-1} @ 100 A g^{-1}), estabilidad de ciclado (74% después de 30000 ciclos @ 50 A g^{-1}), eficiencia culómbica (~ 100%) y carga ultrarrápida (~ 7 segundos @ 100 A g^{-1}). Estos resultados son muy superiores a los valores reportados anteriormente para ánodos de baterías de litio basados en TiO_2. La celda completa de iones de litio compuesta por un ánodo de nanocables de TiO_2 rutilo, con vacantes de oxígeno, y un cátodo de $LiNiMnCoO_2$ verificó una excelente estabilidad de ciclado (80% después de 2500 ciclos a 1 A g^{-1}). Los estudios mecanísticos demostraron que la vacancia de oxígeno inducía la transición de los nanocables TiO_2 rutilo de una estructura cristalina a amorfa. El excelente rendimiento del ánodo de nanocables de rutilo $TiO_{1.7}$ se atribuye a la pseudocapacitancia de intercalación de iones de litio resultante de las vacantes de oxígeno.

Se presentaron baterías de iones de litio de alto rendimiento basadas en ánodos de nanoláminas de Co_3O_4 con defectos extremadamente pseudocapacitivos. El ánodo de nanoláminas de Co_3O_4 que se presenta aquí está compuesto de vacantes, dislocaciones y bordes de grano. La exclusiva microestructura 2D perforada permite un transporte de carga eficiente y se adapta a la expansión de volumen durante el proceso de carga/descarga. Estos ánodos exhibieron una pseudocapacitancia excelente (hasta 87%), capacidad específica (1490 mAh g^{-1} @ 25 mA g^{-1}), capacidad de ciclado (592 mAh g^{-1} @ 30 A g^{-1}), estabilidad de ciclado (85% después 500 ciclos @ 1 A g^{-1}) y eficiencia culómbica (~ 100%). El excelente rendimiento electroquímico de las nanoláminas de Co_3O_4 se atribuye a la pseudocapacitancia extrema resultante de la difusión ultrarrápida de iones de litio debido a la presencia de defectos.

Las estrategias de pseudocapacitancia, inducida mediante defectos, demostradas anteriormente se pueden extender fácilmente a varios ánodos de óxidos de metales de transición ecológicos/económicos (Fe_2O_3, MnO_2, etc.) para la próxima generación de baterías recargables de vida útil ultralarga y alta densidad de energía / potencia.

Table of Contents

Appendices

List of Abbreviations

EES	Electrical energy storage
Li-ion	Lithium-ion
LIBs	Lithium-ion batteries
SHE	Standard hydrogen electrode
SEI	Solid electrolyte interface
1D	One-dimensional
2D	Two-dimensional
3D	Three-dimensional
Co_3O_4	Cobalt oxide
CoO	Cobalt monoxide
$TiCl_3$	Titanium chloride
$Co(NO_3)_2 \cdot 6H_2O$	Cobalt nitrate hexahydrate
H_3PO_4	Phosphoric acid
H_2SO_4	Sulfuric Acid
TiO_2	Titanium oxide
TiO_2 **(R)**	Rutile titanium oxide
TiO_2 **(A)**	Anatase titanium oxide
TiO_2 **(B)**	Bronze titanium oxide
CH_4N_2O	Urea
HCl	Hydrochloric acid
EG	Ethylene glycol
Li_2O	Lithium oxide
$LiPF_6$	Lithium hexafluorophosphate
EC	Ethylene carbonate
EMC	Ethyl methyl carbonate
DEC	Dimethyl carbonate
PVDF	Poly(vinylidene difluoride)
NMP	N-Methyl-2-Pyrrolidone
GO	Graphene oxide
RGO	Reduced graphene oxide

N-RGO	Nitrogen-doped reduced graphene oxide
XRD	X-ray diffraction
XPS	X-ray photoelectron spectroscopy
TGA	Thermogravimetric analysis
SEM	Scanning electron microscopy
TEM	Transmission electron microscopy
SAED	Selected area electron diffraction
EELS	Electron energy loss spectroscopy
BET	Brunauer−Emmett−Teller
BJH	Barret−Joyner−Halenda
CV	Cyclic voltammetry
EIS	Electrochemical impedance spectroscopy
OCV	Open circuit voltage
FWHM	Full width at half maximum
nm	Nanometre
µm	micrometre
g	Gram
e^-	Electron
V	Voltage
mA	Milliampere
h	hour
secs	seconds
mAh g^{-1}	Milliampere hour per gram
A g^{-1}	Ampere per gram
Wh kg^{-1}	Watt hour per kilogram
W kg^{-1}	Watt per kilogram

List of Figures

Chapter 1

Introduction

1.1 Background and Motivation

Gradual exhaustion of fossil fuel as well as the increase of carbon dioxide emissions has been the major concern of global warming. These environmental impacts associated with greenhouse gas emissions have led to increase in global demands to develop renewable and sustainable energy sources.[1-3] Renewable sources such as solar, hydro, wind and geothermal power are considered as alternative and promising solutions to combat these concerns.[4-6] Renewable energy resources are only intermittently available and are dependent on time, weather, and location, while the demands and consumption of electric energy are relatively constant. Effective usage of these new energy sources is vital concerning their unbalanced power generation. Hence, a popular strategy is to develop advanced energy storage devices for delivering energy on demands. Essential criteria required for large-scale energy storage systems are low costs, less risk of safety for long-term utilisation, high round-trip efficiency, and long cycle life.[7] Presently available energy storage systems for various large-scale applications are classifieds into mechanical, chemical, electrical and electrochemical as shown in figure 1.1.[3, 7, 8]

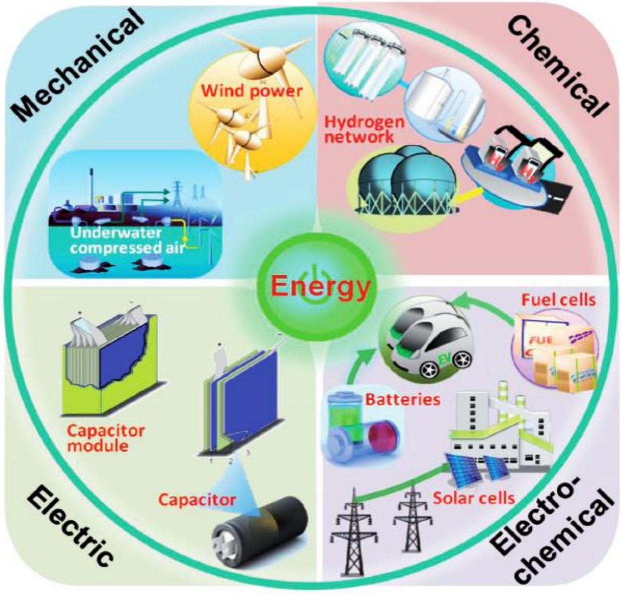

Figure 1.1. Different types of energy storage technologies for various applications.[7]

Energy storage in recent years is dominated by mechanical energy through pumped hydroelectricity, electrochemical storage systems that could possess a number of desirable characteristics such as long cycle life, pollution-free operation, controllable power and sufficient energy to meet different grid functions.[2, 3, 8] In this regard, various electrochemical storage systems like electrochemical capacitors, and rechargeable batteries have been considered as a promising candidate for large-scale applications. Rechargeable batteries in recent years demonstrated a great potential in powering portable electronics and electrification of transportation sector due to their beneficial features that includes various chemistries based on cheap, low maintenance, sustainable and recyclable materials.[1, 9, 10] Therefore, the demand for alternative clean and advanced renewable energy storage systems for instance rechargeable batteries, is experiencing a considerable growth.

1.2 Rechargeable Batteries

Development of rechargeable battery technology for highly efficient energy conversion and storage is fetching more importance in recent years. Battery technology has come a long way since the Italian physicist Alessandro Volta in 1800 described the first electrochemical cell, which came to be known as the Volta pile. Batteries are electrochemical devices that can store chemical energy and converts to electrical energy when connected to supply.[4, 11] They are divided into primary and secondary batteries based upon their reaction mechanisms. Primary batteries involve irreversible reactions that are limited in large scale applications due to their short life-time, high replacement cost and self-discharge. Secondary batteries also known as rechargeable batteries that can store chemical energy via redox reactions reversibly. Rechargeable battery systems should be compatible with complementary technologies such as solar, wind and geo-thermal so as to store the energy harvested from these intermittent sources. A typical battery includes anode and cathode coated on conductive substrates, an electrolyte solution and a separator that avoids short-circuit.

In this case, electrode materials with high electropositivity acts as anode and those with low electropositivity as cathode. Battery mechanism includes shuttling of ions between cathode and anode while charging and vice-versa during discharge. Hence, electrons flow to an external circuit producing electrical energy that determines the capacity (Ah kg^{-1}) of the device. Rechargeable batteries are currently being developed to power a diverse range of applications including portable electronics (mobiles, laptops, e-books etc.), electric vehicles and grid storage.[6, 9, 12-14]

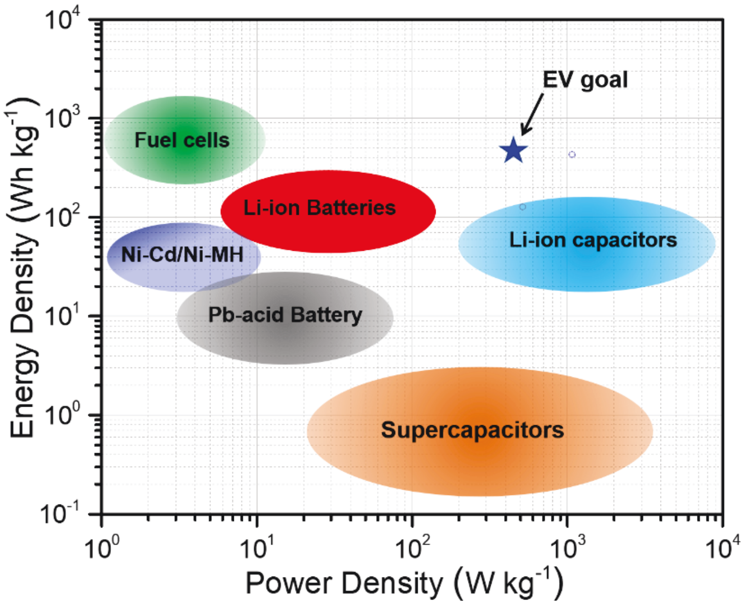

Figure 1.2. Ragone plot comparing different energy storage systems

Conventional battery technologies, such as lead-acid and nickel cadmium, are easily replaced by metal-ion batteries, fuel-cells and nickel metal hydride batteries due to their high energy density (Figure 1.2). Current rechargeable batteries are based on ion insertion/extraction in electrodes like lithium (Li)-, sodium (Na)-, magnesium (Mg)-, and aluminium (Al)-ion batteries. However, Na, Mg and Al have lower reducing potentials (-2.71, -2.37 and -1.66 V vs. S.H.E., respectively, compared to -3.04 V for Li) and low gravimetric capacities (1165, 2046, and 2978 mAh g^{-1}, respectively; compared to Li, 3850 mAh g^{-1}) than Li.[15-19] Lithium-ion batteries have achieved a great success due to their ample battery performance, higher operating voltages, superior energy and power densities, compared to other conventional battery systems as demonstrated in ragone plot (Figure 1.2). Rechargeable Li-ion batteries till date have comfortably replaced the existing batteries and captured a significant part of the portable battery market within a few years of their introduction.

1.3 Lithium-Ion Batteries

Lithium is the lightest of all metals that has a high electrochemical potential and superior energy density for weight than other elements. Lithium is used in several industrial applications including heat-resistant glass, and ceramics, lithium grease lubricants, flux additives for iron, steel and aluminium production, lithium batteries and lithium-ion batteries. Modern research in battery world is mostly focused on Li-ion battery, which has a great advantage over other systems.[1, 12, 13] G. N. Lewis initiated the first work on lithium-based batteries in 1912, but it was not until the early 1970s that the first commercial primary lithium battery reached the market. In 1970s, Whittingham proposed a rechargeable lithium-ion battery (LIBs) system with TiS_2 as active cathode material, lithium foil as anode and lithium perchlorate in dioxolane electrolyte.[11] Following ground breaking cathode research by a team of John Goodenough, the first commercial lithium-ion battery was released by Sony in 1991.[14, 20]

Secondary rechargeable lithium-ion batteries (LIBs) are attractive power sources due to their high energy density, and cycling stability compared to several rechargeable battery technologies.[1, 9, 10] Capability of storing large amounts of energy in a given volume and mass in a short time is the crucial characteristic of a battery for portable applications. This feature has guided most investigations of LIBs to achieve high volumetric (<600 Wh L^{-1}) and gravimetric (or specific) energy density (<250 Wh kg^{-1}) combined with high volumetric (<800 W L^{-1}) and gravimetric power density (<400 W kg^{-1}).[10, 21-23] As a result, LIBs have been successfully commercialised in various applications including portable electronics. Lithium-ion battery chemistry is similar to an electrochemical cell that transports lithium ions between positive and negative electrodes in an ion conducting electrolyte as shown in figure 1.3. Faster lithium-ion diffusion than commercial lead-acid and Ni-MH batteries enables LIBs to charge and discharge at higher rates. Advances in LIB technology also led to the development of electric-powered transportation vehicles and power grids. Portable energy solutions that carry out the practical use of electric vehicles (EVs), hybrid electric vehicles (HEVs) and plug-in hybrid electric vehicles (PHEVs) will further reduce dependence on fossil fuels. Hence, the primary challenge is to develop safe, rechargeable batteries for larger PHEVs and all-EVs of longer driving range, faster charging rates, and lower cost that can be extended to power grids.

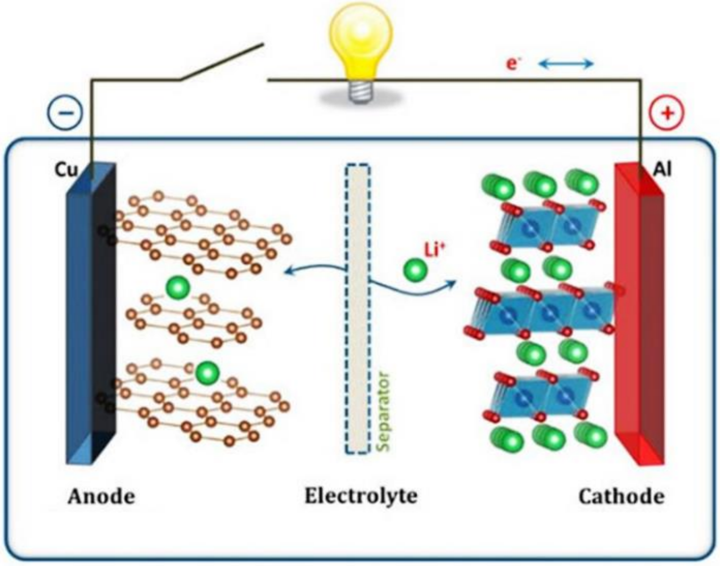

Figure 1.3. Schematic representation of a Li-ion battery mechanism.

1.4 General Trends of Lithium-Ion Battery Market and Development

Lithium-ion batteries have been leading the rechargeable battery market with continuous growth and rapid developments in various sectors. Application of lithium-ion battery technology for small scale industry is mainly related to the specific capacity growth of 18650 cylindrical-type cells. Increase in capacities of 18650 cylindrical-type cells could be credited to the improved electrode material performance and energy density. Over the past 30 years, specific energy of lithium-ion batteries has steadily increased while their cost has drastically decreased. Batteries used in most of the present electric vehicles and hybrid cars are usually based on lithium-ion technology. Electric vehicles came into the market with mass production of hybrid electric vehicle (HEV) models, such as Insight (Honda corp.) and Prius (Toyota corp.) in 1997.[20] Hybrid electric vehicles have a limited effect on fuel efficiency and reduction of CO_2 emissions since the rechargeable batteries are just used as an auxiliary power source. While the plug-in hybrid electric vehicles (PHEVs) receive more attention as environmentally friendly vehicles as they are driven by only electricity from high-energy rechargeable batteries. Currently, driving ranges for commercial electric vehicles from rechargeable batteries are 100-250 miles for one complete charge which is superior to any other systems (10 miles in case of Ni-MH batteries).[24] According to the United States Advanced Battery Consortium (USABC), the requirements defined for LIBs in PHEV applications are to have an energy density of 400 Wh kg^{-1} with 90% efficiency with a 5-year calendar life (Figure 1.2). Hence, hybrid electric vehicles, plug-in hybrid electric vehicles and electric vehicles developments have been the focus of the research in automotive sectors (Figure 1.4).

There are rising demands for power storage units that supplement irregular power generation and consumption patterns as the power generation from renewable energy sources, such as solar cells and wind power have recently increased. Rechargeable batteries with a good rate capability and rapid response are appropriate for short time power variation applications, such as through frequency regulation, for which Li-ion batteries have been recently employed. On the other hand, high capacity rechargeable batteries are required for load-levelling purposes, that are relatively cheaper to repeat charge-discharge cycle within a few hours, such as redox flow batteries.[20] Market for power storage applications is at the initial stage, but it is expected to grow rapidly in next 10 years with an expansion of renewable energy supplies and the smart grid system. Market share of rechargeable batteries in power storage applications such as long-range EVs, smart grid etc. will be dependent on their long-term reliability and charging times. Recent research is motivated on developing advanced battery systems that has the potential to attain the energy demands of next-generation applications by use of high-capacity electrode materials. Consequently, modern electrochemistry is focused on developing electrodes with high charge capacity (anodes) and high voltage stability (cathodes) for ultralong-life lithium-ion batteries.

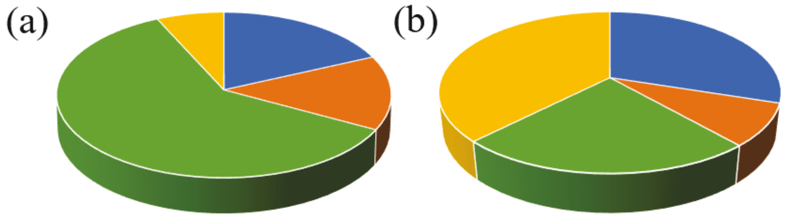

Sector	2010	2021
🟦 Automotive	18.30%	30.00%
🟧 Industrial	14.50%	8.50%
🟩 Consumer	60.30%	23.90%
🟨 Grid and renewable energy storage	6.90%	37.60%

Figure 1.4. Lithium-ion battery market in various sectors from 2010 to 2021.

1.5 Electrode Materials

Research and development on next-generation lithium-ion batteries are mostly focused on developing high-performance electrode materials.[10, 13, 25-27] Electrode materials should combine the advantage of high specific capacity, extended cycle life, safety, low cost, good mechanical and improved chemical stability. The deliverable energy of batteries is a function of its voltage and current that can be enhanced by (i) achieving a large voltage difference between anode and cathode, (ii) minimizing the volume and mass of active electrode material per exchanged electron, and (iii) avoiding side-reactions like oxidation or reduction (and thus compensation) of the liquid electrolyte.[28-30] Moreover, rechargeable cell reactions at both positive and negative electrode have to be highly reversible in order to maintain the specific charge for extended number of charge/discharge cycles. Performances of lithium-ion batteries largely depend on the inherent properties that includes morphology, composition, diffusion kinetics, conductivity, and surface characteristics of electrode materials.

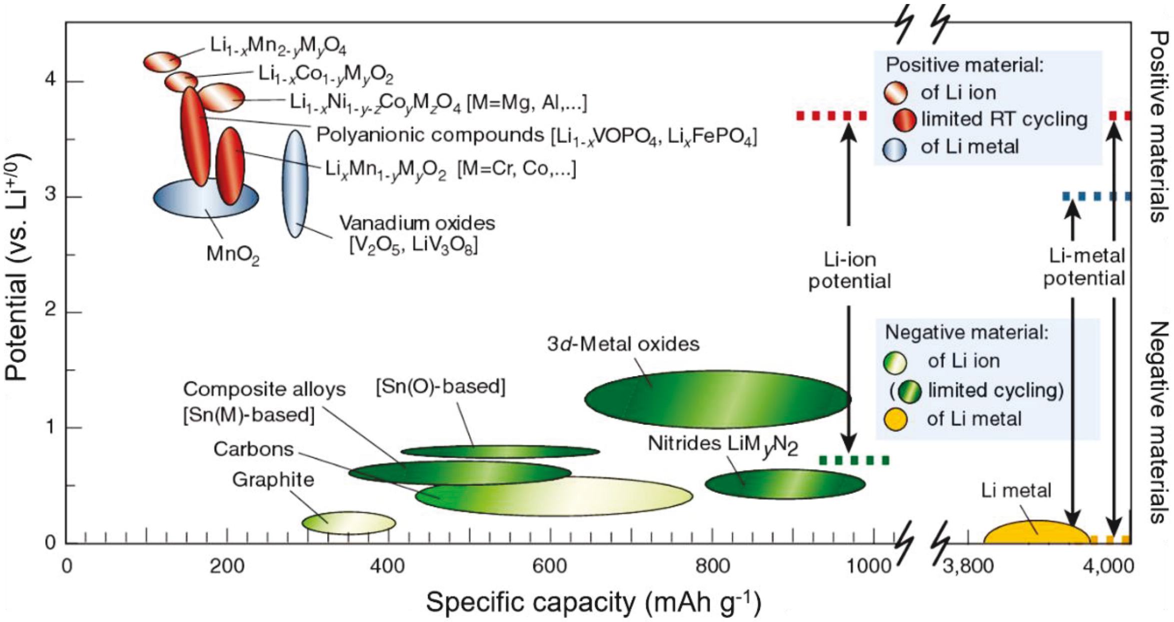

Figure 1.5. Voltages and specific capacities of positive and negative electrode materials.[34]

Commercial lithium-ion batteries that power the portable electronic equipment today are comprised of a graphite anode and a layered lithium transition metal oxide cathode (~3.6 V system) that can reach a practical energy density of 90-150 Wh kg^{-1} for a single cell.[18, 25, 31-33] This battery technology is not practical for electric vehicle applications due to its limited cycle life (especially at elevated temperatures) and safety features. However, there are ongoing developments in hybrid electric vehicle markets in which only part of the propulsion of the vehicle is driven by a battery, but the main aim is to develop full electric vehicles. This demands the progress in lithium-ion batteries with higher energy and power densities compared to the conventional state-of-the-art LIBs. Energy and power density of a battery is mainly determined by its output voltage and specific capacity, which are mainly dependent on the electrochemical performance of electrode materials (anode and cathode) (Figure 1.5). Various efforts in developing anode, cathodes and suitable electrolyte solutions, their advantages and disadvantages for lithium-ion battery application are summarized in the following section.

1.5.1 Anode Materials

Today's rechargeable lithium-ion batteries are developed after early batteries with metallic lithium anodes were plagued by the growth of lithium dendrites. It was later found that the lithium could intercalate into graphite and remain ionised (as Li^+) at the graphite lattice accepting an electron for the charge balance (LiC_6), hence the term lithium-ion battery was devised and marketed by Sony in 1991. Till now, most of the commercial lithium-ion batteries are usually based on carbonaceous anodes materials, mainly graphite.[18, 27, 35, 36] However, substantial research has been devoted for developing alternative high-capacity anode materials to further improve energy density and safety although graphite's performance is not the limiting factor in commercial systems. In this aspect, several anodes were investigated based on their reaction mechanism including intercalation, alloying and conversion.[36-39] Most promising electrode materials in each mechanism and their challenges for facilitating their use as higher capacity anode materials in rechargeable batteries are discussed below.

Intercalation type anodes

Intercalation based electrode materials are well-known for their widespread applications in most of the ambient temperature rechargeable battery systems. By definition, electrochemical intercalation of an ions from electrolyte into a crystal lattice of a solid host coupled with charge transfer between them (Figure 1.6).[10, 36] Stability of the host structure after insertion of guest ions is the key feature for intercalation mechanism. Lithium intercalation reaction of electrode materials significantly depends on surface properties like crystallinity, defects, or interfaces etc.[21, 36] Intercalation electrodes are capable of providing rapid Li ion transport through Li conductive 1D paths, 2D planes or 3D networks within relatively large individual particles. This property of intercalation mechanism offers the advantage of low-volume expansion on lithiation and delithiation that results in high mechanical and electrochemical stability to the electrodes. Li-intercalation reaction in electrodes can be represented by equation 1.1, where M_x signifies intercalation lithium host.

$$M_x + yLi^+ + ye^- \Leftrightarrow Li_yM_x \qquad (1.1)$$

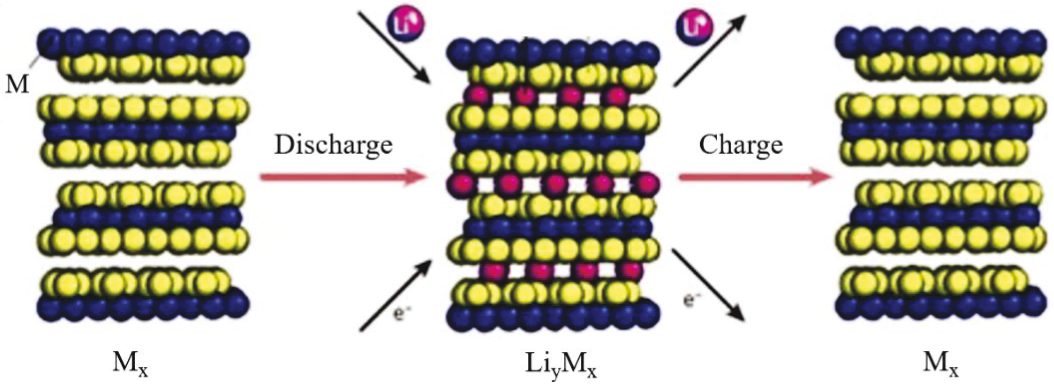

Figure 1.6. Schematic of Li-ion intercalation mechanism

Since the introduction of the first commercial LIBs, predominantly graphite has been the anode material of choice that is widely used in several portable applications.[17, 35, 40] Carbon has low cost, abundant availability, low lithiation potential vs $Li^{+/0}$, enhanced conductivity and relatively low volume expansion during charge-discharge processes. Li-ion intercalation into graphite at very low electrochemical potential (0.15-0.25 V vs $Li^{+/0}$) makes it a very attractive anode material among different insertion-type anodes.[10, 21] Electrochemical activity in carbon occurs with the intercalation of Li between the graphene planes that offer better conductivity, 2D mechanical stability, and improved Li transport. Its electrochemistry is based on the reversible reaction of Li ion into graphite inter-layers: $6C + xLi^+ + xe^- \Leftrightarrow Li_xC_6$ $(0 < x < 1)$, that includes 1 Li atom per 6 C.[40-42] Formation of LiC_6 during discharge yields a theoretical capacity of 372 mAh g^{-1}, which satisfies the demand of current portable electronic devices. However, graphite anodes are not attractive for wide range of applications due to its low energy density, and safety issues.[12, 35, 36]

Lithium titanate (LTO) is another intercalation type anode that has huge potential to replace graphite and it has already been successfully commercialized for few applications.[21, 43] High-rate capability, improved cycle life, negligible SEI formation and high lithiation potential are key features of LTO based anodes. Phase change caused by lithiation/delithiation is trivial (0.2%) as LTO results in zero strain intercalation reaction and hence low volume changes during charge-discharge process. Moreover, a high equilibrium potential (1.55 V vs. $Li^{+/0}$) allows LTO to be operated in a voltage window >1 V, largely eluding the SEI growth and Li dendrite formation.[43-45] However, low specific capacity (175 mAh g^{-1}) and surface reactions that are unavoidable causes severe gassing issues due to a reaction between organic electrolyte and electrodes, which hinders LTO anode from high power applications.[10, 46] Though this reaction can be suppressed by carbon coating, but carbon can catalyze and accelerate electrolyte decomposition in formation of an SEI, particularly at high temperatures. Further, most successful class of intercalation materials next to carbon and LTO are titanium dioxide-based anodes. All the polymorphs of TiO_2, namely anatase, rutile, bronze and anionic or cationic deficient designs, defect structures etc. were investigated as possible insertion type anodes.[45, 47-49] Irrespective of the phase, TiO_2 materials have a theoretical capacity of 335 mAh g^{-1}. Additionally, TiO_2 phases usually share all characteristic features of LTO anodes like higher intercalation potential, near zero SEI layer, thermally stable and long cycle life. Moreover, V_2O_5, $TiNb_2O_5$, black phosphorus, Nb_2O_5, etc. have also been extensively studied as intercalation type anodes due to their vivid properties.[21, 50-53] However, intercalation-type anodes are limited due to their higher irreversible capacity loss, larger voltage hysteresis, lower volumetric capacity, moderate energy and power density.

Alloying types anodes

Alloying materials are considered as one of the promising anodes for lithium-ion batteries because of their characteristics including safety, and high specific capacity compared to conventional intercalation-based anodes. Schematic of the Li-alloying reaction mechanism is briefed in figure 1.7. There are numerous metals and metalloids that can be alloyed with Li electrochemistry that includes elements from group III (B, Al, Ga, and In), group IV (Si, Ge, Sn, and Pb), and group V (P, As, Sb, and Bi) in the periodic table.[14, 26, 37, 54-58] However, only a few elements like Si, Sn, Al, Sb and P have been widely investigated due to their abundance, low cost, and environmentally benign. In particular, Si and Sn have been intensively focused because of their promising electrochemical properties, such as large capacities (4200 mAh g^{-1} for Si and 993 mAh g^{-1} for Sn) and moderate operating potentials.[59, 60] Theoretical specific capacities of alloy anodes are 2-10 times higher than that of graphite and 4-20 times higher than LTO. Moreover, alloy anodes exhibit moderate operating potentials below 1 V (Si vs. $Li^{+/0}$: 0.4-0.5 V and Sn vs. $Li^{+/0}$: 0.5-0.6 V). This moderate potential averts the safety concern of lithium deposition unlike graphite anodes (~0.02 V vs. $Li^{+/0}$). Lithium alloying mechanism could be represented as in equation (1.2), where M represents alloying anode.

$$M + xLi^{+} + xe^{-} \Leftrightarrow Li_{x}M \tag{1.2}$$

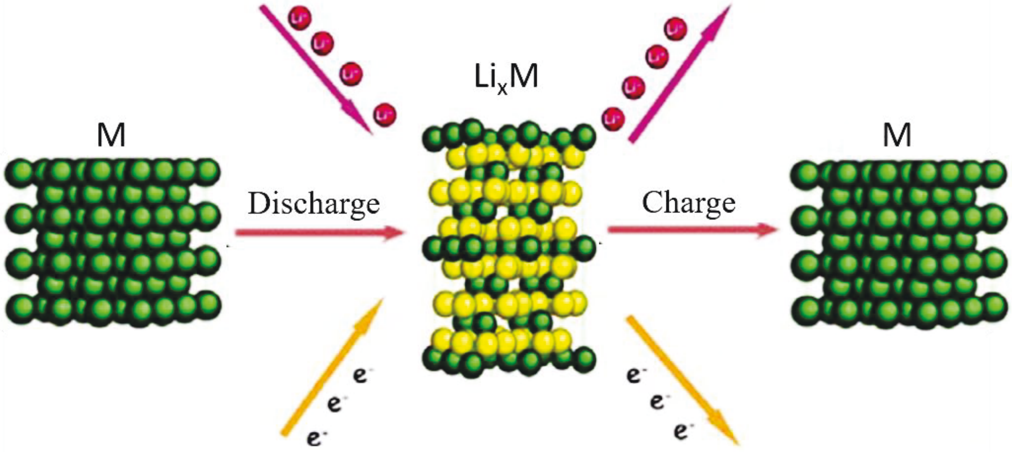

Figure 1.7. Schematic of Li-ion alloying mechanism

However, the main challenge for the implementation of alloy anodes is their large volume expansion up to ~300% , which often leads to pulverization of electrode and results in poor cycle stability.[26, 37] In addition, first-cycle irreversible capacity loss of alloy anodes is too high that largely hinders them from practical applications. Immense first-cycle capacity loss compared to intercalation and conversion anodes is attributed to (a) loss of active material, (b) SEI formation, (c) Li trap in the host alloy, (d) reaction with oxide impurities and (e) agglomeration of electrode material. These capacity loss and huge volume change largely affects the cycling stability of alloying-based electrodes. Significant features in reducing the irreversible capacity of alloy anodes are to improve the purity of alloy materials, tuning the particle size and reducing the capacity loss incurred from conductive stabilizers like carbon. Several approaches were widely employed for improving the cycling performance of alloy anodes that includes (a) multiphase composites, (b) porous structures, (c) increasing intermetallic phases, and (d) electrolyte additives. Multiphase hybrid carbon-matrix nanocomposites exhibited the most promising performance for practical use. Besides, production cost for these pure elementary substances can be quite high since most of the alloying-type anode materials (e.g., Si) are not in their natural forms (e.g., SiO_2). Nevertheless, extensive research has been carried out to address these issues and significant progress has been made during the last two decades.

Conversion type anodes

Conversion reaction based anode materials theoretically store lithium with high specific capacities through reversible redox reactions between Li^+ and transition metal cations. A wide range of transition metal oxides, sulfides, selenides, fluorides, nitrides and phosphides have been explored as conversion-type anode materials for lithium-ion batteries.[38, 39, 61-64] Considering that many conversion type anodes (e.g., FeS_2, Fe_3O_4, and MnO_2) are in their natural forms (pyrite, magnetite, and pyrolusite), the production costs might be relatively low in comparison with that of alloy-type anode materials. Reaction mechanism involved during Li-ion storage and cycling is different from that of intercalation and alloying mechanisms as presented in figure 1.8 and equation 1.3, where M is the transition metal and X is anion.

$$M_aX + nLi^+ + ne^- \Leftrightarrow aM + Li_nX \tag{1.3}$$

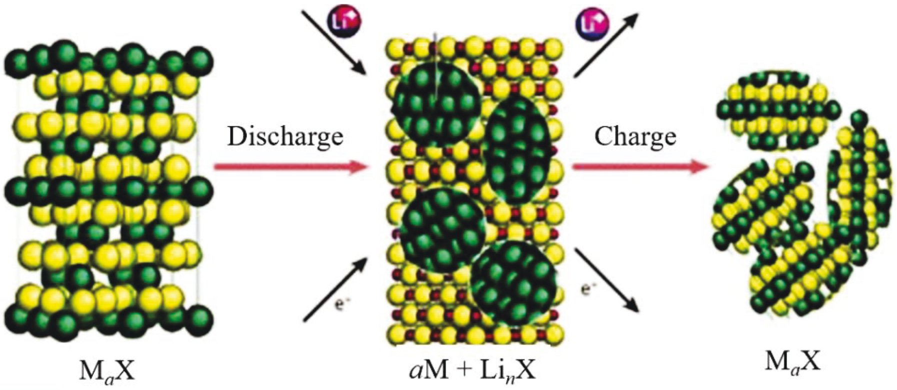

Figure 1.8. Schematic of Li-ion conversion reaction.

Extensive research have been focused on conversion type transition metal oxide anodes since Tarascon proposed them as efficient anode materials in 2000.[35] These anodes exhibit higher theoretical specific capacities and several oxides (such as 890 mAh g^{-1} for Co_3O_4, 1007 mAh g^{-1} for Fe_2O_3 etc.) can deliver 3-4 times high stable gravimetric capacities than that of intercalation and carbon anodes respectively.[65-71] High working potential (0.8-1.3 V) of these anodes avoid the formation of lithium dendrites on electrode surface and hence extremely safe than graphite anodes. Hence, conversion type anodes are more promising due to their higher specific capacity, better safety than intercalation-type materials, and their low production cost, over intercalation and alloying-type anodes.

However, conversion type anodes are limited in battery applications due to their intrinsically poor electronic and ionic conductivity, large volume expansion (~200%) and agglomeration of active materials during charge-discharge process. In this case, a large volume expansion occurs due to the excess formation of insulating Li_2O, which forms as a part of solid electrolyte interfaces (SEI) in the initial cycles.[72, 73] Moreover, Li_2O has low electrical conductivity that can result in large irreversible capacity and a huge voltage hysteresis, much of which remains even at extremely higher rates. These drawbacks of conversion type transition metal oxides largely affects the capacity at high currents and also cycling stability. Recently, researchers have been exploring several techniques to minimize the capacity decay at higher rates and increase cycling performance of transition metal oxides. Nevertheless, conversion type anodes are widely investigated, as it is believed that the use of transition metal phases reacting with Li-ions through conversion reactions holds the promise of high energy density Li-ion devices. In addition, materials with different degrees of covalence and transition metal oxidation state exhibiting this mechanism could enable the tuning of operating voltages, with values suited for application in positive (fluorides) or negative electrodes.

1.5.2 Cathode Materials

Many efforts have been devoted in recent years to develop high capacity and high voltage stable cathode materials for large scale applications including grid storage and electric vehicles. In general, the cathode materials for commercial rechargeable batteries involve transition metal oxides or phosphate based active materials such as $LiCoO_2$, $LiMn_2O_4$, $LiFePO_4$, etc.[74-76] Goodenough et al. revolutionised LIB research by introducing $LiCoO_2$ (LCO), one of the commercially successful layered transition metal oxide cathodes. Main features of cathode material should include low diffusion barrier, good electrical conductivity, high specific capacity, and excellent structural stability at higher voltages during charge-discharge process. Three different choices of cathodes materials employed in lithium-ion batteries (Figure 1.9) are: (1) Layered compounds with a closely packed anionic lattice in which alternate layers are occupied by a redox-active transition metal. This group includes $LiMX_2$ (e.g., $LiTiS_2$, $LiCoO_2$, $LiNi_{1-y}Co_yO_2$, $LiNi_yMn_yCo_{1-2y}O_2$ etc.) where M is transition metal. (2) Olivine cathodes that have more open structures, and polyanion $(XO_4)_n$ arrangements to reduce the redox energy of 3d-metals and suit fermi level of anode materials such as transition metal phosphates. (3) Spinel $Li[M_2]O_4$ structure that offers a 3-D framework of face-sharing tetrahedral and octahedra with a cubic symmetry $Fd\overline{3}m$ for an effective diffusion process. Each of these three cathodes have their advantages and disadvantages.

Layered structure gives the highest practical capacity (currently up to ~180 mAh g^{-1}) among the three, but suffers from structural and/or chemical instabilities during extended cycles depending on the chemical composition and state of charge (lithium content in the electrode)[28].

Structural instability arises from a migration of the transition-metal ions from the octahedral sites of the transition-metal layer to the octahedral sites of the lithium layer via a neighbouring tetrahedral site.[77] Low octahedral site stabilization energy of Mn^{3+} (i.e., a small difference between the crystal field stabilization energies in the octahedral and tetrahedral sites), can easily migrate and suffer from a structural transition from layered to spinel phase during cycling.

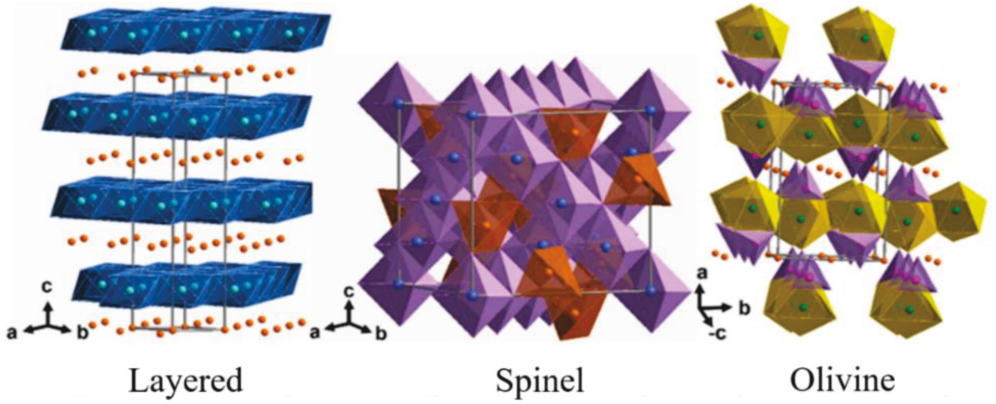

Figure 1.9. Schematic of layered, spinel and olivine crystal structures.[28]

On the other hand, Co^{3+} with high energy offers excellent structural stability, but it suffers from poor chemical stability on extracting >50% lithium from $LiCoO_2$ (>50% charge).[78, 79] In contrast, Mn offers excellent chemical stability and interestingly, Ni is between Mn and Co in structural and chemical stabilities as Ni^{3+} has higher stabilization energy than Mn^{3+}. Moreover, $Co^{3+/4+}$:t_{2g}^{6-x} with a direct Co−Co interaction along the shared octahedral edges and a partially filled t_{2g} band makes $Li_{1-x}CoO_2$ a metallic conductor for x>0.1. In contrast, both $Li_{1-x}NiO_2$ and $Li_{1-x}MnO_2$ remain semiconductors for $0 \leq (1 - x) \leq 1.0$ as the redox-active or partially filled e_g band is involved in a 90° M−O−M (M = Mn or Ni) bonding. Nevertheless, with a high degree of Ni−O covalence, $Li_{1-x}NiO_2$ offers adequate electronic conductivity. With a 2-D lithium-ion diffusion, all three $Li_{1-x}MO_2$ (M = Mn, Co, and Ni) systems offer good lithium-ion conduction. Considering the advantages and disadvantages among the three, the industry largely uses compositions, such as $LiNi_{1/3}Mn_{1/3}Co_{1/3}O_2$ (NMC-333), to realize the best possible among the three metal ions.[28, 32, 80]

$LiMn_2O_4$ with spinel cathode with a 3-D structure and lithium-ion diffusion offers high rate capability and good structural stability without phase transformation. However, it suffers from a limited practical capacity (<120 mAh g^{-1}) and Mn dissolution caused by a disproportionation of Mn^{3+} into Mn^{4+} and Mn^{2+} ions. On the other hand, olivine $LiFeO_4$ cathode offers good thermal stability and safety without oxygen release as the covalently bonded PO_4 groups tightly hold the oxygen. However, $LiFePO_4$ cathode suffers from limited practical capacity (<160 mAh kg^{-1}), in particular volumetric capacity, lower operating voltage of ~3.4 V, poor electronic and lithium-ion conductivity. Although $Fe^{2+/3+}$ redox couple lies at a much higher energy than the $M^{3+/4+}$ (M = Mn, Co, and Ni), inductive effect lowers the $Fe^{2+/3+}$ energy and increases the operating voltage to ~3.4 V.[52, 81] Limited electronic and ionic conductivity have to be controlled by reducing the particles to nanosize and by carbon coating, which further decrease the existing low volumetric energy density. Volumetric energy density is influenced by the crystallographic density of the structures. Therefore, among the three insertion cathodes, the layered oxides can provide the highest energy density. Hence, lithium-rich layered oxides have been widely investigated due to their high specific capacities than other cathodes and high operating potential windows compared to stoichiometric layered oxides, which are much more suitable for next-generation LIBs.

1.6 Electrolytes and Separators

Electrolytes in batteries must cater to the needs of both electrodes, and hence new battery chemistries have incurred new electrolyte compositions. Improvements in electrolytes have been incremental in the past decade as compared to the active dynamics of cathode research. This is due to lack of understanding in molecular interactions occurring within the electrolyte and at the solid interfaces with which electrolyte is in contact. Moreover, these solid electrolyte interfaces (SEI) can be on electrode surface or at the complex porous structure of electrodes.[82, 83] An advanced electrolyte for a battery will require

- Higher ionic conductivity to give high cycling rates over a wide range of temperature, ideally from -30°C to 100°C.
- Higher stability, both chemical and electrochemical, to allow for higher voltage systems and to increase safety.
- Higher compatibility with other cell components, both for better wettability and for lower corrosion/reactions rates.
- Lower cost and decreased environmental impact.

Currently, lithium-ion batteries employ electrolytes containing lithium hexafluorophosphate ($LiPF_6$) salt dissolved in the organic carbonate solvents. $LiPF_6$ salt can produce hydrogen fluoride (HF) in even traces of moisture that can cause dissolution of cathode metals causing severe capacity loss.[84-86] However, usage of this salt could be attributed to three distinct but interdependent factors: (1) Electrolyte components (especially solvents) are more sensitive to operating potentials rather than capacity of electrodes. Therefore, major changes in these compositions are not mandatory, provided that the new chemistries operate reasonably within the electrochemical stability window of carbonate-based electrolytes. (2) More effective design and use of electrolyte additives (VC or FEC) became customary practices, aided by the significant advances in tuning of solid electrolyte interphases (SEI) on electrode surfaces. These facilitated sacrificial components to maintain the electrolyte compositions more static. (3) Perhaps most importantly, confined by cost consideration, the battery industry has been reluctant to change existing supply chain, unless there is sufficient incentive or benefit. In a sense, the established infrastructures producing $LiPF_6$ and organic carbonates constitute the biggest hurdle to the adoption of any new electrolyte components. A few exceptions do exist, such as the 5 V class spinel ($LiNi_{0.5}Mn_{1.5}O_4$, 4.6 V) or cobalt phosphate ($LiCoPO_4$, 4.8 V) chemistry, whose operating potentials are beyond the stability limit of the carbonate-based electrolytes (4.5 V) would require new bulk electrolyte solvents other than some additives. Similar requirements might also arise from "Beyond Li -ion" chemistries, in which dynamic phase/structural changes present severe challenge to carbonate-based electrolytes.

Separator is a safety component between the cathode and anode, preventing direct contact, i.e., short-circuiting, while being permeable to lithium ions. Most common separator materials are polyethylene and polypropylene. These materials can melt resulting in degradation of micro-porous properties and block the ion flow when the internal cell heats excessively due to thermal runaway. This "shutdown" function damages the cell irreparably, but avoids major negative consequences. Li-ion cells can also include other safety features and elements such as components that strengthen the cell mechanically, insulators on the edges of the electrodes where short circuit accidents are most likely to occur.

1.7 Drawbacks of Lithium-Ion Batteries

Although the progress of lithium-ion batteries has been significant since their introduction, there are numerous technical limitations for the future needs of several high-power and high energy applications including automotive sector. Current lithium-ion technology based on insertion-anodes and cathodes will continue for foreseeable future, despite their limited energy density (100-300 Wh kg^{-1}) dictated by their crystallographic sites available besides the structural and chemical instabilities at deep charge. Numerous efforts have been made towards alloying and conversion anodes as they offer up to an order of magnitude higher capacities than insertion electrodes, but their practical viability is encountered with challenges. Major drawbacks of current Li-ion battery technology include

- Capacity decay upon extended cycling
- Energy efficiency at higher current rates is too low due to large polarization losses during charge and discharge.
- Energy density and power density (or rate capability) of present battery technology is insufficient for the intended applications.

When compared to consumer electronics, automotive applications have more stringent technical requirements such as calendar life (10 years), cycle life (1000 cycles), temperature range (-30 to 52 °C), and cost ($100/kWh).[15, 28] This high performance requirements are largely responsible for the 17-year delay between the introductions of LIBs in consumer versus automotive applications.

A variety of challenges and opportunities exist for automotive LIBs in the present day. Further developments in energy storage efficiency (by both weight and volume) are necessary to advance the competitiveness of electrified vehicles. Ability in rapid and accurate validation and predict long battery life is an important area of development. Also, continued cost reduction of LIBs on a $/kWh basis is both challenging and necessary to increase the opportunity for wide-scale adoption of electric transportation. Automotive LIBs are also expected to meet or exceed the safety performance of existing gasoline powered internal combustion engine (ICE) vehicles. ICE powered vehicles have also created a customer expectation of fast refueling, which is a large challenge for LIB technology to match. Although the overall performance of automotive LIBs has improved greatly in recent years, major challenges and opportunities remain unaddressed. Depending on the application, trade-offs among the various performance parameters that includes energy, power, cycle life, cost, safety, and environmental impact are often needed that are linked to severe materials chemistry challenges.

1.7.1 Energy-Density and Cycle-Life Limitations

Higher energy-density (100-250 Wh kg^{-1}) and specific energy of LIBs have allowed the technology to supplant competing battery chemistries in almost all markets and applications. Non-aqueous LIBs are able to maintain cell-voltage levels approximately 3-times greater than incumbent aqueous rechargeable chemistries such as nickel metal hydride (NiMH) and nickel cadmium (NiCd).[87] However, since their introduction, the basic electrochemical couple of high-energy designs (transition metals vs. graphite) have not changed, leading to only marginal improvements in nominal voltages of LIBs. Hence, recently verified progress in specific energy advances resulted from engineering improvements in active material capacity and cell/electrode optimization, posing a significant challenge for implementations in several high-power applications. Moreover, battery durability is a critical requirement for the continued proliferation of EVs and smart grids.[88] In addition, adequately precise test equipment is required to avoid propagating uncertainty in derived quantities such as battery power and energy.[89] Nevertheless, lack of viable future cathode material to continue LIB energy improvement provides a significant challenge to the continued development of the field.

1.7.2 Power-Density Limitations

Charging time is a key parameter for several applications including long-range electric vehicles and power grids that exceeds the total range of their battery. LIBs offer high-energy in part because of the low electrochemical potential for lithium-ion insertion in carbon which maximises the available cell-energy. Unfortunately, this places the negative electrode potential close to that of lithium metal, which raises the risk of unintended lithium plating. This in turn leads to irreversible capacity loss, reduced performance, and increased risk of short-circuiting and thermal runaway.[33] This is the primary factor limiting adoption of faster charging rates, i.e. power density (250-400 W kg^{-1}). As a result, electrochemistry society is also focused on developing advanced charging techniques for healthy and safe fast charge. Recent studies demonstrated that the development of advanced electrode materials for fast-charging batteries can be achieved through improving diffusion coefficient of lithium-ions.[90, 91]

1.7.3 Recent Developments in LIB Technology

Lithium-ion batteries will be able to achieve >250 Wh/kg total cell energy at beginning of the life based on the current progress and materials chemistry research efforts.[30] Unfortunately, this energy content is not sufficient to meet the automotive energy targets once this performance is converted to usable, battery pack-level.[30, 92] This looming challenge led to the initiation of various beyond lithium ion research initiatives approximately a decade ago. Many approaches are being pursued in developing lithium metal, lithium air and lithium sulfur batteries that has higher energy densities compared to Li-ion batteries (100-250 Wh kg^{-1}).[15] Lithium air has struggled with cycle life and energy efficiency challenges that limited its significant contribution to the research.[93] Sulfur chemistries revealed superior potential than lithium air, finding use in niche market applications, but are restricted by formation of polysulfides, stability and volume concerns, given their low densities.[94] Beyond lithium-ion technology that has advanced the furthest in the past decade has been the lithium metal system. Progress and potential impact of lithium metal cells are underscored by recent issuance of automotive lithium metal cell targets. Challenges of developing long-lasting lithium metal cells will require an improved understanding of lithium mechanics, lithium-electrolyte interfaces and unavoidable dendrites growth.[19, 30, 95] However, the basic design of these metal cells will inherit majority of the engineering and materials chemistry improvements of the system.

Table 1. International electric vehicle battery pack goals at end of life.

Groups	Specific energy (Wh/kg)	Specific power (W/kg)	Cost ($/kWh)	Calendar life (years)	Cycles
USABC	235	470	125	10	1000
EUCAR	288	1152	84	Vehicle life	24 MWh
NEDO	250	1500	190	10-15	1000–1500

Automotive industries have published cathode and anode specific energy goals to help guide the research community with targets as demonstrated in table 1. As discussed earlier, LIB anode market has historically been dominated by carbon anodes, which are incapable of meeting future energy targets. Hence, most widely researched lithium and silicon anode materials are both capable of meeting the energy targets, depending on how they were used. Technical issues involved in utilizing lithium metal in automotive applications are large and require significant engineering and concerns on availability are too high. On the other hand, carbon/silicon have been commercialized recently and silicon has almost an order of magnitude greater gravimetric energy than that of carbon. However, pure silicon has practical limitations due to the large volume changes during charge-discharge cycles and results continuous solid electrolyte interphase (SEI) formation and particle isolation during cycling. Hence, conversion-based transition metal oxides with higher capacity of 1000-2000 mAh g^{-1}, has potential to meet the industrial targets. As a result, this system can afford to tolerate additional weight and volume from strategies that accommodate the lithium storage capacity while maintaining the electrode structure and stable interfacial chemistry.

There are several opportunities at the cell and battery levels to improve fast charging, such as electrode engineering, new electrode chemistry, and thermal management. Electrode engineering can lead to optimised thicknesses and porosities that can reduce voltage polarization. This in turn helps stabilize the voltage to allow for lithium intercalation. Further, electrode engineering is able to modify the power-to-energy ratio (P/E) of cells across a substantial range, even considering the same basic chemistry. Based on charge rates defined by the highlighted region for each cathode chemistry (Figure 1.10), it is clear that the high power can be achieved through proper engineering of electrode structure while using same active material. As a result, researchers should mainly focus on high-energy materials for next generation Li-ion battery technology.

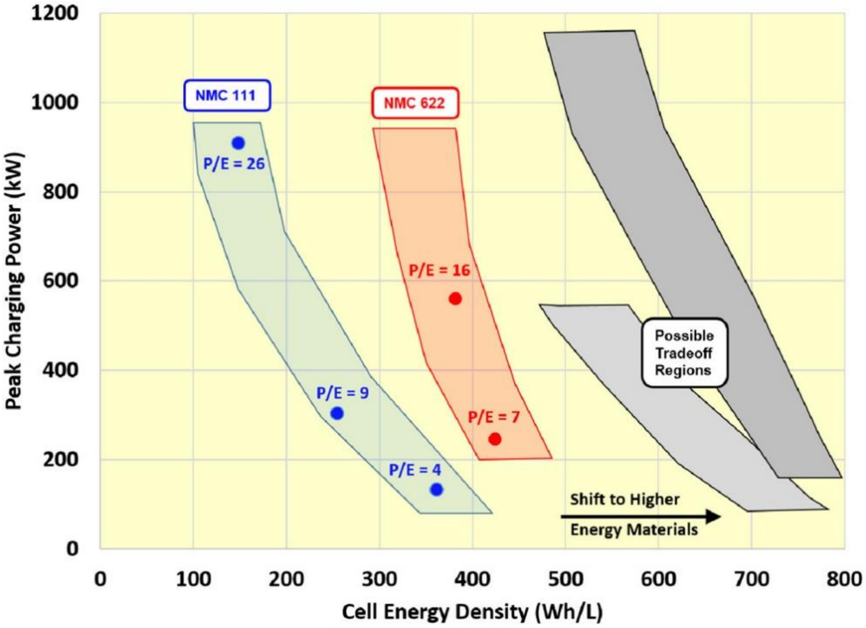

Figure 1.10. Estimated battery peak charging power versus cell energy density for groupings of similar active material chemistry. All data points feature graphitic carbon anodes paired with the noted cathode chemistry.[30]

With the challenges encountered, a feasible near-term strategy is to focus on high-capacity electrodes, liquid electrolytes compatible with and forming stable SEI on anodes and cathodes. This could only be achieved through a properly designed nanostructured electrode materials as well as cheaper and safer materials and with lower productions costs. Most widely used strategies to improve the LIB performance include fabrication of nanostructures such as nanoparticles, nanosheets, nanorods, nanowires etc.[34, 38, 68, 69, 96-100] Another major approach employed is the hybridization of active materials with carbonaceous substrates such as graphene, carbon nanotubes and carbon fibres.[72, 101-104] These methods could result in enhanced electronic conductivity and reduced particle agglomeration that leads to superior electrochemical performance, mainly in high-capacity conversion and/or alloy-based anodes.

1.8 Nanostructured Electrode Materials for Lithium-Ion Batteries

Ever-expanding markets of portable electronic products, power grids and electric vehicles stimulate and require the development of LIBs with superior performance such as higher energy density, larger power density, and longer cycle life. Several parameters like morphology, compositions, ion diffusion kinetics, conductivity, and surface characteristics of electrode materials need to be optimised to obtain these performances. Hence, studies to develop various electrode materials for high performance stable lithium-ion batteries are quite active and considerable advancement has been made based on smart material design.[38, 100] One of the most widely used strategies to improve the electrochemical performance is the fabrication of nanostructures such as nanoparticles, nanosheets, nanorods, nanowires, and nanospheres. Development of nanoscience and nanotechnology has enabled a paradigm shift in material design and provided new avenues for improving the performance of LIB electrodes.

Nanostructured materials are currently of interest for various energy storage technologies and mainly lithium-ion batteries due to the improved energy contents per weight and volume at reduced cost.[7, 19, 105] Several characteristics including high surface area, porosity, surface to volume ratio etc. make it possible to introduce new active reactions, reduce the Li-ion diffusion path, and improve electronic conductivity that could decrease the internal resistance and results in higher specific capacities even at larger currents. Benefits of engineering the electrode materials to nanoscale are briefly summarised.

- ✓ Large surface area (or surface to volume ratio) increases the contact area for electrode-electrolyte interaction and hence escalate the number of active sites for electrochemical reactions to reduce the electrode polarization and improve power stability (rate capability), energy efficiency, and usable energy density.
- ✓ Short diffusion length associated with the nano-sized electrodes effectively reduces the ion and electron transport path during charge-discharge process.
- ✓ Particularly, reducing materials to nanoscale can also increase lifespan by withstanding the volume-changes during extended cycling besides providing a short diffusion path for fast charging and more electroactive sites for enhanced capacity.
- ✓ Improved mechanical strength and structural integrity of electrodes represent another unique property of well-engineered nanostructure. It is well-known that low-dimensional nanomaterials have high mechanical strength, more resistance to mechanical damage and can be engineered to allow volume-change only in particular directions.
- ✓ Bulk electrodes materials that are inactive towards Li-ion electrochemistry, becomes active in nano-regime. These findings have led to revisiting electrode materials thought to be non-

promising in the past. Specific examples include nano-sized transition metal oxides, which show sluggish kinetics in the bulk become promising in the nanoscale regime.

- ✓ Redox potentials of electrode materials can also be modified by tuning the nanostructures that could result in high cell operating voltage and hence high energy-density.

Recently demonstrated nanostructured materials led to a new Li-ion storage mechanism, enhancing specific capacities compared to the conventional electrodes and bulk.[106-108] These studies reported the interfacial Li-ion storage on the surface and/or defects is the cause of additional specific capacities. However, increased reactivity in nanostructured materials often leads to excess SEI growth and Li_2O formation in case of transition metal oxides, thus leading to capacity decay on extended cycling. Nevertheless, development of fast charging, high-capacity electrode materials with excellent cycling stability remains as a challenge.

1.9 Pseudocapacitive Charge Storage

Pseudocapacitive charge storage has been recently demonstrated as a promising strategy to achieve ultrafast charge storage, mainly in high-capacity electrodes such as transition metal oxides and sulfide. Pseudocapacitance is a faradaic energy storage based on fast redox reactions at the surface or near-surface region of electrodes, where electrosorption/ electrodesorption occurs with charge transfer without any bulk phase transformations.[7, 109-111] Main advantage of this process is its diffusion-independent nature, which is superior to conventional conversion, insertion and alloying process.[109] Charge storage process in this case is independent of the bulk electronic-ionic conductivity of electrodes because of its surface phenomena. Ultralong cycling stabilities and high-power densities and can be obtained for pseudocapacitive electrodes due to the minimum structural changes and diffusion independent Li-ion intercalation, respectively.

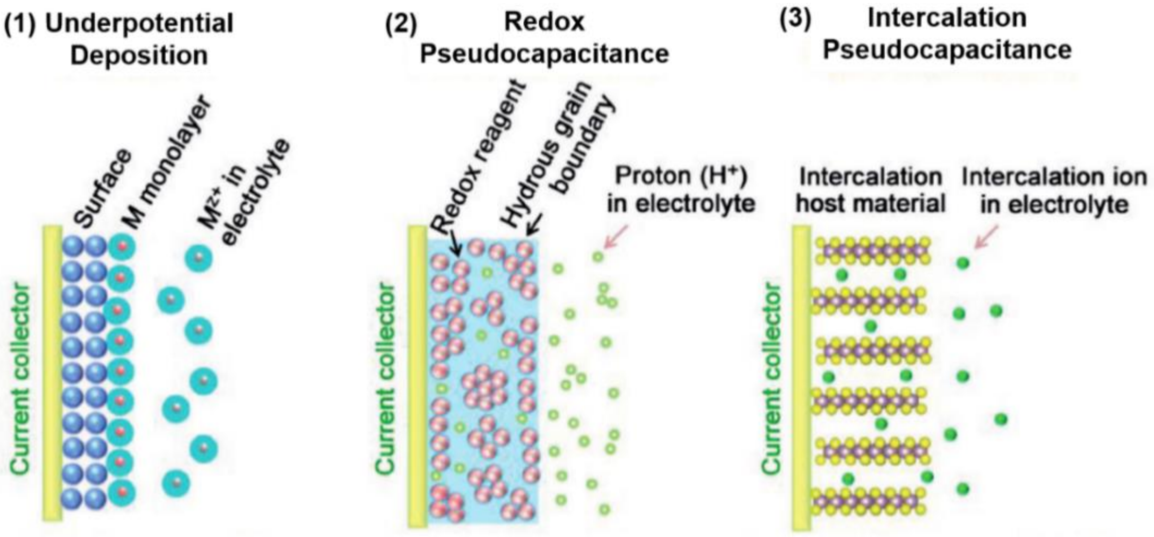

Figure 1.11. Different types of reversible redox mechanisms that give rise to pseudocapacitance: (1) underpotential deposition, (2) redox pseudocapacitance, and (3) intercalation pseudocapacitance.[7]

According to Conway et al., pseudocapacitive charge storage can be classified into three types: (1) underpotential deposition, (2) surface redox system, and (3) intercalation system as shown by the schematic diagrams in figure 1.11.[109, 111-114] An adsorbed monolayer forms on the electrode surface when a potential is applied due to the reduction of metal ion resulting in a less negative potential than their equilibrium potential, this process is referred to as underpotential deposition.[115] This pseudocapacitance can be applied to metal deposition and other adsorbed layers, for example, deposition of Pb on Au, H from H_2O or H_3O^+ etc.[116] Surface redox pseudocapacitive mechanism involves the adsorption of electroactive ions onto the surface or near-surface region of electrode materials and hence faradaic reactions occurs with charge-transfer. Typical examples include transition metal oxides like RuO_2, MnO_2, Fe_2O_3, TiO_2, V_2O_5, Nb_2O_5, $Li_4Ti_5O_{12}$ and conducting polymers generated using electrochemical methods.[117-124] No chemical transformation take place in this case during lithiation and delithiation reactions. However, a reversible functionalized molecular layer forms on electrode surface due to the faradaic reactions. Potential of electrode has a linear dependence on charge and is proportional to the area of electrode surface with electroactive ions. Intercalation pseudocapacitance is another faradaic process occurring without any crystallographic phase change unlike the conventional insertion mechanism. Some of examples includes transition metal carbides (MXenes), TiS_2, MoS_2 and V_6O_{13}.[116, 125-128]

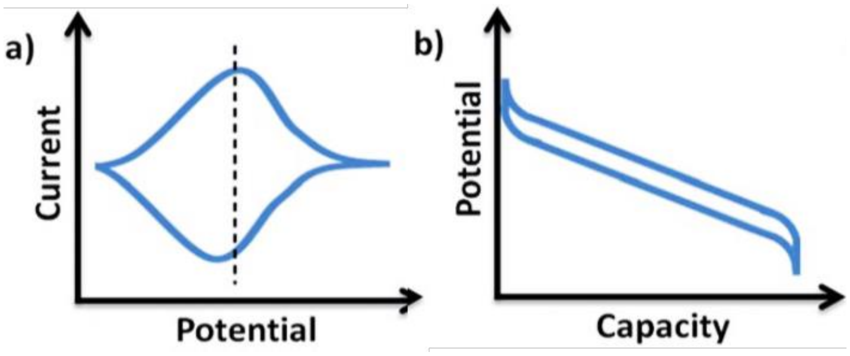

Figure 1.12. Characteristic behavior of pseudocapacitive electrode materials.[109]

Although these pseudocapacitive charge storage mechanisms are based on different faradaic processes and occur in variety of materials, they deliver similar thermodynamic features that is logarithmic relationship between the electrode potential and current.[7, 113, 129] Difference in charge storage mechanism leads to different kinetic behavior upon the application of potentiodynamic sweep (CV) and constant current (galvanostatic charge/discharge curves). Anodic and cathodic peaks during cyclic voltammetry exhibits an ideal capacitive system with symmetric voltammograms at various sweep rates with ideally no or minimum potential shifts.[109] On the other hand, a large anodic and cathodic shift is generally observed for battery type materials that undergo crystallographic phase transformation during electrochemical performance. Therefore, a broad redox peak from CV measurements can indicate pseudocapacitive behavior when the change in potentials of peak current is small or remains constant over a wide range of sweep rates (Figure 1.12).[7, 109] Moreover, slopping profiles observed from galvanostatic discharge curves is also a characteristic of pseudocapacitive type charge storage. Hence, synergy between conventional Li-ion storage mechanism and unconventional pseudocapacitive surface Li-ion storage often result in high energy and power densities that are difficult to achieve otherwise.

Pseudocapacitance can be intrinsic to a material or extrinsic based on the property that can emerge through appropriate material engineering. Intrinsic pseudocapacitive materials display the characteristics of capacitive charge storage regardless of their crystalline properties, particle size or morphology. Some of intrinsic pseudocapacitive materials include RuO_2, MnO_2 and Nb_2O_5.[124, 130-132] In addition, other pseudocapacitive materials, such as TiO_2 (B), α-MoO_3, T-Nb_2O_5, and $Li_4Ti_5O_{12}$, have been identified as intrinsic based on the quantitative differentiation of the capacitive effect from diffusion process.[7, 109] On the other hand, extrinsic materials do not exhibit pseudocapacitance in the bulk state due to phase transformations during charge storage. In these materials, increasing the surface area through nanostructuring leads to improved high-rate behavior due to a decrease in diffusion distances and in some cases, suppression of a phase transformation. Hence, materials that exhibit pseudocapacitive behavior on the nanoscale but battery-type behavior in the bulk state are therefore denoted as extrinsic pseudocapacitive materials. Capacitive behavior becomes dominant with decreasing crystallite size and it can be clearly observed from a typical discharge curve that changes from flat for bulk materials to sloping curve for nanostructured materials due to extrinsic faradaic reactions on the surface or near-surface region that replace diffusion-controlled process. Therefore, a superior rate performance has been reported for pseudocapacitive nanosized electrodes compared to bulk battery-type materials. These factors are mostly exhibited by a number of transition metal oxides and includes V_2O_5, CeO_2, and anatase TiO_2.[50, 118, 133] Pseudocapacitive charge storage is even superior to conventional conversion, insertion and alloying process due to its diffusion independent nature.

Pseudocapacitance in insertion-type anodes

Some intercalation type metal oxides such as TiO_2, Nb_2O_5, $TiNb_2O_5$, $Li_4Ti_5O_{12}$, and MoO_3 were reported to exhibit fast charge storage rates or even higher than the traditional pseudocapacitive materials reported.[117, 121, 134-137] Some of these materials exhibited intercalation pseudocapacitance that occurs when ions intercalate into the tunnels or layers of the electrode material accompanied by a faradaic charge transfer with no crystallographic phase change. For instance, pseudocapacitive current emerges in the redox faradaic peaks of $Li_4Ti_5O_{12}$ at ~1.55 V vs. $Li^{0/+}$ without ion diffusion limitation.[43, 44] Moreover, nanocrystalline TiO_2 (anatase) nanoparticles exhibited the capacitive lithium intercalation dominating the total charge storage due to a fast pseudocapacitance at high rates.[132] Like other titanium oxides, TiO_2 (B) has low density and an open structure, which is particularly suitable for pseudocapacitive faradaic process via Li^+ intercalation. In most of the cases, accommodation of Li into TiO_2 (B) is dominated by capacitive effect and capacitance contribution was calculated to be ~2 fold higher than TiO_2 (A). Dunn and co-workers also revealed that Li ions intercalation into T-Nb_2O_5 possess similar trend with α-MoO_3 where the kinetics of charge storage is mostly influenced by crystallisation.[132] These results also demonstrated the improvements of pseudocapacitance that can be achieved by designing of unique iso-oriented crystalline mesoporous structures. Hence, gaining insight into the charge storage mechanisms in different crystalline structure is another effective method for selecting high performance electrode materials.

Pseudocapacitance in alloying-type anodes

Pseudocapacitive charge storage has been successfully introduced into several alloying-type anodes (Sn, Si, SnO_2, Zn, Al etc.) of lithium-ion batteries.[56, 59, 60, 91] For instance, Jiang et al. demonstrated pseudocapacitive storage in Sn-based alloying anodes that achieved ultrahigh rate capability and excellent cycling stability. It is also observed that the high pseudocapacitive contribution in ultrathin Si-based anodes enhanced the rate capabilities compared to bulk Si anodes.[59] Moreover, several reports claim that Si-C or Si-metal hybrids exhibit excellent high-rate capability and stable full-cell performance due to pseudocapacitive charge storage by tuning the alloying-anodes at nanoscale. In another example of using SnO_2 composites as a alloying anode for LIBs, the capacity percentage of non-diffusion controlled process even reached 82% at 1 mV s^{-1}.[56] Such large non-diffusion current contribution has been reported in a wide range of alloying-mechanism based anodes materials in recent years.

Pseudocapacitance in conversion-type anodes

Conversion-type anodes have demonstrated excellent pseudocapacitive charge storage in recent years resulting in higher specific capacities and improved electrochemical performance. Transition metal oxides/sulphides among conversion-type anodes are dominating due to their redox pseudocapacitive mechanism for fast kinetics.[110, 138-140] Pseudocapacitance contribution in conversion-based anodes has resulted in reversible specific capacities exceeding the theoretical capacity value that includes Fe_2O_3, Co_3O_4, RuO_2 etc.[108, 139, 140] For instance, Xiang et al. found a new direction of optimising the capacities, rate and cycling performance based on the pseudocapacitive behavior of Fe_2O_3 anodes through surface morphologies and structures modifications at nanoscale.[71] Similarly, other metal oxides like Co_3O_4, MnO_2 and RuO_2 exhibited improved electrochemical performance and pseudocapacitive charge storage through interfacial Li-ion storage by nanoengineering the electrodes.[131, 140] However, pseudocapacitance is nominal in the case of conversion-type transition metal oxide anodes.

Synergistic pseudocapacitive charge storage and spatially confined electrochemical reactions in rational nanocomposite design may pave the way for realizing high power/energy lithium-ion batteries. However, specific capacity of intercalation type electrodes is low and pseudocapacitive Li-ion storage is minimal in the case of high-capacity conversion and alloying type anodes. Extrinsic pseudocapacitance, which can be induced through nano-structuring, remains elusive in the case of conversion and alloying-type anodes. Li-ion storage in metal oxide and phosphate-based cathodes also follow a diffusion-limited intercalation mechanism.[7, 109-111] Pseudocapacitive and double layer type Li-ion storage is also negligible in these cathodes due to their low surface area and large particle size. It is therefore necessary to induce pseudocapacitive Li-ion storage in high-capacity electrodes through defects and interface engineering to further enhance energy/power density and cycling stability.

1.10 Defect-Engineering of Electrode Materials

Rational design of electrode materials for rechargeable batteries plays an important role in promoting the developments of renewable energy technology.[141-143] Battery performances has significantly been optimized through the introduction of defects with in-depth understanding of electrode reaction mechanisms and rapid development of advanced technology. A large number of coordination and unsaturated sites can be exposed by defect generation in electrode materials, which play a crucial role in electrochemical reactions. Defects can also provide more storage/ adsorption/ electroactive sites for guest ions and intermediate species other than effectively promoting ion diffusion and charge transfer. Moreover, many studies have revealed that the introduction of defects produces a large number of active sites, which can effectively promote reaction kinetics and enhances electrochemical phase transition.[41, 42, 144, 145] High structural flexibility and stability can be achieved during insertion and extraction of ions through the introduction of defects in electrode materials.[140] Hence, major effects from defect engineering on electrode materials can be summarized as (1) supplementary electrochemical active sites, (2) promoting ion diffusion and electron transfer, and (3) structural stability.

Both experimental and theoretical studies proved that defects such as heteroatom doping, grain boundaries or interfaces and various vacancies in nanostructure electrode materials can regulate the dynamic process of local lithium-ion diffusion.[143, 146, 147] In recent years, it has been studied that the introduction of defective electrode materials can improve the conductivity, cycle stability, and rate performance of the LIBs. Chang and co-workers studied the insertion and diffusion behavior of lithium in TiO_2 with and without oxygen deficiency by using first-principle calculations. Narrowing of the bandgap and movement of the fermi energy level indicated that the electron conductivity increased after the introduction of oxygen vacancy.[148] As discussed, transition metal oxides are considered as promising pseudocapacitive electrodes but are limited by their poor ion diffusion and slow charge transfer. Hence, crystal defects have significant meaning for the properties of transition metal oxides. Oxygen vacancy is the most common anion defect and its formation energy is low and easy to form.[149] Presence of oxygen vacancy can effectively modify the surface electronic structure and improve electron and ion transfer, thus contributing to high electrochemical performance. For example, introducing oxygen vacancy defects into titanium dioxide can induce changes in electronic structure that is beneficial to accelerate metal ions adsorption and diffusion kinetics, thereby improving its electrical conductivity.[47, 134, 150] Recently, it has been recognised that cation vacancies can be used as storage sites for the insertion of additional cations in electrode materials to improve energy storage capacity.[151-153] It is also stated that the presence of cation vacancy in metal oxide nanoparticles has been the reason for improving the reaction kinetics and storage capacity of lithium ions.[154] Moreover, introduction of cation vacancy can also be employed for the reversible insertion of other metal-ion based battery technologies such as Na^+, Mg^{2+}, Zn^{2+}, etc.[155] In addition, the presence of defects can also increase the surface energy of the system and promote electrochemical phase transitions in addition to active sites, faster ion diffusion etc. Therefore, it is essential to effectively construct defects on electrode materials and understand the mechanism of defects on electrochemical reactions for rechargeable batteries.

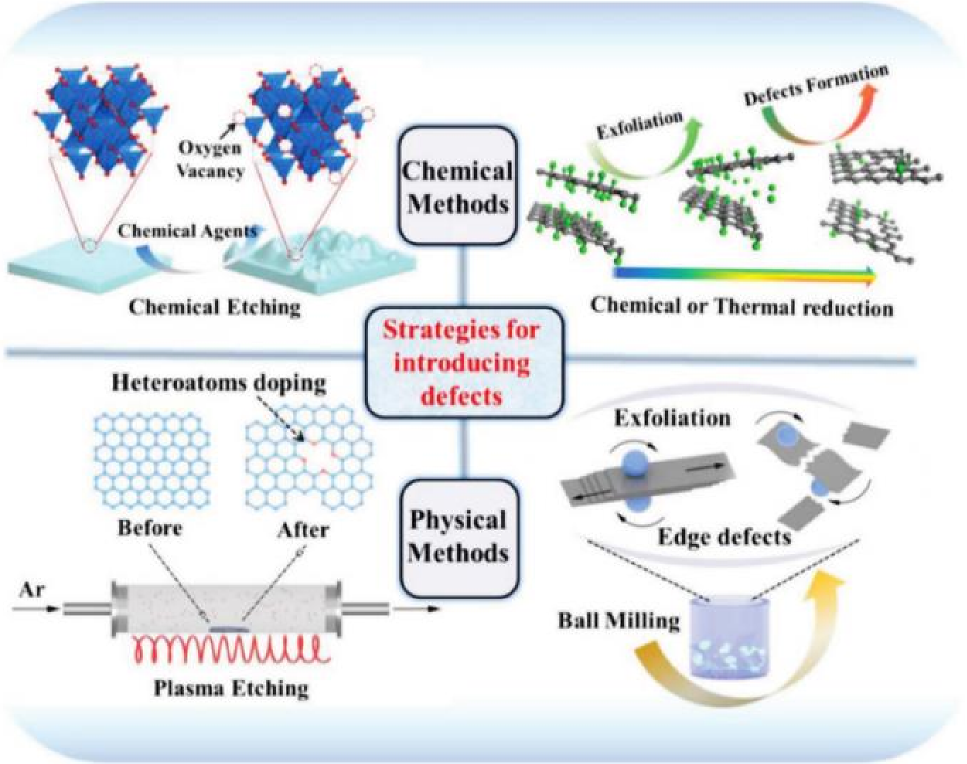

Figure 1.13. Schematic of the strategies for introducing defects.[141]

Defect engineering to crystalline materials can significantly alter the electronic structure and affect the physical and chemical properties of materials. Thus, it is crucial for effectively introducing defects and understanding the internal formation mechanism. At present there are several techniques to facilitate host defects as shown in figure 1.13, mainly including (1) chemical strategies- reduction and etching, (2) physical strategies- plasma technology and mechanical ball milling.[141] For non-layered composite materials, anion vacancies are often generated on the surface by high-temperature reduction and/or chemical synthesis under pressure and elevated temperatures. Moreover, some metal elements of the materials are easily dissolved with the formation of a large number of vacancy defects.[156, 157] In recent years, plasma technology is also considered as an effective means to generate defects on the surface of nanomaterials. Plasma technology can quickly generate defects and can be doped on the surface of materials without damaging the nanostructure.[62] In addition to the construction of intrinsic defects of carbon-based materials, introduction of defects on transition metal oxide through these methods is also beneficial to control the surface structure, valence state and electronic properties of materials.[158]

It should be noted that the concentration of defects in electrode materials is an important factor affecting its electronic structure and electrochemical property. Introducing optimal amount of defects into crystal structure can generally improve conductivity and thus enhance reversibility of electrochemical reactions to improve the initial coulombic efficiency. However, too high defect concentration will sacrifice the prolonged charge-discharge cycles of the electrode materials. Therefore, it is important to control the appropriate concentration of defects to improve initial coulombic efficiency and maintain the cyclic stability of the battery. Engineering of electrode materials containing defects (anion/ cation vacancies, dislocations, grain boundaries etc.) and interfaces (metal oxide-metal oxide, metal-metal oxide, metal oxide-carbon etc.) are key to induce pseudocapacitive type Li-ion storage in Li-ion battery electrodes, and more research is essential in this direction.

1.11 Drawbacks of Current Generation Pseudocapacitive Anodes

Electrochemical performance of secondary lithium-ion batteries are hindered by conventional intercalation-electrodes with their limited charge storage capacity (372 mAh g^{-1} in case of graphite) and sluggish Li-ion diffusion kinetics. Conversion type transition metal oxides and alloying type materials have been investigated as high capacity anode materials for Li-ion batteries.[55, 60, 70, 127, 159-162] Average working voltages of conversion (~1 V) and alloying type anodes (~0.5 V) are higher than those of graphite (~150 mV), leading to low voltage (<3 V) of Li-ion full-cells. Consequently, high specific capacities are necessary to compensate the low energy density resulting from the high operating voltage of conversion and alloying type anodes. Most widely used strategies to improve the electrochemical performance are the fabrication of nanostructures, hybridization of active material etc. Increased reactivity in either case often leads to excessive Li_2O formation, huge irreversible capacity loss and capacity fading on prolonged cycling. Moreover, pseudocapacitive behavior of insertion type anodes are (TiO_2, $TiNb_2O_7$, $Li_4Ti_5O_{12}$ and V_2O_5) reported as beneficial to achieve high-rate performance and cycling stability.[50, 121, 132] These intrinsically pseudocapacitive anodes are not suitable for high energy and power density Li-ion batteries and hybrid capacitors due to their limited specific capacity (≤300 mAh g^{-1})[7,117, 118]. Nevertheless, energy density of these intercalation type electrodes are low and pseudocapacitive Li-ion storage is minimal in the case of conversion and alloying type high capacity anodes.

Pseudocapacitance in alloying-type anodes are hindered by high-capacity materials that exhibits sluggish kinetics at higher current rates. Primary challenges faced by alloying anodes are unsatisfactory rate performance of the alloying reaction, capacity decay induced by volume change, and particle aggregation upon charge-discharge cycles. Pseudocapacitive Li-ion storage of high-capacity conversion-type anodes are limited due to sluggish Li-ion diffusion (10^{-14}-10^{-16} cm^2 s^{-1}).[163] Moreover, pseudocapacitance can be also be induced through defect and interface engineering of nanostructured electrode materials, which remains obscure in the case of conversion-type anodes. Diffusion-independent pseudocapacitive Li-ion storage requires an electrode material with optimum electronic and ionic conductivity. Despite of the implementation of several strategies for improved electrochemical performance, defect/ interface-induced pseudocapacitance of transition metal oxides anodes were not investigated previously.

1.12 Overview of the Thesis

Applications of current generation lithium-ion batteries in power grids and automotive industry are limited by their low energy density and power density. In this regard, many approaches are being pursued to improve the electrochemical performance of Li-ion battery electrochemistry with the use of high-performance nanostructured electrode materials. In this thesis, problems related to the materials and applications currently being investigated were addressed and technical issues of Li rechargeable batteries that remain to be worked out in the near future were also discussed. This thesis mainly focuses on the nanoscale defect and interface engineered electrode materials that can store Li-ions through multiple mechanisms for the development of next-generation lithium-ion batteries. Another important objective is the development of a high-energy/power density lithium-ion full-cells using the developed anodes and commercial cathode materials. This thesis is organized into seven chapters and contains the information as stated below.

Chapter 1 contains information regarding the lithium-ion batteries, different electrode materials with their ion-storage mechanisms, advantages and limitations. Various methods such as nanostructuring and defect engineered electrodes for enhancing the electrochemical performance of LIBs and concept of pseudocapacitive charge storage are also discussed in this section.

Chapter 2 illustrates the synthesis methods employed for various nanoscale engineered anode materials and basic principles of the instruments used for their characterization.

Chapter 3 demonstrates the extremely pseudocapacitive interface engineered CoO@3D-NRGO hybrid anodes for high energy/power density and ultralong life lithium-ion batteries.

Challenges such as agglomeration, volume change and limited cycling stability of conversion-based transition metal oxides are addressed in this section.

Chapter 4 reveals the high energy/power density lithium-ion batteries through nanograin-boundary induced pseudocapacitive charge storage. Origin of additional specific capacities and pseudocapacitive Li-ion storage at nanograin-boundaries were investigated using various *in-situ* and *ex-situ* techniques.

Chapter 5 explains the oxygen vacancy induced pseudocapacitance of rutile TiO_2 nanowires towards superfast charging ultralong life lithium-ion batteries. Influence of oxygen vacancies on electrochemical performance and pseudocapacitance are investigated in detail using various *in-situ* and *ex-situ* techniques.

Chapter 6 demonstrates the unusual pseudocapacitive lithium-ion storage on defect-rich Co_3O_4 nanosheets. Effect of defects on pseudocapacitance, specific capacity and long cycling are investigated.

Chapter 7 contains a number of possible future works that can be carried out by utilising the nanoscale engineered anode materials developed in this study.

1.13 References

1. M. Armand and J. M. Tarascon, *Nature*, **2008**, 451, 652-657.
2. Z. Yang, J. Zhang, M. C. W. Kintner-Meyer, X. Lu, D. Choi, J. P. Lemmon and J. Liu, *Chem. Rev.*, **2011**, 111, 3577-3613.
3. B. Dunn, H. Kamath and J.-M. Tarascon, *Science*, **2011**, 334, 928-935.
4. M. Winter and R. J. Brodd, *Chem. Rev.* , **2004**, 104, 4245-4270.
5. J. Desilvestro and O. Haas, *J. Electrochem. Soc.* , **1990**, 137, C5.
6. H. Kim, J. Hong, K.-Y. Park, H. Kim, S.-W. Kim and K. Kang, *Chem. Rev.* , **2014**, 114, 11788-11827.

7. J. Liu, J. Wang, C. Xu, H. Jiang, C. Li, L. Zhang, J. Lin and Z. X. Shen, *Adv. Sci.*, **2017**, 5, 1700322.
8. G. L. Soloveichik, *Annu. Rev. Chem. Biomol. Eng.*, **2011**, 2, 503-527.
9. J. M. Tarascon and M. Armand, *Nature*, **2001**, 414, 359-367.
10. K. Kang, Y. S. Meng, J. Bréger, C. P. Grey and G. Ceder, *Science*, **2006**, 311, 977-980.
11. M. S. Whittingham, *Chem. Rev.*, **2004**, 104, 4271-4302.
12. J. B. Goodenough and Y. Kim, *Chem. Mater.*, **2010**, 22, 587-603.
13. V. Etacheri, R. Marom, R. Elazari, G. Salitra and D. Aurbach, *Energy Environ. Sci.*, **2011**, 4, 3243-3262.
14. M. R. Palacín, *Chem. Soc. Rev.*, **2009**, 38, 2565-2575.
15. J. Liu, Z. Bao, Y. Cui, E. J. Dufek, J. B. Goodenough, P. Khalifah, Q. Li, B. Y. Liaw, P. Liu, A. Manthiram, Y. S. Meng, V. R. Subramanian, M. F. Toney, V. V. Viswanathan, M. S. Whittingham, J. Xiao, W. Xu, J. Yang, X.-Q. Yang and J.-G. Zhang, *Nat. Energy*, **2019**, 4, 180-186.
16. F. Wu, J. Maier and Y. Yu, *Chem. Soc. Rev.*, **2020**, 49, 1569-1614.
17. Y. Huang, Y. Wang, C. Tang, J. Wang, Q. Zhang, Y. Wang and J. Zhang, *Adv. Mater.* , **2019**, 31, 1803800.
18. X. Zeng, M. Li, D. A. El-Hady, W. Alshitari, A. S. Al-Bogami, J. Lu and K. Amine, *Adv. Energy Mater*, **2019**, 9, 1900161.
19. P. Albertus, S. Babinec, S. Litzelman and A. Newman, *Nat. Energy*, **2018**, 3, 16-21.
20. G. Jeong, Y.-U. Kim, H. Kim, Y.-J. Kim and H.-J. Sohn, *Energy Environ. Sci.*, **2011**, 4, 1986-2002.
21. M. Winter, J. O. Besenhard, M. E. Spahr and P. Novak, *Adv. Mater.*, **1998**, 10, 725-763.
22. J. Hong, H.-D. Lim, M. Lee, S.-W. Kim, H. Kim, S.-T. Oh, G.-C. Chung and K. Kang, *Chem. Mater.* , **2012**, 24, 2692-2697.
23. H. Kim, H.-D. Lim, S.-W. Kim, J. Hong, D.-H. Seo, D.-C. Kim, S. Jeon, S. Park and K. Kang, *Sci. Rep.* , **2013**, 3, 1506.
24. B. G.Polleta, I. Staffell and J. L. Shang, *Electrochim. Acta*, **2012**, 84 235-249.
25. G. E. Blomgren, *J. Electrochem. Soc.*, **2017**, 164, A5019.
26. M. N. Obrovac and V. L. Chevrier, *Chem. Rev.* , **2014**, 114, 11444-11502.

27. J. P. Pender, G. Jha, D. H. Youn, J. M. Ziegler, I. Andoni, E. J. Choi, A. Heller, B. S. Dunn, P. S. Weiss, R. M. Penner and C. B. Mullins, *ACS Nano*, **2020**, 14, 1243-1295.
28. A. Manthiram, *ACS Cent. Sci.*, **2017**, 3, 1063-1069.
29. A. Manthiram, *J. Phys. Chem. Lett.*, **2011**, 2, 176-184.
30. A. Masias, J. Marcicki and W. A. Paxton, *ACS Energy Lett.* , **2021**, 6, 621-630.
31. D. Liu and G. Cao, *Energy Environ. Sci.*, **2010**, 3, 1218-1237.
32. R. Schmuch, R. Wagner, G. Hörpel, T. Placke and M. Winter, *Nat. Energy*, **2018**, 3, 267-278.
33. S.-T. Myung, F. Maglia, K.-J. Park, C. S. Yoon, P. Lamp, S.-J. Kim and Y.-K. Sun, *ACS Energy Lett.* , **2017**, 2, 196-223.
34. C. Bommier, W. Chang, Y. Lu, J. Yeung, G. Davies, R. Mohr, M. Williams and D. Steingart, *Cell Reports Physcial Science*, **2020**, 1, 100035.
35. P. Poizot, S. Laruelle, S. Grugeon, L. Dupont and J.-M. Tarascon, *Nature*, **2000**, 407, 496-499.
36. J. Cabana, L. Monconduit, D. Larcher and M. R. Palacín, *Adv. mater.*, **2010**, 22, E170-E192.
37. W.-J. Zhang, *J. Power Sources*, **2011**, 196, 13-24.
38. A. S. Aricò, P. Bruce, B. Scrosati, J. M. Tarascon and W. V. Schalkwijk, *Nat. Mater.*, **2005**, 4, 366-377.
39. S. Hariharan, V. Ramar, S. P. Joshia and P. Balaya, *RSC Adv.*, **2013**, 3, 6386-6394.
40. X. Chen and Y. Ma, *Adv. Mater. Technol.*, **2018**.
41. F. Zheng, Y. Yang and Q. Chen, *Nat. Commun.* , **2014**, 5, 5261.
42. C. Hang, J. Zhang, J. Zhu, W. Li, Z. Kou and Y. Huang, *Adv. Energy Mater.* , **2018**, 8, 1703539.
43. T.-F. Yi, S.-Y. Yanga and Y. Xie, *J. Mater. Chem. A*, **2015**, 3, 5750-5777.
44. X. Lu, L. Zhao, X. He, R. Xiao, L. Gu, Y.-S. Hu, H. Li, Z. Wang, X. Duan, L. Chen, J. Maier and Y. Ikuhara, *Adv. Mater.* , **2012**, 24, 3233-3238.
45. M. Madian, A. Eychmüller and L. Giebeler, *Batteries*, **2018**, 4, 7.
46. Y.-Q. Wang, L. Gu, Y.-G. Guo, H. Li, X.-Q. He, S. Tsukimoto, Y. Ikuhara and L.-J. Wan, *J. Am. Chem. Soc.*, **2012**, 134, 7874-7879.

47. Y. Zhang, Z. Ding, C. W. Foster, C. E. Banks, X. Qiu and X. Ji, *Adv. Funct. Mater.* , **2017**, 27, 1700856.

48. X.-Y. Yu, H. B. Wu, L. Yu, F.-X. Ma and X. W. D. Lou, *Angew. Chem. Int. Ed.*, **2015**, 54, 4001-4004.

49. P. Kubiak, M. Pfanzelt, J. Geserick, U. Hörmann, N. Hüsing, U. Kaiser and M.Wohlfahrt-Mehrens, *J. Power Sources* **2009**, 194, 1099-1104.

50. B.-T. Liu, X.-M. Shi, X.-Y. Lang, L. Gu, Z. Wen, M. Zhao and Q. Jiang, *Nat Commun*, **2018**, 9, 1375.

51. C. Yang, Y. Zhang, F. Lv, C. Lin, Y. Liu, K. Wang, J. Feng, X. Wang, Y. Chen, J. Li and S. Guo, *J. Mater. Chem. A*, **2017**, 5, 22297-22304.

52. A. Manthiram and J. B. Goodenough, *J. Power Sources* **1980**, 26, 403-406.

53. D. Wang, D. Choi, Z. Yang, V. V. Viswanathan, Z. Nie, C. Wang, Y. Song, J.-G. Zhang and J. Liu, *Chem. Mater.*, **2008**, 20, 3435-3442.

54. W. Luo, X. Chen, Y. Xia, M. Chen, L. Wang, Q. Wang, W. Li and J. Yang, *Adv. Energy Mater*, **2017**.

55. V. Etacheri, G. A. Seisenbaeva, J. Caruthers, G. Daniel, J.-M. Nedelec, V. G. Kessler and V. G. Pol, *Adv. Energy Mater*, **2014**, 1401289.

56. Y. Yang, X. Zhao, H.-E. Wang, M. Li, C. Hao, M. Ji, S. Ren and G. Cao, *J. Mater. Chem. A*, **2018**, 6, 3479-3487.

57. J.-I. Lee, J. Song, Y. Cha, S. Fu, C. Zhu, X. Li, Y. Lin and M.-K. Song, *Nano Research*, **2017**, 10, 4398–4414.

58. X. Wang, X. Cao, L. Bourgeois, H. Guan, S. Chen, Y. Zhong, D.-M. Tang, H. Li, T. Zhai, L. Li, Y. Bando and D. Golberg, *Adv. Funct. Mater.*, **2012**.

59. Y. Son, J. Ma, N. Kim, T. Lee, Y. Lee, J. Sung, S. H. Choi, G. N. Cho, Y. Yoo and J. Cho, *Adv. Energy Mater*, **2019**, 9, 1803480.

60. Y. Jiang, Y. Li, P. Zhou, Z. Lan, Y. Lu, C. Wu and M. Yan, *Adv. Mater.*, **2017**, 29.

61. A.-L. Dalverny, J.-S. Filhol and M.-L. Doublet, *J. Mater. Chem.*, **2011**, 21, 10134–10142.

62. Y. Zhang, R. S. Rawat and H. J. Fan, *Small Methods*, **2017**, 1, 1700164.

63. S.-H. Yu, S. H. Lee, D. J. Lee, Y.-E. Sung and T. Hyeon, *small*, **2016**, 12, 2146-2172.

64. C. Hou, B. Wang, V. Murugadoss, S. Vupputuri, Y. Chao, Z. Guo, C. Wang and W. Du, *Engineered Science*, **2020**, 11, 19-30.

65. K. Bindumadhavan, M.-H. Yeh, T.-c. Chou, P.-Y. Chang and R. Doong, *ChemistrySelect*, **2016**, 1, 5758-5767.

66. S. Chen, Y. Zhao, B. Sun, Z. Ao, X. Xie, Y. Wei and G. Wang, *ACS Appl. Mater. Interfaces* **2015**, 7, 3306-3313.

67. W.-Y. Li, L.-N. Xu and J. Chen, *Adv. Funct. Mater.*, **2005**, 15, 851-857.

68. Y. Li, B. Tan and Y. Wu, *Nano Lett.*, **2008**, 8, 265-270.

69. X. Wang, X.-L. Wu, Y.-G. Guo, Y. Zhong, X. Cao, Y. Ma and J. Yao, *Adv. Funct. Mater.*, **2010**, 20, 1680-1686.

70. G. Xia, N. Li, D. Li, R. Liu, C. Wang, Q. Li, X. Lu, J. Spendelow, J. Zhang and G. Wu, *ACS Appl. Mater. Interfaces*, **2013**, 5, 8607-8614.

71. Y. Xiang, Z. Yang, S. Wang, M. S. A. Hossain, J. Yu, N. A. Kumar and Y. Yamauchi, *Nanoscale*, **2018**, 10, 18010-18018.

72. V. Etacheri, C. Hong, J. Tang and V. G. Pol, *ACS Appl. Mater. Interfaces*, **2018**, 10, 4652-4661.

73. G. Patrinoiu, V. Etacheri, S. Somacescu, V. S. Teodorescu, R. Birjega, D. C. Culita, C. N. Hong, J. M. Calderon-Moreno, V. G. Pol and O. Carp, *Electrochim. Acta*, **2018**, 264, 191-202.

74. K. Mizushima, P. C. Jones, P. J. Wiseman and J. B. Goodenough, *Mater. Res. Bull.*, **1980**, 15, 783-789.

75. M. M. Thackeray, W. I. F. David, P. G. Bruce and J. B. Goodenough, *Mater. Res. Bull.*, **1983**, 18, 461-472.

76. A. K. Padhi, K. S. Nanjundaswamy and J. B. Goodenough, *J. Electrochem. Soc.*, **1997**, 144.

77. R. V. Chebiam, F. Prado and A. Manthiram, *J. Electrochem. Soc.*, **2001**, 148, A49-A53.

78. S. Venkatraman, Y. Shin and A. Manthiram, *Electrochem. Solid-State Lett.* , **2003**, 6, A9-A12.

79. R. V. Chebiam, A. M. Kannan, F. Prado and A. Manthiram, *Electrochem. Commun.*, **2001**, 3, 624-627.

80. U.-H. Kim, G.-T. Park, B.-K. Son, G. W. Nam, J. Liu, L.-Y. Kuo, P. Kaghazchi, C. S. Yoon and Y.-K. Sun, *Nat. Energy*, **2020**, 5, 860-869.
81. W. Li, B. Song and A. Manthiram, *Chem. Soc. Rev.*, **2017**, 46, 3006-3059.
82. R. Marom, S. F. Amalraj, N. Leifer, D. Jacob and D. Aurbach, *J. Mater. Chem.*, **2011**, 21, 9938-9954.
83. D. Aurbach, B. Markovsky, G. Salitra, E. Markevich, Y. Talyossef, M. Koltypin, L. Nazar, B. Ellis and D. Kovacheva, *J. Power Sources*, **2007**, 165, 491-499.
84. D. Aurbach, Y. Ein-Eli, B. Markovsky, A. Zaban, S. Luski, Y. Carmeli and H. Yamin, *J. Electrochem. Soc.* , **1995**, 142, 2882.
85. D. Aurbach, E. Zinigrad, Y. Cohen and H. Teller, *Solid State Ion.*, **2002**, 148, 405-416.
86. J. W. Choi and D. Aurbach, *Nat Rev Mater*, **2016**, 1, 16013.
87. M. Winter, B. Barnett and K. Xu, *Chem. Rev.*, **2018**, 118, 11433-11456.
88. J.Belt, V.Utgikar and I.Bloom, *J. Power Sources*, **2011**, 196, 10213-10221.
89. M. M. Forouzan, B. A. Mazzeo and D. R. Wheeler, *J. Electrochem. Soc.*, **2018**, 165, A2127.
90. H. Ji, J. Wu, Z. Cai, J. Liu, D.-H. Kwon, H. Kim, A. Urban, J. K. Papp, E. Foley, Y. Tian, M. Balasubramanian, H. Kim, R. J. Clément, B. D. McCloskey, W. Yang and G. Ceder, *Nat. Energy*, **2020**, 5, 213-221.
91. X. Li, X. Sun, Z. Gao, X. Hu, R. Ling, S. Cai, C. Zheng and W. Hu, *Nanoscale*, **2018**, 10, 2301-2309.
92. A. Masias, in *Behaviour of Lithium-Ion Batteries in Electric Vehicles: Battery Health, Performance, Safety, and Cost*, eds. G. Pistoia and B. Liaw, Springer International Publishing, 2018, pp. 1-34.
93. P. G. Bruce, S. A. Freunberger, L. J. Hardwick and J.-M. Tarascon, *Nat. Mater.*, **2012**, 11, 19-29.
94. A. Manthiram, Y. Fu, S.-H. Chung, C. Zu and Y.-S. Su, *Chem. Rev.*, **2014**, 114, 11751-11787.
95. J. Wang, W. Huang, A. Pei, Y. Li, F. Shi, X. Yu and Y. Cui, *Nat. Energy*, **2019**, 4, 664-670.
96. Y. Wang and G. Cao, *Adv. Mater.*, **2008**, 20, 2251-2269.
97. X. Li and C. Wang, *J. Mater. Chem. A*, **2013**, 1, 165-182.

98. C. C. Li, X. M. Yin, Q. H. Li, L. B. Chen and T. H. Wang, *Chem. Eur. J.*, **2011**, 17, 1596-1604.

99. M. Zheng, H. Tang, L. Li, Q. Hu, L. Zhang, H. Xue and H. Pang, *Adv. Sci.*, **2018**, 5, 1700592.

100. N. Mahmood, T. Tang and Y. Hou, *Adv. Energy Mater*, **2016**.

101. Z.-S. Wu, W. Ren, L. Wen, L. Gao, J. Zhao, Z. Chen, G. Zhou, F. Li and H.-M. Cheng, *ACS Nano*, **2010**, 4, 3187-3194.

102. G. Binitha, A. G. Ashish, D. Ramasubramonian, P. Manikandan and M. M. Shaijumon, *Adv. Mater. Interfaces*, **2015**, 3, 1500419.

103. P. Zhang, R. Wang, M. He, J. Lang, S. Xu and X. Yan, *Adv. Funct. Mater.*, **2016**, 26, 1354-1364.

104. M. Zhang, F. Yan, X. Tang, Q. Li, T. Wang and G. Cao, *J. Mater. Chem. A*, **2014**, 2, 5890-5897.

105. C. Liu, F. Li, L.-P. Ma and H.-M. Cheng, *Adv. Mater.*, **2010**, 22, E28-E62.

106. Y.-Y. Hu, Z. Liu, K.-W. Nam, O. J. Borkiewicz, J. Cheng, X. Hua, M. T. Dunstan, X. Yu, K. M.Wiaderek, L.-S. Du, K. Chapman, P. J. Chupas, X.-Q. Yang and C. P. Grey, *Nat. Mater.*, **2013**, 12, 1130-1136.

107. J. K. Shon, H. S. Lee, G. O. Park, J. Yoon, E. Park, G. S. Park, S. S. Kong, M. Jin, J.-M. Choi, H. Chang, S. Doo, J. M. Kim, W.-S. Yoon, C. Pak, H. Kim and G. D. Stucky, *Nat Commun*, **2016**, 7, 11049.

108. S. Kim, G. Evmenenko, Y. Xu, D. B. Buchholz, M. Bedzyk, K. He, J. Wu and V. P. Dravid, *Adv. Funct. Mater.*, **2018**, 28, 1805723.

109. V. Augustyn, P. Simon and B. Dunn, *Energy Environ. Sci.*, **2014**, 7 1597-1614

110. X. Yu, S. Yun, J. S. Yeon, P. Bhattacharya, L. Wang, S. W. Lee, X. Hu and H. S. Park, *Adv. Energy Mater*, **2018**, 8, 1702930.

111. Y. Jiang and J. Liu, *Energy Environ. Mater.*, **2019**, 2, 30-37.

112. B. E. Conway, *Plenum Publishers, New York*, **1999**.

113. B. E. Conway, *J. Electrochem. Soc.*, **1991**, 138, 1539.

114. B. E. Conway and W. G. Pell, *J Solid State Electrochem*, **2003**, 7, 637-644.

115. K. Engelsmann, W. J. Lorenz and E. Schmidt, *J. Electroanal. Chem.*, **1980**, 114, 1-10.

116. B. E. Conway, *Electrochim. Acta* **1993**, 38, 1249-1258.

117. M. Lübke, J. Shin, P. Marchand, D. Brett, P. Shearing, Z. Liu and J. A. Darr, *J. Mater. Chem. A*, **2015**, 3, 22908-22914.

118. J. Wang, J. Polleux, J. Lim and B. Dunn, *J. Phys. Chem. C* **2007**, 111, 14925-14931.

119. L. Wang, H. Yang, T. Shu, Y. Xin, X. Chen, Y. Li, H. Li and X. Hu, *ACS Appl. Energy Mater.*, **2018**, 1, 1708-1715.

120. S. Huang, L. Zhang, X. Lu, L. Liu, L. Liu, X. Sun, Y. Yin, S. Oswald, Z. Zou, F. Ding and O. G. Schmidt, *ACS Nano*, **2017**, 11, 821-830.

121. S. Lou, X. Cheng, J. Gao, Q. Li, L. Wang, Y. Cao, Y. Ma, P. Zuo, Y. Gao, C. Du, H. Huo and G. Yin, *Energy Storage Materials*, **2018**, 11, 57-66.

122. V.Subramanian, S. C.Hall, P. H.Smith and B.Rambabu, *Solid State Ion.*, **2004**, 175, 511-515.

123. H. Xia, Y. S. Meng, G. Yuan, C. Cui and L. Lu, *Electrochem. Solid State Lett.* , **2012**, 15, A60.

124. H. Jiang, C. Li, T. Sun and J. Ma, *Nanoscale* **2012**, 4, 807-812.

125. G. Sun, J. Liu, X. Zhang, X. Wang, H. Li, Y. Yu, W. Huang, H. Zhang and P. Chen, *Angew. Chem. Int. Ed.*, **2014**, 53, 12576-12580.

126. M. Yang, Jae-MinJeong, Y. SukHuh and B. GillChoi, *Compos. Sci. Technol.*, **2015**, 121, 123-128.

127. H. D. Yoo, Y. Li, Y. Liang, Y. Lan, F. Wang and Y. Yao, *ChemNanoMat*, **2016**, 2, 688-691.

128. H.M.Zeng, Y.Zhao, Y.J.Hao, Q.Y.Lai, J.H.Huang and X.Y.Ji, *J. Alloys Compd.*, **2009**, 477, 800-804.

129. B. E. Conway, *Prog. Surf. Sci.* , **1995**, 49, 331-452.

130. J. P. Zheng, P. J. Cygan and T. R. Jow, *J. Electrochem. Soc.*, **1995**, 142, 2699-2703.

131. N. Kumar, K. G. Prasad, A. Sena and T.Maiyalagan, *Appl. Surf. Sci.*, **2018**, 449, 492-499.

132. V. Augustyn, J. Come, M. A. Lowe, J. Kim, P.-L. Taberna, S. H. Tolbert, H. D. Abruña, P. Simon and B. Dunn, *Nat. Mater.*, **2013**, 12, 518-522.

133. T. Brezesinski, J. Wang, R. Senter, K. Brezesinski, B. Dunn and S. H. Tolbert, *ACS Nano*, **2010**, 4, 967-977.

134. H.-S. Kim, J. B. Cook, H. Lin, J. S. Ko, S. H. Tolbert, V. Ozolins and B. Dunn, *Nat. Mater.*, **2016**, 16, 454-460.

135. T. Brezesinski, J. Wang, S. H. Tolbert and B. Dunn, *Nat. Mater.*, **2010**, 9, 146-151.

136. P. Yu, C. Li and X. Guo, *J. Phys. Chem. C* **2014**, 118, 10616-10624.

137. H.-S. Kim, J. B. Cook, S. H. Tolbert and B. Dunn, *J. Electrochem. Soc.* , **2015**, 162, A5083.

138. J. B. Cook, H.-S. Kim, Y. Yan, J. S. Ko, S. Robbennolt, B. Dunn and S. H. Tolbert, *Adv. Energy Mater.*, **2016**, 6, 1501937.

139. H. Qi, L. Cao, J. Li, J. Huang, Z. Xu, Y. Cheng, X. Kong and K. Yanagisawa, *ACS Appl. Mater. Interfaces*, **2016**, 8, 35253-35263.

140. J. Zhang, H. Jiang, Y. Zenga, Y. Zhang and H. Guo, *J. Power Sources*, **2019**, 439, 227026.

141. Y. Zhang, L. Tao, C. Xie, D. Wang, Y. Zou, R. Chen, Y. Wang, C. Jia and S. Wang, *Adv. Mater.*, **2020**, 32, 1905923.

142. Y. Zhang, L. Guo, L. Tao, Y. Lu and S. Wang, *Small Methods*, **2019**, 3, 1800406.

143. N. Wang, Y. Wang, X. Xu, T. Liao, Y. Du, Z. Bai and S. Dou, *ACS Appl. Mater. Interfaces*, **2018**, 10, 9353-9361.

144. W. Ren, M. Qin, Z. Zhu, M. Yan, Q. Li, L. Zhang, D. Liu and L. Mai, *Nano Lett.* , **2017**, 17, 4713-4718.

145. J. Dong, Y. Xue, C. Zhang, Q. Weng, P. Dai, Y. Yang, M. Zhou, C. Li, Q. Cui, X. Kang, C. Tang, Y. Bando, D. Golberg and X. Wang, *Adv. Mater.* , **2017**, 29, 1603692.

146. H. Xiong, M. D. Slater, M. Balasubramanian, C. S. Johnson and T. Rajh, *J. Phys. Chem. Lett.*, **2011**, 2, 2560-2565.

147. Z. Xu, Z. Jiang, C. Kuai, R. Xu, C. Qin, Y. Zhang, M. M. Rahman, C. Wei, D. Nordlund, C.-J. Sun, X. Xiao, X.-W. Du, K. Zhao, P. Yan, Y. Liu and F. Lin, *Nat Commun*, **2020**, 11, 83.

148. H.-L. Yeh, S.-H. Tai, C.-M. Hsieh and B. K. Chang, *J. Phys. Chem. C*, **2018**, 122, 19447-19454.

149. H. He, D. Huang, W. Pang, D. Sun, Q. Wang, Y. Tang, X. Ji, Z. Guo and H. Wang, *Adv. Mater.* , **2018**, 30, 1801013.

150. J.-Y. Shin, J. H. Joo, D. Samuelis and J. Maier, *Chem. Mater.* , **2012**, 24, 543-551.

151. W. Li, D. Corradini, M. Body, C. Legein, M. Salanne, J. Ma, K. W. Chapman, P. J. Chupas, A.-L. Rollet, C. Julien, K. Zhagib, M. Duttine, A. Demourgues, H. Groult and D. Dambournet, *Chem. Mater.* , **2015**, 27, 5014-5019.
152. B. P. Hahn, J. W. Long, A. N. Mansour, K. A. Pettigrew, M. S. Osofsky and D. R. Rolison, *Energy Environ. Sci.*, **2011**, 4, 1495-1502.
153. B. P. Hahn, J. W. Long and D. R. Rolison, *Acc. Chem. Res.*, **2013**, 46, 1181-1191.
154. B. Koo, H. Xiong, M. D. Slater, V. B. Prakapenka, M. Balasubramanian, P. Podsiadlo, C. S. Johnson, T. Rajh and E. V. Shevchenko, *Nano Lett.* , **2012**, 12, 2429-2435.
155. B. Koo, S. Chattopadhyay, T. Shibata, V. B. Prakapenka, C. S. Johnson, T. Rajh and E. V. Shevchenko, *Chem. Mater.* , **2013**, 25, 245-252.
156. Y. Wang, M. Qiao, Y. Li and S. Wang, *Small* **2018**, 14, 1800136.
157. J. T. Mefford, W. G. Hardin, S. Dai, K. P. Johnston and K. J. Stevenson, *Nat. Mater.*, **2014**, 13, 726-732.
158. L. Xu, Q. Jiang, Z. Xiao, X. Li, J. Huo, S. Wang and L. Dai, *Angew. Chem., Int. Ed.*, **2016**, 55, 5277.
159. L. L. Perreault, F. Colò, G. Meligrana, K. Kim, S. Fiorilli, F. Bella, J. R. Nair, C. Vitale-Brovarone, J. Florek, F. Kleitz and C. Gerbaldi, *Adv. Energy Mater*, **2018**, 8, 1802438.
160. M.F.Hassan, Z.P.Guo, Z.Chen and H.K.Liu, *J. Power Sources* **2010**, 195, 2372-2376.
161. S. Yoon, C. Jo, S. Y. Noh, C. W. Lee, J. H. Song and J. Lee, *Phys. Chem. Chem. Phys.*, **2011**, 13, 11060-11066.
162. H. Xu, S. Li, X. Chen, C. Zhang, W. Liu, H. Fan, Y. Yu, Y. Huang and J. Li, *Adv. Energy Mater*, **2019**, 1902150.
163. J. Wang, Q. Deng, M. Li, K. Jiang, Z. Hu and J. Chu, *Nanoscale*, **2018**, 10, 2944-2954.

Chapter-2

Synthesis and Characterisation Techniques

2.1 Synthesis of Defect and Interface Engineered Anode Materials

Nanostructured defect and interface engineered anode materials were prepared through various soft-chemical methods. Interface engineered cobalt mono-oxide uniformly anchored on nitrogen doped reduced graphene oxide nanosheets (CoO@3D-NRGO) were synthesised through a solvothermal method followed by heat treatment. Nanograin-boundary and defects induced cobalt oxide anodes were prepared through the hydrothermal and solvothermal techniques respectively using urea as reducing agent. Moreover, oxygen deficient rutile TiO_2 nanowires were synthesized through a solvothermal method using $TiCl_4$ as precursor and ethylene glycol solvent. Details of synthesis procedures and chemicals used are described in the following sections.

2.1.1 Chemicals Used

Chemical	Chemical formula	Supplier	Purity
Cobalt nitrate hexahydrate	$Co(NO_3)_2.6H_2O$	Honeywell	99.0%
Urea	NH_2CONH_2	Sigma-Aldrich	99.9%
Ethylene glycol	$C_2H_6O_2$	Fisher Scientific	99.0%
Hydrochloric acid	HCl	Sigma-Aldrich	98.0%
Titanium chloride	$TiCl_4$	Sigma-Aldrich	99.9%
Potassium permanganate	$KMnO_4$	Sigma-Aldrich	99.0%
Sulfuric acid	H_2SO_4	Sigma-Aldrich	98.0%
Phosphoric acid	H_3PO_4	Sigma-Aldrich	98.0%
Ethanol	C_2H_5OH	Sigma-Aldrich	96.0%
Potassium nitrite	KNO_2	Fisher Scientific	97.0%
Acetic acid	CH_3COOH	Sigma-Aldrich	99.7%
Sodium hydroxide	$NaOH$	Fisher Scientific	98.0%

2.1.2 Interface Engineered CoO@3D-NRGO Hybrid Anode

Graphene oxide (GO) was synthesised from graphite flakes through an improved hummers' method.[1] Briefly, 1.0 g graphite flakes (98%, 50 mesh, Georg H. LUH GmbH) and 6.0 g $KMnO_4$ (99.0%, Sigma-Aldrich) were added successively into a 9:1 mixture of concentrated H_2SO_4/H_3PO_4 (98% Sigma-Aldrich). The reaction system was kept under continuous stirring for 12 h at 50 °C, cooled to room temperature, and poured onto ice (200 g) with 3 mL of 30% H_2O_2 (99% Sigma-Aldrich). The precipitate obtained was centrifuged (4000 rpm for 30 min) and the supernatant was decanted. The remaining solid material was then washed in succession with 200 mL of water, 37% HCl (98% Sigma-Aldrich), and ethanol (96% Sigma-Aldrich). The resulting material was finally washed thoroughly with deionized water, and subsequently dried under vacuum at 80 °C for 12 h.

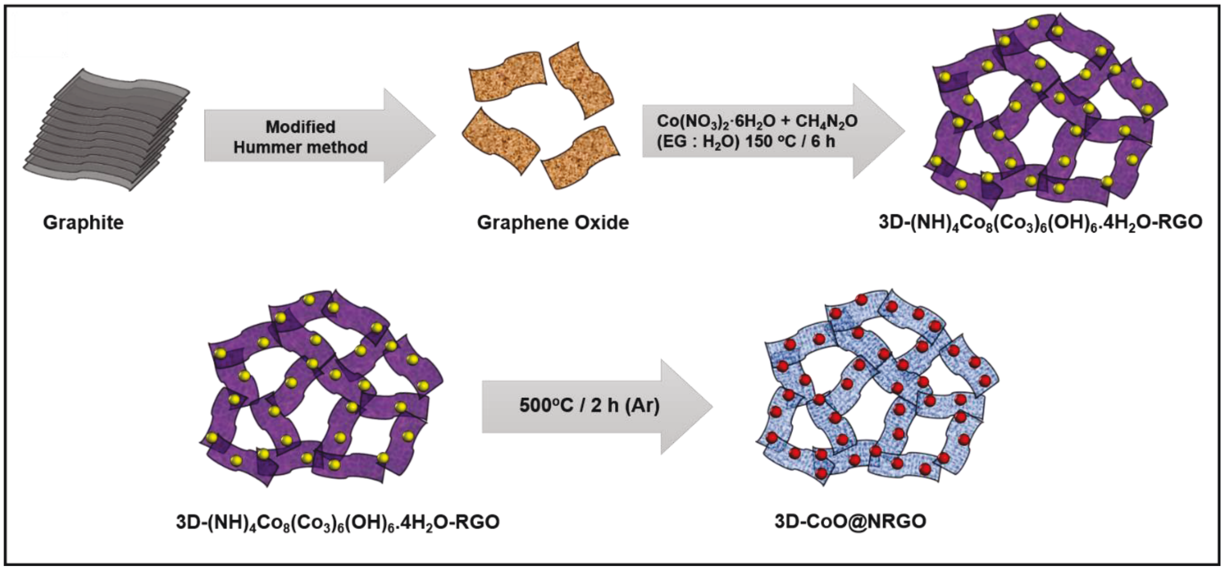

Figure 2.1. Schematic of the synthesis of CoO@3D-NRGO hybrid.

CoO@3D-NRGO hybrid was prepared through a solvothermal method followed by heat treatment under inert condition. In a typical synthesis of sample containing ~60% CoO, 4 mM of cobalt (II) nitrate hexahydrate (99.0%, Honeywell) and 2 mM of urea (99.9%, Sigma-Aldrich) were dissolved in a 9:1 mixture of ethylene glycol (99.0%, Fisher Scientific) and deionised water along with 150 mg of GO and stirred for 30 min. The obtained solution was then transferred into Teflon lined stainless steel autoclaves (Parr Instrument, USA) and heated to 150 °C for 6 h at a rate of 10 °C min^{-1}. The precipitate obtained was then centrifuged, washed with deionised water and ethanol followed by drying at 80 °C for 12 h. Finally, resulting powder $(NH)_4Co_8(Co_3)_6(OH)_6.4H_2O$@3D-NRGO was heat treated at 500 °C under Ar-flow for 2 h to obtain CoO@3D-NRGO (heating and cooling rates of 10 °C min^{-1}). CoO@3D-NRGO samples containing higher and lower CoO loading were prepared by using appropriate amounts of cobalt (II) nitrate hexahydrate. Control samples CoO@2D-NRGO and Co_3O_4@3D-NRGO for comparing electrochemical performance were synthesized by similar solvothermal synthesis without using ethylene glycol and calcination of $(NH)_4Co_8(Co_3)_6(OH)_6.4H_2O$@3D-NRGO at 500 °C under air-flow for 2 h respectively. Physically mixed samples CoO/3D-NRGO and sample without nitrogen (CoO@3D-RGO) (without using urea) were also prepared for comparing the electrochemical performance.

2.1.3 Nanograin-Boundary Rich Hierarchical Co_3O_4 Nanorods

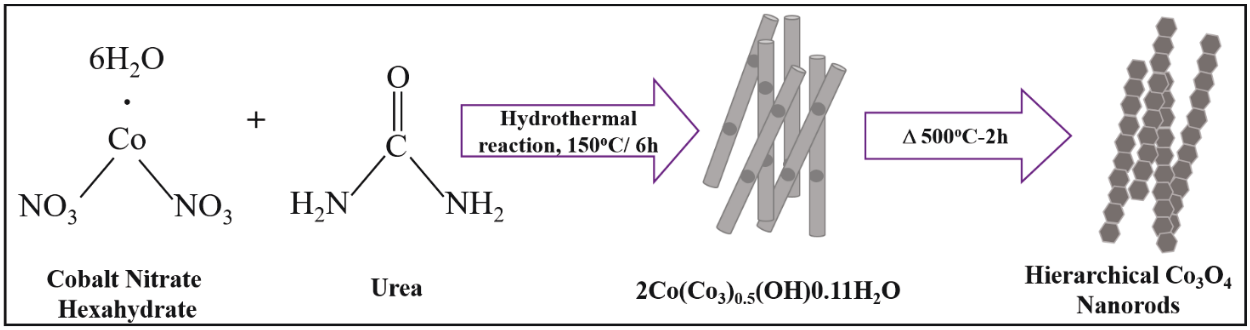

Figure 2.2. Schematic of the synthesis of nanograin-boundary rich hierarchical Co_3O_4 nanorods.

Nanograin-boundary rich hierarchical Co_3O_4 nanorods was prepared through a hydrothermal method followed by controlled annealing. In a typical synthesis, 4 mM of cobalt (II) nitrate hexahydrate ($Co(NO_3)_2 \cdot 6H_2O$) (99.0%, Honeywell) and 2 mM of urea (CH_4N_2O) (99.9% Sigma-

Aldrich) were dissolved in 100 mL of deionized water under stirring for 30 min at room temperature. The solution obtained was then heated to 150 °C for 6 h in a 100 mL PTFE lined stainless steel autoclaves (Parr Instrument, USA). Obtained precipitate dicobalt dihydroxide carbonate ($Co(Co_3)_{0.5}(OH)0.11H_2O$) was then washed with de-ionised water, dried and calcined at 500 °C under air flow for 2h (heating and cooling rate of 10 °C/min). Co_3O_4 nanoparticles for comparing the electrochemical performance were prepared by ball milling hierarchical Co_3O_4 nanorods at 500 rpm for 24 h.

2.1.4 Oxygen Deficient Rutile TiO_2 Nanowires

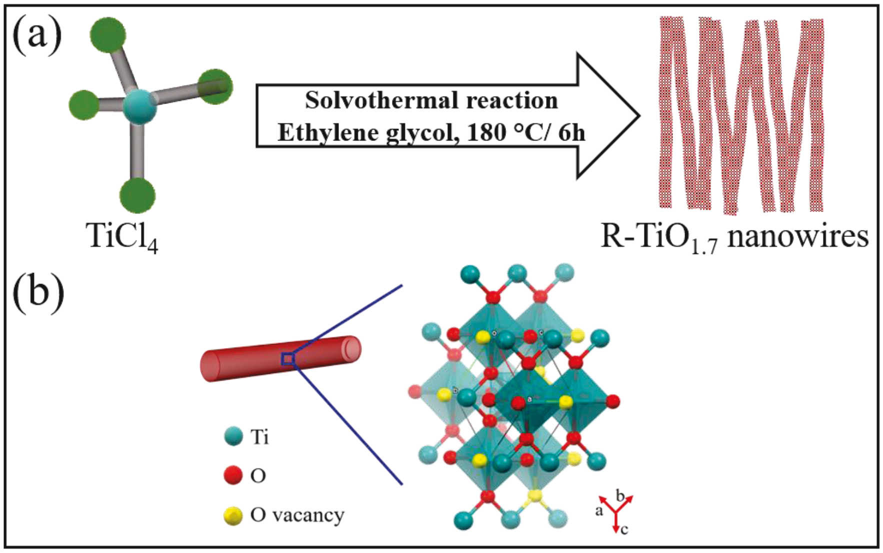

Figure 2.3. Schematic of the (a) synthesis and (b) crystal structure of rutile TiO_{2-x} nanowires.

Rutile TiO_{2-x} nanowires were synthesized through a solvothermal method using $TiCl_4$ as precursor (0.1 M in HCl) and mixture of ethylene glycol and water solvent (12.5:1). In a typical synthesis of rutile $TiO_{1.7}$ nanowires, 18 mL of $TiCl_4$ (99.9%, Sigma-Aldrich) was added dropwise into a mixture of 230 mL ethylene glycol glycol (99.0%, Fisher Scientific) and 18 mL deionized water. The solution obtained was then transferred to teflon lined stainless steel autoclave and heated to 180 °C for 6 h. Obtained white TiO_2 precipitate was then washed with deionized water-ethanol (1:1) mixture and dried under vacuum at 80 °C overnight to form ultrathin oxygen deficient rutile TiO_2 nanowires. For comparing the electrochemical performance, stoichiometric (TiO_2) and excess oxygen deficient ($TiO_{1.5}$) rutile TiO_2 nanowires were prepared by heat-treating the obtained rutile $TiO_{1.7}$ nanowires at 1000°C in air and 500°C in argon-hydrogen atmosphere respectively.

2.1.5 Defective Co_3O_4 Nanosheets

Defective Co_3O_4 nanosheets was synthesised through a solvothermal method followed by controlled calcination. In a typical synthesis, 4 mM of cobalt (II) nitrate hexahydrate (99.0%, Honeywell) and 2 mM of urea (99.9%, Sigma-Aldrich) were dissolved in a 9:1 mixture of ethylene glycol (99.0%, Fisher Scientific) and deionised water and stirred for 30 min at room temperature. The solution obtained was then heated to 150°C for 6h in a 100 mL PTFE lined stainless steel autoclaves (Parr Instrument, USA). Obtained $(NH)_4Co_8(Co_3)_6(OH)_6.4H_2O$ precipitate was then washed with deionised water, dried and calcined at 500 °C under air flow for 2 h (heating and cooling rates of 10 °C min^{-1}).

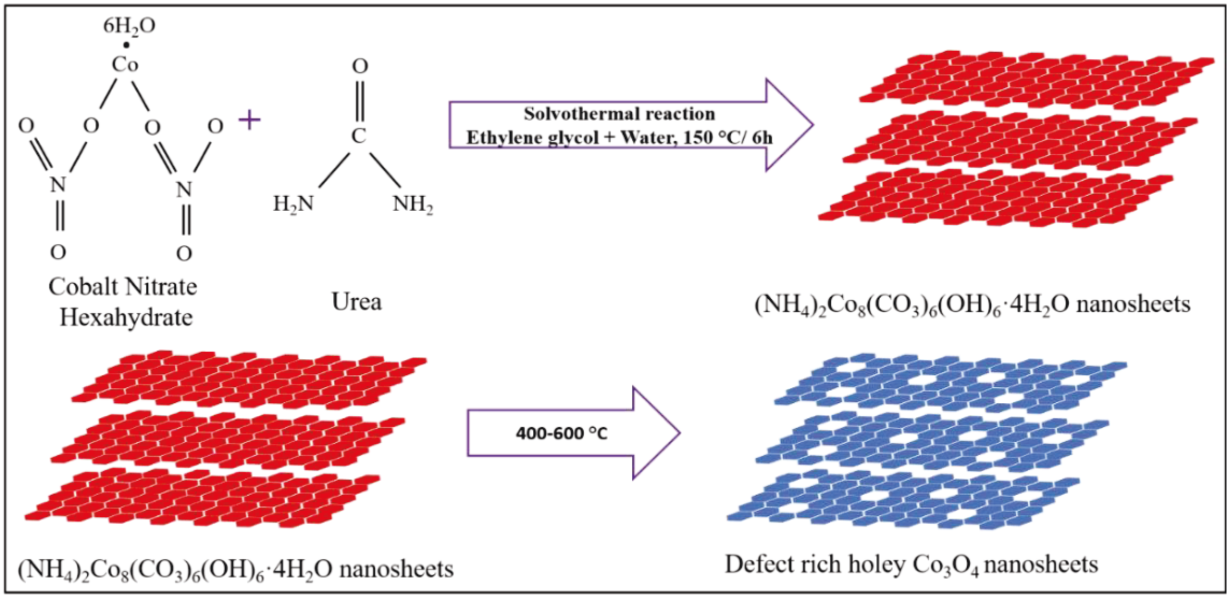

Figure 2.4. Schematic of the synthesis of defective Co_3O_4 nanosheets.

Defect-free Co_3O_4 nanosheets for comparing electrochemical performance were synthesized by following the report 2 and used without any further modifications[2]. In a typical synthesis, 0.145 g (0.5 mmol) cobalt nitrate hexahydrate $[Co(NO_3)_2.6H_2O]$ was dissolved in 11 mL deionised water and stirred for 30 min at room temperature. Then, 0.5 g (6 mM) potassium nitrite (98.0%, Fisher Scientific, KNO_2) and 4 mL of 36 wt% (24 mM) acetic acid (99.7%, Sigma-Aldrich, CH_3COOH) were added to the above solution that resulted in hexanitrito cobalt(III) trianion ($K_3[Co(NO_2)_6]$) solution. Aqueous sodium hydroxide (97.0%, Fisher Scientific, NaOH) solution (10 mL, 5 M) was added dropwise into the obtained hexanitrito cobalt(III) trianion ($K_3[Co(NO_2)_6]$) solution (0.5 mmol) until the NaOH concentration in the mixture reduces to 2 M. The solution obtained was then transferred into a Teflon-lined stainless steel autoclave, and heated at 120 °C for 6 h. Obtained CoOOH precipitate was then washed with deionised water, dried and calcined at 300 °C under air flow for 1 h (heating and cooling rates of 10 °C min^{-1}) to form defect free Co_3O_4 nanosheets.

2.1.6 Electrochemical Study

Composite electrodes for evaluating the electrochemical performance were prepared by mixing 80% active material with 10% carbon black and 10% of polyvinylidene fluoride (MW: 600,000, MTI Chemicals) in N-methylpyrrolidone solvent (99.9%, Aladdin Chemicals) followed by coating on a copper foil (10 μm thickness) using doctor blade. Coin-type 2032 two-electrode cells were fabricated using the composite working electrode containing 2-3 mg of the active material, Li-foil counter/ reference electrode and a glass fiber separator (Whatman, GF/B type). Electrolyte consists of a 1 M solution (99.99%, Sigma-Aldrich) of $LiPF_6$ in a 1:1 mixture of ethylene carbonate (EC) and ethyl methyl carbonate (EMC). A glove box (Vigor Tech USA) filled with high-purity argon (99.999%) and equipped with oxygen and moisture sensors/absorbers (H_2O and O_2 content < 1 ppm) was used for assembling the electrochemical cells. All potentials presented are vs. Li/Li^+, and the specific capacity values based on the active material weight are within 5% error limit.

2.2 Characterisation Techniques

Techniques, working principles and specifications of instruments used for characterizing defect and interface engineered anode materials are described in the following sections.

2.2.1 Scanning Electron Microscopy (SEM)

Scanning electron microscopy is a technique in which focused beam of electrons interacts with atoms in the sample to generate various signals that have information about the surface topography and composition.[3] An image is formed as a result of the signals produced after the interaction of electron beam with the samples. Different types of signals produced after interaction of electron beam with sample includes secondary electrons, back-scattered electrons, and transmitted electrons.[4] Secondary electrons (SEs) are mostly ejected from top few nanometers of sample surface and limited from their mean free path in solid matter due to their low energies (50 eV). A high-resolution image can be achieved from secondary electrons as they tend to be highly localised at point of impact. As secondary electrons are used for studying the morphology, back scattered electrons collect crystallographic information of the sample. Back scattered electrons (BEs) are reflected from the sample through elastic scattering, since they have much higher energy than SEs. Back scattered electrons images can provide information about the distribution, but not the identity of different elements in the sample.

Field-emission scanning microscope (FESEM) is a technique that provides a wide variety of information from the sample surface with higher resolution and a much greater energy range. Working principle of FESEM is similar to a conventional SEM, where the sample is scanned with an electron beam and then the information is displayed on the basis of the detectors available

(Figure 2.5).[5] FESEM uses a field emission gun that provides extremely focused high and low energy electron beams unlike SEM. High energy electron beams can greatly improve the resolution and also it can be operated at low potentials (0.02-20 kV). This helps to minimise the charging effect on non-conductive samples and prevents sensitive samples from impairment due to electron beam.

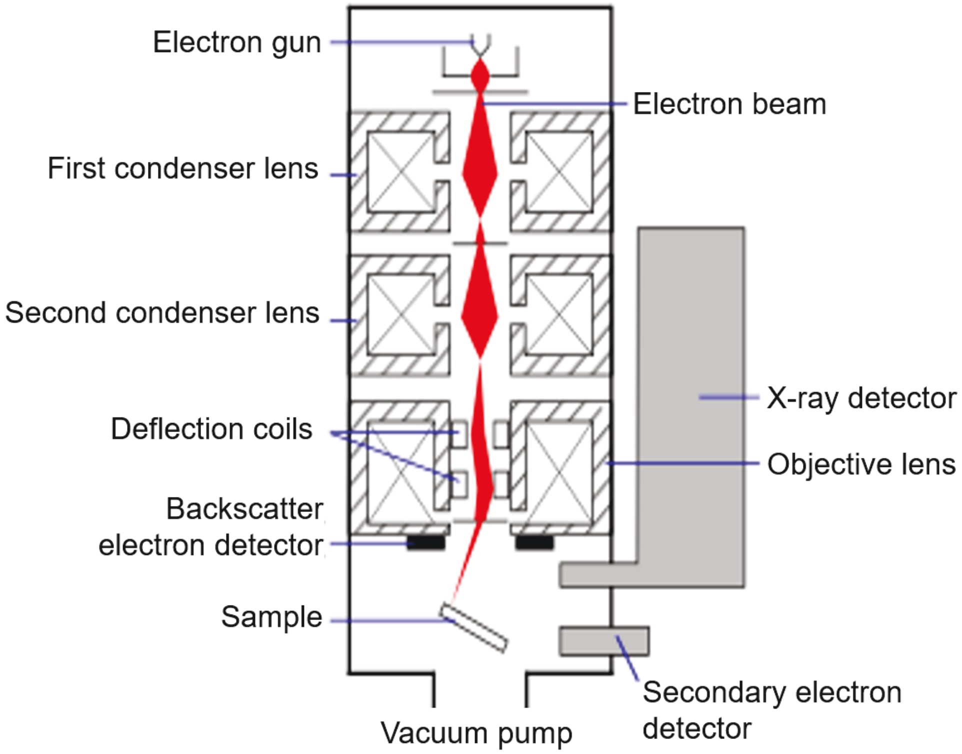

Figure 2.5. Schematic of field emission scanning microscopy

Another highly remarkable feature of FESEM is its use of in-lens detectors. These detectors, which are optimised to work at high resolution and very low acceleration potential, are fundamental for getting the maximum performance from the equipment. In this work, FEI Helios NanoLab 600i scanning electron microscope operating at 5-20 kV was used for recording the high-resolution SEM images.

2.2.2 Transmission Electron Microscopy (TEM)

Transmission electron microscopy is a microscopy technique in which an electron beam is transmitted through a specimen to form an image. This image is then magnified and focused onto an imaging device, such as a fluorescent screen, or can be detected by a sensor such as a CCD camera.[6] These transmitted electrons are used for focusing and forming an image with spatial resolution much greater than optical microscope. TEM functioning is mainly dependent on 3 functional units namely (a) illuminating system, (b) specimen stage, and (c) imaging system as demonstrated in figure 2.6.

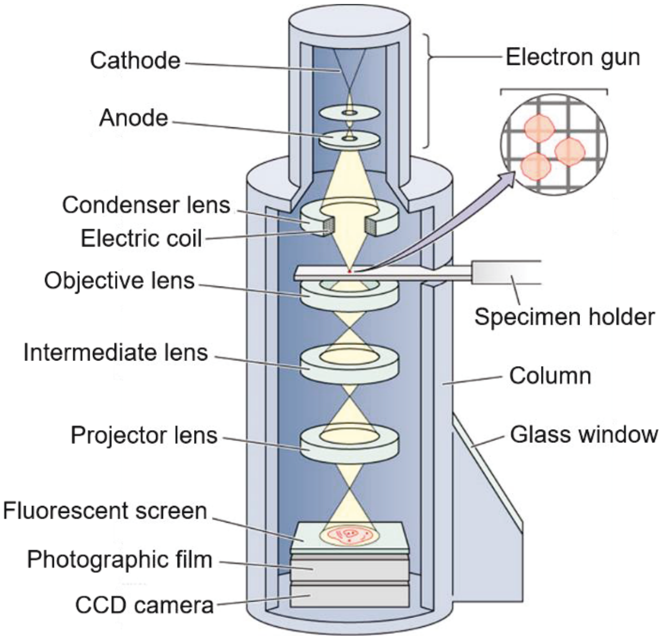

Figure 2.6. Schematic of transmission electron microscopy

Illuminating system has an electron gun to emit high energy electrons and a condenser lens to focus the beam of electrons. Specimen stage holds the sample constant and mostly copper grids are used. Finally, imaging system consists of a fluorescent screen, photographic film and a CCD camera that are used to obtain high resolution images. TEMs are capable of imaging at a significantly higher resolution than light microscopes due to the small de Broglie wavelength of electrons. For the analysis, powder samples are dispersed in a solution (ethanol) and sonicated for 20-30 minutes before being deposited onto a carbon coated copper grids. The sample loaded grids were studied under FEI Talos F200X FEG microscope operating at an accelerating voltage upto 200 kV. Distance (d) between the adjacent crystal planes in electrode materials were calculated from the selected area electron diffraction (SAED) pattern using $d = \lambda L/R$, where λ is wavelength of accelerated electrons used, L is the camera length and R is diffraction pattern radius.

2.2.3 X-ray Diffraction (XRD) Analysis

X-ray diffraction is a non-destructive analytical technique that gives information about the crystallographic structure and chemical composition at normal atmospheric conditions. X-ray are a form of electromagnetic radiation having a wavelength in the range of 10 to 0.01 nm, and energies in the range 120 eV to 120 keV. Powder XRD is used for powdered solid samples to characterise the crystallographic structure, crystalline size (grain size) and preferred crystal orientation. X-ray diffraction is commonly used for unidentified materials, by comparing diffraction data against a database maintained by the international centre for diffraction data (ICDD).

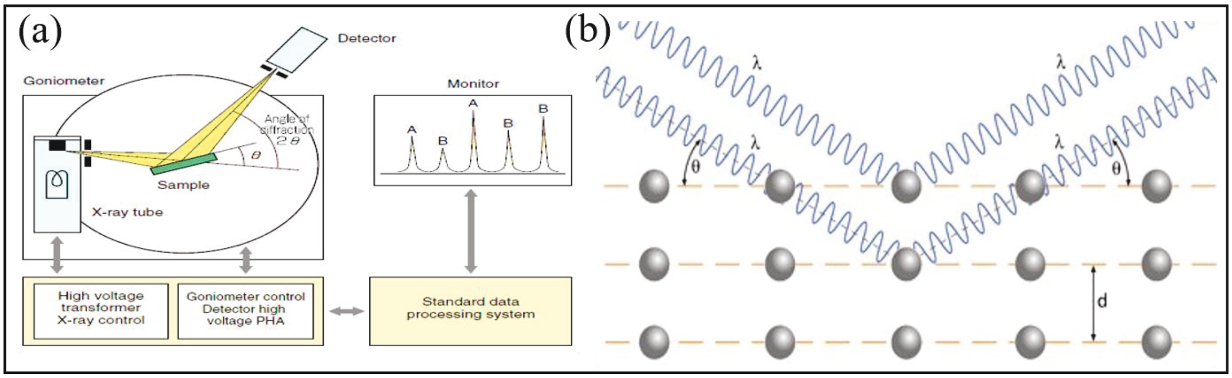

Figure 2.7. Schematic of the interaction of X-ray beam with a crystalline material.

Basic principle of XRD analysis is Bragg diffraction that occurs when electromagnetic radiations having a wavelength comparable to the atomic spacing incident upon a crystalline sample (Figure 2.7).[7] Diffraction occurs when a monochromatic x-ray beam with wavelength (λ) is projected onto a crystalline material at an angle (θ) and then the distance travelled by reflected x-rays from successive planes differs by n number of wavelengths. These x-rays are generated by a cathode ray tube, filtered to produce monochromatic radiation, focused, and directed on to the sample. Interaction of incident rays with sample produces a diffracted ray and undergoes constructive interference in accordance to Bragg's Law (equation 2.1).

$$n\lambda = 2d \sin \theta \qquad 2.1$$

Bragg's law relates the wavelength of electromagnetic radiation to diffraction angle and the lattice spacing in sample. Hence, a diffraction pattern is obtained by measuring the intensity of scattered waves as a function of scattering angle. By scanning the sample through a range of 2θ angles, very strong intensities known as Bragg peaks are obtained in the diffraction pattern only when scattered waves satisfy the Bragg condition. A PANalytical Empyrean high-resolution diffractometer equipped with a Cu-Kα source (λ=0.15418 nm) and Lynx detector was used for recording the X-ray diffraction pattern of various samples in this work. Average crystallite sizes of samples were calculated using Debye –Scherrer equation 2.2[8]

$$D = K\lambda/\beta\, Cos\, \theta \qquad 2.2$$

Where D is the particle size, K = 0.9, λ = 0.154 nm, and β is the full width at half maximum (FWHM) of the corresponding diffraction peak.

2.2.4 Raman Spectroscopy

Raman spectroscopy (named after C.V. Raman) is a technique used to study vibrational, rotational and other low-frequency modes in a molecule. It is based on inelastic scattering (Raman scattering) of monochromatic light, usually from a laser source in visible, infrared or near ultraviolet range. Inelastic scattering is the change of proton frequency in monochromatic light when interacting with the sample. Photons of monochromatic light (laser) are absorbed by molecules in the sample and then reemitted. A photon excites the molecule from the ground state to a virtual energy state and when the molecule relaxes, it emits a photon and returns to a different rotational or vibrational state, known as Raman effect. Difference in energy between the original state and this new state leads to a shift in the emitted photon's frequency away from the excitation wavelength. If the final vibrational state of molecule is more energetic than the initial state, then emitted photon will be shifted to a lower frequency in order to maintain the balance in total energy of system. This shift in frequency is designated as a Stokes shift. If the final vibrational state is less energetic than the initial state, then the emitted photon will be shifted to a higher frequency, and this is designated as an Anti-Stokes shift (Figure 2.8). These shifts in photon energy gives information about phonon modes in system. The amount of the polarizability change of the molecule determines the Raman scattering intensity and the pattern of shifted frequencies is determined by the rotational and vibrational states of the sample. Raman spectroscopy can also be used to study solid, liquid and gaseous samples.

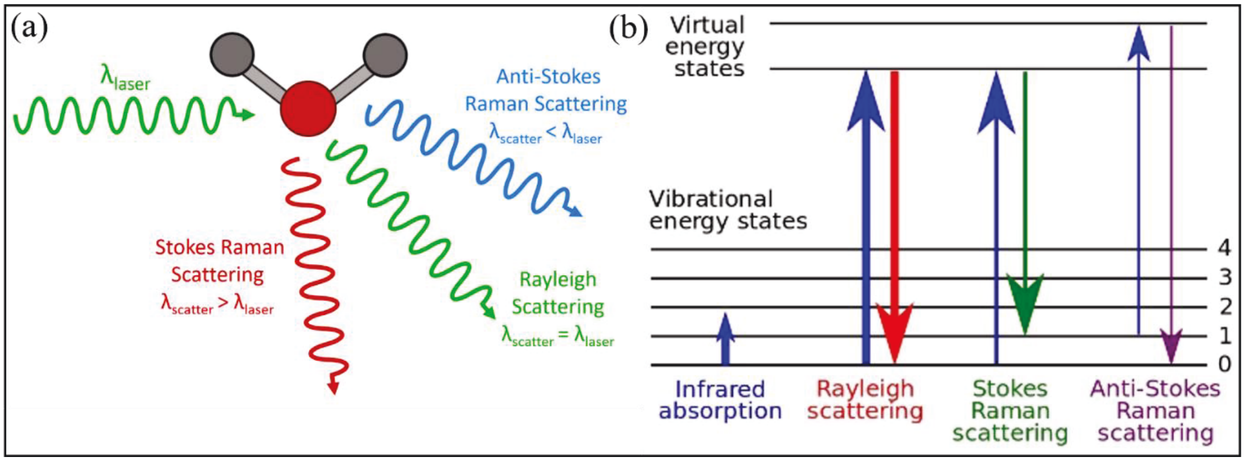

Figure 2.8. Different types of Raman scattering.[9]

Raman spectrum can be used as a fingerprint for the identification of unknown materials by direct comparison of the spectrum of the unknown with spectra in a reference catalogue. It is also used to study ordering in structures and phase transitions at different temperatures since Raman pattern changes with phase transitions. In this work, Micro-Raman analysis was performed by a Renishaw PLC Raman spectrometer equipped with a 532 nm Nd: YAG laser. Laser power was restricted to 5 mW to avoid sample damage.

2.2.5 X-ray Photoelectron Spectroscopy (XPS)

X-ray photoelectron spectroscopy is a quantitative technique that gives information on the chemical and electronic state of the elements present in a material. XPS measurement requires ultra-high vacuum (UHV) conditions. XPS spectra is acquired by irradiating a material with beam of X-rays and measuring the number of electrons emitted from the surface (1-10 nm depth) of material with respect to kinetic energy (KE) simultaneously.

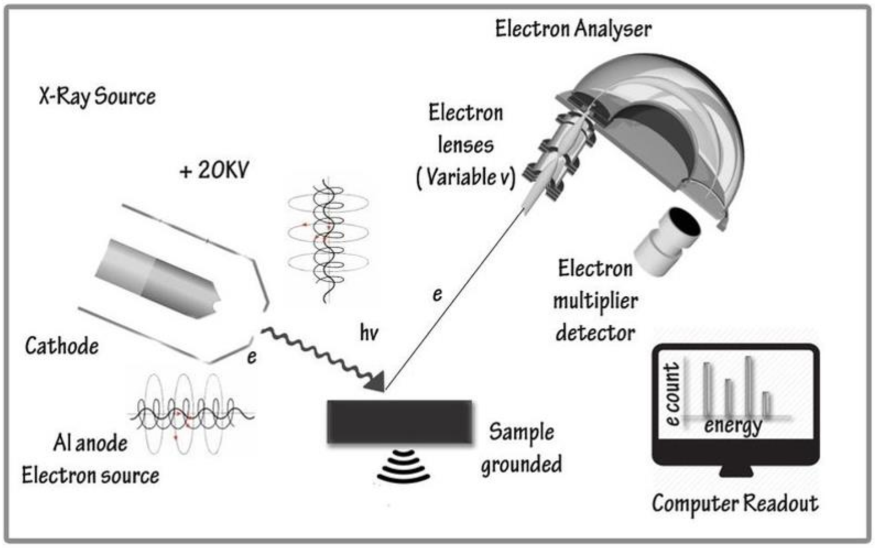

Figure 2.9. Schematic of X-ray photoelectron spectroscopy.[11]

Binding energy (BE) of each emitted electrons can be determined according to the Ernest Rutherford (1914) equations (equation 2.3) from the energy of an x-rays wavelength.[10]

$$E_{binding}=E_{photon}-(E_{kinetic}+\vartheta) \qquad 2.3$$

Where $E_{binding}$ is the binding energy of the electron, E_{photon} is the energy of the X-ray photons being used, $E_{kinetic}$ is the kinetic energy of the electron as measured by the instrument and φ is the work function of the spectrometer. Schematic of a typical XPS instrument is presented in figure 2.9.

XPS analyses in this work were performed on a Thermo Fisher Scientific Instruments (East Grinstead, UK) spectrometer fitted with Al Kα (hν = 1486.6 eV) X-ray source was used for collecting the XPS spectra. Survey spectra were acquired employing a Pass Energy of 200 eV. High-resolution, core level spectra for all elements were acquired with a Pass Energy of 50 eV and a 0.2 eV step size. All spectra were referenced against the C1s peak at 284.5 eV to compensate charging effects during acquisition. Quantitative surface chemical analyses were calculated from the high-resolution, core level spectra following the removal of a non-linear (Shirley) background.

2.2.6 Surface Area Analysis

Brunauer-Emmett-Teller (BET) is most widely used analysis for the surface area determination of solid or porous materials. It gives the information on physical structure as the region over materials surface affects upon the interaction of solid with its environment. Specific surface area, including surface irregularities and pore size distribution of a particle is determined at an atomic level by adsorption of an unreactive gas by using the BET theory.[12] Solid materials are cooled down initially using cryogenic liquid since most gases and solids interact weakly. Later, temperature of the solid sample is kept constant, or under isothermal conditions and simultaneously pressure/concentration of adsorbing gas is increased. As the relative pressure is increased, a thin layer of molecules adsorbs over the entire surface and form a monolayer. Number of gas molecules in the monolayer is recorded from the volume adsorbed and the area of accessible surface is calculated from cross-sectional area of adsorbate. However, gas adsorption as a function of pressure does not follow a simple linear relationship (as shown in Figure 2.10). Therefore, this analysis is mainly based on the BET equation (equation 2.4), in which W is the weight of gas adsorbed at a relative pressure P/P_o and W_m is the weight of adsorbate constituting a monolayer of surface coverage. BET constant C is related to the energy of adsorption in the first adsorbed layer, and its value indicates the magnitude of the adsorbent/adsorbate interactions.[12]

$$\frac{1}{W\left(\left({}^{P_{\circ}}/_{P}\right)-1\right)} = \frac{1}{W_{\mathrm{m}}C} + \frac{C-1}{W_{\mathrm{m}}C}\left(\frac{P}{P_{\circ}}\right) \tag{2.4}$$

Figure 2.10 depicts a typical surface area isotherm, where the x-axis is the relative pressure of the gas and the y-axis is its volume adsorbed onto the sample.

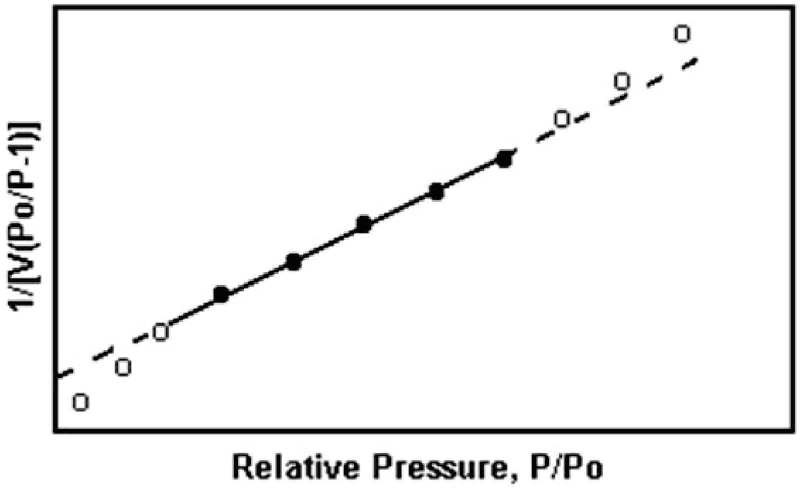

Figure 2.10. Multipoint BET plot.[12]

Nitrogen adsorption and desorption isotherms were collected at liquid nitrogen temperature using a Quantachrome QudraSorb surface area analyser. All samples were degassed at 300 °C for 2 h under vacuum prior to the analysis. Specific surface area was calculated using the linear portion of Brunauer-Emmett-Teller (BET) model ($P/Po= 0.05-0.2$). Desorption branch of Barret-Joyner-Halenda (BJH) model was employed for the precise determination of pore diameter and pore volume.[13]

2.2.7 Thermogravimetric Analysis (TGA)

Thermogravimetric analysis (TGA) is a technique used to measure mass changes in a material as a function of temperature (or time) under a controlled atmosphere during decomposition reactions.[14] A TGA analysis is performed by gradually raising the temperature of a furnace and simultaneously measuring the sample weight using an analytical balance inside the furnace. Further mass loss is observed when a thermal event involves loss of a volatile component and/or chemical reactions such as combustion, while physical changes like melting makes no such mass loss. Weight of the sample is plotted against temperature or time to illustrate thermal transitions in the material such as impurities, loss of moisture or solvent and decomposition of the material. Perkin-Elmer Pyris-1 instrument was used for TGA investigation of samples in the temperature range of 25-600 °C under air or Ar-atmosphere (heating rate of 10 °C min^{-1}).

2.3 Electrochemical Techniques

Electrochemical methods are used to probe reactions involving electron transfers in electrode materials with respect to applied potential/current. These methods relate the flow of electrons to chemical changes and resulting chemical change is often the oxidation or reduction of a material in the system. Electrochemical techniques are measured in an electrochemical cell, which consists of two or three electrodes in an electrolyte media that transport the charge generated on electrodes through ionic conduction. In three-electrode configuration, reference electrodes (RE) with constant electrochemical potential measures and controls the potential on working electrode (WE) without applying current. While the current to WE are balanced by applying through counter electrode (CE). Thus, potential variations of WE are measured independent of changes occurring at CE that enables to study the specific processes at WE. In this case, employed CE must possess higher capacity than WE to avoid any limitations in the kinetics of electrochemical process. In two electrode configurations, CE and RE are coupled and the potential across complete cell (WE, electrolyte and CE) is measured. Two-electrode configuration is used whenever the precise control of interfacial potential is not critical. Thus, various methods to characterise electrochemical properties of electrode materials and devices are galvanostatic charge-discharge, cyclic voltammetry (CV) and electrochemical impedance spectroscopy (EIS), as described in the following sections.

2.3.1 Galvanostatic Charge-Discharge

Galvanostatic charge-discharge (CD) is a technique used to evaluate the electrochemical performance of electrodes in a battery module such as coin cells, pouch cells etc. Dynamic performance of battery charge and discharge is the speed at which current can be applied in and out from the storage system and consequently, terminal voltage increases and decreases respectively. Charge and discharge dynamics of batteries can be characterised by measuring voltage under constant charge and discharge current inputs.[15] Charge and discharge are mainly controlled by either current or voltage. This study usually involves periods of constant-current (CC) and/or constant-voltage (CV) charging and discharge. A CC charge is applied initially to increase the voltage upto CV for stabilising the system and to avoid high currents that can lead to excessive temperatures and hence damages the battery. Therefore, charge-discharge curves represents the changes in voltage with respect to time when a constant positive (charge) and negative (discharge) currents are applied within limited potential range. Currents (i) applying to the cell are calculated using current density (A g^{-1}), where g is the electrodes active material weight in grams. Thus, the resultant specific capacity (Ah g^{-1}) is the product of current density (A g^{-1}) and charging time (in hours). In this study, Li-ion batteries were subjected to galvanostatic charge-discharge studies (rate performance and long-term cycling) at various current densities in the voltage range of 3.0 - 0 V using a Neware BTS-4000 multi-channel battery tester.

2.3.2 Cyclic Voltammetry (CV)

Cyclic voltammetry (CV) is one of the most powerful electrochemical techniques employed to investigate the reduction and oxidation processes in electrode materials. It further provides the information about the kinetics and thermodynamics of electron-transfer processes, and analysis of electrochemical reactions on anodes and cathodes.[16] CV is also a potential controlled method that measures the current flowing through a cell while sweeping the voltage applied between two potential limits. It is commonly represented by plotting current response as a function of voltage as shown in figure 2.11. A purely capacitive material demonstrates rectangular CV curve, where the total area of the box in the CV corresponds to the total charge associated with ion adsorption and desorption. Any deviation from ideal capacitive behaviour from the CV curves, signifies the nature of reaction mechanism in specific material (e.g. presence of redox reactions, electrochemical degradation of the electrolyte, low electrical conductivity of the electrode material etc).

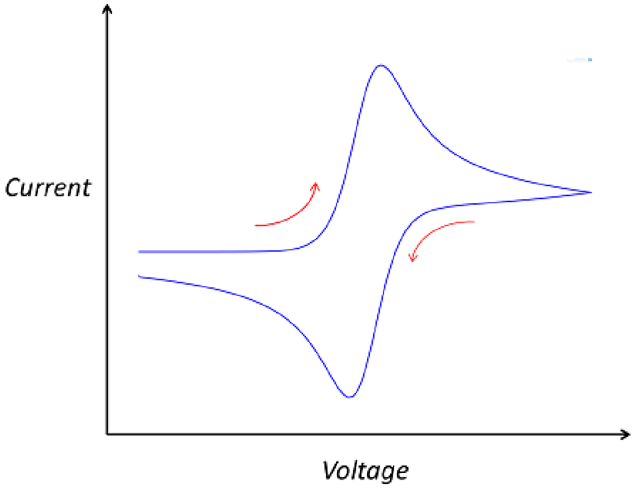

Figure 2.11. Schematic of cyclic voltammetry (CV) plot.

In this work, biologic SP-200 potentiostat is used for cyclic voltammetry (CV) measurements. Pseudocapacitance contribution is calculated from the measured CV plots at different scan rates. Capacitive and diffusion-controlled contribution to the applied current (i) at a fixed potential (V) can be described by equation 2.5.[17]

$$i(V) = k_1 v + k_2 v^{1/2} \tag{2.5}$$

Where v is the sweep rate, $k_1 v$ and $k_2 v^{1/2}$ are current contributions from capacitive and diffusion-controlled process respectively. k_1 and k_2 are constants, determined from the slope and intercept of scan rate dependence of current plot. The percentage of capacitive contribution at specific potentials can be quantitatively determined through k_1 and k_2.

2.3.3 Electrochemical Impedance Spectroscopy (EIS)

Electrochemical impedance spectroscopy (EIS) is a highly versatile technique used to study the function of modulation frequency and applied potential to reveal significant information about the capacitance of electronic states and their resistance for electron transfer. EIS is fundamentally an AC technique in which an applied potential $E(t)$ is modulated over time with small amplitude at a controlled frequency (ω) according to equation 2.6, where, ω is an angular frequency defined by $\omega = 2\pi f$, and f is frequency in Hz.[18] Small perturbation in potential $|E_0|$ ensures linear behavior of current following Butler-Volmer model. Current response $I(t)$ in this case is measured in frequency but offset by a phase angle (φ) depending on the electrochemical circuit parameters (equation 2.7). Hence, impedance is defined as the AC analogue to resistance and is thus related to the alternating potential and current through Ohm's law as shown in equation 2.8.

$$E(t) = |E_o|\sin(\omega t) \tag{2.6}$$

$$I(t) = |I_o|\sin(\omega t + \varphi) \tag{2.7}$$

$$Z(\omega) = E(t)/I(t) \tag{2.8}$$

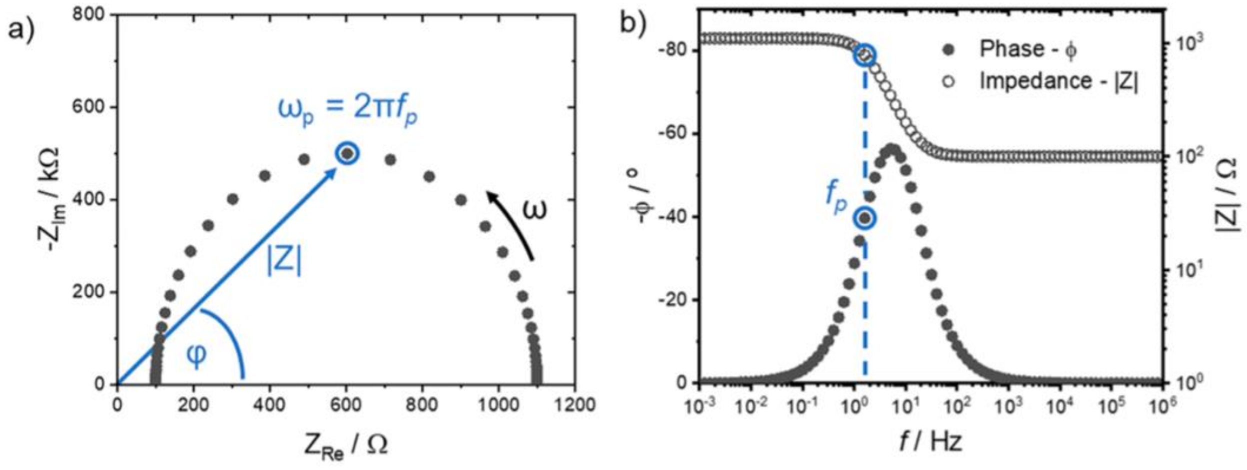

Figure 2.12. (a) Nyquist and (b) Bode plots model.

In a typical EIS experiment, the modulation frequency is sampled over a wide range (~1 mHz to 1 MHz) for a fixed applied potential (E_{app}) on top of which the small modulation amplitude $|E_0|$ is applied such that $E(t) = E_{app} + |E_0|\sin(\omega t)$. Collected data is then interpreted using different plots such as nyquist and bode plot. Predominantly nyquist plot is widely used, in which impedance is plotted as a complex number ($j = \sqrt{-1}$) according to equation 2.9 with Z_{Im} (Z'') along y-axis and Z_{Re} (Z') along x-axis (Figure 2.12a). Characteristic semicircle arises from the parallel combination of a resistor and capacitor designated in figure 2.12a. Another method of graphing EIS data is the bode plot, which is a combination of two plots that show the magnitude of impedance |Z| and the phase angle φ on the y-axis and the modulation frequency f along the x-axis. Each data point represents a unique frequency which can be correlated directly with |Z| and φ.

$$Z(\omega) = |Z|(\cos(\varphi) - j\sin(\varphi)) = Z_{Re} - jZ_{Im} \tag{2.9}$$

A simulated bode plot is shown in Figure 2.12b with the same parameters used in the nyquist plot for comparison. In case of nyquist plot, frequencies associated with each peak are not identical although peak observed for φ results from the semicircle. However, peak in nyquist plot is directly related to R_{ct} and C_{int} at electrode surface according to $f_p = 1/R_{ct}C_{int}$, where $R_{ct}C_{int}$ is known as time constant for parallel circuit.[19] However, peaks in bode plot does not correlate with f_p and can be difficult to interpret directly due to the presence of additional circuit elements such as series resistance. Hence, extracted EIS data must be fit to an equivalent circuit model that includes fundamental parameters such as resistors, capacitors, inductors, and diffusion elements to understand clearly the electron transfer mechanisms.

In this work, biologic SP-200 potentiostat is used for electrochemical impedance spectroscopy (EIS) measurements. Potentiostatic EIS measurements were carried out on fresh batteries at open circuit voltage in the frequency range of 1 MHz to 0.01 Hz. Lithium-ion diffusion coefficients of various defect-engineered electrodes employed in this work were calculated using equation 2.10.[20]

$$D = \tfrac{1}{2}(RT/\ AF^2\sigma_\omega C) \tag{2.10}$$

Where D is the diffusion coefficient, R the gas constant, T the absolute temperature in Kelvin, F the Faraday's constant, C the lithium concentration, and A the electrode area. Warburg impedance coefficient σ_W is determined from the slope of the linear plot between Z' and $\omega^{-1/2}$.

2.4 References

1. D. C. Marcano, D. V. Kosynkin, J. M. Berlin, A. Sinitskii, Z. Sun, A. Slesarev, L. B. Alemany, W. Lu and J. M. Tour, *ACS Nano*, **2010**, 4, 4806-4814.
2. B. Geng, F. Zhan, C. Fang and N. Yua, *J. Mater. Chem.*, **2008**, 18, 4977-4984.
3. R. F. W. Pease and W. C. Nixon, *J. Sci. Instrum.* , **1965**, 42, 81.
4. L. Reimer, *Springer, Berlin*, **1984**, 135-184.
5. J. Wall, J. Langmore, M. Isaacson and A. V. Crewe, *Proc. Natl. Acad. Sci.*, **1974**, 71, 1-5.
6. Z. L. Wang, *J. Phys. Chem. B*, **2000**, 104, 1153-1175.
7. W. L. Bragg, *Proc. Cambridge Philos. Soc.*, **1913**, 17, 43.
8. A. L. Patterson, *Phys. Rev.,* **1939**, 56, 978.
9. G. D. J., *Springer-Verlag.*, **1989**.
10. C. D. Wanger, W. M. Riggs, L. E. Davis, J. F. Moulder and G. E.Muilenberg, *Perkin-Elmer Corp. Eden Prairie, MN, USA*, **1992**.

11. J. Matthew, *Surf. Interface Anal.*, **2004**, 36, 1647.
12. S. Brunauer, P. H. Emmett and E. Teller, *J. Amer. Chem. Soc.*, **1938**, 60, 309-319.
13. E. P. Barrett, L. G. Joyner and P. P. Halenda, *J. Am. Chem. Soc.* , **1951**, 73, 373-380.
14. R. Bottom, in *Principles and Applications of Thermal Analysis*, 2008, DOI: https://doi.org/10.1002/9780470697702.ch3, pp. 87-118.
15. Y. Zhu and C. Wang, *J. Phys. Chem. C* **2010**, 114, 2830-2841.
16. T. Kim, W. Choi, H.-C. Shin, J.-Y. Choi, J. M. Kim, M.-S. Park and W.-S. Yoon, *J. Electrochem. Sci. Technol.*, **2020**, 11, 14-25.
17. V. Augustyn, P. Simon and B. Dunn, *Energy Environ. Sci.*, **2014**, 7 1597-1614
18. W. Choi, H.-C. Shin, J. M. Kim, J.-Y. Choi and W.-S. Yoon, *J. Electrochem. Sci. Technol.*, **2020**, 11, 1-13.
19. A. R. C. Bredar, A. L. Chown, A. R. Burton and B. H. Farnum, *ACS Appl. Energy Mater.*, **2020**, 3, 66-98.
20. A. J. Bard and L. R. Faulkner, *Electrochemical Methods: Fundamentals and Applications, 2nd Edition*, John Wiley & Sons, **2001**.

Chapter 3

Extremely Pseudocapacitive Interface Engineered CoO@3D-NRGO Hybrid Anodes for High Energy/ Power Density and Ultralong Life Lithium-Ion Batteries

3.1 Introduction

Cobalt oxides (Co_3O_4 & CoO) are considered as promising anodes due to their high theoretical capacity (890 & 716 mAh g^{-1} respectively). Although CoO and Co_3O_4 based anodes has been studied for the last 20 years, their applications are limited due to its low electronic conductivity, large volume change (up to ~200%), and particle agglomeration, which result in severe capacity fading during extended cycling.[1-5] Unavoidable formation of electronically insulating Li_2O ($Co_3O_4 + 8e^- + 8Li \leftrightarrow 4Li_2O + 3Co$) during the lithiation of Co-oxides also deteriorate the electrochemical performance at fast charge-discharge rates.[3, 6] Due to the high operational voltage of CoO (~1.2V), Li-ion full-cells also experienced low voltage (<3 V). Hence, it is essential to develop high capacity transition metal oxide based anodes with ultralong cycling stability for next-generation Li-ion batteries.

One of the most widely used strategies to improve the electrochemical performance is the fabrication of nanostructures such as nanoparticles, nanosheets, nanorods, nanowires, and nanospheres.[1, 7-12] Increased reactivity in this case often leads to excessive Li_2O formation and capacity fading on prolonged cycling.[13] Porosity control and optimization are also found to be effective for improving the Li-ion storage and electrochemical performance of Co-based anodes.[2] Superior contact with the electrolyte solution is identified as the key factor responsible for the improved performance of mesoporous Co_3O_4 electrodes.[9, 14] Another approach is the hybridization of active material with carbonaceous substrates such as graphene, carbon nanotubes and carbon fibres.[4, 15-17] This method resulted in enhanced electronic conductivity and reduced particle agglomeration that leads to superior electrochemical performance.[3, 4] Nevertheless, development of fast charging and high capacity Co-based anodes with excellent cycling stability remains as a challenge.

Pseudocapacitance is nominal in the case of conversion type transition metal oxide anodes. [18, 19] While pseudocapacitance can be induced (extrinsic pseudocapacitance) by nanostructuring, that remains elusive in the case of conversion type anodes. The main reason being the sluggish Li-ion diffusion kinetics (diffusion coefficients in the 10^{-14}-10^{-16} cm^2 s^{-1} range), which does not satisfy the requirement of pseudocapacitive type Li-ion storage.[20] An electrode microstructure facilitating high electronic and ionic conductivity is crucial to induce pseudocapacitive type Li-ion storage in conversion type materials.[19] Although hybrids of Co-oxides with 2-dimensional carbonaceous substrates such as graphene and RGO are reported earlier, superior pseudocapacitive Li-ion storage were not achieved as a result of increased particle size, less efficient charge transfer and lack of well-defined interfaces due to particle agglomeration.[10, 21]

In this chapter, we demonstrate a high energy (400 Wh kg^{-1}) and power density (1 kW kg^{-1}) secondary Li-ion batteries based on extremely pseudocapacitive interface engineered CoO@3D-NRGO hybrid anode and $LiNiMnCoO_2$ cathode. Design and synthesis of CoO@3D-NRGO is based on the following aspects. (i) CoO is chosen as the active material instead of Co_3O_4 to reduce the formation of electronically insulating Li_2O. (ii) 3-D morphology is aimed at facilitating superior contact with electrolyte solution and strain relaxation during prolonged cycling at higher charge-discharge rates. (iii) Chemical bonding between Co and NRGO (Co–O–C bonds) is intended for immobilizing CoO nanoparticles to prevent agglomeration and providing efficient charge separation. Metal oxide surface modification also prevents the restacking of graphene sheets, and provides ample surface area for fast reaction kinetics. (iv) Nitrogen doping of RGO is meant for improving the electronic conductivity to achieve superior charge separation and high rate performance. These morphological and microstructural advantages enable optimum electronic and ionic conductivities that are crucial for pseudocapacitive Li-ion storage. Highly pseudocapacitive CoO@3D-NRGO hybrid anode exhibited outstanding Li-ion storage specific capacity, rate performance and cycling stabilities compared to CoO/ Co_3O_4 nanoparticles and previous reports. Excellent Li-ion storage performance of interface engineered CoO@3D-NRGO hybrid electrode is credited to the synergy between conversion reaction of ultrafine CoO and pseudocapacitive Li-ion storage at the Co/Li_2O/NRGO nanointerfaces.

3.2 Results and Discussion

3.2.1 Synthesis and Characterization of CoO@3D-NRGO Hybrid Anode

Schematic of the synthesis of interface engineered CoO@3D-NRGO hybrid composed of ultrafine CoO nanoparticles chemically bonded to nitrogen-doped reduced graphene-oxide is presented in figure 2.1**.** Graphite flakes are selected as the RGO precursor due to its low cost and natural abundance. Exfoliation of the individual graphene layers are achieved in this case through improved Hummer's method. This soft-chemical method resulted in the formation of individual GO layers rich in oxygen containing functional groups. Urea played multiple roles in the demonstrated synthetic method of CoO@3D-NRGO hybrid. Firstly, it acts as a complexing agent that facilitates the integration (through Co–O–C) and uniform distribution of CoO nanoparticles on RGO layers.[22] Urea also reduces surface functional groups of GO resulting in improved electronic conductivity. Moreover, NH_4^+ ions produced by the decomposition of urea results in the nitrogen doping of RGO. Glycol in this case acts as a mild reducing agent and assist 3D-morphology formation through the interaction of –OH groups with C=O and C-OH groups of GO. Electrostatic interaction between Co^{2+} ions and oxygen containing functional groups assist the uniform distribution of CoO nanoparticles on RGO surface, which minimize RGO restacking during the solvothermal reduction and electrode preparation.

As expected, scanning electron microscopy (SEM) image of GO revealed a 2D morphology with an average size of 20-30 μm (Figure 3.1a). Whereas, 3D porous microstructure composed of interconnected NRGO sheets are evident from the SEM images of CoO@3D-NRGO at various magnifications (Figure 3.1b and c).

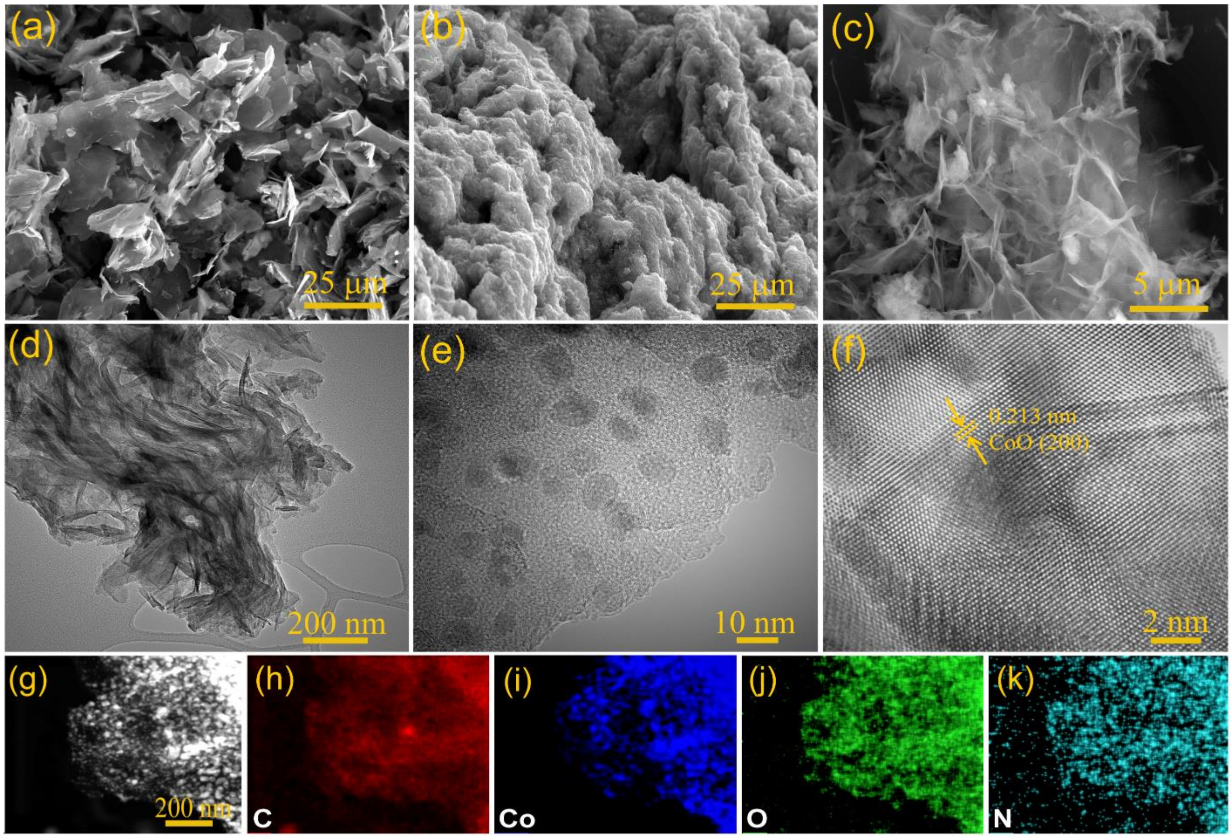

Figure 3.1 SEM images of (a) graphene oxide and (b-c) CoO@3D-NRGO. (d-f) TEM images at various magnifications of CoO@3D-NRGO. (g) HAADF image and (h-i) corresponding EDX elemental mapping of CoO@3D-NRGO.

Analogous images of the precursor $(NH)_4Co_8(Co_3)_6(OH)_6.4H_2O$@3D-NRGO (Appendix 1) also confirmed the 3D microstructure formation during solvothermal reaction as a result of self-assembly. Further microstructural analysis using transmission electron microscopy (TEM) confirmed the hierarchical interconnected 3D-porous nature (Figure 3.1d). High-resolution image (Figure 3.1e) confirmed the uniform anchoring of CoO nanoparticles of 10±2 nm size on NRGO sheets. In this case, part of NRGO sheets are still exposed, which is essential for maintaining superior contact between individual sheets and electrolyte solution to maintain excellent electronic and ionic conductivity respectively. HRTEM image (Figure 3.1f) verified high crystallinity of CoO nanoparticles with an interplanar spacing of 0.213 nm corresponding to (200) plane. EDX elemental mapping (Figure 3.1g-k) displayed uniform distribution of carbon, nitrogen, oxygen and cobalt on the CoO@3D-NRGO surface. Homogenous distribution of ultrafine CoO nanoparticles on NRGO sheets can effectively maintain large effective surface area and contact with electrolyte solution, enabling superior Li-ion storage performance.

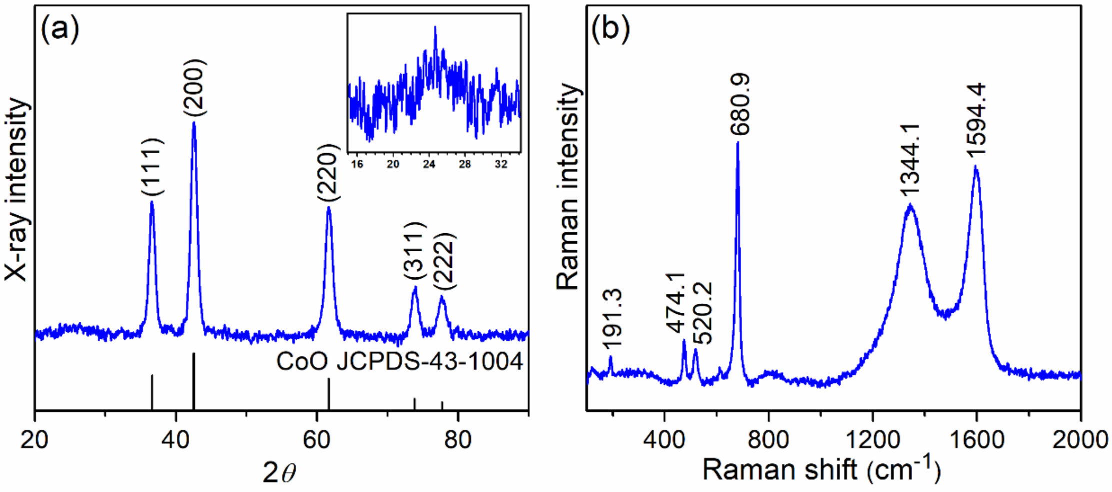

Figure 3.2 (a) X-ray diffraction pattern and (b) Raman spectra of CoO@3D-NRGO.

X-ray diffraction (XRD) pattern of CoO@3D-NRGO hybrid (Figure 3.2a) exhibited distinctive peaks of CoO (JCPDS card No. 43-1004).[22, 23] Interlayer spacing of 9.0Å in the case of GO is identified from the characteristic (001) peak (Appendix 2a).[24] Disappearance of this signal designate the lack of RGO restacking in CoO@3D-NRGO hybrid due to CoO anchoring.[22] A broad XRD signal at 24.7º (Figure 3.2a inset) represent the formation of nitrogen doped RGO with large interlayer spacing.[25] XRD pattern of the precursor (Appendix 2b) correspond to $(NH)_4Co_8(Co_3)_6(OH)_6.4H_2O$@3D-NRGO (JCPDS card No. 52-0552), and its complete decomposition during annealing is demonstrated by the absence of cobalt hydroxide/ cobalt carbonate peaks in the XRD pattern of CoO@3D-NRGO hybrid. Average particle-size calculation using Debye-Scherrer equation indicated the presence of 10±2 nm sized CoO nanoparticles in the hybrid, which is in line with the TEM results. Raman spectra of CoO@3D-NRGO hybrid (Figure 3.2b) designated phase purity and uniform surface distribution of phase pure CoO. Raman signals at 474.1 and 680.9 cm^{-1} correspond to the E_g and A_{1g} vibrational mode of CoO, while the peaks at 191.3 and 520.2 cm^{-1} represent the F_{2g} modes.[26, 27] Raman signals at 1344.1 (D-band) and 1594.4 cm^{-1} (G-band) also evidence the presence of NRGO in the hybrid. The D-band of A_{1g} symmetry can be endorsed to the presence of disordered carbon and structural defects in the hybrid, and G-band represents E_{2g} mode of the ordered graphitic layers of 3D-NRGO.[26, 28] Although the D/G ratio of CoO@3D-NRGO is higher than those of GO, full width at half-maximum (FWHM) of the D and G-band decreased confirming the formation of a more ordered structure.[17] Such ordered NRGO network is beneficial for achieving superior electronic conductivity that is essential for pseudocapacitive Li-ion storage.[22]

X-ray photoelectron spectroscopy (XPS) of CoO@3D-NRGO provided additional insight into the surface chemical characteristics responsible for enhanced pseudocapacitive Li-ion storage. High-resolution C 1s spectra of GO (Figure 3.3a) can be deconvoluted into elemental sp^2 hybridised carbon (284.5 eV), C=O (286.8 eV) and O=C–O/ C-N (288.5 eV) groups. [17, 29, 30] In the case of CoO@3D-NRGO hybrid, 286.8 eV signal disappeared and only the high-intensity peak at 284.5 eV corresponding to sp^2 carbons is retained signifying the reduction of most oxygen containing functional groups. [17, 23, 31] High-resolution O 1s spectra of GO (Figure 3.3b) consist of a major peak at 532.8 eV confirming the presence of oxygen-containing functional groups. Signals at 531.8 eV and 530.2 eV of CoO@3D-NRGO hybrid corresponds to the oxygen containing species (Co–O–C bonds, C=O, C-O etc.) and Co-O bonds of CoO respectively. [29, 32]

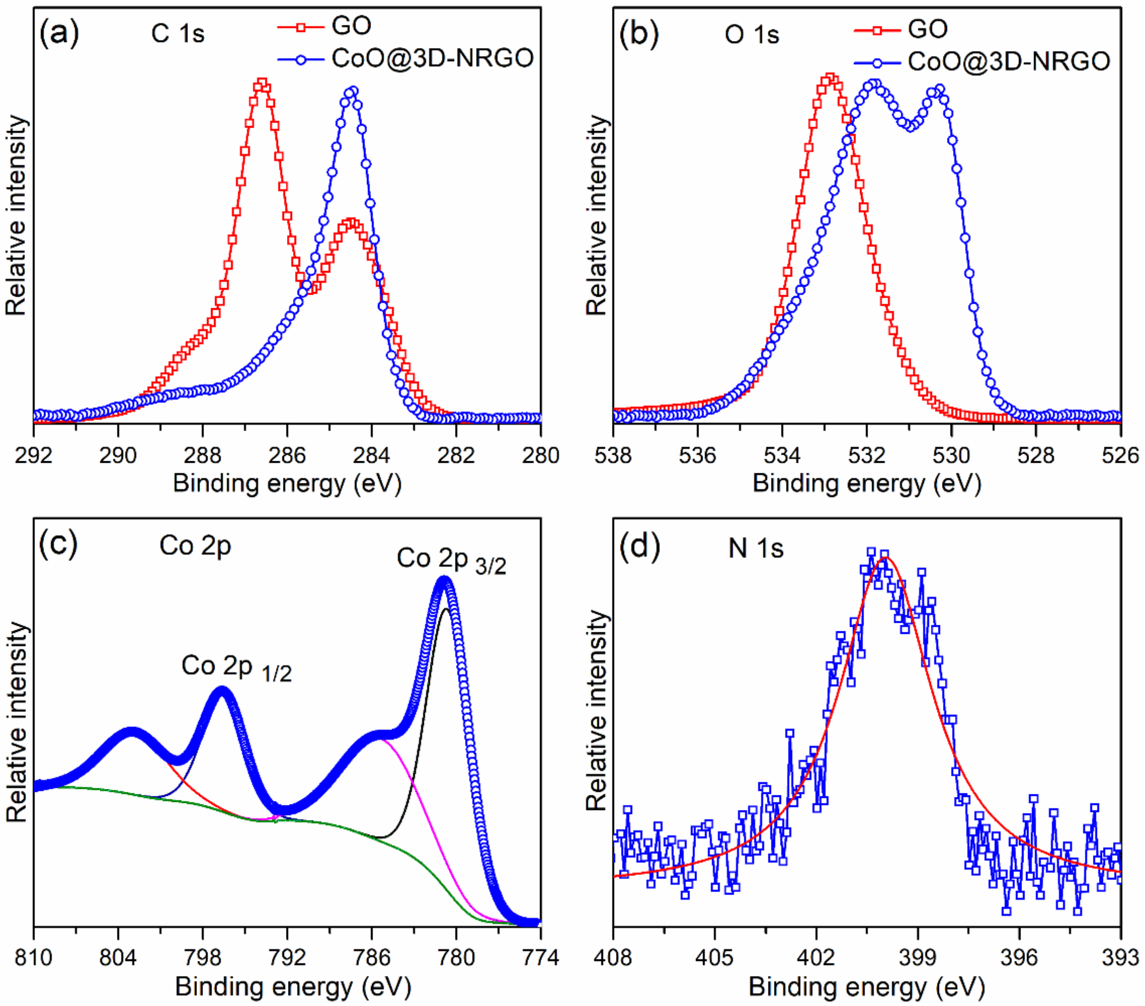

Figure 3.3 High-resolution (a) C 1s, (b) O 1s, (c) Co 2p and (d) N 1s XPS spectra of CoO@3D-NRGO.

Chemical bonding between the CoO nanoparticles and NRGO could benefit the interfacial charge separation and enhance the Li-ion storage electrochemical properties of CoO@3D-NRGO hybrid. Another crucial role of Co–O–C is the strong anchoring of CoO nanoparticles on NRGO surface, which prevent its detachment and agglomeration during prolonged charge-discharge process. High-resolution Co 2p spectra (Figure 3.3c) of CoO@3D-NRGO hybrid exhibited two peaks at

780.7 eV and 796.8 eV corresponding to Co $2p_{3/2}$ and Co $2p_{1/2}$ components respectively, and their spin-orbit separation of 15.9 eV are identical to previous reports.[16] Satellite peaks of Co^{2+} at 786.4 eV and 802.6 eV further confirmed the formation of phase pure CoO and the absence of other Co-oxides such as Co_3O_4. Surface quantitative analysis from high-resolution N 1s spectra (Figure 3.3d) verified the presence of 2% nitrogen, which is beneficial for improved electronic conductivity of CoO@3D-NRGO electrode.[32, 33]

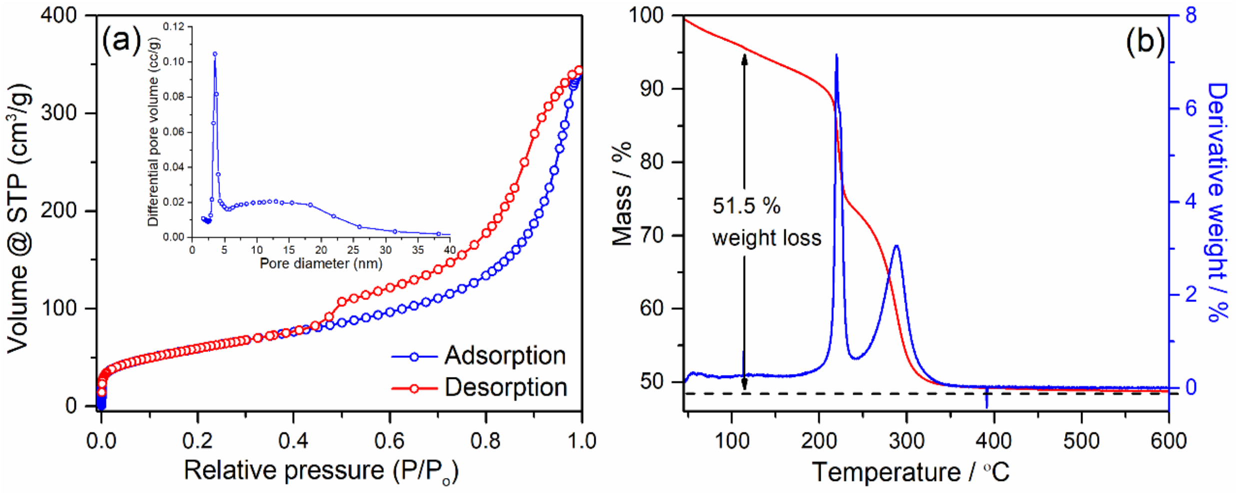

Figure 3.4 (a) N_2 adsorption-desorption isotherm of CoO@3D-NRGO. Inset: pore-size distribution of CoO@3D-NRGO. (b) Thermogravimetric analysis of Precursor $(NH)_4Co_8(Co_3)_6(OH)_6.4H_2O$@3D-NRGO under air-atmosphere at a heating rate of 10 °C min^{-1}.

Nitrogen adsorption-desorption isotherm of CoO@3D-NRGO hybrid displayed type IV hysteresis, and increased slope at a relative pressure between 0.4 and 1.0 associated with the presence of mesopores (Figure 3.4a). Brunauer-Emmett-Teller (BET) and Barret-Joyner-Halenda (BJH) analysis revealed a high specific surface area of 216 m^2 g^{-1}, pore volume of 0.51 cm^3 g^{-1} and an average pore diameter of 8.3 nm (Figure 3.4a inset). Such a high surface area and mesoporosity are favourable for superior Li-ion diffusion and accommodation of large volume changes during charge-discharge process. Thermogravimetric analysis (TGA) of the precursor

(Figure 3.4b) $(NH)_4Co_8(Co_3)_6(OH)_6.4H_2O$@3D-NRGO is carried out to follow the CoO@3D-NRGO hybrid formation. Weight loss of 24% in the temperature range of 30-220 °C represent loss of water and surface functional groups. Further weight loss of 27.5% in the range of 220-330 °C corresponds to the precursor decomposition. Precursor in total experienced no weight loss after 330 °C, which signify the complete decomposition of the precursor $(NH)_4Co_8(Co_3)_6(OH)_6.4H_2O$. Based on this analysis, the precursor is heat treated at 500 °C under Ar-flow to obtain CoO@3D-NRGO hybrid. CoO@3D-NRGO hybrid experienced a total weight loss of 26%, which correspond to ~60% CoO loading (Appendix 3). In summary, simultaneous solvothermal reduction of GO and cobalt nitrate in presence of urea resulted in the formation of 3D hybrid anode composed of ultrafine CoO nanoparticles chemically bonded to NRGO.

3.2.2 Electrochemical Performance of CoO@3D-NRGO Hybrid Anode

Lithium-ion storage performance of interface engineered CoO@3D-NRGO hybrid anodes are tested in the voltage range of 0-3 V in a half-cell configuration. Galvanostatic rate performance of electrodes containing various amounts of CoO are initially performed (Figure 3.5a) to identify the optimal loading. It is clear that the electrodes containing ~60% CoO nanoparticles exhibited superior performance compared to those consisting higher and lower amounts. Low specific capacities and rate performance of electrodes containing ~50 and ~70% CoO can be credited to the low active material loading and increased formation of electronically insulating Li_2O/ particle agglomeration respectively.[2, 34-36] Li-ion intercalation into the interlayers of NRGO also contributed to the overall specific capacity of CoO@3D-NRGO hybrid anode. However, capacity contribution of 3D-NRGO is negligible at higher current densities, which confirmed conversion and pseudocapacitance as the major Li-ion storage processes. Li-ion storage performance of interface engineered CoO@3D-NRGO is considerably higher than CoO and Co_3O_4-nanoparticles under similar experimental conditions (Figure 3.5b). Irreversible SEI formation resulted in the first cycle capacity loss of CoO@3D-NRGO, Co_3O_4 and CoO nanoparticles.

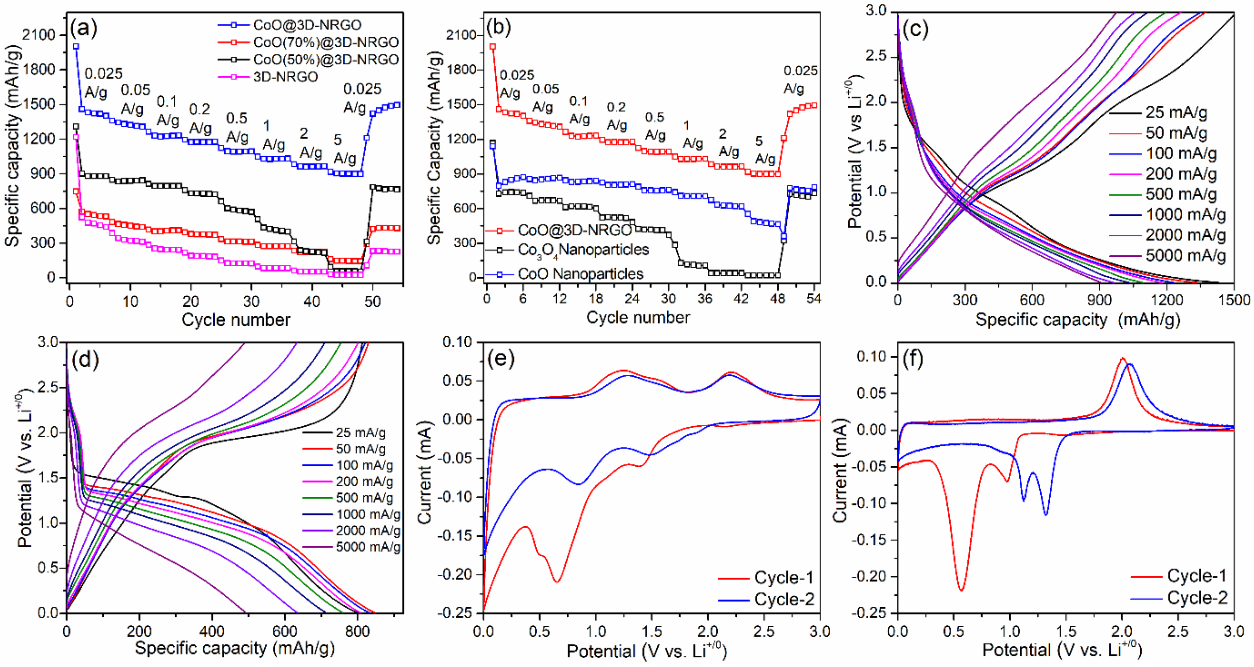

Figure 3.5 Galvanostatic rate performance of (a) with different Co loading, and (b) CoO@3D-NRGO, CoO and Co_3O_4 nanoparticles. Galvanostatic voltage profiles of (c) CoO@3D-NRGO, and (d) CoO nanoparticles at various current densities. Cyclic voltammograms at a scan rate of 0.1 mV s^{-1} of (e) CoO@3D-NRGO, and (f) CoO nanoparticles.

However, initial coulombic efficiency of CoO@3D-NRGO (~80%) is significantly higher than the conventional CoO (~70%) and Co_3O_4 anodes (~65%). This is one of the lowest irreversible capacity loss reported for conversion-type anode materials.[2, 12-16] First cycle coulombic efficiency can be further improved with electrolyte additives or prelithiation strategy. CoO@3D-NRGO anode delivered an outstanding reversible capacity of 1429 compared to CoO (798 mAh g^{-1}) and Co_3O_4 nanoparticles (731 mAh g^{-1}) at a low current density of 25 mA g^{-1}. CoO and Co_3O_4 nanoparticles experienced severe capacity fading (Figure 3.5b) at higher current densities, which is in good agreement with previous reports. [2, 3, 27] On the other hand, CoO@3D-NRGO retained an excellent capacity of 964 and 906 mAh g^{-1} even at higher current densities of 2 and 5 A g^{-1} respectively, and regained 1420 mAh g^{-1} on lowering the current density to 25 mA g^{-1}. These values are considerably higher than the theoretical capacity of graphite anodes used in state-of-the-art Li-ion batteries.[37] It is also worth noting that the maximum specific capacity exhibited by CoO@3D-NRGO is even superior to the theoretical capacities of Co_3O_4 (890 mAh g^{-1}) and CoO (716 mAh g^{-1}).

Galvanostatic charge-discharge profiles of CoO@3D-NRGO hybrid and CoO nanoparticles at various current densities are presented in figure 3.5c and d respectively. CoO@3D-NRGO electrode displayed a sloping profile unlike the voltage profile of CoO and Co_3O_4 nanoparticles (Appendix 4a) that consist of a plateau corresponding to conversion reaction. This indicates different Li-ion storage mechanisms of these electrodes, which dictate the specific capacity, rate performance and cycling stability. Average operational voltage of CoO@3DNRGO (~0.7V) is also lower than those of CoO and Co_3O_4 electrodes (~1 V), which makes it suitable for high energy density Li-ion full-cells. In the case of CoO and Co_3O_4 nanoparticles, discharge profile regions 3-1.2 V, 1.2-1 V and 1-0 V corresponds to the surface, bulk and interfacial Li-ion storage (pseudocapacitive process) respectively. Voltage profiles of these single-phase CoO and Co_3O_4 anodes varied considerably with current densities and only surface storage occurs at higher rates due to sluggish Li-ion diffusion. In contrast, voltage profiles of CoO@3D-NRGO remain identical irrespective of the current densities, which is characteristic of similar Li-ion storage mechanism at various charge-discharge rates. Slopping voltage profile is also indicative of dominant diffusion independent pseudocapacitive process. Capacity gain of CoO@3DNRGO anode also occurs in a wide voltage range unlike CoO and Co_3O_4 nanoparticles, where the conversion plateau is mainly contributing the charge/ discharge capacity. Coulombic efficiency of this electrode at current densities ranging from 25 mA g^{-1} to 5A g^{-1} are outstanding (99.9%) demonstrating the complete reversibility of the Li-ion storage mechanism. Such high coulombic efficiency is one of the key requirements for the fabrication of stable Li-ion full-cells.[2]

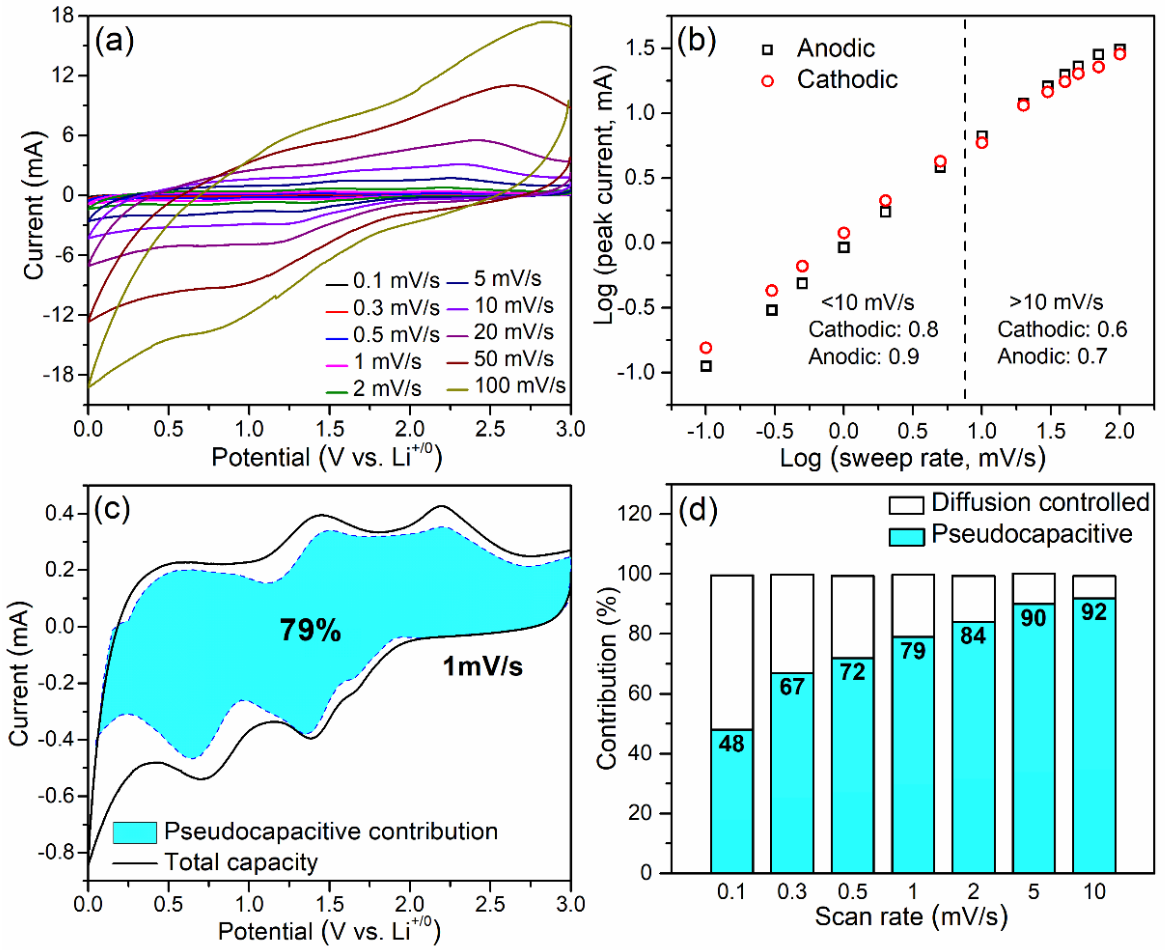

Figure 3.6 (a) Cyclic voltammetry of CoO@3D-NRGO at different scan rates. (b) Peak current dependence of scan rates, and (c) cyclic voltammograms of CoO@3D-NRGO at a scan rate of 1 mV s^{-1}. Pseudocapacitive capacity contribution is shown in the shaded region. (d) Capacity contribution at different scan rates of CoO@3D-NRGO.

Cyclic voltammetry (CV) of CoO, Co_3O_4 and CoO@3D-NRGO hybrid electrodes are performed in the voltage range of 0-3 V for a detailed investigation of redox processes. In the case of CoO@3D-NRGO electrode (Figure 3.5e), peaks at 1.4 V of the first cathodic scan correspond to the surface Li-ion storage on the hierarchical interconnected 3D-NRGO possessing high surface area and porosity.[26] Broad cathodic signal centered at 0.65 V corresponds to CoO reduction ($CoO + 2Li^+ + 2e^- \rightarrow Co + Li_2O$) and solid electrolyte interface (SEI) formation.[38, 39] Cathodic peak at lower potential range of 0.5-0V is characteristic of the Li-ion intercalation reaction of 3D-NRGO. These cathodic responses resemble very well with the irreversible capacity loss and sloping galvanostatic voltage profiles. Reduced cathodic signal intensities in the potential range of 1.0 to 0 V during the second scan signify the complete SEI formation in the first cycle. Shifting of second cycle cathodic signals towards higher potentials can be assigned to the Li_2O formation in the first cycle.[2] Anodic signals at 1.2 V, and 2.2 V corresponds to Co oxidation ($Co + Li_2O \rightarrow CoO + 2Li^+ + 2e^-$) and removal of surface adsorbed Li-ions respectively.[38] Cyclic voltammograms of CoO (Figure 3.5f) and Co_3O_4 nanoparticles (Appendix 4b) displayed completely different electrochemical responses compared to CoO@3D-NRGO hybrid anode. In the case of CoO, cathodic peaks at 0.9 V and 0.6 V represent SEI formation and CoO reduction respectively. First cycle cathodic peak of Co_3O_4 at 0.8 V corresponds simultaneous conversion reaction and unavoidable Li_2O formation.[40] Broad anodic signals observed for both CoO and Co_3O_4 nanoparticles around 2 V in the first and second cycle represent Co oxidation. These anodic and cathodic responses are in good agreement with the previous reports.[10, 31, 41] It is thus clear that Li-ion storage mechanism of interface engineered CoO@3D-NRGO hybrid is considerably different from CoO and Co_3O_4 nanoparticles.

Further quantitative analysis of pseudocapacitive Li-ion storage is performed by collecting cyclic voltammograms of CoO@3D-NRGO hybrid at various scan rates (Figure 3.6a). Both anodic and cathodic peak current intensities followed a linear dependence with scan rate, which is typical of pseudocapacitive type charge storage. Anodic and cathodic current as a function of scan rate can be expressed by power law $i=av^b$. Where i is the current (mA), a and b are arbitrary constants, and v is the sweep rate (mV s^{-1}). In general, parameter b determines the nature of charge storage indicating that the current is controlled by semi-infinite linear diffusion for b=0.5, and b=1 for surface-controlled behaviour. Figure 3.6b displayed linear dependence of log (i) vs log (v) plot for the CoO@3D-NRGO hybrid anode. Calculated b-values for the cathodic and anodic peaks in the scan rate range of 0.1-10 mV s^{-1} are 0.8 and 0.9 respectively signifying that the current response is surface controlled and thus mostly pseudocapacitive Li-ion storage.[18, 42] Although b-values decreased to 0.6 and 0.7 respectively with an increase of sweep rates to 10-1000 mV s^{-1}, these values still represent a high degree of pseudocapacitive process. Small drop in b-value can be credited to an increased ohmic resistance and diffusion constraints at very high sweep rates. Such phenomena have also been previously observed for intercalation type (T-Nb_2O_5 and TiO_2) and alloying type pseudocapacitive electrodes.[42-44]

Li-ion storage through diffusion dependent conversion reaction and diffusion independent pseudocapacitive interfacial storage are further distinguished using equation 2.5 (Figure 3.6c).[18] Pseudocapacitive Li-ion storage dominates the entire voltage range of CoO@3D-NRGO hybrid electrode with least contribution in the 1.0-0 V range, where the diffusion-controlled conversion and intercalation reaction occurs. A high pseudocapacitive contribution of 79% is exhibited by CoO@3D-NRGO electrode at a scan rate of 1 mV s^{-1}, suggesting surface dominated Li-ion storage mechanism. Gradual increase of pseudocapacitive contribution is observed with an increase of scan rates from 0.1 to 10 mV s^{-1} (Figure 3.6d), and achieved a maximum of 92% at 10 mV s^{-1}. This observation is in good agreement with the slopping voltage profiles at higher current densities that is distinctive of pseudocapacitive Li-ion storage. Reduced diffusion controlled capacity contribution should be expected in this case at higher current densities due to the well-known kinetic limitation of conversion reaction.[10] This is further verified by the low pseudocapacitive contributions of CoO and Co_3O_4 nanoparticles at various scan rates in comparison to the CoO@3D-NRGO hybrid anode (Appendix 5). High pseudocapacitive contribution of interface engineered CoO@3D-NRGO hybrid anode even at slow charge-discharge rates is beneficial for achieving high energy density, which is usually lacking in the case of pseudocapacitive anodes such as TiO_2, V_2O_5, Nb_2O_5, $TiNb_2O_7$ and $Li_4Ti_5O_{12}$.[44, 45]

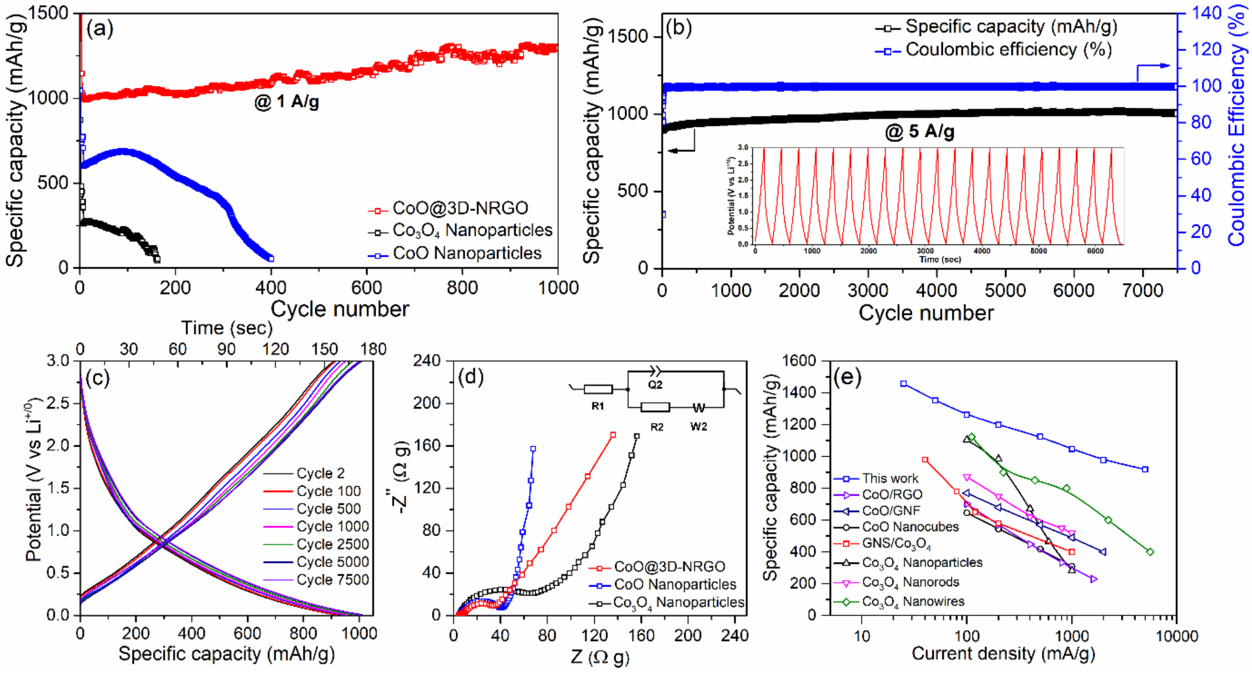

Figure 3.7 (a) Galvanostatic cycling for CoO@3D-NRGO, CoO nanoparticles and Co_3O_4 nanoparticles at a current density of 1 A g^{-1} (b) Galvanostatic cycling for CoO@3D-NRGO at a current density of 5 A g^{-1} (c) Galvanostatic voltage profiles of CoO@3D-NRGO correspond to various galvanostatic cycles at a current density of 5 A g^{-1}. (d) Nyquist plots of CoO@3D-NRGO, CoO nanoparticles, and Co_3O_4 nanoparticles. Inset: Randles equivalent circuit used for fitting the EIS pattern. (e) Li-ion storage performance comparison of CoO@3D-NRGO with other Co-based anodes reported earlier.

Galvanostatic cycling stability of interface engineered CoO@3D-NRGO hybrid anode is exceptional compared to Co_3O_4 and CoO nanoparticles-based electrodes. For instance, at a current density of 1 A g^{-1}, CoO@3D-NRGO hybrid achieved a high reversible specific capacity of 1020 mAh g^{-1} and retained 1290 mAh g^{-1} (120% of the initial capacity) after 1000 charge-discharge cycles (Figure 3.7a). Both CoO and Co_3O_4 nanoparticle-based anodes exhibited poor cycling stability and failed after 400 and 170 cycles respectively. This should be expected due to electrode pulverization related to the excessive volume change, particle agglomeration and formation of electronically insulating Li_2O during lithiation-delithiation process.[10] Improved cycling stability of CoO compared to Co_3O_4 originated mainly from the reduced Li_2O formation. Although cycling stability of CoO is superior to Co_3O_4, it is still far from the requirements of practical applications. CoO@3D-NRGO hybrid exhibited outstanding cycling stability even at a high current density of 5A g^{-1}, retaining 990 mAh g^{-1} (110% of the initial capacity) after 7500 galvanostatic cycles (Figure 3.7b). Coulombic efficiency on extended cycling is also superb, retaining 99.9% (Figure 3.7b) even at a high current density of 5 A g^{-1}. It is also interesting to note the specific capacity of CoO@3D-NRGO hybrid anode increased on extended cycling, especially at lower current densities. This specific capacity increase can be ascribed to (a) partial pulverisation of CoO nanoparticles (b) increased formation of Li_2O/Co/NRGO interfaces (c) reversible SEI formation, and (d) exfoliation of NRGO that can create additional sites for Li-ion storage by increasing the exposed surface area.[46-48] Voltage profiles of CoO@3D-NRGO at various stages of extended cycling (Figure 3.7c) exhibited identical shapes, which clearly established high reversibility and identical Li-ion storage mechanism during numerous charge-discharge processes. It is worth noting that commonly used electrolyte additives such as vinylene carbonate (VC) or fluoroethylene carbonate (FEC) are not used for CoO@3D-NRGO anode, demonstrating its ability to work in commercial standard electrolyte solution.

Electrochemical impedance spectroscopic (EIS) measurements provided further details regarding the Li-diffusion kinetics of Co based electrodes (Figure 3.7d). Nyquist plots of all Co-based electrodes composed of a low frequency slopping line and high frequency semicircle representing solid-state diffusion (Z_w) and charge-transfer resistance (R_{ct}) respectively.[49, 50] Fitting of the Nyquist plots to the equivalent circuit (Figure 3.7d inset) revealed charge transfer resistances of 34 Ω (CoO@3D-NRGO hybrid), 40 Ω (CoO nanoparticles), and 65 Ω (Co_3O_4 nanoparticles). Lower charge transfer resistance in the case of CoO@3D-NRGO hybrid compared to CoO and Co_3O_4 nanoparticles can be related to the hierarchical 3D porous microstructure and increased surface area (216 $m^2 g^{-1}$) compared to CoO (30 $m^2 g^{-1}$) and Co_3O_4 (34 $m^2 g^{-1}$) that allows superior contact with the electrolyte solution. It is interesting to note that electrochemical performance of higher surface area Co_3O_4 is inferior to lower surface area CoO nanoparticles. Hence, surface area is not the only factor deciding the Li-ion storage performance of these conversion type anodes. Lithium-ion diffusion coefficients calculated from the Warburg impedance (Equation 2.10) are 1.0×10^{-13} $cm^2 s^{-1}$, 1.1×10^{-14} $cm^2 s^{-1}$ and 1.4×10^{-14} $cm^2 s^{-1}$ for CoO@3D-NRGO hybrid, CoO and Co_3O_4 nanoparticles respectively. Such a 10-fold higher Li-ion diffusion coefficient of CoO@3D-NRGO hybrid anode is vital for achieving excellent pseudocapacitive performance. These values validated the strong dependence of Li-ion diffusion kinetics with pseudocapacitance, specific capacities and cycling stabilities. Increased pseudocapacitive charge storage is beneficial for achieving fast charging and ultra-long cycling stability. Specific capacities of interface engineered CoO@3D-NRGO hybrid anode at various current densities are radically superior to the values reported in the literature (Figure 3.7e).[9, 11, 16, 33, 51-53] Ultra-long cycling stability of CoO@3D-NRGO hybrid anode is also superior to any of the transition metal oxide based anodes reported to date.

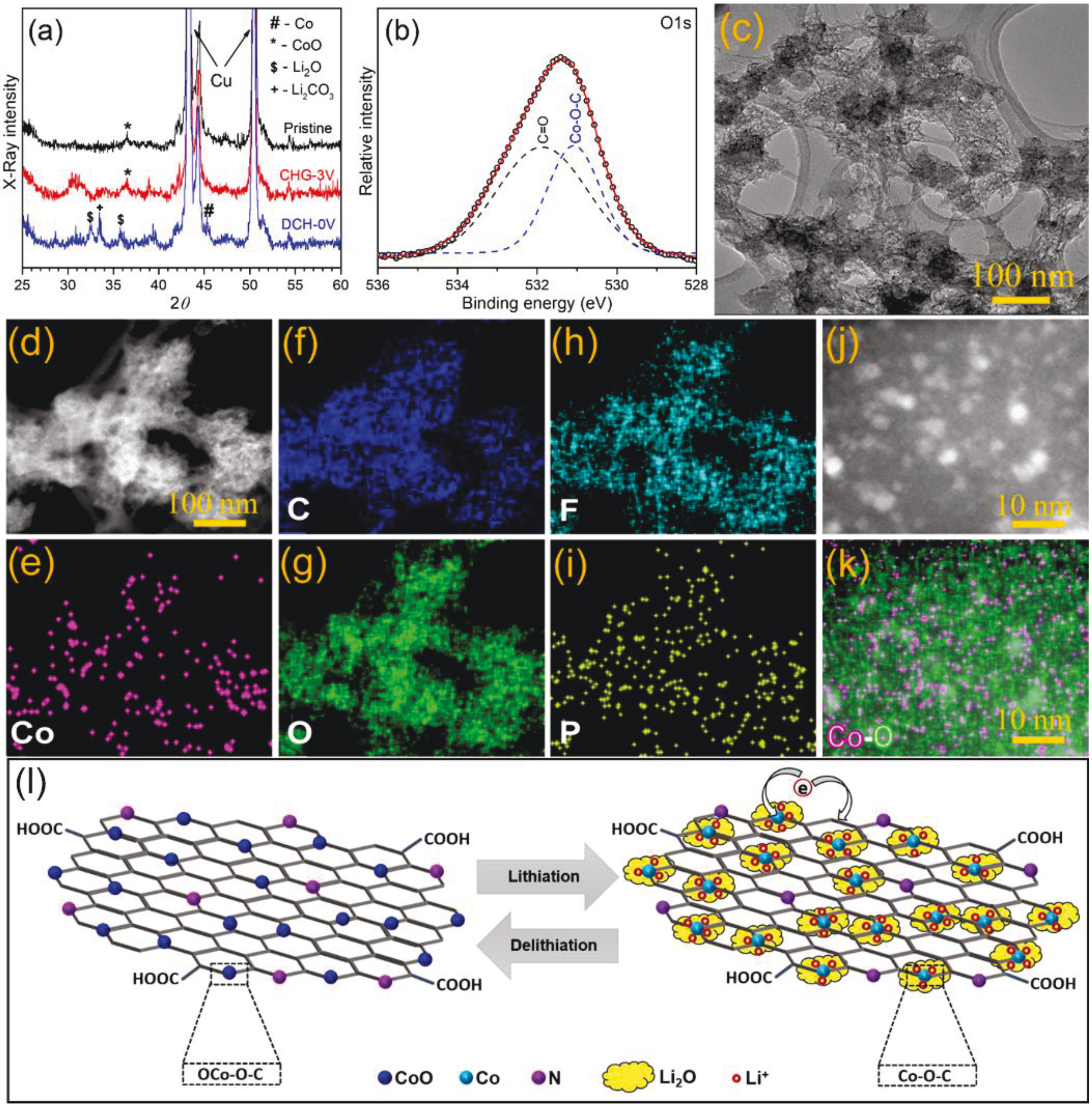

Figure 3.8 (a) X-ray diffraction patterns of CoO@3D-NRGO electrode at different state of charge, (b) High-resolution O 1s XPS spectra and (c) TEM image of cycled CoO@3D-NRGO electrode. (d) HAADF image and (e-i) corresponding EDX elemental mapping. (j) High-resolution HAADF image and (k) corresponding layered Co/ O EDX elemental mapping of CoO@3D-NRGO discharged to 0V in 1M LiPF$_6$/ EC-EMC electrolyte solution. (l) Schematic representation of the Li-ion storage mechanism in CoO@3D-NRGO anode.

Post-cycling XRD and TEM analysis are performed to investigate the compositional, morphological and microstructural changes during the lithiation-delithiation course of CoO@3D-NRGO hybrid anode. XRD patterns of pristine, discharged and charged electrode (Figure 3.8a) verified conventional conversion reaction ($CoO + 2Li^+ + 2e^- \leftrightarrow Co + Li_2O$). Peaks characteristic of metallic Co, Li_2O and Li_2CO_3 are identified in the discharged sample.[1, 26] Metallic Co diffraction peaks disappeared and CoO signals emerged after charging the electrode to 3V, signifying the complete reversibility of the process. Lack of metallic Li peaks in the lithiated CoO@3D-NRGO hybrid electrode rule out the unusually high specific capacity resulting from possible Li-metal deposition.[14] XPS analysis of the cycled CoO@3D-NRGO hybrid electrodes confirmed Co-O-C bond retention even after numerous charge discharge cycles (Figure 3.8b). Formation of SEI layer containing C=O groups are also evident in this XPS pattern. *Ex-situ* HRTEM analysis of CoO@3D-NRGO hybrid anode after 1000 discharge/charge cycles verified its excellent structural stability (Figure 3.8c). EDX elemental mapping of cycled anode (Figure 3.8d-i) demonstrated homogenous distribution of Co, O, C, confirming its compositional homogeneity. Presence of F and P components designate the existence of a uniform SEI, which is a crucial component for achieving stable electrochemical performance. Retention of 3D microstructure and Co-O-C bonds during lithiation-delithiation process is in line with the outstanding pseudocapacitance and cycling stability of CoO@3D-NRGO anode even at high current densities. Hence, in this case structural stability of the hybrid electrode is one of the major reasons for the outstanding cycling stability. High-resolution TEM image and corresponding EDX mapping of the CoO@3D-NRGO anode discharged to 0 V (Figure 3.8j-k) is performed to investigate the factors responsible for outstanding specific capacity (1429 mAh g^{-1}) and unusually high pseudocapacitive Li-ion storage (79%), which is typically not observed for conversion type anodes. It is clear that discharged electrode composed of ~3 nm sized Co nanoparticles dispersed in the Li_2O matrix on 3D-NRGO creating numerous Li_2O/Co/NRGO nanointerfaces that can act as additional sites for pseudocapacitive type interfacial Li-ion storage (Figure 3.8l). Although interfacial Li-ion storage occurs in the case of conversion type anodes such as CoO and Co_3O_4, capacity contribution is limited due to sluggish Li-ion diffusion, lack of well-defined Co-Li_2O interfaces resulting from active material agglomeration and inefficient charge separation.

Outstanding Li-ion storage performance of interface engineered CoO@3D-NRGO hybrid anode can be endorsed to its unique physiochemical properties such as 3D microstructure, chemical bonding of ultrafine CoO nanoparticles on NRGO, mesoporosity and high surface area. Anchoring of CoO nanoparticles on 3D-NRGO support through robust Co–O–C bonds prevent their agglomeration during charge discharge process, which is one of the key requirements of cycling stability. Immobilization of CoO nanoparticles on 3D-NRGO also maintains well-defined Co-Li_2O interfaces that are crucial for pseudocapacitive interfacial Li-ion storage. CoO-O-C bonds also act as electronic pathways, facilitating superior charge separation that is essential for interfacial Li-ion storage. In addition to acting as a support for CoO nanoparticles, 3D-NRGO also facilitates charge separation due to its high electronic conductivity. Interconnected 3D network of NRGO can accommodate the large volume change associated with the conversion reaction of CoO, facilitating stable cycling performance. Ultrafine size of CoO nanoparticles is also beneficial for accommodating the volume changes during charge-discharge process. 3-D microstructure, mesoporosity and high surface area facilitate improved contact with electrolyte solution. Moreover, reduced Li_2O formation due to the use of CoO nanoparticles instead of Co_3O_4 could also increase the rate performance. Although 3D microstructure, ultrafine CoO nanoparticles, high surface area and mesoporosity are decisive factors for the improved electrochemical performance of CoO@3D-

NRGO over Co_3O_4 and CoO nanoparticles, they are only secondary reasons compared to Co-O-C bonds. This is further validated by the reduced Li-ion storage performances of physically mixed CoO-3D-NRGO sample lacking Co-O-C bonds. It is thus clear that Co-O-C bonding play a crucial role in the Li-ion storage performance of interface engineered CoO@3D-NRGO anode. Three-dimensional hybrid anode architecture demonstrated herein integrates intercalation, conversion and pseudocapacitive Li-ion storage mechanisms. Synergistic effect of these multiple mechanisms and microstructural advantages of CoO@3D-NRGO make it an excellent anode material for high energy and power density Li-ion batteries with long cycle-life.

3.2.3 Full-cell Performance

Finally, we implemented interface engineered CoO@3D-NRGO hybrid anode in a lithium-ion full-cell with commercial $LiNiMnCoO_2$ cathode (rate performance and cycling stability provided in Appendix 6) and 1M $LiPF_6$-EC/EMC electrolyte solution (Figure 3.9a). CoO@3D-NRGO‖$LiNiMnCoO_2$ full-cell exhibited a high reversible capacity of 430 mAh g^{-1} at a high current density of 1 A g^{-1} (based on anode weight) in the potential window of 3.0-4.3 V (Figure 6b). This is 4-fold higher than the specific capacity obtained for graphite anodes (90 mAh g^{-1}) in full-cell configuration, which should be expected due to the sluggish Li-ion diffusion kinetics. Galvanostatic cycling stability of CoO@3D-NRGO‖$LiNiMnCoO_2$ full-cell is also excellent, maintaining 95% of the initial capacity after 200 charge-discharge cycles (Figure 3.9b). Graphite‖$LiNiMnCoO_2$ full cell displayed less stable charge-discharge cycles (78% after 200 cycles) and good coulombic efficiency of 99.7% (Appendix 7a) under similar experimental conditions. Galvanostatic charge-discharge profiles of CoO@3D-NRGO‖$LiNiMnCoO_2$ full-cell (Figure 3.9c) displayed slopping behaviour that is distinctive of pseudocapacitive Li-ion storage unlike the diffusion limited behaviour of graphite‖$LiNiMnCoO_2$ system (Appendix 7b).[20, 54] It is thus clear that the use of extremely pseudocapacitive CoO@3D-NRGO hybrid anode also resulted in the diffusion independent Li-ion storage behavior of the full-cell, which is advantageous for achieving high energy and power density. Current density used in this case is notably higher than previous reports of Li-ion full-cells based on graphite and other conversion/ alloying type anodes.[55]

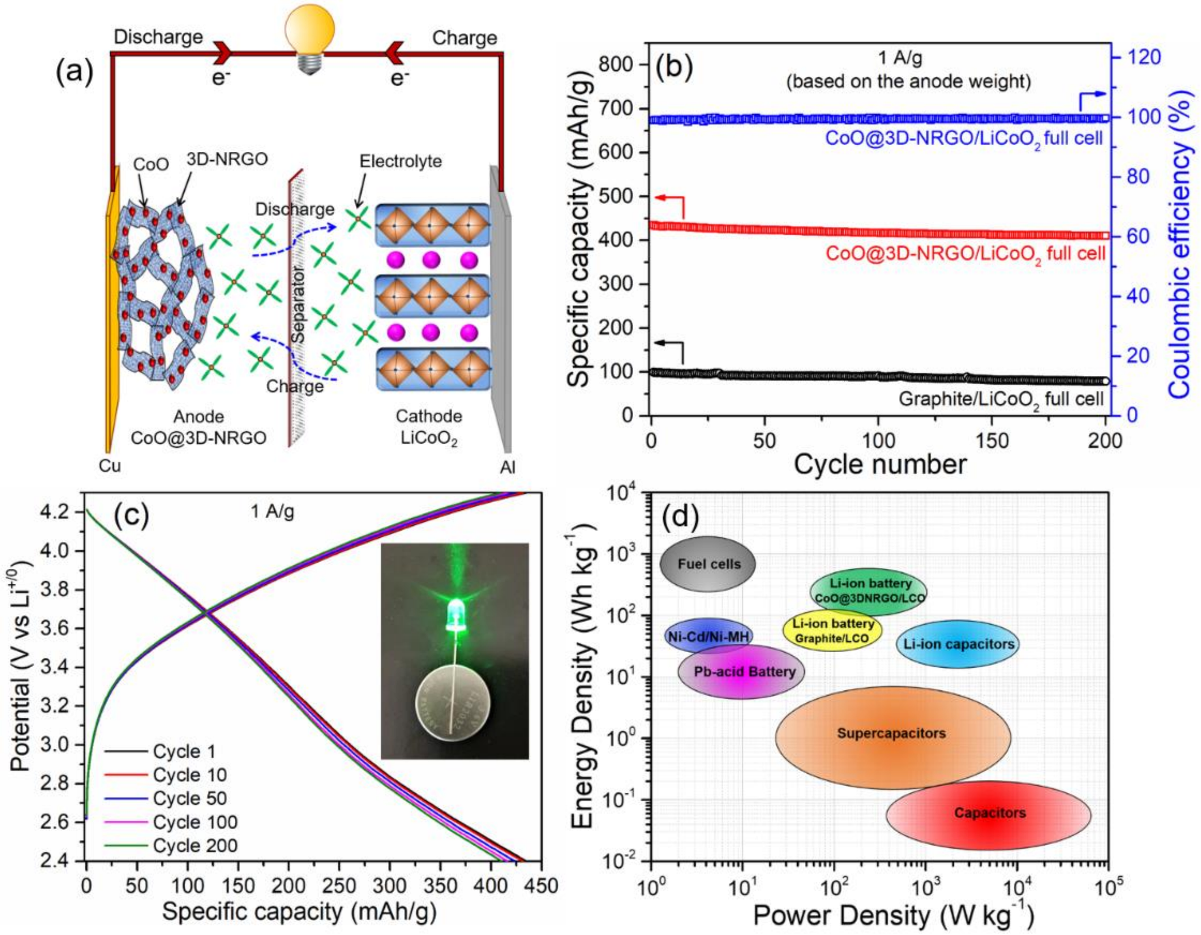

Figure 3.9 (a) Schematic of the Li-ion full-cell composed of CoO@3D-NRGO anode and $LiNiMnCoO_2$ cathode. (b) Galvanostatic cycling performance of CoO@3D-NRGO‖$LiNiMnCoO_2$ and Graphite‖$LiNiMnCoO_2$ full-cells at a current density of 1 A g^{-1} after 5 cycles at a current density of 100 mA g^{-1}. Specific capacities expressed are based on the anode weight (c) Galvanostatic charge-discharge profiles of CoO@3D-NRGO‖$LiNiMnCoO_2$ full cell at a current density of 1 A g^{-1} (d) Ragonne plot of CoO@3D-NRGO‖$LiNiMnCoO_2$ Li-ion full-cell, and comparison with various energy storage devices.

Operating potential of the CoO@3D-NRGO‖$LiNiMnCoO_2$ full-cell (~3.6 V @ 1 A g^{-1}) is comparable to those of secondary graphite‖$LiNiMnCoO_2$ battery (3.8 V @ 1 A g^{-1}) and superior to the previously reported values for Li-ion full-cells based on conversion and alloying type anodes.[56-59] Output voltage of this full-cell can light up a 3 V green LED of 0.06 W power (Figure 3.9c inset), demonstrating its practical application. Energy and power density of CoO@3D-NRGO‖$LiNiMnCoO_2$ full-cell are 400 Wh kg^{-1} and 1 kW kg^{-1} respectively (based on the weight of both electrodes). Graphite‖$LiNiMnCoO_2$ full-cell only achieved energy and power densities of 141 Wh kg^{-1} and 427 W kg^{-1} under similar electrochemical testing conditions. This 2.8-fold higher energy density and 2.3-fold higher power densities are particularly attractive for applications such as fast-charging electric vehicles capable of long-range driving. Energy and power densities demonstrated herein are also considerably higher than previously reported Li-ion full-cells based on conversion-type anodes.[55, 58] Power density of this full-cell is even on par with the lithium ion capacitors and supercapacitors (Figure 3.9d). Use of $LiNiMnCoO_2$ cathode is limiting the power density in this case, and ultrafast charging cathodes are required to exploit the full potential of CoO@3D-NRGO hybrid anode. Although conversion type anodes are not suitable for Li-ion full-cells due to high operating potentials, interface engineered CoO@3D-NRGO resulted in outstanding performance due to high specific capacity, extreme pseudocapacitance and lower operating voltage compared to conventional CoO/Co_3O_4 nanoparticles. Cycling stability, energy and power densities of the demonstrated CoO@3D-NRGO‖$LiNiMnCoO_2$ full-cell could be further improved by optimization of electrode weight, thickness, porosity, cell balancing, voltage window, and charge-discharge protocols.

3.3 Conclusion

In summary, a high energy and power density rechargeable Li-ion batteries based on extremely pseudocapacitive interface engineered CoO@3D-NRGO hybrid anode is demonstrated in this chapter. This 3D electrode exhibited outstanding specific capacities and rate performances compared to any of the transition metal-oxide based anodes reported earlier. Long-term cycling stability and coulombic efficiencies are also excellent. Unusual Li-ion storage performances are credited to the synergy between conversion reaction of CoO and pseudocapacitive Li-ion storage at numerous Li_2O/Co/NRGO nanointerfaces resulting from the dispersion of ~3 nm sized Co nanoparticles in Li_2O matrix. Additionally, anchoring of CoO nanoparticles on 3D-NRGO support prevent their agglomeration and accommodate the volume change during charge discharge process. Chemical bonding (Co-O-C bonds) between CoO nanoparticles and NRGO is identified as the crucial factor responsible for the superior charge separation and pseudocapacitive Li-ion storage. Stupendous pseudocapacitance enhanced electrochemical performance of interface engineered CoO@3D-NRGO hybrid anode makes it a potential candidate for the next-generation high energy/ power density and ultra-long-life Li-ion batteries.

3.4. References

1. X. Wang, X.-L. Wu, Y.-G. Guo, Y. Zhong, X. Cao, Y. Ma and J. Yao, *Adv. Funct. Mater.*, **2010**, 20, 1680-1686.
2. V. Etacheri, C. Hong, J. Tang and V. G. Pol, *ACS Appl. Mater. Interfaces*, **2018**, 10, 4652-4661.
3. X. Leng, S. Wei, Z. Jiang, J. Lian, G. Wang and Q. Jiang, *Sci. Rep.*, **2015**, 5.
4. Z.-S. Wu, W. Ren, L. Wen, L. Gao, J. Zhao, Z. Chen, G. Zhou, F. Li and H.-M. Cheng, *ACS Nano*, **2010**, 4, 3187-3194.
5. H. Li, G. Richter and J. Maier, *Adv. Mater.*, **2003**, 15, 736-739.

6. Y. Kim, J.-H. Lee, S. Cho, Y. Kwon, I. In, J. Lee, N.-H. You, E. Reichmanis, H. Ko, K.-T. Lee, H.-K. Kwon, D.-H. Ko, H. Yang and B. Park, *ACS Nano* **2014**, 8, 6701-6712.
7. Y. Wang and G. Cao, *Adv. Mater.*, **2008**, 20, 2251-2269.
8. X. Li and C. Wang, *J. Mater. Chem. A*, **2013**, 1, 165-182.
9. Y. Li, B. Tan and Y. Wu, *Nano Lett.*, **2008**, 8, 265-270.
10. K. Cao, L. Jiao, Y. Liu, H. Liu, Y. Wang and H. Yuan, *Adv. Funct. Mater.* , **2015**, 25, 1082-1089.
11. S. Sun, X. Zhao, M. Yang, L. Ma and X. Shen, *Nanomaterials*, **2015**, 5, 2335-2347.
12. C. C. Li, X. M. Yin, Q. H. Li, L. B. Chen and T. H. Wang, *Chem. Eur. J.*, **2011**, 17, 1596-1604.
13. G. Binitha, A. G. Ashish, D. Ramasubramonian, P. Manikandan and M. M. Shaijumon, *Adv. Mater. Interfaces*, **2015**, 3, 1500419.
14. R. Thorpe, S. Rangan, M. Sina, F. Cosandey and R. A. Bartynski, *J. Phys. Chem. C*, **2013**, 117, 14518-14525.
15. P. Zhang, R. Wang, M. He, J. Lang, S. Xu and X. Yan, *Adv. Funct. Mater.*, **2016**, 26, 1354-1364.
16. M. Zhang, F. Yan, X. Tang, Q. Li, T. Wang and G. Cao, *J. Mater. Chem. A*, **2014**, 2, 5890-5897.
17. V. Etacheri, J. E. Yourey and B. M. Bartlett, *ACS Nano*, **2014**, 8, 1491-1499.
18. V. Augustyn, P. Simon and B. Dunn, *Energy Environ. Sci.*, **2014**, 7 1597-1614
19. Y. Xiang, Z. Yang, S. Wang, M. S. A. Hossain, J. Yu, N. A. Kumar and Y. Yamauchi, *Nanoscale*, **2018**, 10, 18010-18018.
20. J. Wang, Q. Deng, M. Li, K. Jiang, Z. Hu and J. Chu, *Nanoscale*, **2018**, 10, 2944-2954.
21. H. Qi, L. Cao, J. Li, J. Huang, Z. Xu, Y. Cheng, X. Kong and K. Yanagisawa, *ACS Appl. Mater. Interfaces*, **2016**, 8, 35253-35263.
22. L. Cao, Q. Kang, J. Li, J. Huang and Y. Cheng, *Appl. Surf. Sci.*, **2018**, 455, 96-105.
23. Y. Sun, X. Hu, W. Luo and Y. Huang, *J. Phys. Chem. C*, **2012**, 116, 20794-20799.
24. D. C. Marcano, D. V. Kosynkin, J. M. Berlin, A. Sinitskii, Z. Sun, A. Slesarev, L. B. Alemany, W. Lu and J. M. Tour, *ACS Nano*, **2010**, 4, 4806-4814.
25. L. Wang, Y. Zheng, X. Wang, S. Chen, F. Xu, L. Zuo, J. Wu, L. Sun, Zhuang Li, H. Hou and Y. Song, *ACS Appl. Mater. Interfaces*, **2014**, 6, 7117-7125.

26. K. Bindumadhavan, M.-H. Yeh, T.-c. Chou, P.-Y. Chang and R. Doong, *ChemistrySelect*, **2016**, 1, 5758-5767.
27. S. Sun, X. Zhao, M. Yang, L. Wu, Z. Wen and X. Shen, *Sci. Rep.*, **2016**, 6, 19564.
28. L. Zhou, M. Zhou, Z. Hu, Z. Bi and K. G. Serrano, *Electrochim. Acta*, **2014**, 140, 376-383.
29. X. Zhang, J. Zhou, H. Song, X. Chen, Y. V. Fedoseeva, A. V. Okotrub and L. G. Bulusheva, *ACS Appl. Mater. Interfaces*, **2014**, 6, 17236-17244.
30. G. Zhou, D.-W. Wang, L.-C. Yin, N. Li, F. Li and H.-M. Cheng, *ACS Nano*, **2012**, 6, 3214-3223.
31. C. Zhao, Y. Shen, Z. Hu and X. Wang, *Int. J. Electrochem. Sci.*, **2018**, 13, 5184-5194.
32. H. Wang, C. Zhang, Z. Liu, L. Wang, P. Han, H. Xu, K. Zhang, S. Dong, J. Yao and G. Cui, *J. Mater. Chem.*, **2011**, 21, 5430-5434.
33. K. Xie, P. Wu, Y. Zhou, Y. Ye, H. Wang, Y. Tang, Y. Zhou and T. Lu, *ACS Appl. Mater. Interfaces*, **2014**, 6, 10602-10607.
34. W. Yao, J. Yang, J. Wang and Y. Nuli, *J. Electrochem. Soc.* , **2008**, 155, A903-A908.
35. A. K. Rai, L. T. Anh, J. Gim and J. Kim, *Ceram. Int.* , **2013**, 39, 9325-9330.
36. L. Zhang, P. Hu, X. Zhao, R. Tian, R. Zou and D. Xia, *J. Mater. Chem.* , **2011**, 21, 18279-18283.
37. V. Etacheri, R. Marom, R. Elazari, G. Salitra and D. Aurbach, *Energy Environ. Sci.*, **2011**, 4, 3243-3262.
38. G. Patrinoiu, V. Etacheri, S. Somacescu, V. S. Teodorescu, R. Birjega, D. C. Culita, C. N. Hong, J. M. Calderon-Moreno, V. G. Pol and O. Carp, *Electrochim. Acta*, **2018**, 264, 191-202.
39. X.-l. Huang, R.-z. Wang, D. Xu, Z.-l. Wang, H.-g. Wang, J.-j. Xu, Z. Wu, Q.-c. Liu, Y. Zhang and X.-b. Zhang, *Adv. Funct. Mater.*, **2013**, 23, 4345-4353.
40. C. Yan, Y. Zhu, Z. Fang, C. Lv, X. Zhou, G. Chen and G. Yu, *Adv. Energy Mater*, **2018**, 8, 1800762.
41. L. Fan, W. Zhang, S. Zhu and Y. Lu, *Ind. Eng. Chem. Res.*, **2017**, 56, 2046–2053.
42. Y. Jiang, Y. Li, P. Zhou, Z. Lan, Y. Lu, C. Wu and M. Yan, *Adv. Mater.*, **2017**, 29.
43. N. Wang, Y. Wang, X. Xu, T. Liao, Y. Du, Z. Bai and S. Dou, *ACS Appl. Mater. Interfaces*, **2018**, 10, 9353-9361.

44. V. Augustyn, J. Come, M. A. Lowe, J. Kim, P.-L. Taberna, S. H. Tolbert, H. D. Abruña, P. Simon and B. Dunn, *Nat. Mater.*, **2013**, 12, 518-522.
45. J. Wang, J. Polleux, J. Lim and B. Dunn, *J. Phys. Chem. C* **2007**, 111, 14925-14931.
46. Y.-Y. Hu, Z. Liu, K.-W. Nam, O. J. Borkiewicz, J. Cheng, X. Hua, M. T. Dunstan, X. Yu, K. M.Wiaderek, L.-S. Du, K. Chapman, P. J. Chupas, X.-Q. Yang and C. P. Grey, *Nat. Mater.*, **2013**, 12, 1130-1136.
47. W.-H. Ryu, J. Shin, J.-W. Jung and I.-D. Kim, *J. Mater. Chem. A*, **2013**, 1, 3239-3243.
48. D. Kang, Q. Liu, R. Si, J. Gu, W. Zhang and D. Zhang, *Carbon*, **2016**, 99, 138-147.
49. L. Li, J. Dai, G. Jiang, X. Sun, Z. Huang, Z. Xie and B. Cao, *ChemistrySelect*, **2019**, 4, 6879-6885.
50. C. Zhang, Y. Song, L. Xu and F. Yin, *Chemical Engineering Journal*, **2020**, 380, 122545.
51. M. Zhang, M. Jia, Y. Jin and X. Shi, *Appl. Surf. Sci.*, **2012**, 263, 573-578.
52. Y. Huang, C. Chen, C. An, C. Xu, Y. Xu, Y. Wang, L. Jiao and H. Yuan, *Electrochim. Acta*, **2014**, 145, 34-39.
53. L. Pan, H. Zhao, W. Shen, X. Dong and J. Xu, *J. Mater. Chem. A*, **2013**, 1, 7159-7166.
54. X. Yu, S. Yun, J. S. Yeon, P. Bhattacharya, L. Wang, S. W. Lee, X. Hu and H. S. Park, *Adv. Energy Mater*, **2018**, 8, 1702930.
55. S. Hariharan, V. Ramar, S. P. Joshia and P. Balaya, *RSC Adv.*, **2013**, 3, 6386-6394.
56. H. Xu, S. Li, X. Chen, C. Zhang, W. Liu, H. Fan, Y. Yu, Y. Huang and J. Li, *Adv. Energy Mater*, **2019**, 1902150.
57. H. Xu, S. Li, C. Zhang, X. Chen, W. Liu, Y. Zheng, Y. Xie, Y. Huang and J. Li, *Energy Environ. Sci.*, **2019**, 12, 2991-3000.
58. A. Varzi, D. Bresser, J. v. Zamory, F. Müller and S. Passerini, *Adv. Energy Mater*, **2014**, 4, 1400054.
59. R. Verrelli, J. Hassoun, A. Farkas, T. Jacob and B. Scrosati, *J. Mater. Chem. A*, **2013**, 1, 15329-15333.

Chapter 4

Realization of High Energy/ Power Density Lithium-Ion Batteries through Nanograin-Boundary Induced Pseudocapacitance

4.1 Introduction

High-capacity anodes based on transition metal-oxides (TMO) have been widely investigated as a substitute for graphite anodes. Reversible conversion reaction of these anodes ($MO_x + xLi^+ + xe^- \leftrightarrow xM^0 + xLi_2O$) resulted in ~3-fold specific capacity compared to graphite anodes.[1-4] Cobalt oxide (Co_3O_4) is considered as a promising candidate due to its high theoretical capacity (890 mAh g^{-1}).[5-7] Although several TMO's are studied since 1990's, rapid capacity fading and mediocre rate performance due to low electronic conductivity, large volume change (~200%) and particle agglomeration hinders their practical application in commercial Li-ion batteries[8, 9]. Several strategies such as nanostructuring, porosity control, and hybrid formation with carbonaceous materials haven been demonstrated to improve the Li-ion storage performance of Co_3O_4 based anodes[10-12]. However, development of a high-performance conversion type Li-ion battery anode remains as a challenge.

Recently investigated pseudocapacitive charge storage process considerably improved ion-diffusion kinetics of nanostructured electrodes[13-15]. This diffusion independent phenomenon allows faster Li-ion storage at or near surface reactions of the active material. Nevertheless, limited specific capacity ($\leq$300 mAh g^{-1}) of intercalation based electrodes restrict their use for high-energy applications[16, 17]. Pseudocapacitive Li-ion storage of high-capacity conversion-type anodes are limited due to sluggish Li-ion diffusion (10^{-14}-10^{-16} cm^2 s^{-1})[18]. Pseudocapacitance can be also be induced through defect and interface engineering of nanostructured electrode materials, which remains obscure in the case of conversion-type anodes. Diffusion-independent pseudocapacitive Li-ion storage requires an electrode material with optimum electronic and ionic conductivity.[19] Despite of the implementation of several strategies for improved electrochemical performance, defect and interface induced pseudocapacitance of Co_3O_4 anodes were not investigated previously.[20, 21]

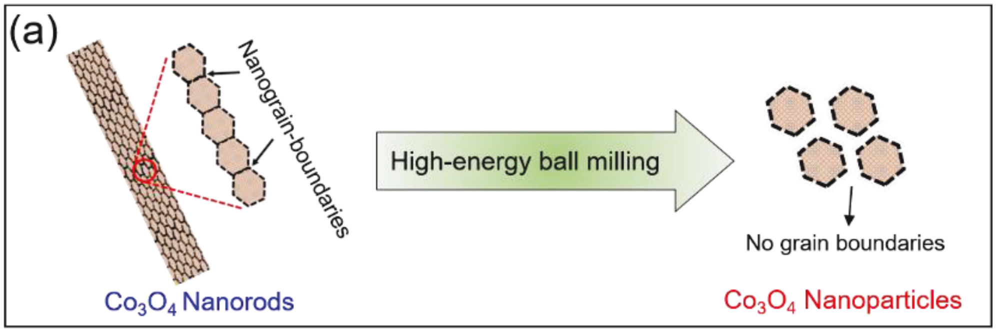

Scheme 1 Presence of nanograin boundaries in hierarchical Co_3O_4 nanorods, and their absence in ball-milled Co_3O_4 nanoparticles.

In this chapter, a high energy (480 Wh kg^{-1}) and power density (980 W kg^{-1}) lithium-ion battery based on nanograin-boundary induced pseudocapacitive Li-ion storage in hierarchical Co_3O_4 nanorods is demonstrated. Following aspects are taken into consideration while designing of hierarchical Co_3O_4 nanorods. (i) Hierarchical microstructure composed of nanocrystallites resulted in numerous nanograin-boundaries (Scheme-1) that can considerably increase the Li-ion diffusion kinetics, which is one of the key requirements for high pseudocapacitance.[22-24] (ii) Nanograin boundaries can possibly act as additional sites for Li-ion storage.[22, 25] (iii) Interconnection between the numerous nanocrystallites is a beneficial factor to reduce particle agglomeration, which is a vital reason for rapid capacity fading of conversion type anodes. (iv) Moreover, 1D morphology and mesoporosity on the nanorods are beneficial to achieve improved charge transfer kinetics by enhancing contact with the electrolyte solution.[26] Outstanding electrochemical performance of Co_3O_4 nanorods is attributed to the synergy between conversion reaction of Co_3O_4 and pseudocapacitive Li-ion storage at numerous nanointerfaces formed between Li_2O, and Co (resulting from conversion reaction), and $Li_{1.47}Co_3O_{3.72}$ formed at nanograin boundaries. This enables the realization of Li-ion full-cells with high energy and power density compared to any of the previous reports.[21, 27-29]

4.2 Results and Discussion

4.2.1 Formation and Structural Characteristics of Hierarchical Co_3O_4 Nanorods

Hierarchical Co_3O_4 nanorods outlined in scheme-1 involves controlled reaction between cobalt (II) nitrate hexahydrate and urea in aqueous media under elevated pressure and temperature. Urea in this reaction follows a complex pathway that decomposes to NH_3 and CO_2 to react with inorganic Co-precursors. Release of NH_3 and CO_2 with the hydrolysis of urea further generates OH^- and CO_3^{2-} anions and creates a weak alkaline condition favouring the heterogeneous nucleation of Co species. Co^{2+} reacts with OH^- and CO_3^{2-} forming the nuclei of negatively charged cobalt carbonate hydroxide hydrate ($2Co(CO_3)_{0.5}(OH).0.11H_2O$) and further results in self-assembly of oriented particle stacking via the electrostatic interactions and hydrogen bonding as described in the following equations.

$$(NH_2)_2CO + H_2O \rightarrow 2NH_3 + CO_2$$

$$NH_3 + H_2O \rightarrow NH_4^+ + OH^-$$

$$CO_2 + H_2O \rightarrow CO_3^{2-} + 2H^+$$

$$Co^{2+} + OH^- + 0.5CO_3^{2-} + 0.11H_2O \rightarrow Co(CO_3)_{0.5}(OH)\cdot 0.11H_2O$$

Initially, crystallized $2Co(CO_3)_{0.5}(OH).0.11H_2O$ nanoparticles grow and stack loosely at high temperatures to form a hierarchical structure before precipitation. Subsequent orientation of $2Co(CO_3)_{0.5}(OH).0.11H_2O$ in anisotropic nanorod structure (1-2 μm length) as a result of Ostwald ripening is evidenced from scanning electron microscopy (SEM) image and transmission electron microscopy (TEM) image (Figure 4.1a and b). HRSEM image (Figure 4.1c) of hierarchical microstructure resulted after the thermal decomposition of $2Co(CO_3)_{0.5}(OH).0.11H_2O$ precursor confirmed the formation of highly oriented Co_3O_4 nanocrystallites as a result of self-assembly. Particle agglomeration and restacking are not observed indicating excellent structural stability. High-resolution TEM image (Figure 4.1d) confirmed the Co_3O_4 nanocrystallites of 20±2 nm size are interconnected resulting in the formation of numerous nanograin-boundaries. HRTEM studies further verified the polycrystalline nature (Figure 4.1e and f) of Co_3O_4 nanocrystallites with an interplanar spacing of 0.28 nm corresponding to (220) pane. In this case, nanograin-boundaries can promote faster Li-ion diffusion and enhances the ionic conductivity that are crucial for pseudocapacitive type storage.

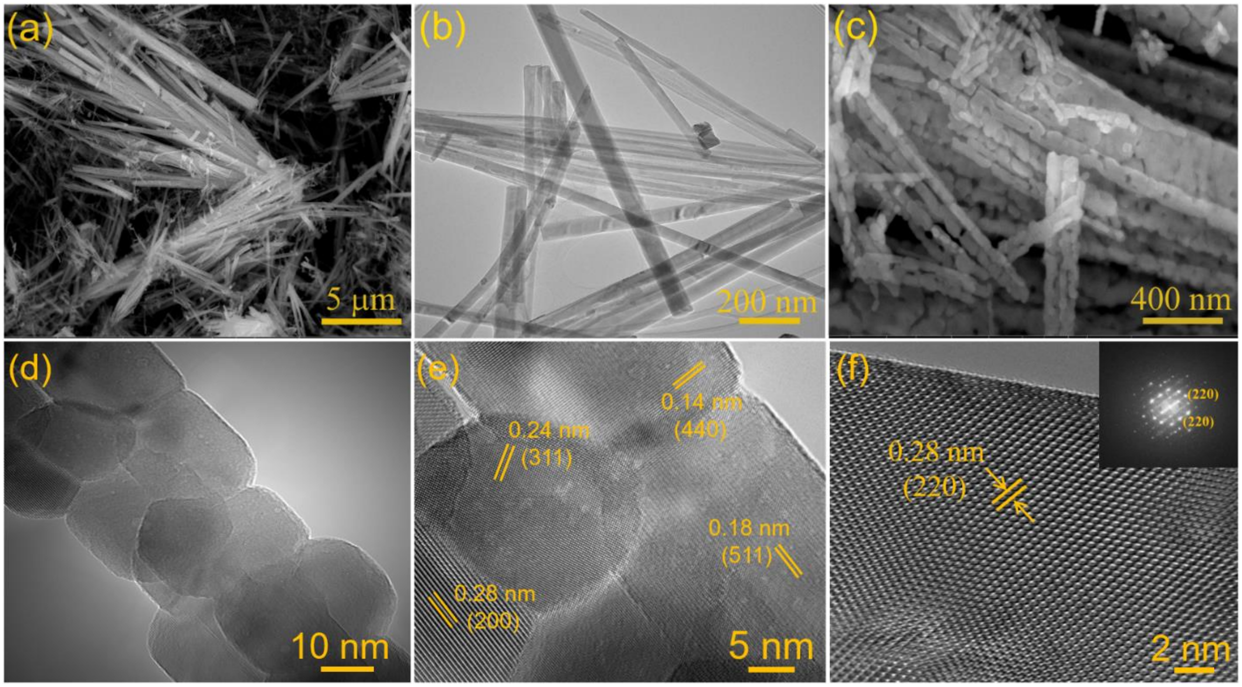

Figure 4.1 (a) SEM and (b) TEM images of precursor $2Co(CO_3)_{0.5}(OH).0.11H_2O$. (c) SEM image of Co_3O_4 nanorods. (d-f) High-resolution transmission electron microscopy images of hierarchical Co_3O_4 nanorods. Inset: Selected area electron diffraction pattern.

X-ray diffraction (XRD) pattern displayed in figure 4.2a correspond to phase-pure cubic spinel Co_3O_4 (JCPDS 65-3103) with a lattice constant of a=b=c=0.808 nm.[30] XRD pattern of precursor (Appendix 8) confirmed the formation of $2Co(CO_3)_{0.5}(OH).0.11H_2O$ (ICSD 16-9233) and its complete decomposition during calcination without the formation of secondary phases.[31] Average particle-size calculation using Debye-Scherrer equation designated the presence of 20±2 nm sized Co_3O_4 nanocrystallites, which is in line with the TEM results. Raman spectra of Co_3O_4 nanorods exhibited (Figure 4.2b) distinctive bands corresponding to the spinel cobalt oxide and an additional peak at 753.3 cm^{-1}, which signifies the presence of surface defects.[32]

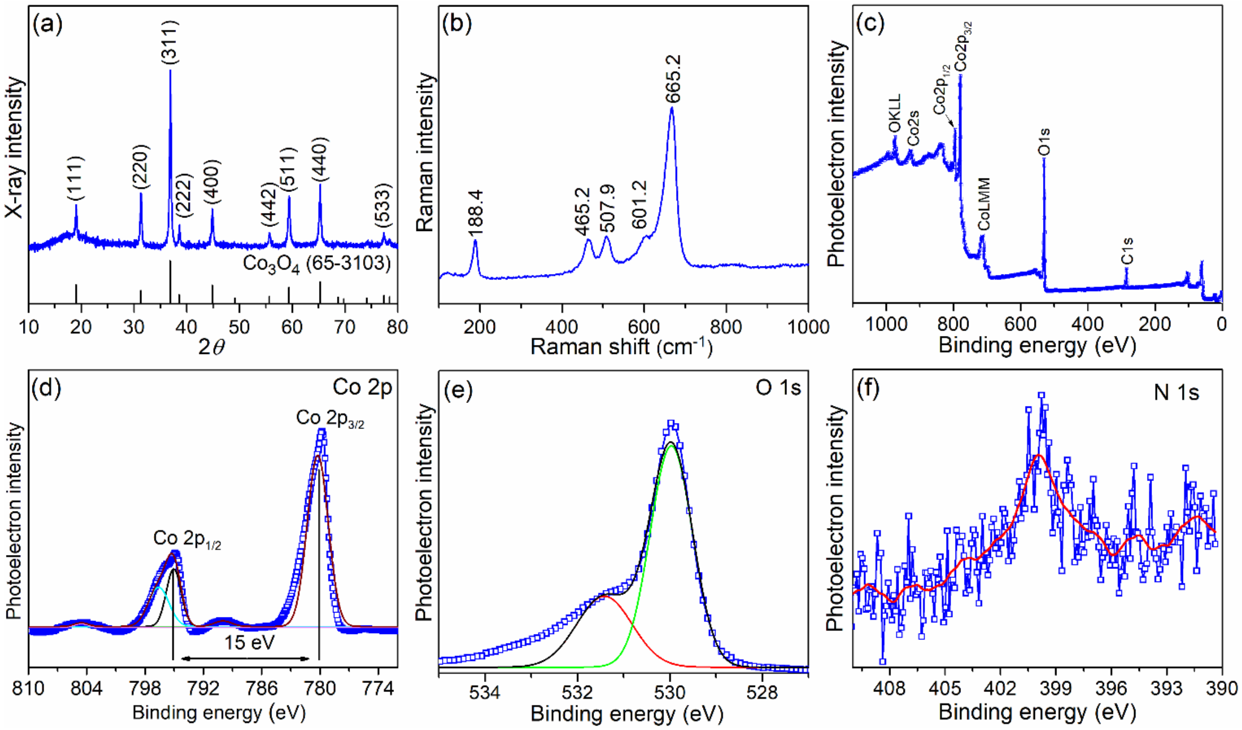

Figure 4.2 (a) X-ray diffraction pattern, and (b) Raman spectra of hierarchical Co_3O_4 nanorods. (c) Survey and (d) Co 2p, (e) O 1s, and (f) N 1s high resolution XPS spectra of hierarchical Co_3O_4 nanorods.

X-ray photoelectron spectroscopy (XPS) of Co_3O_4 nanorods provided additional insight into the surface chemical characteristics responsible for enhanced Li-ion storage kinetics (Figure 4.2c). High-resolution Co 2p spectra (Figure 4.2d) exhibited two distinct peaks at 780.1 and 795.1 eV corresponding to Co $2p_{3/2}$ and Co $2p_{1/2}$ components respectively, with their spin-orbit separation of 15 eV.[30] Satellite peaks of Co^{2+} and Co^{3+} at 790 and 804.5 eV respectively, further confirmed the formation of phase pure Co_3O_4. High-resolution O 1s spectra (Figure 4.2e) of Co_3O_4 nanorods consist of a major peak at 530.1 eV confirming the presence of oxygen atoms of Co_3O_4. Signal at 531.4 eV represent the existence of oxygen vacancies that could assist in additional sites for surface Li-ion storage.[33] Surface quantitative analysis from high-resolution N 1s spectra verified the presence of nitrogen (1%), which could effectively improve electronic conductivity of Co_3O_4 nanorods (Figure 4.2f).[34, 35]

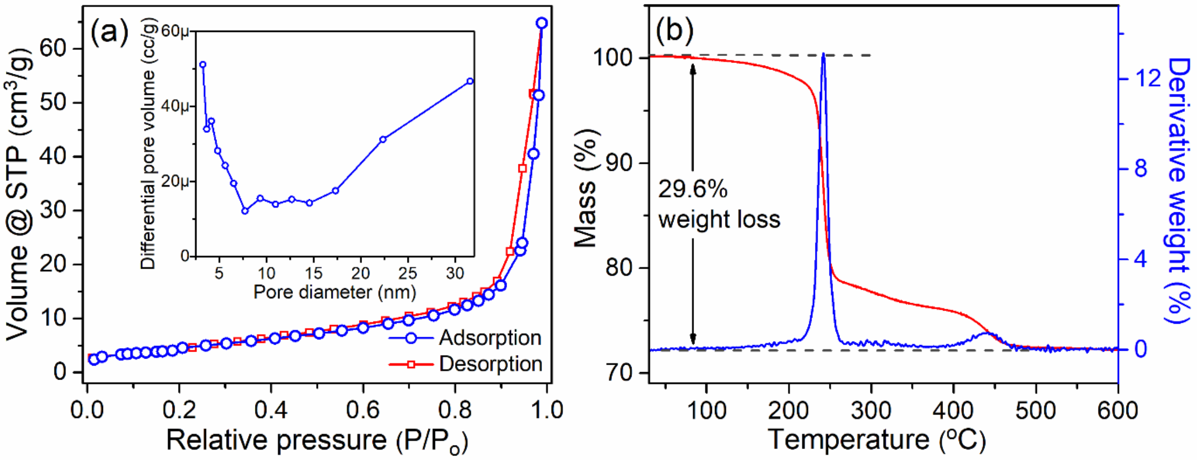

Figure 4.3 (a) N_2 adsorption-desorption isotherm of hierarchical Co_3O_4 nanorods. Inset: Pore-size distribution. (b) Thermogravimetric analysis of Precursor $2Co(CO_3)_{0.5}(OH).0.11H_2O$ under air-flow at a heating rate of 10 °C min^{-1}.

Nitrogen adsorption-desorption isotherm of Co_3O_4 nanorods exhibited type II and IV hysteresis (Figure 4.3a), and Brunauer-Emmett-Teller (BET) model revealed a specific surface area of 16 m^2 g^{-1}. Barret-Joyner-Halenda (BJH) analysis verified a pore volume of 0.1 cm^3 g^{-1} and average pore diameter of 3.24 nm confirming the mesoporosity of Co_3O_4 nanorods (Figure 4.3a inset). Thermogravimetric analysis (TGA) of the precursor $2Co(CO_3)_{0.5}(OH).0.11H_2O$ (Figure 4.3b) is carried out to follow the formation of hierarchical Co_3O_4 nanorods. Weight loss of ~20% occurs between 40 and 250 °C represent loss of physically adsorbed water and oxygen-containing functional groups. Further weight loss of ~8% between 250 and 480 °C can be attributed to the cobalt carbonate decomposition and associated CO_2 release. Precursor experienced no weight loss after 480 °C signifying the complete decomposition of $2Co(CO_3)_{0.5}(OH).0.11H_2O$. Depending on this analysis, precursor is annealed at 500 °C under airflow to obtain phase-pure polycrystalline Co_3O_4 nanorods. In summary, hydrothermal reduction of cobalt nitrate in presence of urea resulted in the formation of hierarchical Co_3O_4 nanorods containing numerous nanograin boundaries. This strategy of nanograin-boundary constructed hierarchical nanorods for conversion-type anodes are beneficial for achieving superior pseudocapacitive and enhanced Li-ion storage capability for next-generation batteries.

4.2.2 Nanograin Boundary Induced Lithium-Ion Storage Mechanism

Hierarchical Co_3O_4 nanorods demonstrated excellent electrochemical performance under various tests in the voltage range 0-3V in a half-cell configuration. Li-ion storage performance and high-rate capability (0.05-30 A g^{-1}) of Co_3O_4 nanorods is much superior to ball-milled Co_3O_4 nanoparticles under similar experimental conditions (Figure 4.4a). Irreversible SEI formation resulted in the first cycle capacity loss of Co_3O_4 nanorods, ball-milled Co_3O_4 nanoparticles and commercial Co_3O_4 nanoparticles (Appendix 4a). First cycle coulombic efficiency can be further improved with electrolyte additives or prelithiation strategy. Hierarchical Co_3O_4 nanorods delivered an outstanding reversible capacity of 1591 mAh g^{-1} compared to ball-milled Co_3O_4 nanoparticles (900 mAh g^{-1}) and commercial Co_3O_4 nanoparticles (731 mAh g^{-1}) at a low current density of 0.05 A g^{-1}. Ball-milled Co_3O_4 nanoparticles and commercial Co_3O_4 nanoparticles (sub-micron) experienced severe capacity decaying at higher current densities, which is in good agreement with the previous reports.[5, 28, 36]. Low specific capacities and rate performance of Co_3O_4 nanoparticles can be ascribed to the reduced hierarchy of the morphology and increased formation of electronically insulating Li_2O/ particle agglomeration respectively. On the other hand, Co_3O_4

nanorods retained an outstanding excellent reversible capacity of 1180 and 805 mAh g^{-1} even at higher current densities of 10 and 30 A g^{-1} respectively. These values are considerably higher than the theoretical capacity of conventional graphite anodes employed in state-of-the-art Li-ion batteries and also superior to the theoretical capacity of Co_3O_4 (890 mAh g^{-1}).[37]

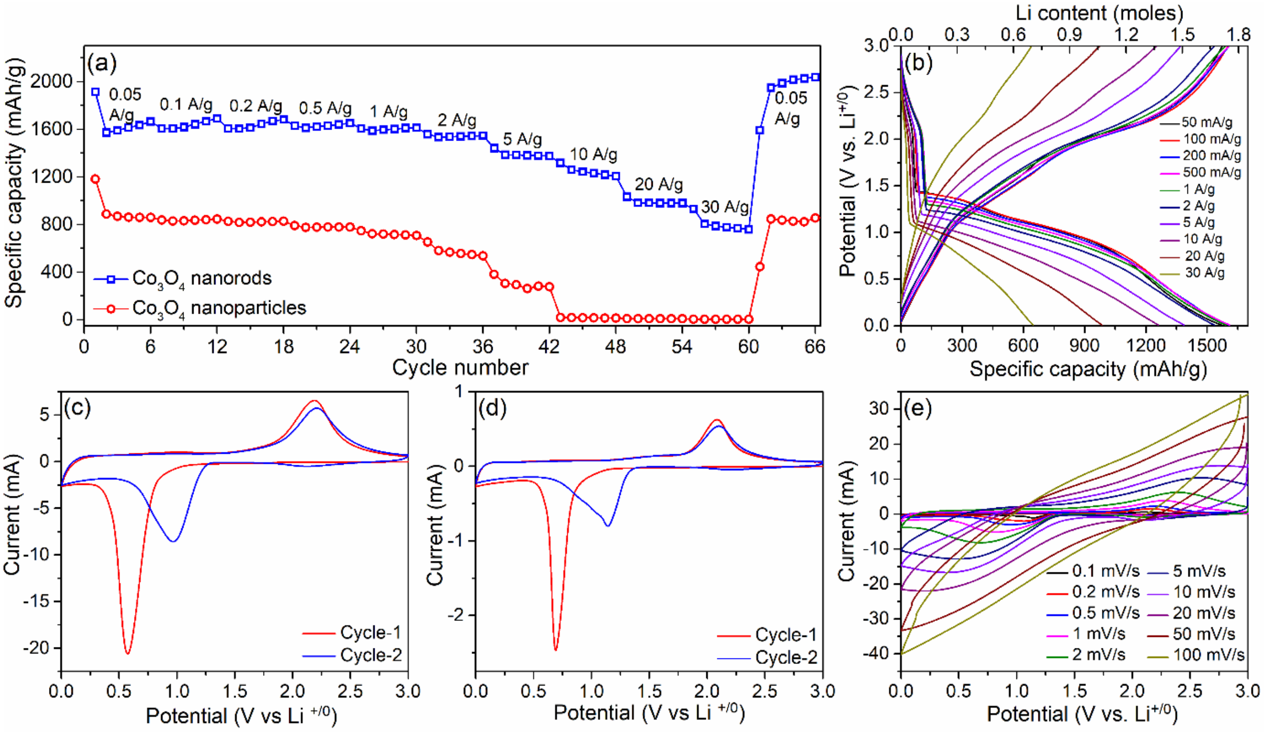

Figure 4.4 Galvanostatic rate performances of (a) hierarchical Co_3O_4 nanorods, and ball-milled Co_3O_4 nanoparticles. Galvanostatic voltage profiles of (b) Co_3O_4 nanorods at various current densities. Cyclic voltammograms of (c) Co_3O_4 nanorods and (d) ball-milled Co_3O_4 nanoparticles at a scan rate of 0.1 mV s^{-1}. (e) Cyclic voltammograms of Co_3O_4 nanorods at different scan rates.

Galvanostatic discharge profiles of Co_3O_4 based anodes exhibited three distinct regions between 3-0V elucidating different Li-ion storage mechanisms (Appendix 9). Initial slopping region from 3.0-1.3V correspond to the adsorption of Li-ions onto electrode surface, mainly at defects (region-I). While the plateau from 1.3-0.8V (region-II) and slopping profile in 0.8-0V (region-III) represent conversion reaction of Co_3O_4 to Co° ($Co_3O_4 + 8Li^+ + 8e^- \leftrightarrow 3Co + 4Li_2O$) and interfacial Li-ion storage (pseudocapacitance) respectively. Galvanostatic charge-discharge profiles of Co_3O_4 nanorods (Figure 4.4b) varied significantly with current densities and region-III dominated at higher current densities. It is also worth noting that the maximum specific capacity delivered by Co_3O_4 nanorods (1.76 moles of Li) is superior to the theoretical capacity of cobalt-oxide (1 mole of Li corresponding to 890 mAh g^{-1}). Charge-discharge profiles of this electrodes demonstrated ~100% coulombic efficiencies which is a crucial parameter for developing stable full lithium-ion batteries.[5]

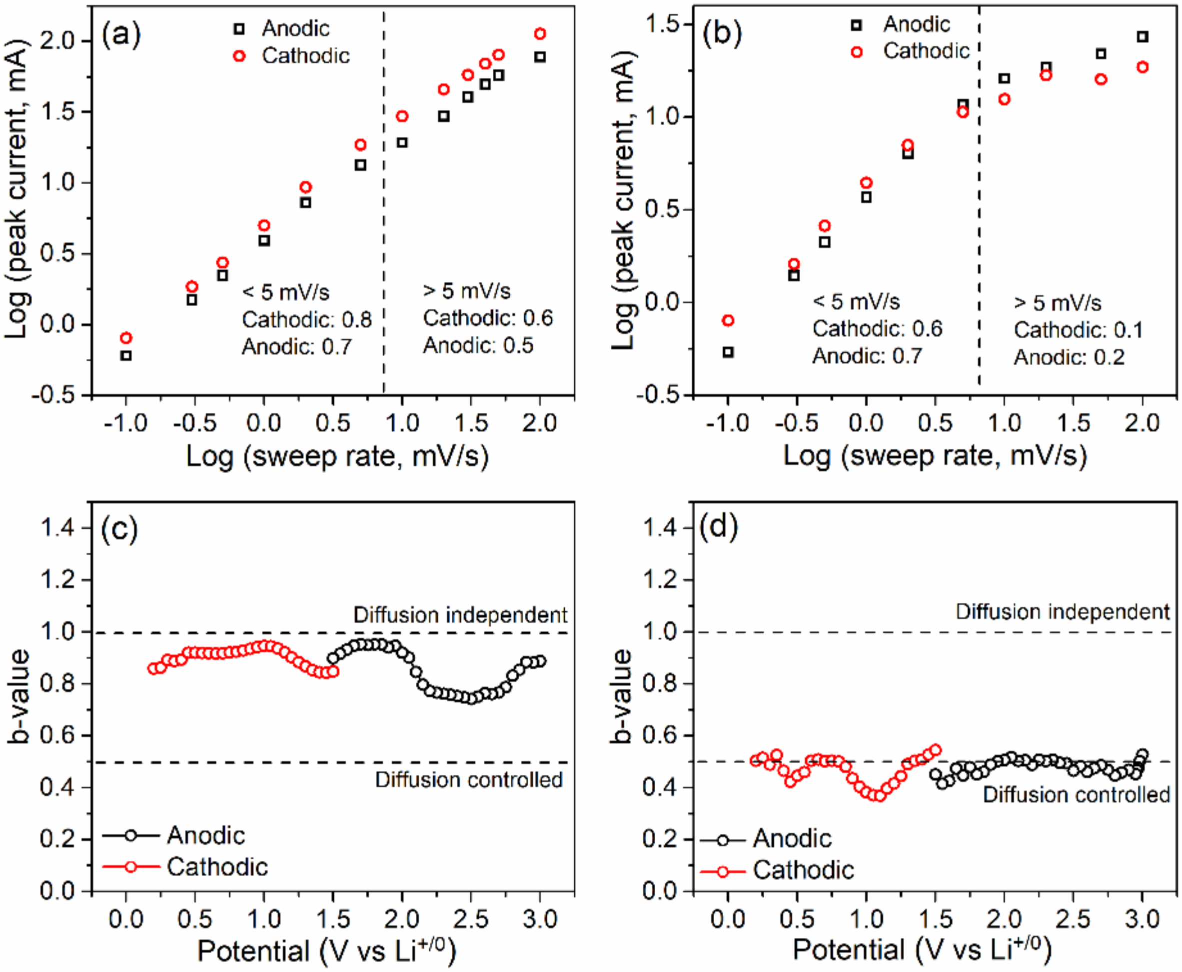

Figure 4.5 Scan rate dependence of peak current density of (a) Co_3O_4 nanorods and (b) ball-milled Co_3O_4 nanoparticles. Anodic and cathodic *b*-values of (c) Co_3O_4 nanorods and (d) ball-milled Co_3O_4 nanoparticles at different state of charge.

Cyclic voltammetry (CV) of Co_3O_4 nanorods and ball-milled Co_3O_4 nanoparticles are performed for a detailed investigation of redox processes in the voltage range 0-3 V vs $Li^{+/0}$ (Figure 4.4c and d). In the case of Co_3O_4 nanorods, broad cathodic peak centered at 0.55 V corresponds to the reduction of Co_3O_4 accompanied with Li_2O formation (SEI) that is in line with the irreversible capacity loss observed on first discharge. Reduced cathodic intensity and shift in peak to higher potentials during second scan signifies complete Li_2O formation in the initial cycle. Broad anodic signal at 2.2 V resembles Co oxidation ($3Co + 4Li_2O \rightarrow Co_3O_4 + 8Li^+ + 8e^-$) and removal of surface adsorbed Li-ions. Cyclic voltammograms of ball-milled Co_3O_4 nanoparticles (Figure 4.4d) displayed cathodic and anodic peak at 0.8 and 2 V corresponds to reduction of Co_3O_4 accompanied with Li_2O and Co oxidation respectively.[38] These anodic and cathodic response are in good agreement with the Co_3O_4 based anodes reported earlier.[27-29, 39]

Further quantitative analysis of pseudocapacitive Li-ion storage is performed by collecting cyclic voltammograms of hierarchical Co_3O_4 nanorod anodes at various scan rates (Figure 4.4e). Redox peak currents from cyclic voltammetry of Co_3O_4 nanorods followed a linear dependence with scan rate that is distinctive pseudocapacitive type Li-ion charge storage. Anodic and cathodic peak currents as a function of scan-rate can be represented by power-law $i=av^b$, where i is the current (mA), a and b are arbitrary constants, and v is the sweep rate (mV s^{-1}). In this case, parameter b defines the nature of charge storage as b=0.5 when current is controlled by semi-infinite linear diffusion and b=1 for surface-controlled behaviour (diffusion -independent). Figure 4.5a and b displayed linear dependence of log (i) vs log (v) plot for the hierarchical Co_3O_4 nanorods and ball-milled Co_3O_4 nanoparticles. In case of Co_3O_4 nanorods, calculated b-values for cathodic and anodic peaks in 0.1-5 mV s^{-1} scan rate are 0.8 and 0.7 respectively indicating that the current response is mostly surface-controlled behavior. On the other hand, b-values for ball-milled Co_3O_4

nanoparticles are 0.6 and 0.7 respectively in scan rates 0.1-5 mV s^{-1} and 0.1 and 0.2 at higher scan rates signifying that the current response is dominated by sluggish diffusion kinetics. Although *b*-values decreased to 0.6 and 0.5 with an increase of sweep rates to 5-1000 mV s^{-1} for cathodic and anodic peaks respectively in Co_3O_4 nanorods, these values still represent a high degree of pseudocapacitive process.

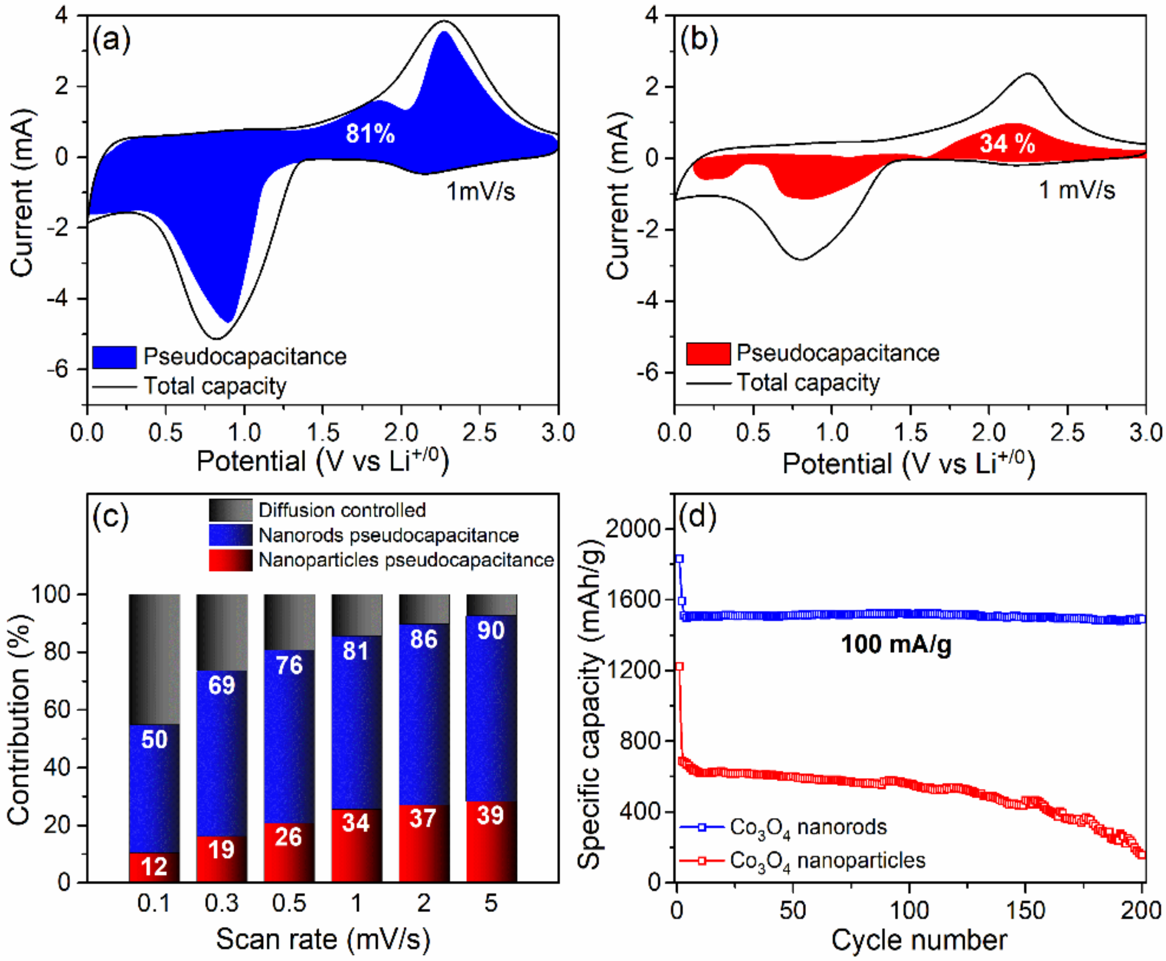

Figure 4.6 Cyclic voltammograms of (a) Co_3O_4 nanorods and (b) ball-milled Co_3O_4 nanoparticles at 1 mV s^{-1} scan rate. Shaded regions represent pseudocapacitive current contribution. (c) Pseudocapacitive and diffusion-dependent capacity contributions of Co_3O_4 nanorods and ball-milled Co_3O_4 nanoparticles at different scan rates. (d) Galvanostatic cycling for Co_3O_4 nanorods and ball-milled Co_3O_4 nanoparticles at a current density of 100 mA g^{-1}.

Drop in b-values at high scan rates is observed due to the increased ohmic resistance and diffusion constraints at higher rates.[23, 40, 41] Cathodic and anodic process b-values for Co_3O_4 nanorods and ball-milled Co_3O_4 nanoparticles provided further insights of potential dependent Li-ion storage mechanism (Figure 4.5c and d). Lithiation (cathodic process) of Co_3O_4 nanorods in voltage range 1.5-1.0 V (conversion reaction) and < 1.0 V (interfacial storage) is mainly dominated by pseudocapacitive process. Delithiation (anodic process) in this case is mixed process of pseudocapacitive and diffusion controlled in the voltage range 1.5-3.0 V, while the anodic and cathodic process in ball-milled Co_3O_4 nanoparticles is completely diffusion controlled. It is thus clear that both conversion reaction and interfacial storage follow a pseudocapacitive diffusion-independent kinetics due to the presence of nanograin-boundaries in Co_3O_4 nanorods.

Li-ion storage mechanism through diffusion dependent conversion reaction and surface controlled pseudocapacitive interfacial storage are further distinguished using equation 2.5 (Figure 4.6a and b).[13] Pseudocapacitive Li-ion storage dominated the entire voltage range of Co_3O_4 nanorods electrode with minimum contribution in 1.5-1.0 V and 2.0-2.5 V, where the diffusion-controlled conversion reaction occurs. Co_3O_4 nanorods exhibited excellent pseudocapacitive contribution of 81% at 1 mV s^{-1}, suggesting surface dominated Li-ion storage mechanism and 34% in case of ball-milled Co_3O_4 nanoparticles. Pseudocapacitive contribution gradually increases with the scan rate from 0.1 to 5 mV s^{-1} with a maximum of 90% at 5mV s^{-1} (Figure 4.6c). This is in line with the dominant interfacial charge storage (sloping region-III) at higher rates observed from charge-discharge profiles at higher current densities. Reduced diffusion-controlled capacity contribution should be expected from the transition metal-oxides at higher current densities due to the well-known kinetic limitation of conversion reaction.[42] This is further verified by the low pseudocapacitive contribution of ball-milled Co_3O_4 nanoparticles at various scan rates compared to hierarchical Co_3O_4 nanorods. High pseudocapacitive contribution of Co_3O_4 nanorods at slow scan rates is further beneficial for achieving greater stability even at lower currents enabling high energy density.

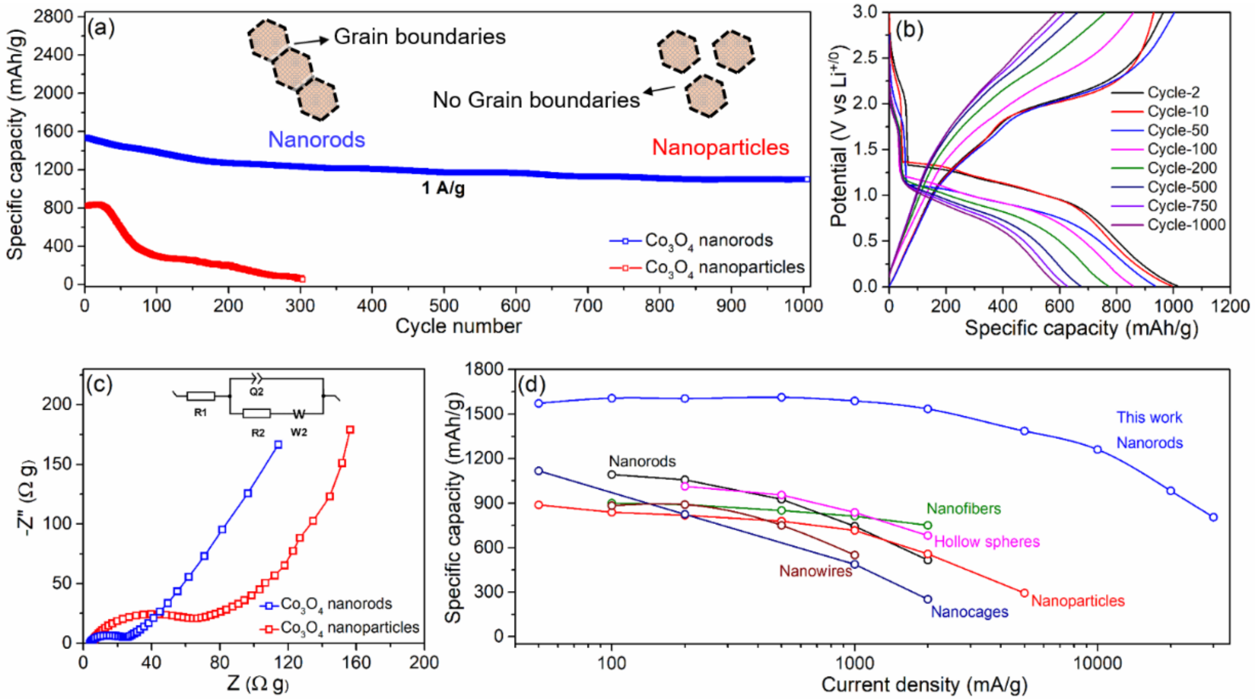

Figure 4.7 (a) Galvanostatic cycling for Co_3O_4 nanorods and ball-milled Co_3O_4 nanoparticles at a current density of 1 A g^{-1}. Inset: Schematic of the presence of grain boundaries in hierarchical Co_3O_4 nanorods, and their absence in Co_3O_4 nanoparticles. (b) Galvanostatic voltage profiles of Co_3O_4 nanorods correspond to various galvanostatic cycles at a current density of 1 A g^{-1}. (c) Nyquist plots of Co_3O_4 nanorods, and ball-milled Co_3O_4 nanoparticles. Inset: Randles equivalent circuit used for fitting the EIS pattern. (d) Li-ion storage performance comparison of Co_3O_4 nanorods with other Co_3O_4 based anodes reported earlier.

For instance, Co_3O_4 nanorod electrodes exhibited excellent galvanostatic cycling stability with a reversible specific capacity of 1129 mAh g^{-1} (92% of initial capacity) compared to ball-milled Co_3O_4 nanoparticles (158 mAh g^{-1}) after 200 cycles at low current density of 100 mA g^{-1} (Figure 4.6d). Moreover, hierarchical Co_3O_4 nanorods demonstrated extraordinary capacity of 1029 mAh g^{-1} even at high current density of 1 A g^{-1} with capacity retention of 60% after 1000 galvanostatic cycles (Figure 4.7a). Ball-milled Co_3O_4 nanoparticles exhibited poor cycling performance and failed after 300 cycles under similar experimental conditions. This should be expected due to the electrode pulverisation and formation of electronically insulating Li_2O in conversion-based anodes.[43] Galvanostatic voltage profiles of Co_3O_4 nanorods at various stages of extended cycling (Figure 4.7b) demonstrated identical behavior, which clearly established high reversibility and identical Li-ion storage mechanism during numerous charge-discharge processes. Coulombic efficiency on extended cycling is also outstanding, retaining ~100 % even at high current densities of 1 A g^{-1}. It is interesting to note that the commonly used electrolyte additives such as vinylene carbonate (VC) or fluoroethylene carbonate (FEC) are not used for nanograin-boundary-rich Co_3O_4 nanorod anodes, demonstrating its ability to work in conventional electrolyte solution.

Electrochemical impedance spectroscopic (EIS) measurements provided further details regarding the Li-diffusion kinetics of Co based electrodes (Figure 4.7c). Nyquist plots of all Co-based electrodes composed of a low frequency slopping line and high frequency semicircle representing solid-state diffusion (Z_w) and charge-transfer resistance (R_{ct}) respectively.[42, 44] Fitting of the Nyquist plots to the equivalent circuit (Figure 4.7c inset) revealed charge transfer resistances of 24 Ω (Co_3O_4 nanorods), and 65 Ω (ball-milled Co_3O_4 nanoparticles). Lower charge transfer resistance in case of Co_3O_4 nanorods can be related to the hierarchical 1D microstructure that allows superior contact with the electrolyte solution without undergoing agglomeration. Li-ion diffusion coefficients for Co_3O_4 nanorods and ball-milled Co_3O_4 nanoparticles calculated from Warburg impedance (equation 2.10) are 1.1×10^{-14} cm^2s^{-1} and 8.5×10^{-15} cm^2s^{-1} respectively. Fast Li-ion diffusion through the nanograin-boundaries improves the ionic conductivity and allows faster charging, which is crucial for inducing pseudocapacitive type charge storage.[45] This is further evidenced by the high Li-ion diffusion coefficient in case of Co_3O_4 nanorods compared to ball-milled Co_3O_4 nanoparticles, which is key for achieving enhanced pseudocapacitive charge storage, specific capacities, rate performance and cycling stability. It is worth noting that Co_3O_4 nanorods demonstrated superior capacities and excellent rate capabilities (0.05-30 A g^{-1}) among all of the reported 1-D Co_3O_4 electrodes for Li-ion batteries (Figure 4.7d).[29, 46-51]

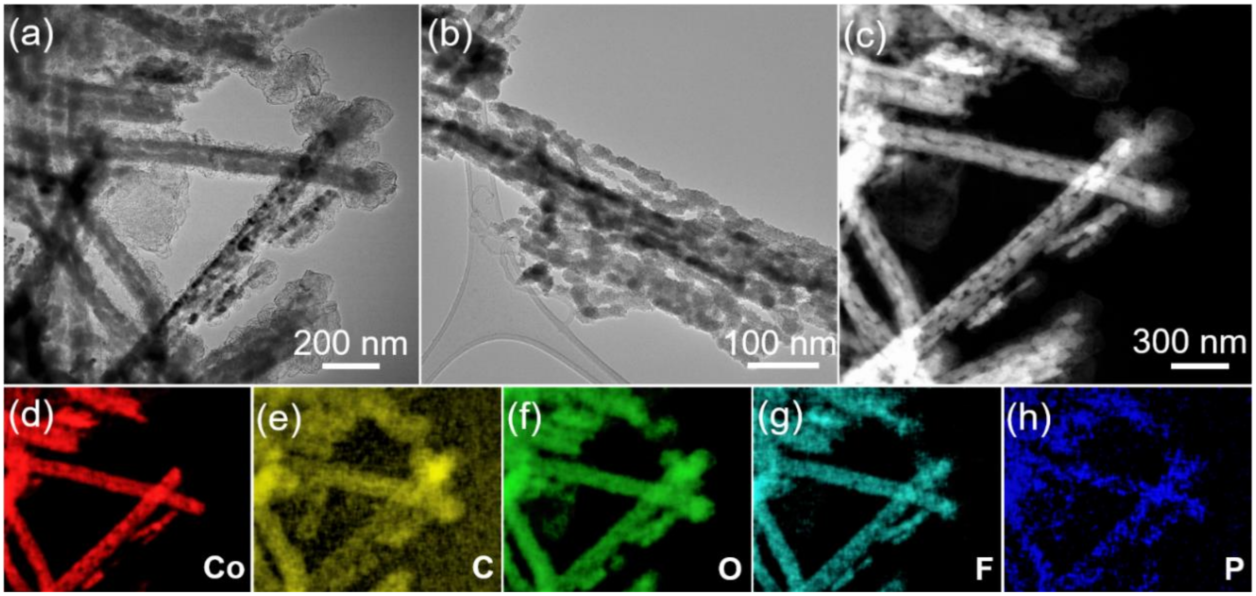

Figure 4.8 (a-b) *Ex-situ* high-resolution TEM images at various magnifications, (c) HAADF image, and (d-h) corresponding EDX elemental mapping of Co_3O_4 nanorods after 1000 charge-discharge cycles at a current density of 1 A g^{-1}.

Post-cycling studies are carried out to follow the compositional, morphology and microstructural changes at various state of charge during lithiation-delithiation course of hierarchical Co_3O_4 nanorods. *Ex-situ* HRTEM of cycled electrodes confirmed its intactly preserved nanorod structure with compositional homogeneity of Co, O and C from EDX elemental mapping even after 1000 galvanostatic cycles (Figure 4.8a-f). Homogeneous distribution of P and F in the electrodes signifies the existence of a uniform SEI that is vital for attaining stable electrochemical performance (Figure 4.8g and h).Further *in-situ* x-ray diffraction is performed to track the phase changes in Co_3O_4 nanorods during discharge (OCV to 0.01 V) and charge (0.01-3 V) processes (Figure 4.9a and b).

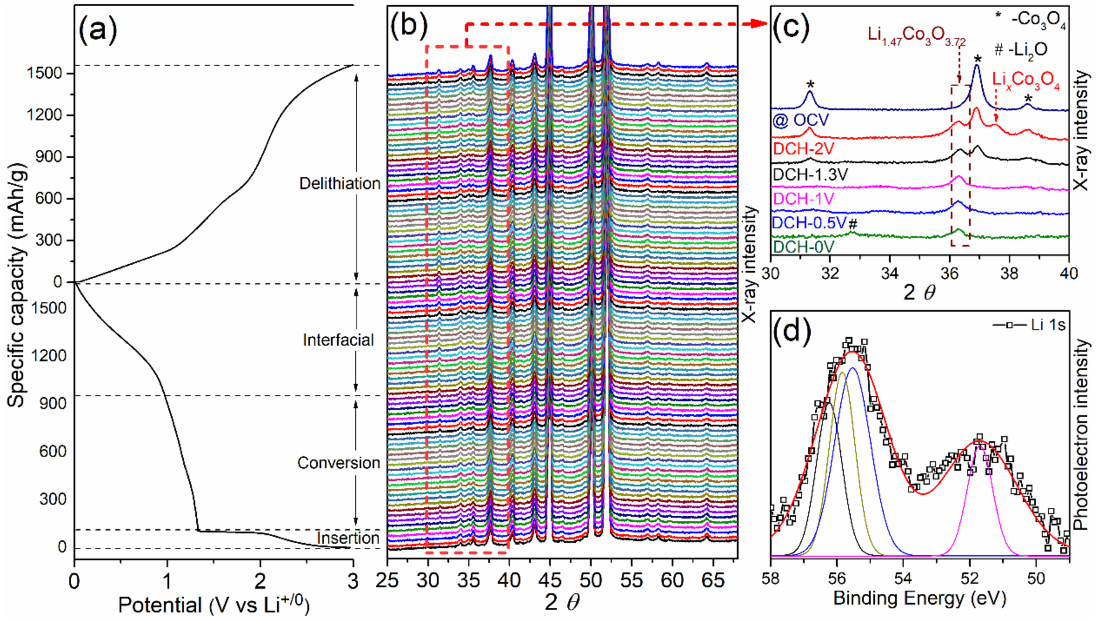

Figure 4.9 (a) Charge-discharge voltage profile of Co_3O_4 nanorods in the voltage range 3.0-0.01 V and (b) corresponding *in-situ* XRD patterns. (c) Selected *in-situ* XRD patterns at specific potentials. (d) High-resolution Li 1s XPS spectra of cycled Co_3O_4 nanorod electrode.

Dynamic phase changes evident from the *in-situ* diffractograms at specified potentials are emphasized in figure 4.9c (after subtracting Be-window peaks). It is observed during discharge process that the diffraction peaks corresponding to cobalt oxide didn't exhibit any phase change until 2V except for two distinct peaks at 36.2° and 37.5° corresponding to $Li_{1.47}Co_3O_{3.72}$ and $Li_xCo_3O_4$.[52-54] These additional peaks are likely due to the reaction of lithium ions with Co_3O_4 at nanograin boundaries and/or on surface of nanorods. While the diffraction peak resembling $Li_xCo_3O_4$ phase slowly disappeared as cell is discharged to 1.3 V. This behavior have also been previously observed for Co_3O_4 and other conversion-type anodes.[53, 55] Well-defined characteristic peaks of Co_3O_4 gradually decreased after 1 V signifying the onset of conversion mechanism ($Co_3O_4 + 8e^- + 8Li \leftrightarrow 4Li_2O + 3Co$).[26] Remarkably, additional $Li_{1.47}Co_3O_{3.72}$ phase and distinctive

Li_2O signals are clearly evidenced after complete discharge (0.01 V). It is interesting to note that the $Li_{1.47}Co_3O_{3.72}$ phase and distinctive Co_3O_4 peaks reappeared after charging to 3V and retained even after 200 galvanostatic cycles (Appendix 10) at low current densities. On the other hand, Co_3O_4 nanoparticles exhibited conventional conversion reaction and no such additional phases are observed (Appendix 11). Retention of additional phase during lithiation-delithiation process is in good agreement with the outstanding rate performance and pseudocapacitance of Co_3O_4 nanorods. Moreover, there is no evidence of metallic lithium peaks in lithiated Co_3O_4 nanorods, which is also supported by high-resolution Li 1s XPS spectra (Figure 4.9d). Broad peak observed at 55.6 eV resembles the SEI components (Li_2O, LiF, Li_2CO_3 etc.) formed upon the decomposition of electrolyte. It is interesting to note that the peak detected at 52.6 eV could be related to additional $Li_{1.47}Co_3O_{3.72}$ phase. Hence, formation of $Li_{1.47}Co_3O_{3.72}$ phase and structural stability of hierarchical Co_3O_4 nanorods is one of the major reasons for the extraordinary specific capacities and rate performance.

Crystallization of $Li_{1.47}Co_3O_{3.72}$ phase at grain boundaries during the lithiation of Co_3O_4 nanorods is further supported by *ex-situ* transmission electron microscopy (TEM) and electron energy loss spectroscopy (EELS). HRTEM and HAADF-STEM images of nanorods lithiated to 1.3 V and individual nanocrystallites respectively is displayed in figure 4.10a and b respectively. It is thus clear from figure 4.10c that the quantitative Li (yellow) at 1.3 V is uniformly distributed along the grain boundaries, with no indication on the surface of Co_3O_4 (red). Hence, this Li-phase at nanograin-boundaries could be ascribed to the additional $Li_{1.47}Co_3O_{3.72}$ phase detected from *in-situ* x-ray measurements. Despite the formation of Li_2O at 0V, Co_3O_4 nanorods clearly preserves the nanograin-boundaries throughout the conversion process evidenced from HRTEM and HAADF-STEM (Figure 4.10d and e).

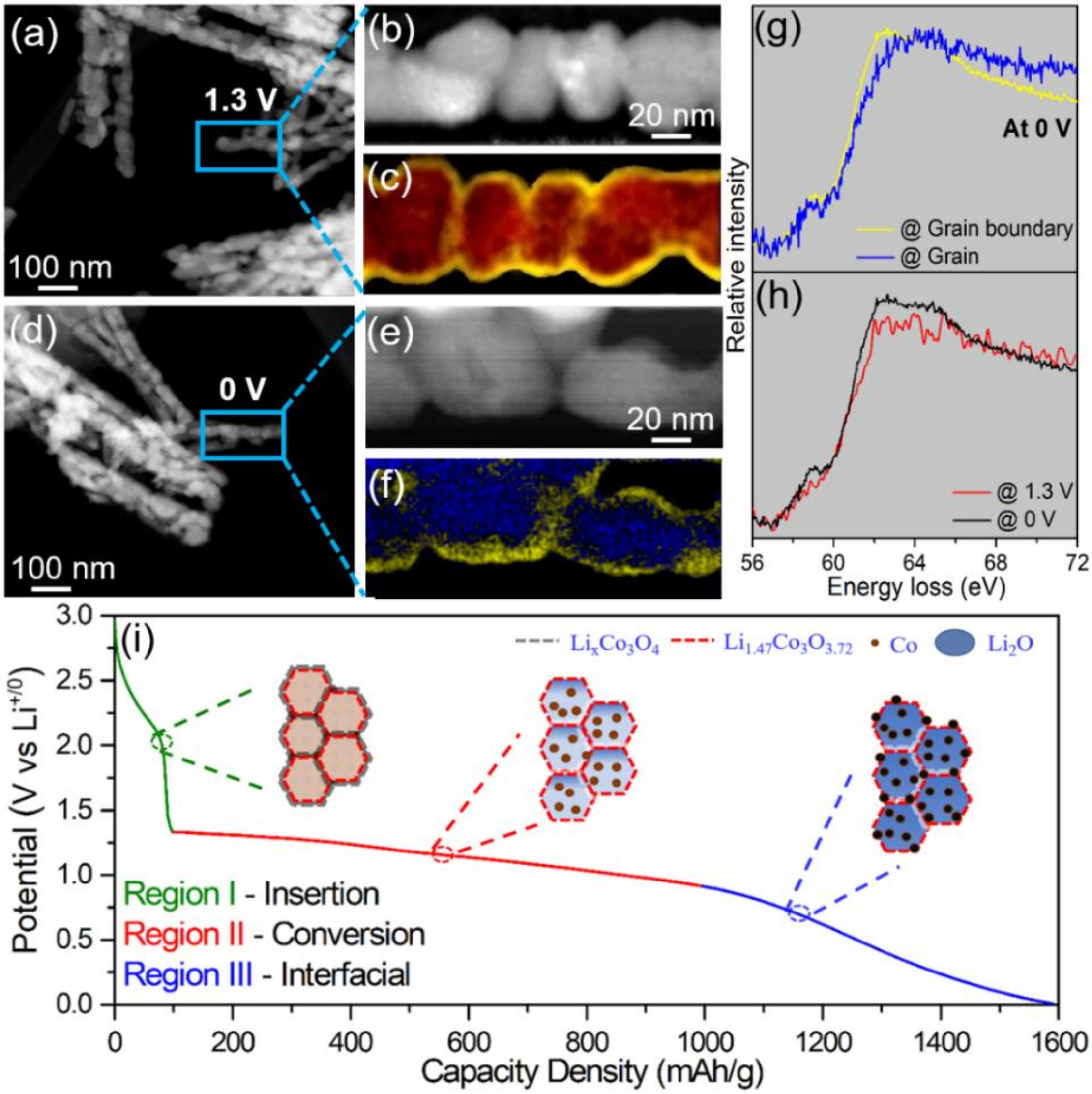

Figure 4.10 High-resolution (a) TEM image, (b) STEM-HAADF image and (c), corresponding EELS spectral mapping showing Li (yellow) and Co_3O_4 (red) distribution of Co_3O_4 nanorod electrodes discharged to 1.3 V. High-resolution (d) TEM, (e) STEM-HAADF image and (f), corresponding EELS elemental mapping showing Li (yellow) at grain-boundaries and Co (blue) distribution of electrodes discharged to 0 V. (g) Li K-edge spectra collected from grain and grain boundary of Co_3O_4 nanorods discharged to 0 V. (h) Li K-edge spectra corresponding to the grain boundary of Co_3O_4 nanorods discharged to 1.3 V and 0 V. (i) Schematic representation of the Li-ion storage mechanism in Co_3O_4 nanorods.

STEM-EELS analysis revealed an initial transition from Co_3O_4 (red) to Co (blue) followed by the homogenous distribution of Li (yellow) at nanograin-boundaries (Figure 4.10 f). Further insight into the EELS spectra of high-resolution Li k-edge display distinctively different peak at nanograin-boundaries compared to surface of Co_3O_4 nanograin at 0 V (Figure 4.10g). In both the spectra, a sharp peak evidenced at ~58.9 eV corresponds to Li_2O and a shift in broad peak from ~64.5 eV resembling SEI components to ~62.5 eV is observed in case of grain boundaries. While the spectra of 0 and 1.3 V demonstrate the peak at 61.2 eV in case of nanograin-boundaries that could be related to the additional $Li_{1.47}Co_3O_{3.72}$ phase (Figure 4.10h). No metallic Li peaks are observed in either case and moreover, absence of 59 eV can eliminate the possible formation of Li_2O before the onset of conversion reaction at 1.3 V. Hence, it is clear that $Li_{1.47}Co_3O_{3.72}$ phase formation at nanograin-boundaries are mainly responsible for large pseudocapacitive interfacial Li-ion storage (region-iii) resulting in high specific capacities and stable cycling of Co_3O_4 nanorods (Figure 4.10i).

Superior Li-ion storage performance of Co_3O_4 nanorod anodes can be credited to its exceptional physiochemical properties resulting from hierarchical microstructure and the presence of nanograin boundaries. Unique hierarchical 1-D nanorod microstructure and polycrystalline Co_3O_4 nanocrystallites are favourable in accommodating the volume change and particle agglomeration during charge-discharge process. Nanograin-boundaries of hierarchical Co_3O_4 nanorods resulted in the crystallization of $Li_{1.47}Co_3O_{3.72}$ phase, which resulted in the increased pseudocapacitance due to the formation of $Li_2O/Co/Li_{1.47}Co_3O_{3.72}$ interfaces. Nanograin boundaries also facilitate ultrafast diffusion of Li-ions, which is crucial to achieve high degree of pseudocapacitance. These claims are further validated by the poor electrochemical performance of ball-milled Co_3O_4 nanoparticles due to the lack of well-defined nanograin-boundaries. In conclusion, nanograin boundaries resulted in the exceptional specific capacity, rate performance, cycling stability and pseudocapacitance of hierarchical Co_3O_4 nanorods. To the best of our knowledge, this is the first report on the nanograin boundary induced pseudocapacitance of a conversion-type anode material.

4.2.3 High Energy/ Power Density Lithium-Ion Full-Cell

Full-cell demonstrations of conversion-type anodes have largely been limited due to their high working voltages and low coulombic efficiencies in early cycles. Here, the advantage of nanograin-boundaries induced pseudocapacitance of hierarchical Co_3O_4 nanorods make them suitable for high-performance Li-ion full-cells. As demonstrated in figure 4.11a, Li-ion full-cells are assembled using Co_3O_4 nanorods anode and $LiNiMnCoO_2$ cathodes (rate capability and cycling provided in Appendix 6). Co_3O_4 nanorods‖$LiNiMnCoO_2$ cell demonstrated excellent cycling stability with a high reversible capacity of 593 mAh g^{-1} at 1 A g^{-1} (with respect to anode) in the 3.0-4.3 V voltage range. These full-cells are relatively stable, exhibiting >90% retention after 200 cycles and high coulombic efficiency (>99.8%) at practical values of current density (1.5 mA cm^{-2}) and areal capacity (4 mAh cm^{-2}). These values are greater than most of the traditional electrodes (<3 mAh cm^{-2}) at similar rates and fast enough (~ ½ hour) for realistic practical applications. Under similar experimental conditions, graphite‖$LiNiMnCoO_2$ full-cells displayed poor electrochemical performance (90 mAh g^{-1}) and unstable cycling (78% after 200 cycles) due to the sluggish Li-ion diffusion kinetics (Appendix 7). It is also worth noting that all of these full-cells are limited by cathode, emphasizing the need to improve high-capacity cathodes.

Galvanostatic charge-discharge profiles for Co_3O_4 nanorods‖$LiNiMnCoO_2$ full-cell at 1 A g^{-1} current density evidenced average cell voltage of approximately 3.9 V, which is higher than graphite‖$LiNiMnCoO_2$ cell (3.8 V). Increase in over potential are not observed in voltage profiles for Co_3O_4 nanorods‖LiNiMnCoO$_2$ full-cells at any cycle number, which indicates that both the electrodes and their electrode–electrolyte interfaces remain stable during cycling. High operational voltage resulted from Co_3O_4 nanorods‖LiNiMnCoO$_2$ full-cell is superior to the previously reported conversion and alloying based anodes in full lithium-ion cell configurations.

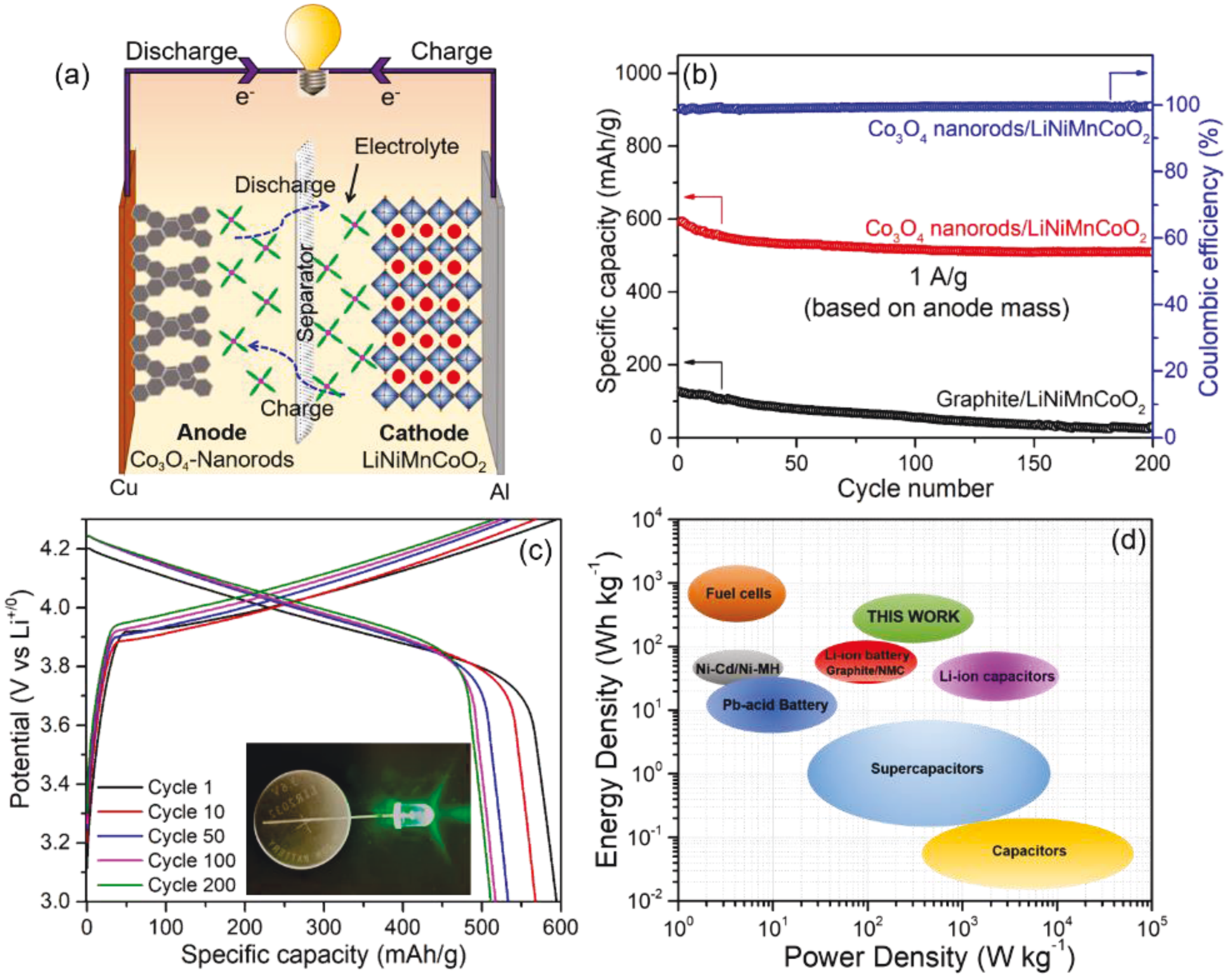

Figure 4.11 (a) Schematic of Li-ion full-cell containing Co_3O_4 nanorods anode and LiNiMnCoO$_2$ cathode. (b) Galvanostatic cycling performance of Co_3O_4 nanorods‖LiNiMnCoO$_2$ and graphite‖LiNiMnCoO$_2$ full-cells at a current density of 1 A g^{-1} after 5 cycles at a current density of 100 mA g^{-1}. Specific capacities and current densities are calculated based on the anode weight. (c) Galvanostatic charge-discharge profiles of Co_3O_4 nanorods‖LiNiMnCoO$_2$ full-cell at a current density of 1 A g^{-1}. (d) Ragone plot of Co_3O_4 nanorods‖LiNiMnCoO$_2$ Li-ion full-cell, and other relevant energy storage devices.

Output potential of Co_3O_4 nanorods‖LiNiMnCoO$_2$ full-cell could light up a 3 V green LED of 0.07 W (Figure 4.11c inset). Discharge curves of Co_3O_4 nanorods‖LiNiMnCoO$_2$ full-cells exhibited slopping profile that is distinctive of pseudocapacitance process resulting from interfacial Li-ion storage. It is thus clear that the use of highly pseudocapacitive hierarchical Co_3O_4 nanorods anode resulted in exceptional capacities and stability. Hence, there is further scope to improve the full-cell stability and performance through optimising the electrolyte composition.

Co_3O_4 nanorods‖LiNiMnCoO$_2$ full-cells exhibited 480 Wh kg^{-1} and 980 W kg^{-1} energy and power density respectively (based on anode and cathode mass) which are ~3-fold higher than graphite‖LiNiMnCoO$_2$ full-cells (150 Wh kg^{-1} and 320 W kg^{-1} respectively). These higher values of Co_3O_4 nanorods‖LiNiMnCoO$_2$ are particularly attractive for applications like electric vehicles for long-driving range and high-power portable electronics. Energy and power density stated herein surpasses the previously reported Li-ion full-cells based on conversion-type anodes.[56, 57] Additionally, power density of this lithium-ion battery is even on par with the supercapacitors and lithium ion capacitors that is demonstrated in Ragone plot (Figure 4.11d). Despite the electrochemically unstable Ni in the cathode, Co_3O_4 nanorods‖LiNiMnCoO$_2$ exhibited excellent cycling and high specific capacity due to the nanograin boundary induced pseudocapacitance. Based on the aforementioned results of Co_3O_4 nanorods in Li-ion full cells, electrochemical performance could be further improved by optimization of cell balancing, electrode thickness, charge-discharge protocols and voltage window.

4.3 Conclusion

In summary, we have demonstrated a high energy and power density Li-ion battery through a grain boundary induced pseudocapacitance of hierarchical cobalt oxide nanorods. These 1D electrodes exhibited exceptional specific capacities and rate capability compared to any of the

Co_3O_4 based anodes reported earlier. Cycling stability and coulombic efficiencies of Co_3O_4 nanorods are also remarkable than ball-milled Co_3O_4 nanoparticles with similar crystallite size. Hierarchical morphology of unique 1-D Co_3O_4 nanorods prevents the electrode from particle agglomeration and buffer the volume change during the charge-discharge process. Numerous nanograin-boundaries of hierarchical Co_3O_4 nanorods enabled ultrafast Li-ion diffusion, which is necessary for achieving high degree of pseudocapacitance. Nanograin-boundaries also facilitated the crystallization of $Li_{1.47}Co_3O_{3.72}$ phase, which resulted in the increased pseudocapacitance due to the formation of $Li_2O/Co/Li_{1.47}Co_3O_{3.72}$ interfaces. Demonstrated approach of nanograin boundary induced pseudocapacitance can be also extended for other metal oxide anodes for the development of next generation Li-ion batteries.

4.4 References

1. A. S. Aricò, P. Bruce, B. Scrosati, J. M. Tarascon and W. V. Schalkwijk, *Nat. Mater.*, **2005**, 4, 366-377.
2. J. Cabana, L. Monconduit, D. Larcher and M. R. Palacín, *Adv. mater.*, **2010**, 22, E170-E192.
3. J. Liu, Z. Bao, Y. Cui, E. J. Dufek, J. B. Goodenough, P. Khalifah, Q. Li, B. Y. Liaw, P. Liu, A. Manthiram, Y. S. Meng, V. R. Subramanian, M. F. Toney, V. V. Viswanathan, M. S. Whittingham, J. Xiao, W. Xu, J. Yang, X.-Q. Yang and J.-G. Zhang, *Nat. Energy*, **2019**, 4, 180-186.
4. A. Manthiram, *ACS Cent. Sci.*, **2017**, 3, 1063-1069.
5. V. Etacheri, C. Hong, J. Tang and V. G. Pol, *ACS Appl. Mater. Interfaces*, **2018**, 10, 4652-4661.
6. G. Binotto, D. Larcher, A. S. Prakash, R. H. Urbina, M. S. Hegde and J. M. Tarascon, *Chem. Mater.* , **2007**, 19, 3032-3040.
7. P. Sennu, S. Madhavi, V. Aravindan and Y.-S. Lee, *ACS Nano* **2020**, 8, 10648-10654.
8. P. Poizot, S. Laruelle, S. Grugeon, L. Dupont and J.-M. Tarascon, *Nature*, **2000**, 407, 496-499.

9. V. Etacheri, R. Marom, R. Elazari, G. Salitra and D. Aurbach, *Energy Environ. Sci.*, **2011**, 4, 3243-3262.
10. P. Zhang, R. Wang, M. He, J. Lang, S. Xu and X. Yan, *Adv. Funct. Mater.*, **2016**, 26, 1354-1364.
11. Z.-S. Wu, W. Ren, L. Wen, L. Gao, J. Zhao, Z. Chen, G. Zhou, F. Li and H.-M. Cheng, *ACS Nano*, **2010**, 4, 3187-3194.
12. J. Xu, J. Wu, L. Luo, X. Chen, H. Qin, V. Dravid, S. Mi and C. Jia, *j. Power Sources*, **2015**, 274, 816-822.
13. V. Augustyn, P. Simon and B. Dunn, *Energy Environ. Sci.*, **2014**, 7 1597-1614
14. J. Liu, J. Wang, C. Xu, H. Jiang, C. Li, L. Zhang, J. Lin and Z. X. Shen, *Adv. Sci.*, **2017**, 5, 1700322.
15. X. Yu, S. Yun, J. S. Yeon, P. Bhattacharya, L. Wang, S. W. Lee, X. Hu and H. S. Park, *Adv. Energy Mater*, **2018**, 8, 1702930.
16. M. Lübke, J. Shin, P. Marchand, D. Brett, P. Shearing, Z. Liu and J. A. Darr, *J. Mater. Chem. A*, **2015**, 3, 22908-22914.
17. J. Wang, J. Polleux, J. Lim and B. Dunn, *J. Phys. Chem. C* **2007**, 111, 14925-14931.
18. V. S. Avvaru, I. J. Fernandez, W. Feng, S. J.Hinder, M. C. Rodríguez and V. Etacheri, *Carbon*, **2021**, 171, 869-881.
19. S. Lou, X. Cheng, Y. Zhao, A. Lushington, J. Gao, Q. Li, P. Zuo, B. Wang, Y. Gao, YulinMa, C. Du, G. Yin and X. Sun, *Nano Energy*, **2017**, 34, 15-25.
20. J. Zhang, H. Jiang, Y. Zenga, Y. Zhang and H. Guo, *J. Power Sources*, **2019**, 439, 227026.
21. H. Duan, L. Du, S. Zhang, Z. Chen and S. Wu, *J. Mater. Chem. A*, **2019**, 7, 8327-8334.
22. Y. Zhang, L. Tao, C. Xie, D. Wang, Y. Zou, R. Chen, Y. Wang, C. Jia and S. Wang, *Adv. Mater.*, **2020**, 32, 1905923.
23. N. Wang, Y. Wang, X. Xu, T. Liao, Y. Du, Z. Bai and S. Dou, *ACS Appl. Mater. Interfaces*, **2018**, 10, 9353-9361.
24. J. Zhu, A. S. Childress, M. Karakaya, S. Dandeliya, A. Srivastava, Y. Lin, A. M. Rao and R. Podila, *Adv. Mater.*, **2016**, 28, 7185-7192.
25. Z. Xu, Z. Jiang, C. Kuai, R. Xu, C. Qin, Y. Zhang, M. M. Rahman, C. Wei, D. Nordlund, C.-J. Sun, X. Xiao, X.-W. Du, K. Zhao, P. Yan, Y. Liu and F. Lin, *Nat Commun*, **2020**, 11, 83.

26. S.-H. Cho, J.-W. Jung, C. Kim and I.-D. Kim, *Sci. Rep.*, **2017**, 7, 45105.

27. D. Su, X. Xie, P. Munroe, S. Dou and G. Wang, *Sci. Rep.* , **2014**, 4, 06519.

28. S. Sun, X. Zhao, M. Yang, L. Wu, Z. Wen and X. Shen, *Sci. Rep.*, **2016**, 6, 19564.

29. S. Sun, X. Zhao, M. Yang, L. Ma and X. Shen, *Nanomaterials*, **2015**, 5, 2335-2347.

30. Z. Wang, W. Wang, L. Zhang and D. Jiang, *Catal. Sci. Technol.*, **2016**, 6, 3845-3853.

31. M. A. Garakani, S. Abouali, B. Zhang, C. A. Takagi, Z.-L. Xu, J.-Q. Huang, J. Huang and J.-K. Kim, *ACS Appl. Mater. Interfaces*, **2014**, 5, 400-405.

32. T. Zhang, C. He, F. Sun, Y. Ding, M. Wang, L. Peng, J. Wang and Y. Lin, *Sci. Rep.*, **2017**, 7, 43638.

33. J. K. Shon, H. S. Lee, G. O. Park, J. Yoon, E. Park, G. S. Park, S. S. Kong, M. Jin, J.-M. Choi, H. Chang, S. Doo, J. M. Kim, W.-S. Yoon, C. Pak, H. Kim and G. D. Stucky, *Nat Commun*, **2016**, 7, 11049.

34. H. Wang, C. Zhang, Z. Liu, L. Wang, P. Han, H. Xu, K. Zhang, S. Dong, J. Yao and G. Cui, *J. Mater. Chem.*, **2011**, 21, 5430-5434.

35. K. Xie, P. Wu, Y. Zhou, Y. Ye, H. Wang, Y. Tang, Y. Zhou and T. Lu, *ACS Appl. Mater. Interfaces*, **2014**, 6, 10602-10607.

36. X. Leng, S. Wei, Z. Jiang, J. Lian, G. Wang and Q. Jiang, *Sci. Rep.*, **2015**, 5.

37. R. Schmuch, R. Wagner, G. Hörpel, T. Placke and M. Winter, *Nat. Energy*, **2018**, 3, 267-278.

38. C. Yan, Y. Zhu, Z. Fang, C. Lv, X. Zhou, G. Chen and G. Yu, *Adv. Energy Mater*, **2018**, 8, 1800762.

39. Y. Li, B. Tan and Y. Wu, *Nano Lett.*, **2008**, 8, 265-270.

40. Y. Jiang, Y. Li, P. Zhou, Z. Lan, Y. Lu, C. Wu and M. Yan, *Adv. Mater.*, **2017**, 29.

41. V. Augustyn, J. Come, M. A. Lowe, J. Kim, P.-L. Taberna, S. H. Tolbert, H. D. Abruña, P. Simon and B. Dunn, *Nat. Mater.*, **2013**, 12, 518-522.

42. L. Li, J. Dai, G. Jiang, X. Sun, Z. Huang, Z. Xie and B. Cao, *ChemistrySelect*, **2019**, 4, 6879-6885.

43. X. Wang, X.-L. Wu, Y.-G. Guo, Y. Zhong, X. Cao, Y. Ma and J. Yao, *Adv. Funct. Mater.*, **2010**, 20, 1680-1686.

44. C. Zhang, Y. Song, L. Xu and F. Yin, *Chemical Engineering Journal*, **2020**, 380, 122545.

45. S. Kim, G. Evmenenko, Y. Xu, D. B. Buchholz, M. Bedzyk, K. He, J. Wu and V. P. Dravid, *Adv. Funct. Mater.*, **2018**, 28, 1805723.

46. L. Fan, W. Zhang, S. Zhu and Y. Lu, *Ind. Eng. Chem. Res.*, **2017**, 56, 2046–2053.

47. N. Yan, L. Hu, Y. Li, Y. Wang, H. Zhong, X. Hu, X. Kong and Q. Chen, *J. Phys. Chem. C* **2012**, 116, 7227-7235.

48. K. Feng, H. W. Park, X. Wang, D. U. Lee and Z. Chen, *Electrochim. Acta*, **2014**, 139, 145-151.

49. J. Guo, L. Chen, X. Zhang and H. Chen, *J. Solid State Chem.*, **2014**, 213, 193-197.

50. H. Sun, G. Xin, T. Hu, M. Yu, D. Shao, X. Sun and J. Lian, *Nat Commun* **2014**, 5, 4526.

51. Y. Huang, C. Chen, C. An, C. Xu, Y. Xu, Y. Wang, L. Jiao and H. Yuan, *Electrochim. Acta*, **2014**, 145, 34-39.

52. L. Luo, J. Wu, J. Xu and V. P. Dravid, *ACS Nano*, **2014**, 8, 11560-11566.

53. M.M.Thackeray, S. D. Baker, K. T. Adendorff and J. B. Goodenough, *Solid State Ion.*, **1985**, 17, 175-181.

54. D. Larcher, G. Sudant, J.-B. Leriche, Y. Chabre and J.-M. Tarascon, *J. Electrochem. Soc.*, **2002**, 149, A234-A241.

55. X. W. Lou, D. Deng, J. Y. Lee, J. Feng and L. A. Archer, *Adv. Mater.*, **2008**, 20, 258-262.

56. A. Varzi, D. Bresser, J. v. Zamory, F. Müller and S. Passerini, *Adv. Energy Mater*, **2014**, 4, 1400054.

57. S. Hariharan, V. Ramar, S. P. Joshia and P. Balaya, *RSC Adv.*, **2013**, 3, 6386-6394.

Chapter 5

Oxygen Vacancy Induced Pseudocapacitance of Rutile TiO_2 Nanowires: Towards Superfast Charging Ultralong Life Lithium-Ion Batteries

5.1 Introduction

Titanium dioxide (TiO_2) is considered as one of the most promising electrode materials due to its low cost, abundance in nature, and low volume change during charge-discharge process.[1-3] Lithium-ion intercalation into TiO_2 at higher potentials (~ 1.5 V vs Li/Li^+) eliminates the possibility of forming dendrites and Li-metal plating that is commonly observed in graphite anodes.[4, 5] Titanium oxide of various polymorphs including bronze, anatase, and rutile have been studied extensively as anode materials for lithium-ion batteries.[2, 6-9] Rutile phase of TiO_2 is the most abundant and thermodynamically stable among the different polymorphs. Lithium-ion intercalation in rutile TiO_2 is highly anisotropic along the crystallographic c-axis rather than ab plane.[10] However, practical applications of TiO_2 anodes are hindered by its inferior rate capabilities resulting from poor electronic conductivity, low specific capacity (maximum Li uptake of 0.5 Li/Ti for anatase and TiO_2 (B), and no activity for rutile), and sluggish Li-ion diffusion kinetics.[11-13] Several strategies including fabrication of nanostructures, hybridization with carbonaceous substrates, and doping with heteroatoms were employed to improve the Li-ion storage performance of TiO_2 based anodes.[6, 14-16] However, these methods only resulted in a marginal increase of electrochemical performance. Alternative strategies and/or Li-ion storage mechanisms are thus vital to significantly enhance the rate performance, specific capacity, and cycle-life of rutile TiO_2 anodes.

Diffusion independent pseudocapacitive charge storage featuring faradaic surface/ near surface reactions is one of the recently investigated mechanisms for achieving ultrafast Li-ion storage.[17] Synergy between pseudocapacitive process and conventional Li-ion storage can ensure superior electrochemical performance even at higher rates. Extreme cycling stabilities are also evidenced in case of pseudocapacitive anodes due to the minimum crystallographic phase changes during the charge-discharge process.[18-20] Several intercalation-type materials such as TiO_2, Nb_2O_5, $TiNb_2O_7$, and $Li_4Ti_5O_{12}$ have been explored as fast-charging anodes with the advantage of pseudocapacitance.[20-24] However, inferior specific capacities of these intrinsically pseudocapacitive electrode materials are insufficient for high power applications like long-driving range electric vehicles. Engineering the electrode materials at nanoscale is a potential solution to overcome the challenges associated with conventional lithium-ion battery electrodes. Subsequently, much attention have been focused on developing various nanostructured rutile TiO_2 anodes such as nanoparticles, nanorods, nanowires, etc. due to their diverse surface properties, tunable structures, improved conductivity, and Li-ion diffusion kinetics.[15, 25-28] Although pseudocapacitance can be induced by nanostructuring and defect/ interface engineering, this method remain elusive in the case of rutile TiO_2 anodes.

In this chapter, we demonstrated an oxygen vacancy induced pseudocapacitance of rutile TiO_2 nanowires for next generation fast charging ultralong life lithium-ion batteries. Rational design and synthesis of these electrode materials are based on the following aspects. (1) One-dimensional nanowire is selected as the preferred morphology due to its superior charge transfer kinetics, improved ionic and electronic conductivity. (2) Oxygen vacancies provide additional Li-ion diffusion pathways by generating disorderness in the crystal structure, promoting pseudocapacitive storage.[25-27] Exceptional Li-ion storage performance of oxygen deficient rutile TiO_2 nanowires makes it a suitable anode material for high rate and ultralong life fast charging lithium-ion batteries.

5.2 Results and Discussion

5.2.1. Synthesis and Characterization of Oxygen Deficient Rutile TiO_2 Nanowires

Oxygen deficient rutile TiO_2 nanowires are synthesized through a solvothermal process using $TiCl_4$ in HCl (30%) precursor in ethylene glycol and water mixture (figure 2.4). Hydrochloric acid used in this case provides sufficient chlorine ions to promote crystallization and growth of one-dimensional nanowires. Ethylene glycol played the role of a protective layer on the particle surfaces prevents from agglomeration through the interactions between OH groups and TiO_2 planes. Chloride ions in presence of ethylene glycol acts as reducing agent in the formation of TiO_2 nanoparticles and inhibits accumulation through electrostatic stabilization.[28, 29]

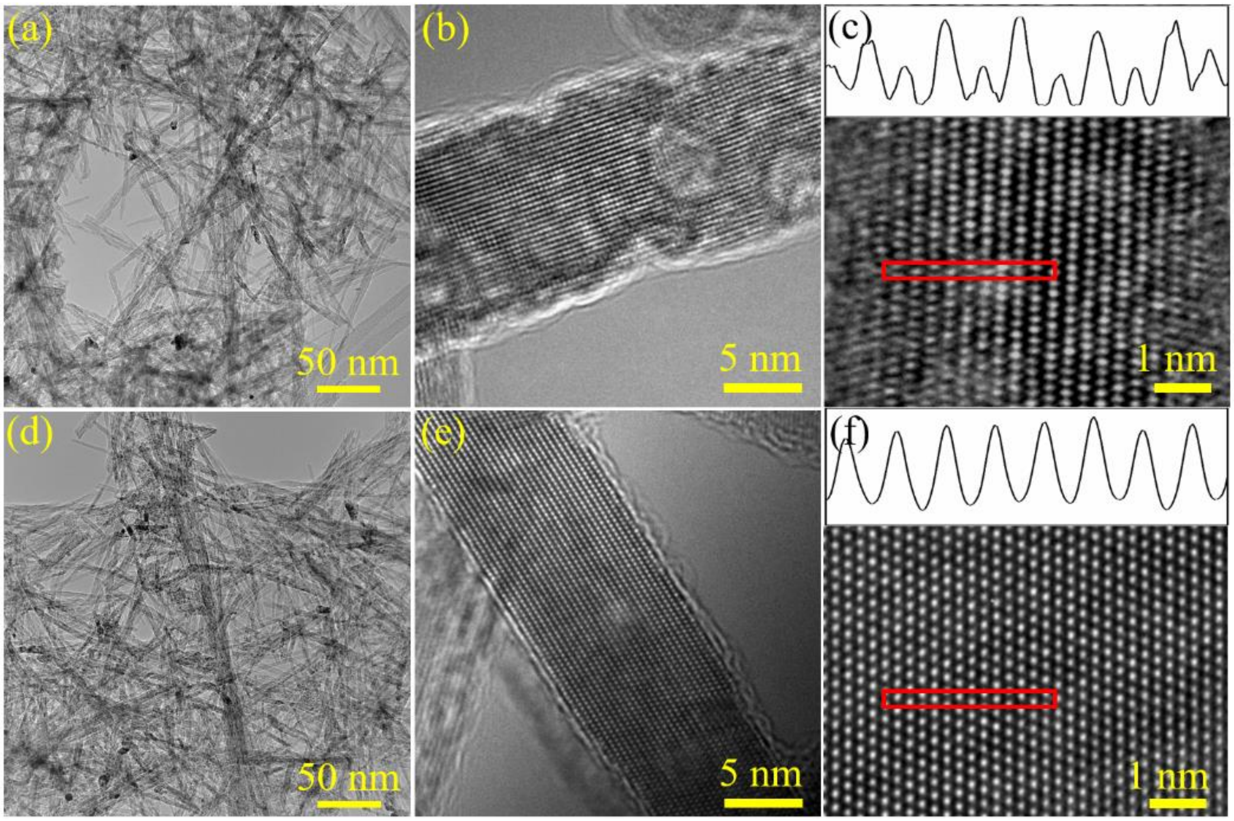

Figure 5.1 (a-b) High-resolution and (c) Atomic resolution TEM images of oxygen deficient rutile TiO_2 nanowires. (d-e) High-resolution and (f) Atomic resolution TEM images of stoichiometric rutile TiO_2 nanowires. Inset: Intensity profiles along the red box.

In a typical synthesis, Cl^- ions facilitates the nucleation sites and play a role as a coordination ligand in the oxidative dissolution process that could control the TiO_2 nanoparticle growth and oxidative etching respectively.[28, 30] Hence, carbothermal reduction of Ti-glycol complex in presence of ethylene glycol and chlorine ions results in the formation of high aspect ratio oxygen vacancy rutile TiO_2 nanowires. Stoichiometric TiO_2 and excess oxygen-vacancies ($TiO_{1.5}$) are also prepared through calcination of $TiO_{1.7}$ nanowires at 1000 °C (air) and 500 °C (Ar-H) respectively for electrochemical performance comparison.

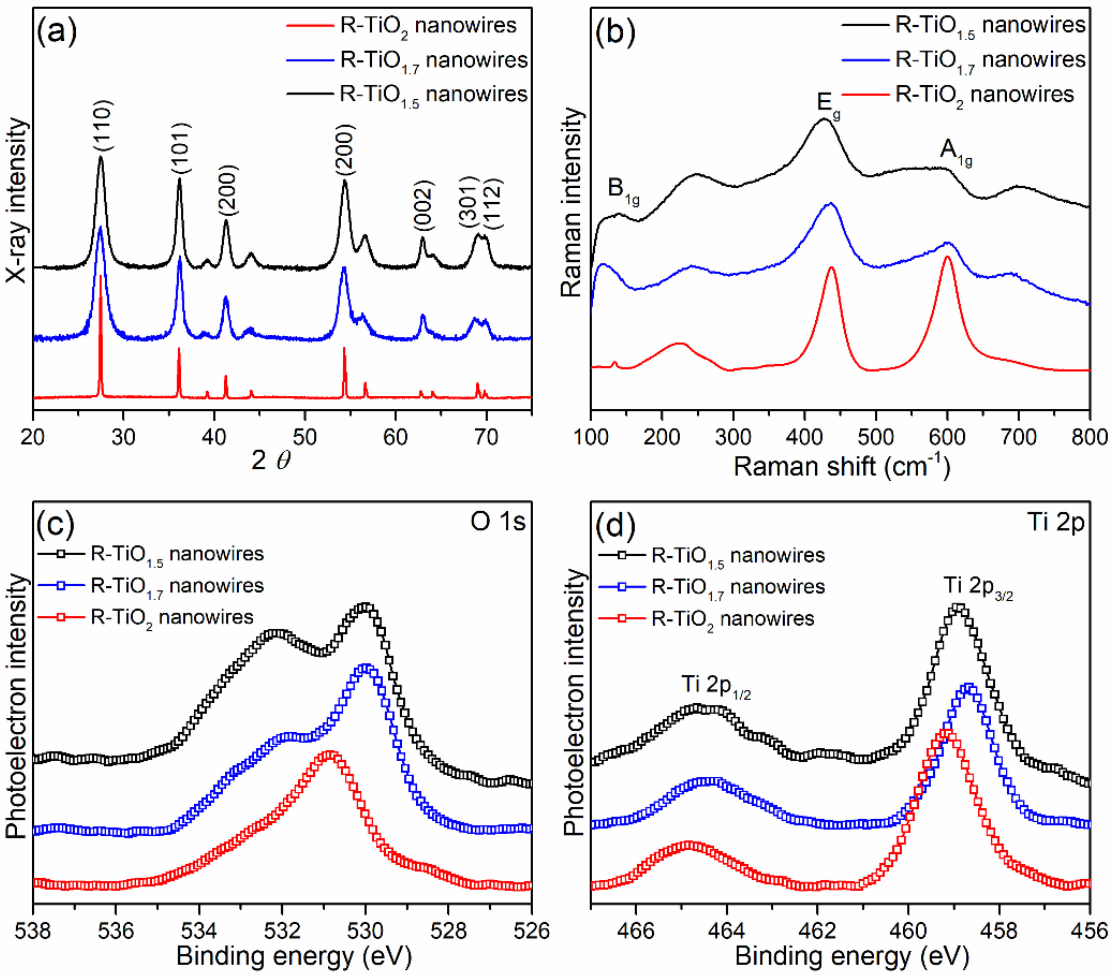

Figure 5.2 (a) X-ray diffraction pattern, and (b) Raman spectra of rutile TiO_2, $TiO_{1.7}$ and $TiO_{1.5}$ nanowires. High-resolution (c) O 1s, and (d) Ti 2p XPS spectra of rutile TiO_2, $TiO_{1.7}$ and $TiO_{1.5}$ nanowires.

Transmission electron microscopy (TEM) images at various magnifications validated the one-dimensional (1-D) nanowire morphology with ~6 nm diameter and ~100 nm length (Figure 5.1a and d). Presence of crystal structure defects in $TiO_{1.7}$ nanowires compared to TiO_2 nanowires are confirmed using high-resolution TEM images (Figure 5.1b and d). Interlayer spacing of 0.32 nm

(Figure 5.1c and f) in $TiO_{1.7}$ and TiO_2 nanowires correspond to (110) planes of rutile phase. These high-resolution STEM images revealed the presence of crystal structure disorderness caused by oxygen vacancies (Figure 5.1c) and stoichiometric pattern (Figure 5.1f) in rutile TiO_2 nanowire at the atomic scale. X-ray diffraction (XRD) pattern of different oxygen-deficient TiO_2 nanowires exhibited distinctive peaks corresponding to the rutile phase of TiO_2 (JCPDS card no. 88-1172) (Figure 5.2a).[31] Crystallinity of rutile TiO_2 nanowires increases with a decrease in concentration of oxygen vacancies. Raman spectroscopy is used for the additional compositional analysis of rutile TiO_2 nanowires. Raman spectra of TiO_2 nanowires with different oxygen vacancies (Figure 5.2b) are consistent with the active modes of pure rutile phase. Raman signals at 141.3, 445.9 and 608 cm^{-1} correspond to the B_{1g}, E_g and A_{1g} modes respectively.[32, 33] Presence of oxygen vacancies is evidenced from the change in full width at half maximum (FWHM) and band shift of A_{1g} and E_g symmetry modes respectively of rutile $TiO_{1.5}$ and $TiO_{1.7}$ compared to stoichiometric rutile TiO_2 nanowires.

X-ray photoelectron spectroscopy (XPS) further provided the quantification of oxygen vacancies in different compositions of rutile TiO_2 nanowires. High-resolution O 1s spectrum (Figure 5.2c) of rutile TiO_2 nanowires exhibited four distinct peaks corresponding to lattice oxygen (529.2 eV) and oxygen vacancies (531.4 eV).[34] Lower intensity peak at 532.4 and 533.4 eV represents chemisorbed oxygen surface adsorbed carbonate groups resulting from Ti-glycolate decomposition.[35, 36] Areal compositions of lattice oxygen and oxygen vacancy peaks (excluding peak overlaps) demonstrated ~20%, ~15%, and 0% oxygen deficiency of $TiO_{1.5}$, $TiO_{1.7}$, and $TiO_{1.2}$ nanowires respectively. High-resolution Ti 2p spectrum (Figure 5.2d) comprised of Ti $2p_{1/2}$ and Ti $2p_{3/2}$ components at 464.4 eV and 458.5 eV respectively for rutile $TiO_{1.7}$ nanowires.[37] Peaks at 458eV and 465eV of oxygen deficient rutile TiO_2 nanowires correspond to Ti^{3+} and Ti^{4+}

respectively. O 1s and Ti 2p spectrums experienced a peak shift to lower binding energies representing Ti^{4+} to Ti^{3+} conversion further confirming the presence of oxygen vacancies due to the reducing atmosphere caused by partial decomposition of ethylene glycol.[38, 39] Oxygen vacancies calculated from the areal comparison of Ti^{3+} to Ti^{4+} bands are in line with the values obtained from O 1s spectrum.

5.2.2. Electrochemical Performance of Oxygen Deficient Rutile TiO_2 Nanowires

Lithium-ion storage performance of oxygen-deficient rutile TiO_2 nanowire-based anodes are tested in a half-cell configuration in 0-3 V range. Galvanostatic rate performances of electrodes with various oxygen-deficiencies are performed to identify the optimum vacancy concentration (Figure 5.3a). It is clear that rutile $TiO_{1.7}$ nanowires electrode demonstrated excellent specific capacities and rate capability compared to rutile $TiO_{1.5}$ and TiO_2 nanowires. Low specific capacities and rate performance of rutile $TiO_{1.5}$ and TiO_2 nanowires are due to the sluggish Li-ion diffusion kinetics associated with TiO_2 based anodes.[40-42] Li-ion storage performance of rutile $TiO_{1.7}$ nanowires is significantly higher than rutile TiO_2 nanoparticles under similar experimental conditions (Appendix 12). As expected, rutile $TiO_{1.7}$, $TiO_{1.5}$, and TiO_2 nanowires experienced an initial cycle capacity loss due to solid-electrolyte interface (SEI) formation. Irreversible capacity loss can be further reduced with appropriate electrolyte additives or prelithiation strategies for the full-cell development. Rutile $TiO_{1.7}$ nanowire anodes delivered an extraordinary reversible capacity of 416 mAh g^{-1} compared to $TiO_{1.5}$ (201 mAh g^{-1}) and TiO_2 (80 mAh g^{-1}) at low current density of 50 mA g^{-1}. Rutile $TiO_{1.5}$ and TiO_2 nanowires exhibited very low specific capacities at higher current densities, which is typical in case of rutile TiO_2 based electrodes as reported earlier.[18, 43] While rutile $TiO_{1.7}$ nanowires retained a specific capacity of 95 mAh g^{-1} and 66 mAh g^{-1} even at very high current densities of 50 A g^{-1} and 100 A g^{-1} respectively. This electrode also retained a high reversible specific capacity of 380 mAh g^{-1} on lowering current density to 50 mA g^{-1}. It is also worth noting that the maximum specific capacity obtained by oxygen deficient rutile TiO_2 nanowires is even superior to the theoretical capacities of TiO_2 (335 mAh g^{-1}) and other TiO_2-based reports to date.[2, 15, 16, 44, 45]

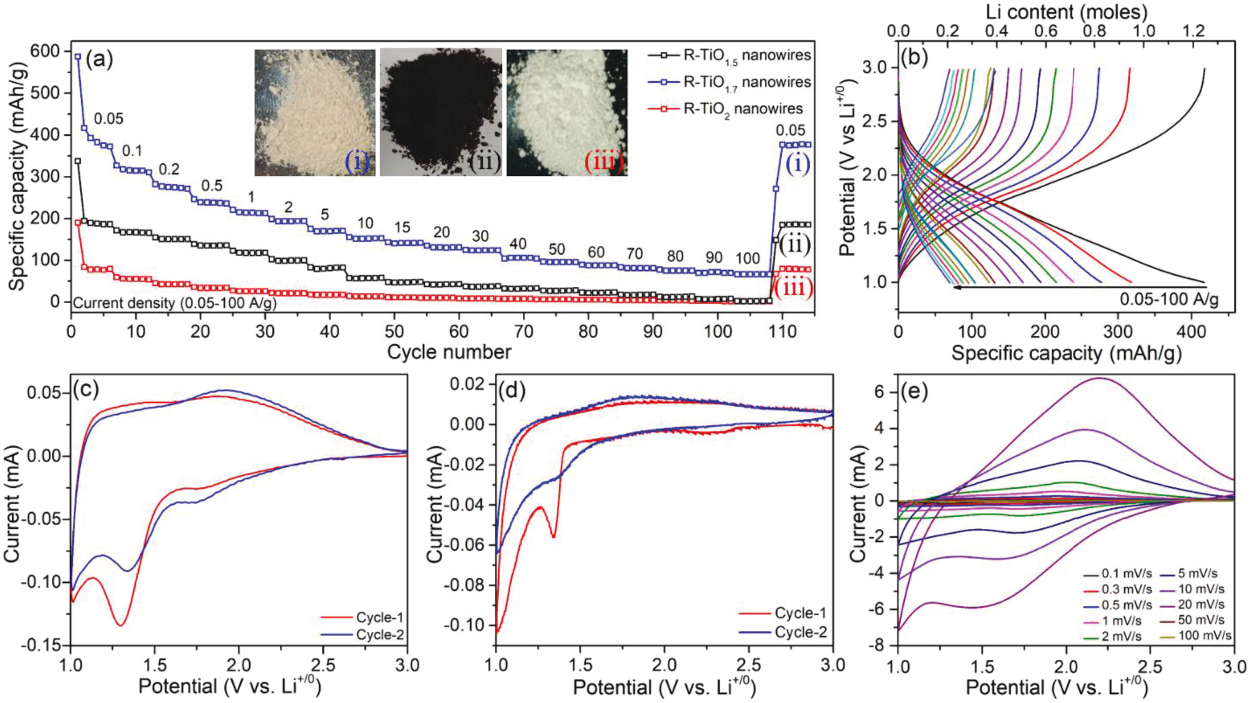

Figure 5.3 (a) Galvanostatic rate performance of rutile TiO_2, $TiO_{1.7}$ and $TiO_{1.5}$ nanowires. (b) Galvanostatic voltage profiles of rutile $TiO_{1.7}$ nanowires. Cyclic voltammograms of (c) rutile $TiO_{1.7}$ nanowires and (d) rutile TiO_2 nanowires at a scan rate of 0.1 mV s^{-1}. (e) Cyclic voltammograms of rutile $TiO_{1.7}$ nanowires at different scan rates.

Galvanostatic charge-discharge profiles of rutile $TiO_{1.7}$ nanowires at various current densities are displayed in figure 5.3b. Oxygen-deficient rutile TiO_2 electrodes exhibited slopping profile unlike the voltage profile of rutile TiO_2 nanoparticles (Appendix 13) that consist of a plateau below 1.5 V corresponding to intercalation mechanism. This signifies a diffusion independent Li-ion storage mechanism of $TiO_{1.7}$ electrodes, which dictate the specific capacity, rate performance and cycling stability. In the case of TiO_2 based anodes, discharge profile regions 3-1.5 V and 1.5-1 V correspond to the surface, and distinctive Li-ion intercalation mechanism respectively. Voltage profiles of rutile TiO_2 nanowires and nanoparticles based anodes varied considerably with current densities and only surface storage occurs at higher rates due to sluggish Li-ion diffusion. In contrast, voltage profiles of oxygen deficient rutile TiO_2 nanowires remain identical irrespective of the current densities, indicating similar Li-ion storage mechanism at various charge-discharge rates. Slopping voltage profiles is also indicative of diffusion independent pseudocapacitive type Li-ion storage. Coulombic efficiencies of these electrodes are remarkable (99.9%) demonstrating the complete reversibility of the Li-ion storage mechanism. Such a high coulombic efficiency is one of the crucial requirements for developing Li-ion full-cells.[46]

Cyclic voltammetry (CV) of oxygen deficient rutile TiO_2 nanowires (Figure 5.3c) are performed at 0.1 mV s^{-1} scan rate in a voltage range of 1-3 V for the detailed investigation of Li-ion intercalation process. In the case of rutile $TiO_{1.7}$ nanowires, peak at 1.7 V of the first cathodic scan correspond to the surface Li-ion storage on nanowires. Broad cathodic signal around 1.3 V represent Li-ion intercalation reaction of $TiO_{1.7}$ ($TiO_{1.7} + xLi^+ + xe^- \rightarrow Li_xTiO_{1.7}$) and solid electrolyte interface (SEI) formation. These cathodic responses are in good agreement with the sloping galvanostatic voltage profiles and irreversible capacity loss. Reduced cathodic peak intensity at 1.3 V and shifting of second cycle cathodic signal towards higher potentials signify complete SEI formation in the first cycle. Lithium-ion deintercalation reactions of $TiO_{1.7}$ are evident from the broad anodic signal at 1.9 V. Although anodic and cathodic signals of stoichiometric rutile TiO_2 nanowires are similar at slightly different potentials, voltage hysteresis and current response in the second scan are inferior to oxygen deficient rutile TiO_2 electrodes. Such a low performance of stoichiometric rutile TiO_2 compared to oxygen deficient rutile TiO_2 nanowire electrodes is also evident from the galvanostatic rate performance and charge-discharge profiles at various current densities. Moreover, rectangular shape of CV curve in the lower potential range of oxygen deficient rutile TiO_2 indicates additional capacitive Li-ion storage contribution. It is thus clear that the lithium-ion storage mechanism of rutile $TiO_{1.7}$ nanowires is marginally different from the rutile TiO_2 nanowires and rutile TiO_2 based anodes reported earlier.[2, 37, 47]

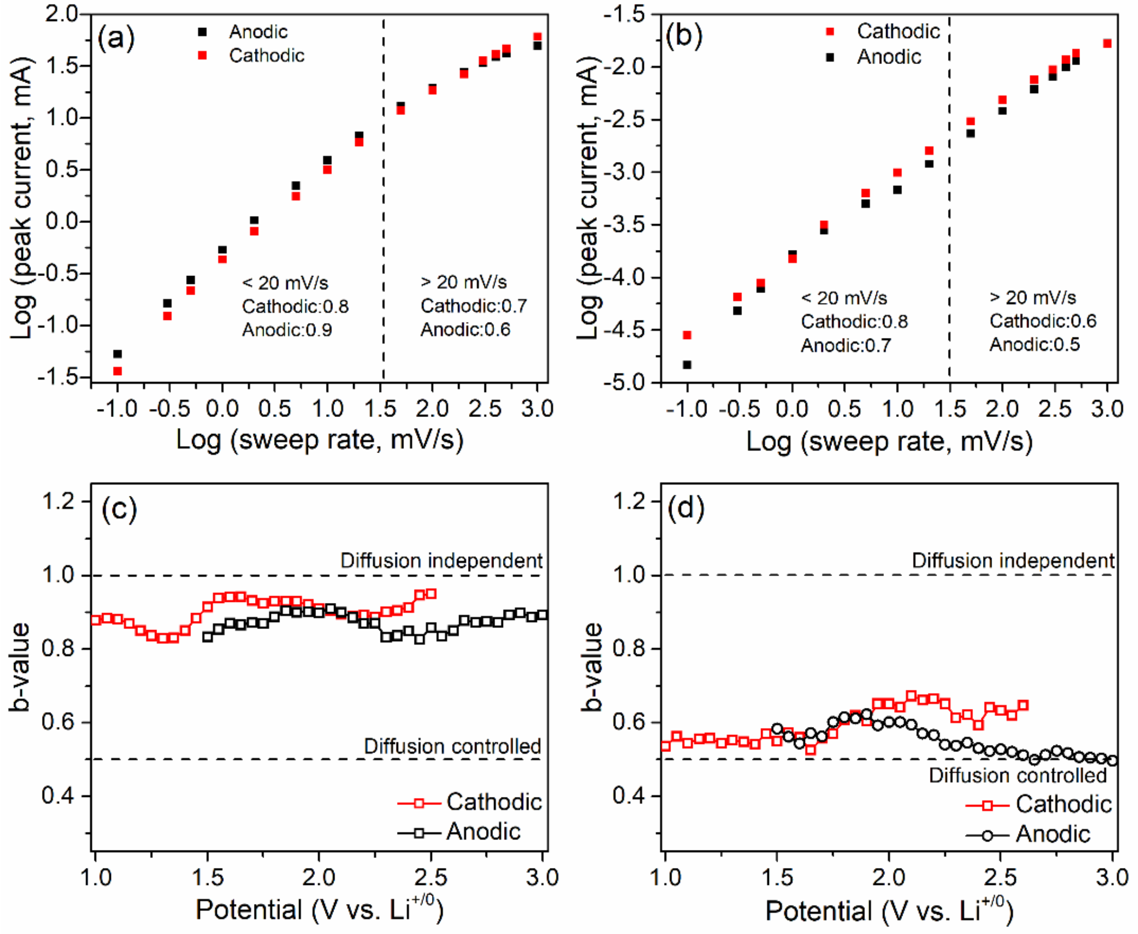

Figure 5.4 Scan rate dependence of peak current density of (a) rutile $TiO_{1.7}$ nanowires and (b) rutile TiO_2 nanowires. Anodic and cathodic *b*-values of (c) rutile $TiO_{1.7}$ nanowires and (d) rutile TiO_2 nanowires at different state of charge.

Quantitative investigation of pseudocapacitive Li-ion storage mechanism is performed by collecting cyclic voltammetry of rutile $TiO_{1.7}$ nanowires at different scan rates (Figure 5.3e).

Linear dependence of both anodic and cathodic peak current intensities with scan rate signifies the dominant pseudocapacitive type charge storage in this case. Relation between anodic and cathodic peak current to scan rates can be represented by the power-law (i=av^b) equation, where i is the output current (mA), a and b are arbitrary constants, and v is the scan rate (mV s^{-1}). Typically, parameter b determines the nature of charge storage representing pseudocapacitive charge storage for b=1 and diffusion-controlled process for b=0.5.

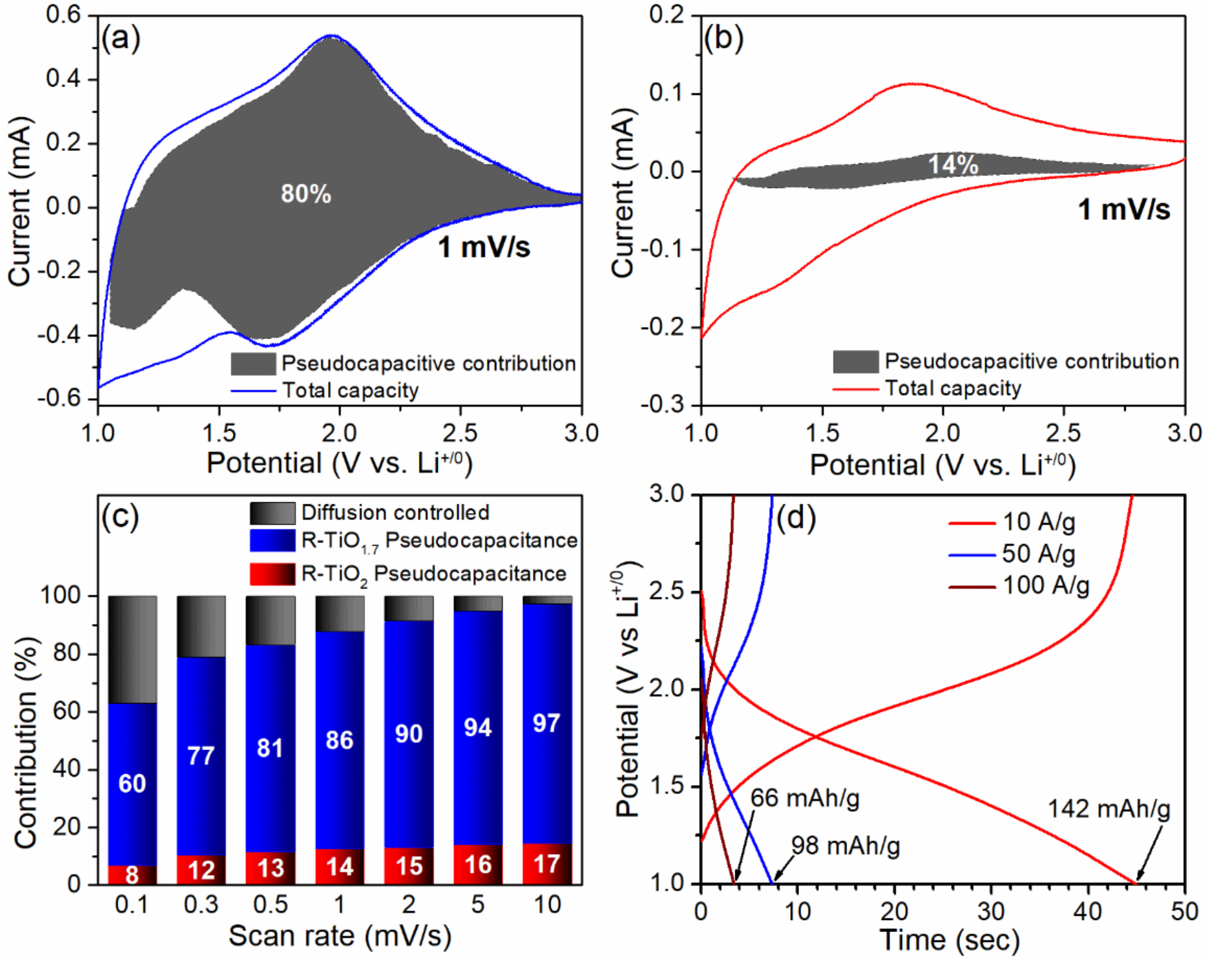

Figure 5.5 Cyclic voltammograms of (a) rutile $TiO_{1.7}$ nanowires and (b) rutile TiO_2 nanowires at 1 mV s^{-1} scan rate. Shaded regions represent pseudocapacitive current contribution. (c) Pseudocapacitive and diffusion-dependent capacity contributions of rutile $TiO_{1.7}$ and TiO_2 nanowires at different scan rates. (d) Charge-discharge time interval of rutile $TiO_{1.7}$ nanowire anodes at various current densities in a Li-ion half-cell configuration.

Anodic and cathodic b-values for oxygen deficient and stoichiometric rutile TiO_2 nanowires are obtained from log (*i*) vs log (*v*) plots (Figure 5.4a and b). In scan range of 0.1-20 mV s^{-1}, oxygen deficient rutile TiO_2 nanowires demonstrated b-values of 0.8 and 0.9 for cathodic and anodic peaks respectively signifying that the current response is surface controlled (diffusion-independent) and thus dominant pseudocapacitive Li-ion storage. While stoichiometric rutile TiO_2 nanowires exhibited 0.8 and 0.7 in 0.1-20 mV s^{-1} scan rate and reduced to 0.6 and 0.5 in sweep rates >20 mV s^{-1} respectively, indicating that the charge storage is mostly diffusion-dependent. In the case of oxygen deficient rutile TiO_2, b-values decreased to 0.7 and 0.6, respectively with an increase of scan rates to 20-1000 mV s^{-1} due to the diffusion constraints and ohmic resistances at higher rates.[18] Anodic and cathodic b-values further provided details of potential-dependent Li-ion storage mechanism. Both oxygen deficient and stoichiometric rutile TiO_2 nanowires exhibited b-values in 0.5-1.0 range that is characteristic of combined pseudocapacitive and diffusion-limited process (Figure 5.4c and d). Li-ion intercalation (cathodic process) and de-intercalation (anodic process) of oxygen deficient rutile TiO_2 nanowires is mostly pseudocapacitive with the highest b-values in the voltage range of 2.5-1.5 V and 2.0-3.0 V respectively. On the other hand, lithiation and delithiation of stoichiometric rutile TiO_2 is highly dominated by diffusion-controlled process over a wide voltage window. This is a clear indication of oxygen vacancy induced pseudocapacitive Li-ion storage process in rutile $TiO_{1.7}$ nanowires.

Pseudocapacitive charge storage and diffusion-dependent intercalation process are further distinguished using equation 2.5 (Figure 5.5a and b).[17] Oxygen deficient rutile TiO_2 nanowires demonstrated ~6-fold higher pseudocapacitance (80%) than stoichiometric rutile TiO_2 nanowires (14%) at 1 mV s^{-1} scan rate. Diffusion-independent pseudocapacitive Li-ion storage in rutile $TiO_{1.7}$ nanowires dominated at higher scan rates with a maximum contribution of 97% at 10 mV s^{-1}

(Figure 5.5c). This is in line with the improved rate performance, high specific capacities, and slopping voltage profiles observed at higher current densities. Diffusion-dependent capacity contribution in case of rutile TiO_2 based anodes is expected to be low due to the well-known sluggish kinetics of TiO_2 anodes at higher rates. This is also verified by the lower pseudocapacitive contributions of rutile TiO_2 nanowires compared to rutile $TiO_{1.7}$ nanowires at various scan rates. Hence, pseudocapacitive Li-ion storage demonstrated by oxygen deficient rutile TiO_2 nanowires is substantially higher than the values previously reported for TiO_2 and graphite anodes. Increased pseudocapacitive Li-ion diffusion is beneficial for achieving fast charging ultra-long cycling stability due to the minimal structural changes and faster Li-ion diffusion. This is further confirmed by the fast charging and discharging intervals (Figure 5.5d) of oxygen deficient rutile TiO_2 nanowire electrodes at very high current densities.

Galvanostatic cycling performance of oxygen deficient rutile TiO_2 nanowire anode (Figure 5.6a) are also superior to most of the promising high performance TiO_2 nanostructures reported previously. For instance, rutile $TiO_{1.7}$ nanowires achieved extremely stable reversible specific capacities of 187 mAh g^{-1} (89% of initial capacity) and 142 mAh g^{-1} (99% of initial capacity) after 10,000 cycles at a high current density of 1 A g^{-1} and 10 A g^{-1} respectively. Even at an extremely high current density of 50 A g^{-1} (~150 C where 1C=335 mA g^{-1}), rutile $TiO_{1.7}$ nanowires retained 88 mAh g^{-1} (92% of the initial capacity) after 30,000 charge-discharge cycles. Charge process in this case could be completed within 43 s and ~8 s while attaining a relatively high specific capacity of 142 mAh g^{-1} and 98 mAh g^{-1} at 10 and 50 A g^{-1} respectively. Coulombic efficiency on extended cycling is also excellent (~100%) at a current density of 50 A g^{-1}. Charge-discharge profiles of rutile $TiO_{1.7}$ nanowires at various stages of extended cycling exhibited identical curves signifying the excellent reversibility and consistent Li-ion storage mechanism (Figure 5.6b). Ultrafast charging exhibited by this electrode with extreme long cycle life is superior to conventional state-of-the-art battery anodes, $Li_4Ti_5O_{12}$, TiO_2 based anodes, and other conversion type materials for LIBs. It is worth noting that commonly used electrolyte additives such as vinylene carbonate (VC) or fluoroethylene carbonate (FEC) are not used for rutile TiO_2 based anodes, demonstrating its ability to work in commercial electrolyte solution.

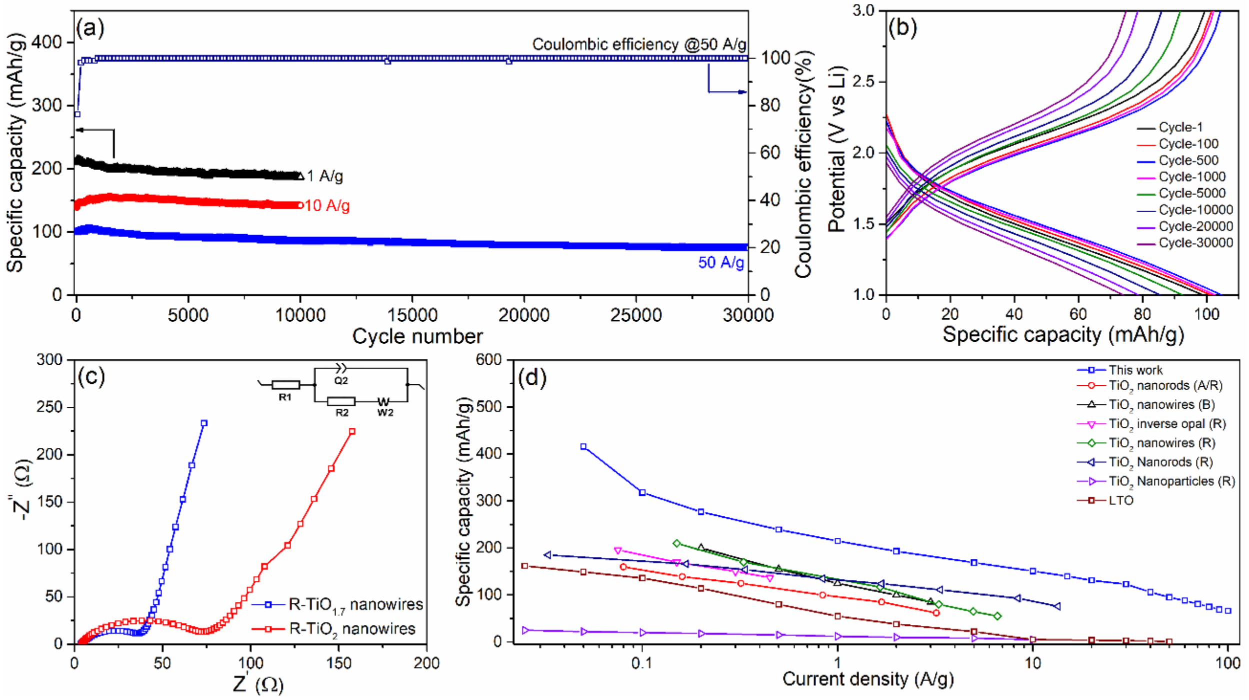

Figure 5.6 (a) Galvanostatic cycling for rutile $TiO_{1.7}$ nanowires at a current density of 1, 10 and 50 A g^{-1}. (b) Galvanostatic voltage profiles of rutile $TiO_{1.7}$ nanowires correspond to various galvanostatic cycles at a current density of 50 A g^{-1}. (c) Nyquist plots of rutile $TiO_{1.7}$ and TiO_2 nanowires. Inset: Randles equivalent circuit used for fitting the EIS pattern. (d) Li-ion storage performance comparison of rutile $TiO_{1.7}$ nanowires with other TiO_2 based anodes reported earlier.

Electrochemical impedance spectroscopy (EIS) measurements are performed to investigate the Li-ion diffusion kinetics of rutile TiO_2 based electrodes (Figure 5.6c). Nyquist plots of TiO_2-based electrodes composed of a low-frequency slopping line and high-frequency semicircle representing solid-state diffusion (Z_w) and charge-transfer resistance (R_{ct}) respectively. Fitting of the Nyquist plots to the equivalent circuit (Figure 5.6c inset) revealed charge transfer resistances of 37 Ω and 73 Ω for rutile $TiO_{1.7}$ and TiO_2 nanowires respectively. Lower charge transfer resistance in the case of rutile $TiO_{1.7}$ nanowires compared to rutile TiO_2 nanowires can be related to the crystal structure disorderness and 1 D microstructure that allows superior contact with the electrolyte solution. Lithium-ion diffusion coefficients calculated from Warburg impedance (equation 2.10) are 1×10^{-14} cm^2 s^{-1} and 2×10^{-15} cm^2 s^{-1} for rutile $TiO_{1.7}$ and TiO_2 nanowires respectively. Such a higher Li-diffusion coefficient of rutile $TiO_{1.7}$ anode is vital for achieving excellent pseudocapacitive performance. These values further validated the strong dependence of oxygen vacancies on Li-ion diffusion kinetics, specific capacities, and pseudocapacitance. Specific capacities of rutile $TiO_{1.7}$ nanowire anodes at various current densities are substantially superior to the values reported in the literature (Figure 5.6d). Moreover, ultra-long cycling stability of oxygen deficient rutile TiO_2 nanowires anode at higher rates is also superior to any of the lithium-ion battery anodes reported to date.[2, 44, 47-51]

In-situ XRD and post-cycling *ex-situ* TEM analysis are performed to investigate the structural and morphological changes during the charge-discharge process of rutile $TiO_{1.7}$ and rutile TiO_2 nanowire anodes. X-ray diffraction patterns of stoichiometric rutile TiO_2 nanowire electrodes at various state of charge (Figure 5.7a) displayed no significant change in the peak at 27.4° during the charge-discharge process. While in case of rutile $TiO_{1.7}$ anodes (Figure 5.7b), characteristic peak intensity gradually decreased on discharge to 1 V and partially appears with a slight shift during charging to 3V. Controlled *in-situ* XRD experiments of rutile $TiO_{1.7}$ nanowire anodes (Appendix 14) after initial charge-discharge cycle confirmed the irreversible crystalline-amorphous transformation due to Li-ion intercalation. This is further verified by the crystalline to amorphous transformation during discharge-charge process evidenced from high-resolution TEM images (Figure 5.7c-e). Moreover, oxygen deficient rutile TiO_2 nanowires also displayed reversible color change during lithiation-delithiation process. Blue coloured TiO_2 powder obtained after complete discharge to 1 V is distinctive of Ti^{3+} formation during lithiation. Loss of crystallinity to amorphous and Ti^{4+} reduction during discharge are not identified previously in the case of rutile TiO_2 anodes due to limited Li-ion intercalation.

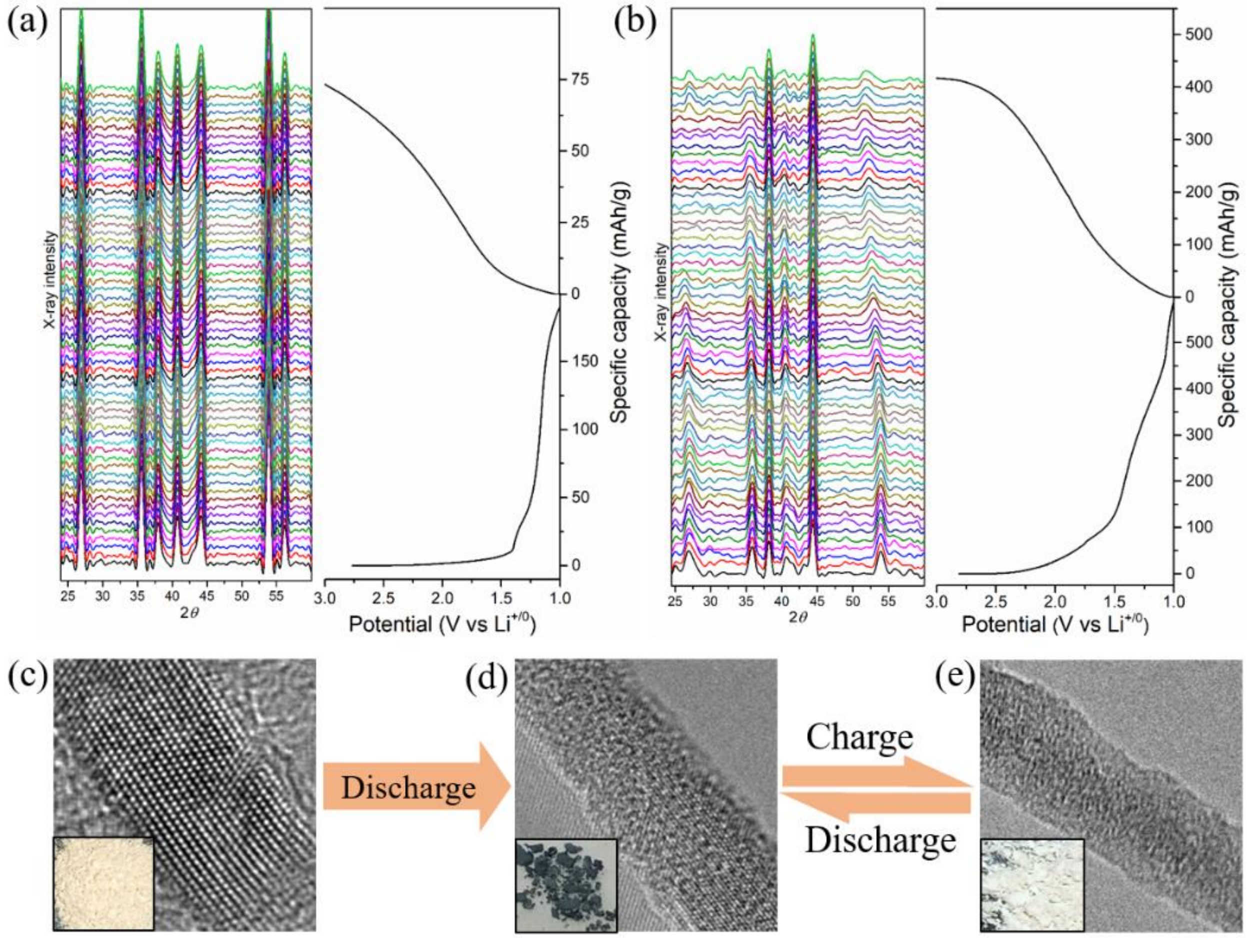

Figure 5.7 *In-situ* XRD patterns of (a) stoichiometric rutile TiO_2 nanowires, and (b) rutile $TiO_{1.7}$ nanowires and corresponding charge-discharge voltage profile in the voltage range 3.0-1.0 V. (c-e) High-resolution TEM images of rutile $TiO_{1.7}$ nanowires at different state of charge. Inset: Photographs of Pristine, discharged and charged rutile $TiO_{1.7}$ nanowires.

It is thus clear that Li-ion storage occurs through a pseudocapacitive type intercalation process resulting from oxygen vacancies. Moreover, excellent morphology retention after 10,000 discharge/charge cycles of rutile $TiO_{1.7}$ nanowires is further evidenced by *ex-situ* TEM analysis (Figure 5.8a and b). EDX elemental mapping of a cycled anode (Figure 5.8c-g) demonstrated the homogenous distribution of Ti, and O confirming its compositional homogeneity. Presence of P and F components designate the existence of a uniform SEI, which is vital for achieving stable electrochemical performance.

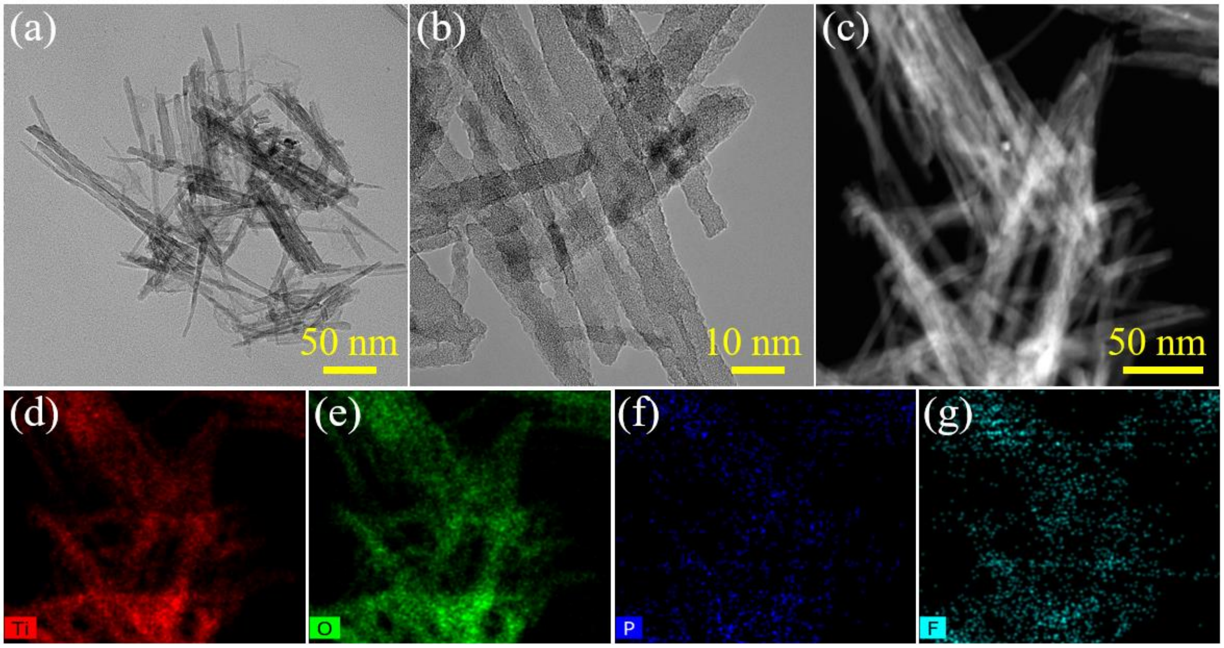

Figure 5.8 (a-b) *Ex-situ* high-resolution TEM images at various magnifications, (c) HAADF image, and (d-g) corresponding EDX elemental mapping of rutile $TiO_{1.7}$ nanowires after 10,000 charge-discharge cycles at a current density of 1 A g^{-1}.

Outstanding Li-ion storage performance of oxygen-deficient rutile TiO_2 nanowires anode can be credited to its unique physiochemical properties including oxygen vacancies, and one-dimensional morphology. Diffusion independent pseudocapacitive Li-ion intercalation into oxygen deficient rutile TiO_2 lattice caused high-rate performance and ultra-long cycling stability. Crystal structure disorderness caused by oxygen vacancies provided additional pathways for ultrafast pseudocapacitive Li-ion intercalation. Additionally, oxygen vacancies also facilitated crystalline to amorphous transition of rutile $TiO_{1.7}$ nanowires during Li-ion intercalation. Moreover, one-dimensional microstructure, mesoporosity, and high-aspect-ratio nanowire acts as secondary factors for improving the ultra-long cycling stability and electrochemical performance through an anisotropic path for faster Li-ion diffusion. In conclusion, oxygen vacancy-induced pseudocapacitive Li-ion storage of rutile $TiO_{1.7}$ nanowires makes it an excellent anode material for next-generation high energy density ultralong-life fast charging Li-ion batteries.

Finally, we employed rutile $TiO_{1.7}$ nanowire anodes in a lithium-ion full-cell with commercial $LiNiMnCoO_2$ cathodes (rate performance and cycling stability provided in appendix 6) and 1M $LiPF_6$-EC/EMC electrolyte solution (Figure 5.9a). Rutile $TiO_{1.7}$ nanowires‖$LiNiMnCoO_2$ full-cell exhibited a high reversible specific capacity of 162 mAh g^{-1} at a high current density of 1 A g^{-1} (based on anode mass) in the potential window of 2.4-3.7 V (Figure 5.9b). Galvanostatic cycling stability of rutile $TiO_{1.7}$ nanowires‖$LiNiMnCoO_2$ full-cell is also excellent, retaining 81% of the initial capacity after 2500 charge-discharge cycles. On the other hand, stoichiometric rutile TiO_2‖$LiNiMnCoO_2$ full-cell displayed a poor electrochemical performance with an initial capacity of 65 mAh g^{-1} at 1 A g^{-1} current density (based on anode weight) and failed after 200 cycles. It should be noted that the specific capacities obtained for rutile $TiO_{1.7}$‖$LiNiMnCoO_2$ are 2.5-fold and 1.5-fold higher than rutile TiO_2 and conventional graphite anodes in full-cell configuration respectively under similar experimental conditions. Graphite‖$LiNiMnCoO_2$ full-cell revealed low cycling stability with 78% capacity retention after 200 cycles and a good coulombic efficiency of 99.7% (Appendix 7a). Current density used in this case is notably higher than previous reports of Li-ion full-cells based on graphite and other conversion/ alloying type anodes.[52]

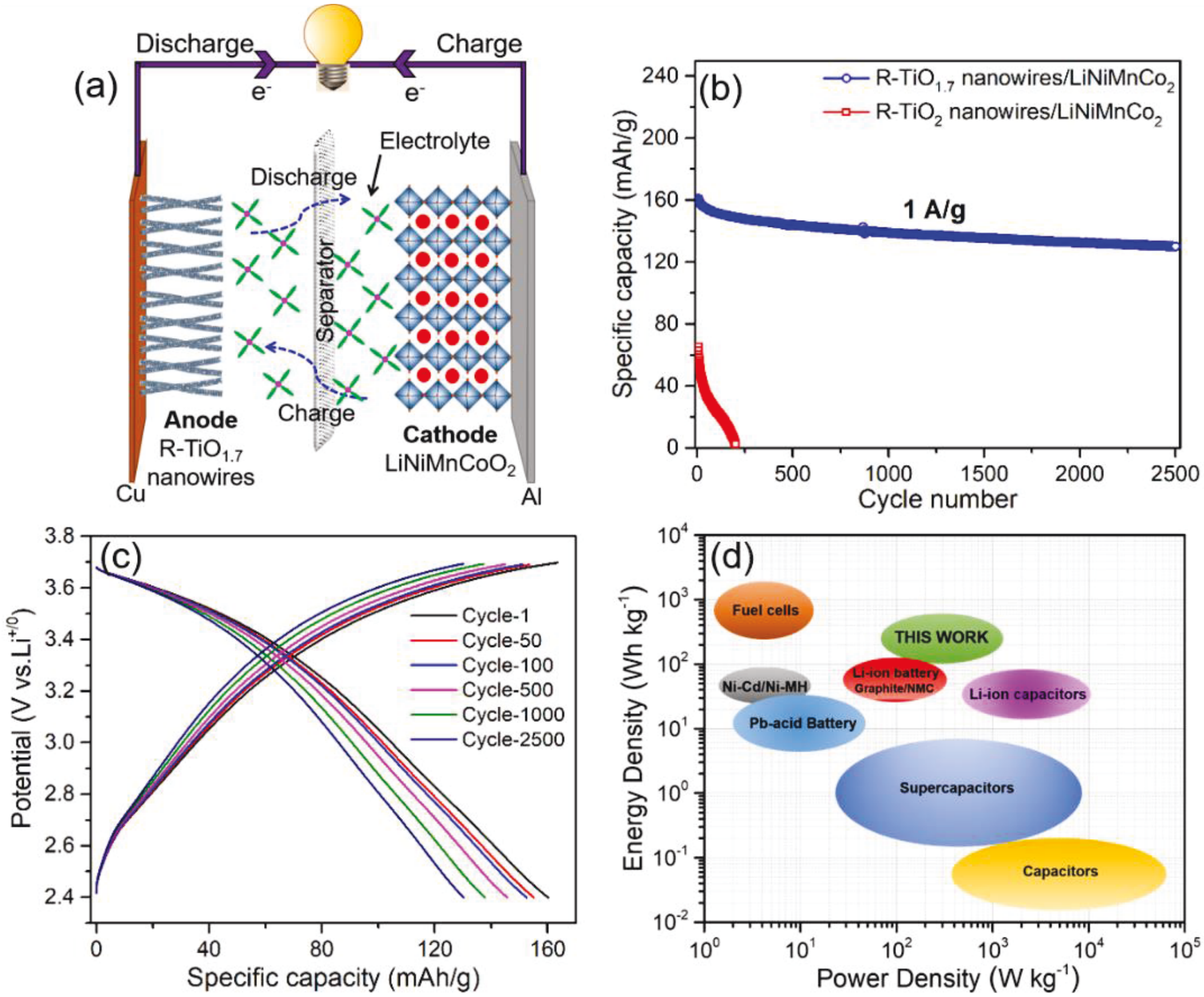

Figure 5.9 (a) Schematic of Li-ion full-cell containing rutile $TiO_{1.7}$ nanowire anode and $LiNiMnCoO_2$ cathode. (b) Galvanostatic cycling performance of rutile $TiO_{1.7}$ nanowires ‖ $LiNiMnCoO_2$ and rutile TiO_2 nanowires ‖ $LiNiMnCoO_2$ full-cells at a current density of 1 A g^{-1} after 5 cycles at a current density of 100 mA g^{-1}. Specific capacities and current densities are calculated based on the anode weight. (c) Galvanostatic charge-discharge profiles of rutile $TiO_{1.7}$ nanowires ‖ $LiNiMnCoO_2$ full-cell at a current density of 1 A g^{-1}. (d) Ragone plot of rutile $TiO_{1.7}$ nanowires ‖ $LiNiMnCoO_2$ Li-ion full-cell and other relevant energy storage devices.

Galvanostatic charge-discharge profiles of rutile $TiO_{1.7}$ ‖ $LiNiMnCoO_2$ full-cell (Figure 5.9c) demonstrated slopping behaviour that is distinctive of pseudocapacitive Li-ion storage unlike the diffusion-limited behaviour of graphite ‖ $LiNiMnCoO_2$ system (Appendix 7b). It is thus clear that the oxygen vacancy induced pseudocapacitance of rutile TiO_2 nanowires resulted in diffusion independent Li-ion storage behaviour of full-cell, which is beneficial for achieving high energy and power density. Operating potential of rutile $TiO_{1.7}$ ‖ $LiNiMnCoO_2$ full-cell (~3.3 V @ 1 A g^{-1}) is comparable to those of secondary graphite ‖ $LiNiMnCoO_2$ (3.8 V @ 1 A g^{-1}). Energy and power density of rutile $TiO_{1.7}$ ‖ $LiNiMnCoO_2$ full-cell are 350 Wh kg^{-1} and 2 kW kg^{-1} respectively (based on anode and cathode mass). On the other hand, graphite ‖ $LiNiMnCoO_2$ full-cell achieved energy and power densities of only 140 Wh kg^{-1} and 420 W kg^{-1} under similar electrochemical testing conditions. This 2-fold higher energy density and 5-fold power densities of rutile $TiO_{1.7}$ ‖ $LiNiMnCoO_2$ full-cells are particularly attractive for applications demanding high energy density and fast charging such as electric vehicles and power grids. Energy and power densities exhibited in this case are considerably higher than previously reported Li-ion full-cells based on intercalation, conversion and alloying type anodes.[1, 47, 53, 54] Moreover, power density of this full-cell is even on par with the lithium-ion capacitors and supercapacitors (Figure 5.9d). It is also worth noting that energy and power density of the demonstrated full-cells are limited by the use of $LiNiMnCoO_2$ cathodes. Hence, additional research in the area of high energy/ power density cathodes are necessary to exploit the full-potential of pseudocapacitive anodes. Electrochemical performance of the demonstrated oxygen deficient rutile TiO_2 nanowires in Li-ion full-cells could be further improved by optimization of cell balancing, electrode thickness, voltage window, and charge-discharge protocols.

5.3 Conclusion

In summary, we demonstrated high energy and power density rechargeable lithium-ion batteries based on highly pseudocapacitive oxygen deficient rutile TiO_2 nanowire anodes. This electrode exhibited outstanding specific capacities, cycling stability, and rate performance compared to conventional TiO_2 based anodes reported earlier. Exceptional Li-ion storage performance of rutile $TiO_{1.7}$ nanowires is credited to the extreme Li-ion intercalation pseudocapacitance. Crystal structure disorderness caused by oxygen vacancies provided additional pathways for ultrafast pseudocapacitive Li-ion intercalation. Additionally, oxygen vacancies also facilitated crystalline to amorphous transition of rutile $TiO_{1.7}$ nanowires during Li-ion intercalation. Hence, tremendous pseudocapacitance enhanced electrochemical performance of oxygen deficient rutile TiO_2 nanowires makes it a potential candidate for the next-generation high energy density and fast-charging and ultra-long-life lithium-ion batteries.

5.4 References

1. M. Madian, A. Eychmüller and L. Giebeler, *Batteries*, **2018**, 4, 7.
2. D. McNulty, E. Carroll and C. O'Dwyer, *Adv. Energy Mater*, **2017**, 7, 1602291.
3. Y. Zhang, Y. Tang, W. Li and X. Chen, *ChemNanoMat*, **2016**, 2, 764-775.
4. M. Armand and J. M. Tarascon, *Nature*, **2008**, 451, 652-657.
5. I. Belharouak, Y.-K. Sun, W. Lu and K. Amine, *J. Electrochem. Soc.*, **2007**, 154, A1083-A1087.
6. V. Etacheri, J. E. Yourey and B. M. Bartlett, *ACS Nano*, **2014**, 8, 1491-1499.
7. L. Kavan, M. Zukalová, M. Kalbáč and M. Graetzel, *J. Electrochem. Soc.* , **2004**, 151, A1301.
8. J. Zheng, L. Liu, G. Ji, Q. Yang, L. Zheng and J. Zhang, *ACS Appl. Mater. Interfaces*, **2016**, 8, 20074-20081.
9. Y. Tang, Y. Zhang, J. Deng, J. Wei, H. L. Tam, B. K. Chandran, Z. Dong, Z. Chen and X. Chen, *Adv. Mater.*, **2014**, 26, 6111-6118.
10. M. V.Koudriachova, N. M.Harrison and S. W. d. Leeuw, *Solid State Ion.*, **2003**, 157, 35-38.
11. B.Zachau-Christiansen, K.West, T.Jacobsen and S.Atlung, *Solid State Ion.*, **1988**, 28-30, 1176-1182.
12. P. G. Bruce, B. Scrosati and J.-M. Tarascon, *Angew. Chem., Int. Ed.*, **2008**, 47, 2930-2946.
13. Z. Yang, D. Choi, S. Kerisit, K. M.Rosso, D. Wang, J. Zhang, G. Graff and J. Liu, *J. Power Sources*, **2009**, 192, 588-598.

14. T. Lan, H. Qiu, F. Xie, J. Yang and M. Wei, *Sci. Rep.*, **2015**, 5, 8498.

15. Y. Gan, L. Zhu, H. Qin, Y. Xia, H. Xiao, L. Xu, L. Ruan, C. Liang, X. Tao, H. Huang and W. Zhang, *Solid State Ion.*, **2015**, 269, 44-50.

16. H. Qiao, Y. Wang, L. Xiao and L. Zhang, *Electrochem. Commun.* , **2008**, 10, 1280-1283.

17. V. Augustyn, P. Simon and B. Dunn, *Energy Environ. Sci.*, **2014**, 7 1597-1614

18. Y. Jiang, Y. Li, P. Zhou, Z. Lan, Y. Lu, C. Wu and M. Yan, *Adv. Mater.*, **2017**, 29.

19. N. Wang, Y. Wang, X. Xu, T. Liao, Y. Du, Z. Bai and S. Dou, *ACS Appl. Mater. Interfaces*, **2018**, 10, 9353-9361.

20. S. Lou, X. Cheng, J. Gao, Q. Li, L. Wang, Y. Cao, Y. Ma, P. Zuo, Y. Gao, C. Du, H. Huo and G. Yin, *Energy Storage Materials*, **2018**, 11, 57-66.

21. S. Lou, X. Cheng, Y. Zhao, A. Lushington, J. Gao, Q. Li, P. Zuo, B. Wang, Y. Gao, YulinMa, C. Du, G. Yin and X. Sun, *Nano Energy*, **2017**, 34, 15-25.

22. V. Augustyn, J. Come, M. A. Lowe, J. Kim, P.-L. Taberna, S. H. Tolbert, H. D. Abruña, P. Simon and B. Dunn, *Nat. Mater.*, **2013**, 12, 518-522.

23. S. Huang, L. Zhang, X. Lu, L. Liu, L. Liu, X. Sun, Y. Yin, S. Oswald, Z. Zou, F. Ding and O. G. Schmidt, *ACS Nano*, **2017**, 11, 821-830.

24. J. Wang, J. Polleux, J. Lim and B. Dunn, *J. Phys. Chem. C* **2007**, 111, 14925-14931.

25. H.-S. Kim, J. B. Cook, H. Lin, J. S. Ko, S. H. Tolbert, V. Ozolins and B. Dunn, *Nat. Mater.*, **2016**, 16, 454-460.

26. J. T. Mefford, W. G. Hardin, S. Dai, K. P. Johnston and K. J. Stevenson, *Nat. Mater.*, **2014**, 13, 726-732.

27. J. Zhang, H. Jiang, Y. Zenga, Y. Zhang and H. Guo, *J. Power Sources*, **2019**, 439, 227026.

28. A. Amirjania, P. Marashi and D. H. Fatmehsari, *Colloid surf. A-physicochem. Eng. Asp*, **2014**, 444, 33-39.

29. L. R. Shobin and S. Manivannan, *Electron. Mater. Lett.* , **2014**, 10, 1027-1031.

30. B. Wiley, T. Herricks, Y. Sun and Y. Xia, *Nano Letters* **2004**, 4, 1733-1739.

31. H. Xu and L. Zhang, *J. Phys. Chem. C* **2009**, 113, 1785-1790.

32. M. Ocaña, J. V. Garcia-Ramos and C. J. Serna, *J. Am. Chem. Soc.*, **1992**, 75, 2010-2012.

33. Q. Gao, X. Wu, Y. Fan and X. Zhou, *Appl. Surf. Sci.*, **2014**, 289, 281-288.

34. A. Ghobadi, T. G. Ulusoy, R. Garifullin, M. O. Guler and A. K. Okyay, *Sci. Rep.*, **2016**, 6, 30587.

35. M. Cargnello, T. R. Gordon and C. B. Murray, *Chem. Rev.* , **2014**, 114, 9319-9345.

36. L.-Q. Wang, D.R.Baer, M.H.Engelhard and A.N.Shultz, *Surf. Sci.*, **1995**, 344, 237-250.

37. J. Chen, W. Song, H. Hou, Y. Zhang, M. Jing, X. Jia and X. Ji, *Adv. Funct. Mater.*, **2015**, 25, 6793-6801.

38. V. Etacheri, M. K. Seery, S. J. Hinder and S. C. Pillai, *Inorg. Chem.* , **2012**, 51, 7164-7173.

39. S. B. Amor, G. Baud, M. Benmalek, H. Dunlop, R. Frier and M. Jacquet, *J. Adhes.*, **1998**, 65, 307-329.

40. D. Liu, P. Xiao, Y. Zhang, B. B. Garcia, Q. Zhang, Q. Guo, R. Champion and G. Cao, *J. Phys. Chem. C* **2008**, 112, 11175-11180.

41. L. Liu, Q. Fan, C. Sun, X. Gu, H. Li, F. Gao, Y. Chen and L. Dong, *J. Power Sources*, **2013**, 221, 141-148.

42. M. L. Sushko, K. M. Rosso and J. Liu, *J. Phys. Chem. Lett.*, **2010**, 1, 1967-1972.

43. C. Jiang, I. Honma, T. Kudo and H. Zhou, *Electrochem. Solid-State Lett.*, **2007**, 10, A127-A129.

44. X. Han, X. Han, L. Sun, P. Wang, M. Jin and X.-J. Wang, *Mater. Chem. Phys.*, **2016**, 171, 11-15.

45. X.-Y. Yu, H. B. Wu, L. Yu, F.-X. Ma and X. W. D. Lou, *Angew. Chem. Int. Ed.*, **2015**, 54, 4001-4004.

46. V. Etacheri, C. Hong, J. Tang and V. G. Pol, *ACS Appl. Mater. Interfaces*, **2018**, 10, 4652-4661.

47. M. Pfanzelt, P. Kubiak, M. Fleischhammer and M. Wohlfahrt-Mehrens, *J. Power Sources* **2011**, 196, 6815-6821.

48. X. Feng, K. Zhu, A. J. Frank, C. A. Grimes and T. E. Mallouk, *Angew. Chem. Int. Ed.*, **2012**, 51, 2727-2730.

49. A. R. Armstrong, G. Armstrong, J. Canales, R. García and P. G. Bruce, *Adv. Mater.* , **2005**, 17, 862-865.

50. Y.-S. Hu, L. Kienle, Y.-G. Guo and J. Maier, *Adv. Mater.*, **2006**, 18, 1421-1426.

51. T.-F. Yi, S.-Y. Yanga and Y. Xie, *J. Mater. Chem. A*, **2015**, 3, 5750-5777.

52. S. Hariharan, V. Ramar, S. P. Joshia and P. Balaya, *RSC Adv.*, **2013**, 3, 6386-6394.

53. A. Varzi, D. Bresser, J. v. Zamory, F. Müller and S. Passerini, *Adv. Energy Mater*, **2014**, 4, 1400054.

54. H. Xiong, H. Yildirim, E. V. Shevchenko, V. B. Prakapenka, B. Koo, M. D. Slater, M. Balasubramanian, S. K. R. S. Sankaranarayanan, J. P. Greeley, S. Tepavcevic, N. M. Dimitrijevic, P. Podsiadlo, C. S. Johnson and T. Rajh, *J. Phys. Chem. C*, **2012**, 116, 3181-3187.

Chapter 6

Unusual Pseudocapacitive Lithium-Ion Storage on Defect-Rich Co_3O_4 Nanosheets

6.1 Introduction

Conversion-type transition metal-oxides have been widely investigated as high-capacity anodes for lithium-ion batteries to substitute conventional graphite anodes.[1-3] Cobalt oxide (Co_3O_4) is considered as a most promising material owing to its high theoretical capacity (890 mAh g^{-1}) compared to commercial intercalation anodes (<400 mAh g^{-1}).[4-6] Reversible conversion reaction of Co_3O_4 based anodes ($Co_3O_4 + 8e^- + 8Li \leftrightarrow 4Li_2O + 3Co$) resulted in ~2.4-fold higher specific capacity compared to graphite anodes. However, rapid capacity fading and modest rate performance of Co_3O_4 due to low electronic conductivity, large volume change (~200%) and particle agglomeration limits their practical application in commercial Li-ion batteries.[7-9] Several strategies have been employed for improving the electrochemical performance of Co_3O_4 based anodes. Nanostructuring, hybrid formation with carbonaceous materials and porosity control are most established methods for enhancing the Li-diffusion kinetics and electronic conductivity.[10-14] Due to the unique electronic properties of 2D morphology, nanosheets and nanoflakes often outperformed other nanostructured anodes in Li-ion batteries.[15-17] Nevertheless, development of high-performance transition metal oxides with excellent cycling stability remains as a challenge.

Pseudocapacitive charge storage has been recently demonstrated as a promising strategy to improve ion-diffusion kinetics of nanostructured electrodes.[18, 19] Diffusion independent pseudocapacitive Li-ion storage usually involves surface or near surface charge-transfer reactions. Nominal pseudocapacitance has been reported for conversion type transition metal oxides (MnO_2, Co_3O_4, Fe_2O_3 etc.) due to the sluggish Li-ion diffusion.[20-22] Several strategies including defect engineering of nanostructured electrode materials have been investigated to induce pseudocapacitance in conversion type anodes. Nanoengineered electrode facilitating high electronic and ionic conductivity is key to induce pseudocapacitive type charge storage in conversion type anodes.[20, 23]

Defect chemistry and intricate interfaces in metal oxides have been playing a vital role in deciding the physiochemical properties and improving the reaction kinetics.[24-26] Various defects that include surface defects (grain boundaries), point (vacancies, interstitial and substitution) and line (screw and edge dislocations) defects are of particular interest in electrode materials as they facilitate superior diffusion and improve ionic conductivity.[27] Moreover, they are known to have a dominating influence on strong coulombic interaction that actuate additional Li adsorption through charge separation and promotes electrochemical phase transition.[28-32] Hence, tailoring the electrode microstructure with intrinsic defects assists in faster diffusion, which is vital to induce pseudocapacitive type charge-storage in conversion-based anodes. Although pseudocapacitance in transition metal-oxides is reported earlier, defect induced pseudocapacitive Li-ion storage has not been systematically studied and/or applied to electrode materials.

In this chapter, an unusual pseudocapacitive Li-ion storage on defect-rich Co_3O_4 nanosheets is demonstrated. Rational design of defective Co_3O_4 nanosheets is based on the following aspects. (i) Two-dimensional morphology is selected for promoting superior contact with electrolyte solution and improved interfacial Li-ion diffusion. (ii) Defect-rich microstructure composed of point defects (vacancies), edge dislocations and grain boundaries that can considerably increase Li-ion diffusion kinetics, which is one of the key requirement for high pseudocapacitance.[24, 33-35] (iii) Holey microstructure is beneficial to prevent electrode pulverisation by buffering volume changes during charge-discharge process.[36] These morphological and microstructural advantages enable optimum ionic conductivities that are crucial for pseudocapacitive type Li-ion storage. Excellent Li-ion storage performance of defective Co_3O_4 nanosheet electrodes is credited to the pseudocapacitive nature of conversion reaction resulting from the ultrafast Li-ion diffusion through crystal defects.

6.2 Results and Discussion

6.2.1 Formation and Structural Characteristics of Defect-Rich Co_3O_4 Nanosheets

Defective Co_3O_4 nanosheets are synthesised using cobalt (II) nitrate hexahydrate, and urea, as precursors in ethylene glycol water mixture under solvothermal conditions (Figure 2.5). Urea in this case acting as a complexing agent by interacting with nitrate groups of Co-precursor through hydrogen bonds, and decompose to NH_4^+ ions (nitrogen source) during solvothermal conditions. Ethylene glycol also played dual role in the formation of defect-rich Co_3O_4 nanosheets. Firstly, its increased viscosity of glycol reduces the crystal growth kinetics, facilitating the crystallization of small crystallites, which is crucial for the generation of several grain boundaries. Additionally, ethylene glycol enables 2D nanosheet morphology formation through anisotropic crystal growth by OH group interaction with crystallographic planes of cobalt precursor. In a typical synthesis, cobalt nitrate hexahydrate react with urea and water in ethylene glycol to form $(NH)_4Co_8(Co_3)_6(OH)_6.4H_2O$ nanosheets.[37]

Transmission electron microscopy (TEM) image (Figure 6.1a) of the precursor $(NH)_4Co_8(Co_3)_6(OH)_6.4H_2O$ confirmed graphene-like 2D microstructure formation during the solvothermal reaction. Scanning electron microscopy (SEM) image displayed in figure 6.1b validated the formation of Co_3O_4 nanosheets with 2-5 μm length after the annealing step. Further microstructural analysis using TEM (Figure 6.1c) confirmed the presence of holey microstructure resulted during the annealing process. High-resolution image (Figure 6.1d-e) verified the presence of various defects including grain boundaries, point defects dislocations and uniform holes with an average hole size of 8-10 nm. In this case, 2D microstructure with defects is crucial for maintaining superior contact with electrolyte solution and ionic conductivity. HRTEM image (Figure 6.1f) verified high crystallinity with an interlayer spacing of 0.28 nm corresponding to (220) plane.

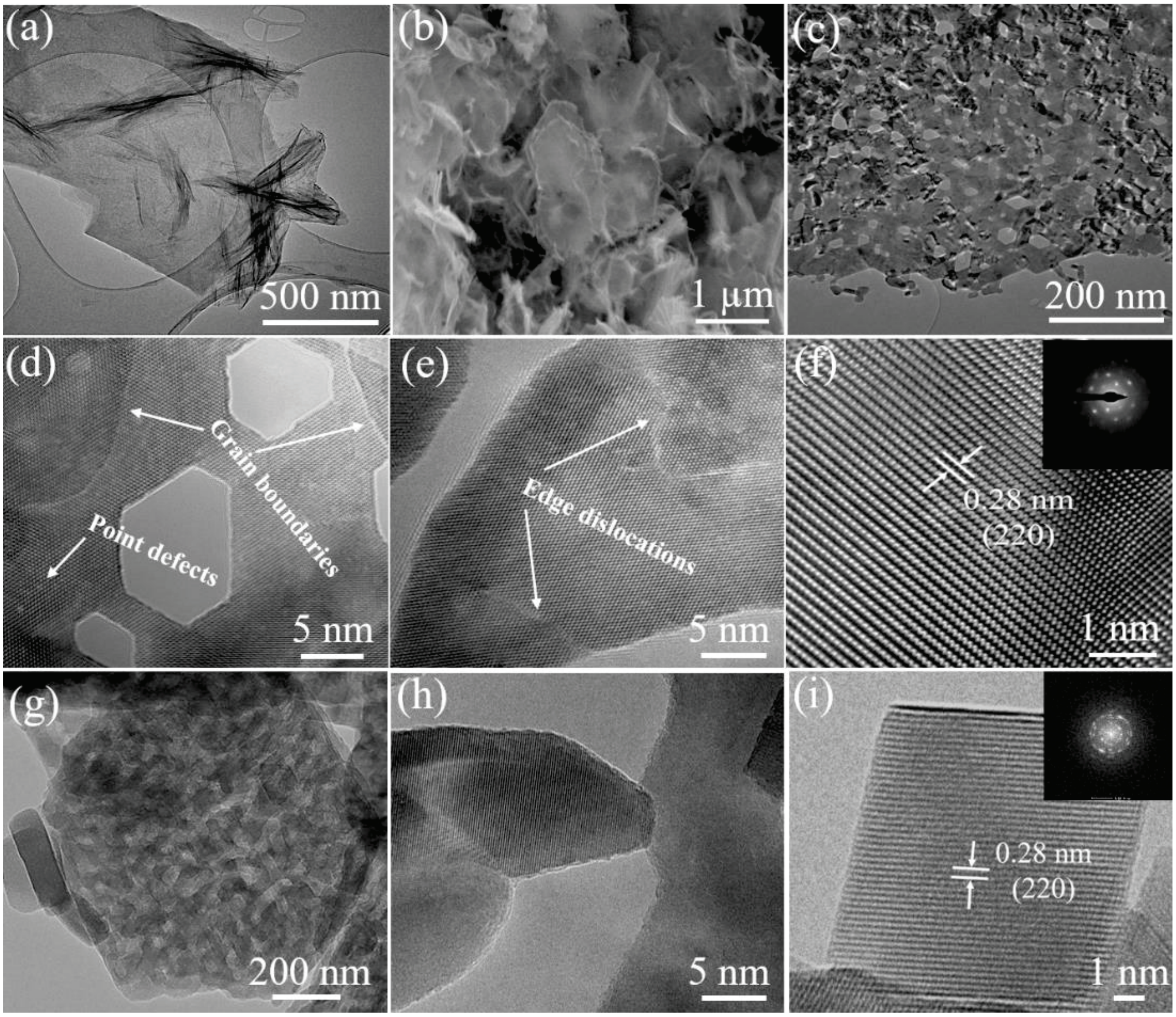

Figure 6.1 (a) TEM image of precursor $(NH)_4Co_8(Co_3)_6(OH)_6.4H_2O$. (b) SEM and (c) TEM image of defect-rich Co_3O_4 nanosheets. (d-f) High-resolution transmission electron microscopy images of defect-rich Co_3O_4 nanosheets. Inset: Selected area electron diffraction pattern. (g-h) High-resolution transmission electron microscopy images of defect-free Co_3O_4 nanosheets.

Formation of hexagonal Co_3O_4 nanosheets without defects compared to defective Co_3O_4 nanosheets is evidenced form the HRTEM images (Figure 6.1g-h). Figure 6.1g revealed defect-free hexagonal Co_3O_4 nanosheets with an edge length of 120-150 nm. Lack of defects in the microstructure is confirmed from the high-resolution image in figure 6.1h-i. Interplanar distances of 0.28 nm in this case correspond to (220) plane of Co_3O_4.

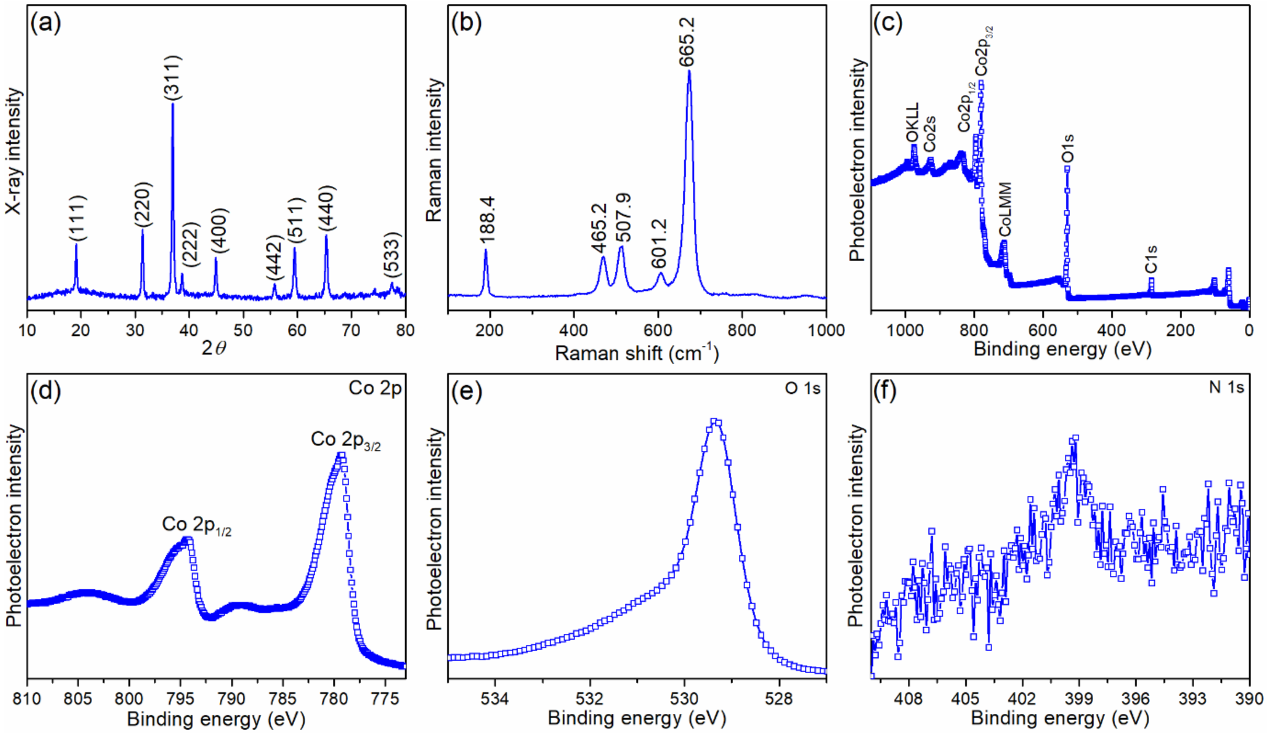

Figure 6.2 (a) X-ray diffraction pattern and (b) Raman spectra of defect-rich Co_3O_4 nanosheets. (c) Survey, and high-resolution (d) Co 2p, (e) O 1s, (f) N 1s XPS spectra of defect-rich Co_3O_4 nanosheets.

X-ray diffraction (XRD) pattern presented in figure 6.2a exhibited distinct peaks of face centered cubic phase Co_3O_4 (JCPDS No. 76-1802).[38] XRD pattern of the precursor (Appendix 15) correspond to $(NH)_4Co_8(Co_3)_6(OH)_6.4H_2O$ (JCPDS No. 52-0552), and its complete decomposition during calcination is verified by the absence of cobalt hydroxide/ cobalt carbonate peaks in the diffraction pattern of Co_3O_4 nanosheets.[39] Raman signals (Figure 6.2b) at 465.2 and 665.2 cm^{-1} correspond to the E_g and A_{1g} vibrational modes of Co_3O_4, while the peaks at 188.4, 507.9 and 601.2 cm^{-1} represent the F_{2g} modes.[40] Additional surface chemical characteristics of defect-rich Co_3O_4

nanosheets are obtained from the X-ray photoelectron spectroscopy (XPS) (Figure 6.2c). High-resolution Co 2p spectrum (Figure 6.2d) consists of two peaks at 779.9 eV and 794.9 eV corresponding to Co 2p3/2 and Co 2p 1/2 components respectively, and their spin-orbit separation of 15.2 eV are identical to previous reports.[36, 41, 42] High-resolution O 1s spectra (Figure 4.2e) of Co_3O_4 nanosheets consists of a major peak at 529.4 eV confirming the presence of lattice oxygen species. Signal at 531.2 eV represent the existence of oxygen vacancies that could assist in additional surface storage of Li-ions.[43] Surface quantitative analysis from high-resolution N 1s spectra verified the presence of nitrogen, which is beneficial for the improved electronic conductivity of defect-rich Co_3O_4 nanosheets (Figure 4.2f).[44, 45]

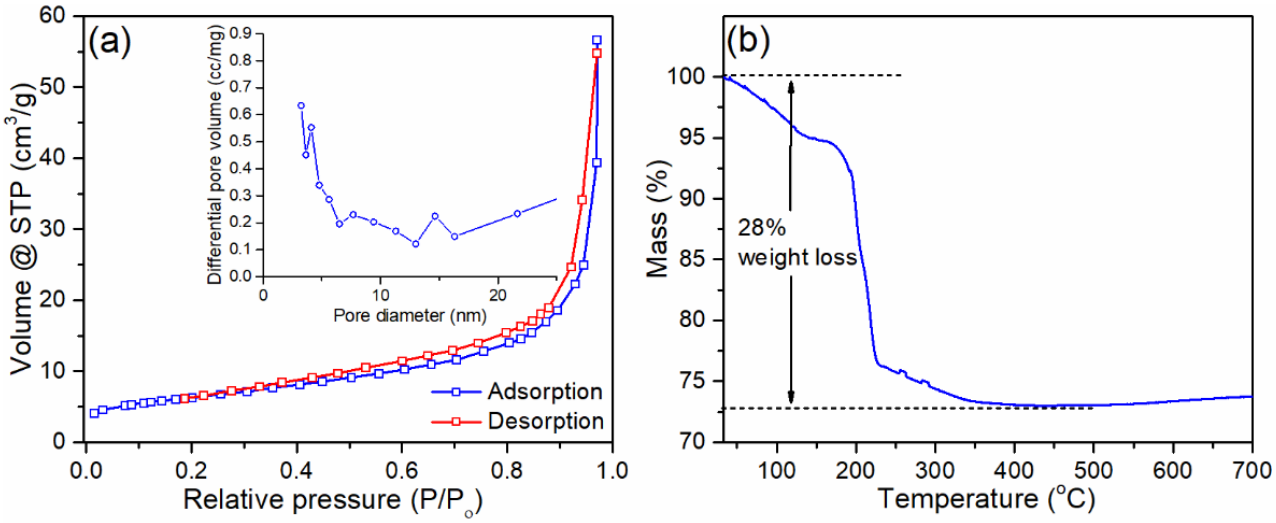

Figure 6.3 (a) N_2 adsorption-desorption isotherm of defect-rich Co_3O_4 nanosheets. Inset: Pore-size distribution. (b) Thermogravimetric analysis of Precursor $(NH)_4Co_8(Co_3)_6(OH)_6.4H_2O$ under air-flow at a heating rate of 10 °C min^{-1}.

Nitrogen adsorption-desorption isotherm of defect-rich Co_3O_4 nanosheets displayed type II hysteresis, and increased slope at a relative pressure between 0.4 and 1.0 associated with the presence of mesopores (Figure 6.3a). Brunauer-Emmett-Teller (BET) and Barret-Joyner-Halenda (BJH) analysis confirmed the mesoporosity of Co_3O_4 nanosheets with a specific surface area of 22

m^2g^{-1}, pore volume of 0.13 cm^3 g^{-1} and an average pore diameter of 67 nm (Figure 6.3a inset). Mesoporosity of Co_3O_4 nanosheets are beneficial for superior Li-ion storage and increase the contact with electrolyte solution for Li storage. Thermogravimetric analysis (TGA) of the precursor $(NH)_4Co_8(Co_3)_6(OH)_6.4H_2O$ (Figure 6.3b) is carried out to follow the defect-rich Co_3O_4 nanosheets formation. Weight loss of 8% in the temperature range of 30-220 °C represent loss of water and surface functional groups. Further weight loss of 20% in the range of 220-380 °C corresponds to the precursor decomposition. No significant weight loss is observed 380 °C, signifying the complete decomposition of precursor $(NH)_4Co_8(Co_3)_6(OH)_6.4H_2O$. Depending on this analysis, precursor is heat treated at 500 °C under air flow to obtain phase-pure defect-rich Co_3O_4 nanosheets. In summary, solvothermal hydrolysis/ condensation of Co-precursor in ethylene glycol followed by controlled heat treatment resulted in the formation of defect-rich Co_3O_4 nanosheets.

6.2.2 Electrochemical Performance of Defect-Rich Co_3O_4 Nanosheets

Lithium-ion storage performances of Co3O4 nanosheet based electrodes are investigated in the voltage range of 0-3 V in a half-cell configuration. Galvanostatic rate-performance of defect-rich and defect-free Co_3O_4 nanosheet electrodes are initially performed (Figure 6.4a) to validate the role of defects. It is clear that the electrodes containing defects demonstrated superior Li-ion storage performance compared to defect-free nanosheets under similar experimental conditions. Irreversible SEI formation resulted in the first cycle capacity loss of both Co_3O_4 nanosheets. However, initial coulombic efficiency of defect-rich Co_3O_4 nanosheets (~82%) is considerably higher than defect-free Co_3O_4 nanosheets (~72%). Full-cell development requires further first-cycle efficiency enhancement that can be achieved through electrolyte additives or chemical/ electrochemical prelithiation strategies. Defect-rich Co_3O_4 nanosheets anode delivered an outstanding reversible capacity of 1490 mAh g^{-1} compared to defect-free Co_3O_4 nanosheets (1170 mAh g^{-1}) at a low current density of 25 mA g^{-1}.

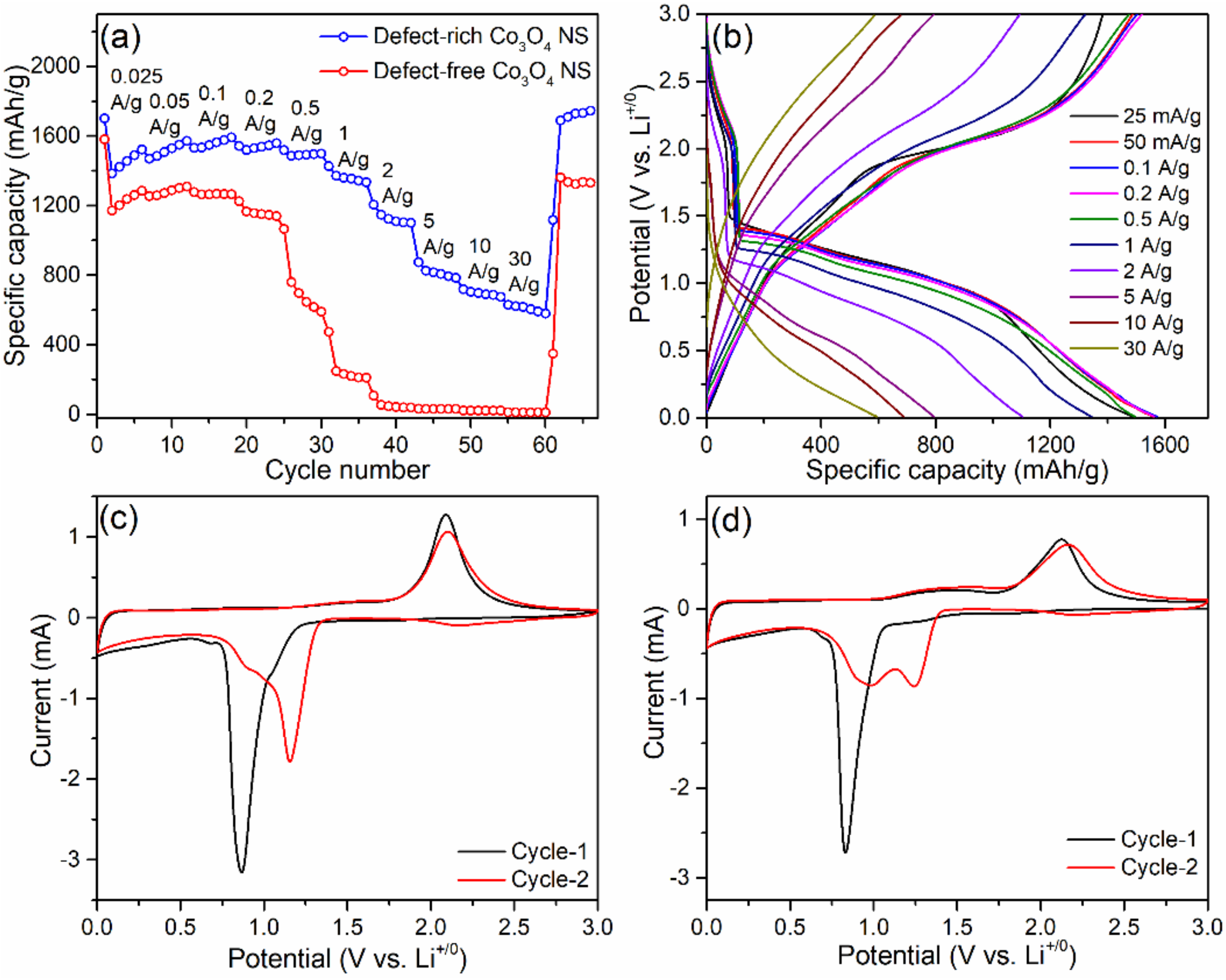

Figure 6.4 (a) Galvanostatic rate performance of defect-rich, and defect-free Co_3O_4 nanosheets. (b) Galvanostatic voltage profiles of defect-rich Co_3O_4 nanosheets at various current densities. Cyclic voltammograms at a scan rate of 0.1 mV s^{-1} of (c) defect-rich, and (d) defect-free Co_3O_4 nanosheets.

Defect-free Co_3O_4 nanosheets experienced severe capacity fading (Figure 6.4a) at higher current densities, which is in good agreement with previous reports.[10, 46] On the other hand, defective Co_3O_4 nanosheets achieved maximum specific capacity of 1577 mAh g^{-1} @ 100 mA g^{-1} and retained 680 mAh g^{-1} and 592 mAh g^{-1} even at higher current densities of 10 and 30 A g^{-1}

respectively. These values are considerably higher than the theoretical capacity of conventional graphite anodes (372 mAh g^{-1}) used in state-of-the-art Li-ion batteries and Co_3O_4 (890 mAh g^{-1}).

Galvanostatic charge-discharge profiles of defective Co_3O_4 nanosheets at various current densities are presented in figure 6.4b. These discharge profiles exhibited three distinct regions between 3-0 V signifying the crucial Li-ion storage mechanism analogous to Co_3O_4 nanorod anodes described in section 4.2.2 (Appendix 9). Initial slopping region from 3.0-1.3V corresponding to the adsorption of Li-ions onto electrode surface, mainly at defects (region-I). While the plateau from 1.3-0.8V (region-II) and slopping profile in 0.8-0V (region-III) resembles the conversion reaction of Co_3O_4 to Co^o ($Co_3O_4 + 8Li^+ + 8e^- \leftrightarrow 3Co + 4Li_2O$) and interfacial Li-ion storage (pseudocapacitance) respectively. Voltage profiles of defective Co_3O_4 nanosheets varied significantly with current densities and region-III dominated at higher current densities. Slopping discharge profile is also indicative of dominant diffusion independent pseudocapacitive process. Moreover, coulombic efficiencies of defective Co_3O_4 nanosheets at current densities ranging from 25 mA g^{-1} to 30 A g^{-1} are outstanding (>99.9%) demonstrating the complete reversibility of the Li-ion storage mechanism.

Cyclic voltammetry (CV) of defect-rich and defect-free Co_3O_4 nanosheet electrodes are performed in the voltage range 0-3 V for a detailed investigation of lithiation-delithiation processes. In the case of defect-rich Co_3O_4 nanosheets (Figure 6.4c), broad cathodic signal centered at 0.86 V corresponds to Co_3O_4 reduction ($Co_3O_4 + 8Li^+ + 8e^- \rightarrow 3Co + 4Li_2O$) and solid electrolyte interface (SEI) formation.[43] These cathodic responses resemble very well with the irreversible capacity loss and sloping galvanostatic voltage profiles. Reduced cathodic signal intensities in the potential range of 1.0- 0.50 V during the second scan signify the complete SEI formation in the first cycle. Shifting of second cycle cathodic signals towards higher potentials can assigned to the complete Li_2O formation in the first cycle.[36] Anodic signals at 2.2 V corresponds to oxidation of Co ($3Co + 4Li_2O \rightarrow Co_3O_4 + 8Li^+ + 8e^-$) and surface adsorbed Li-ion removal. On the other hand, defect-free Co_3O_4 nanosheets (Figure 6.4d) displayed first cathodic peak at 0.83 V corresponding to simultaneous conversion reaction and unavoidable Li_2O formation.

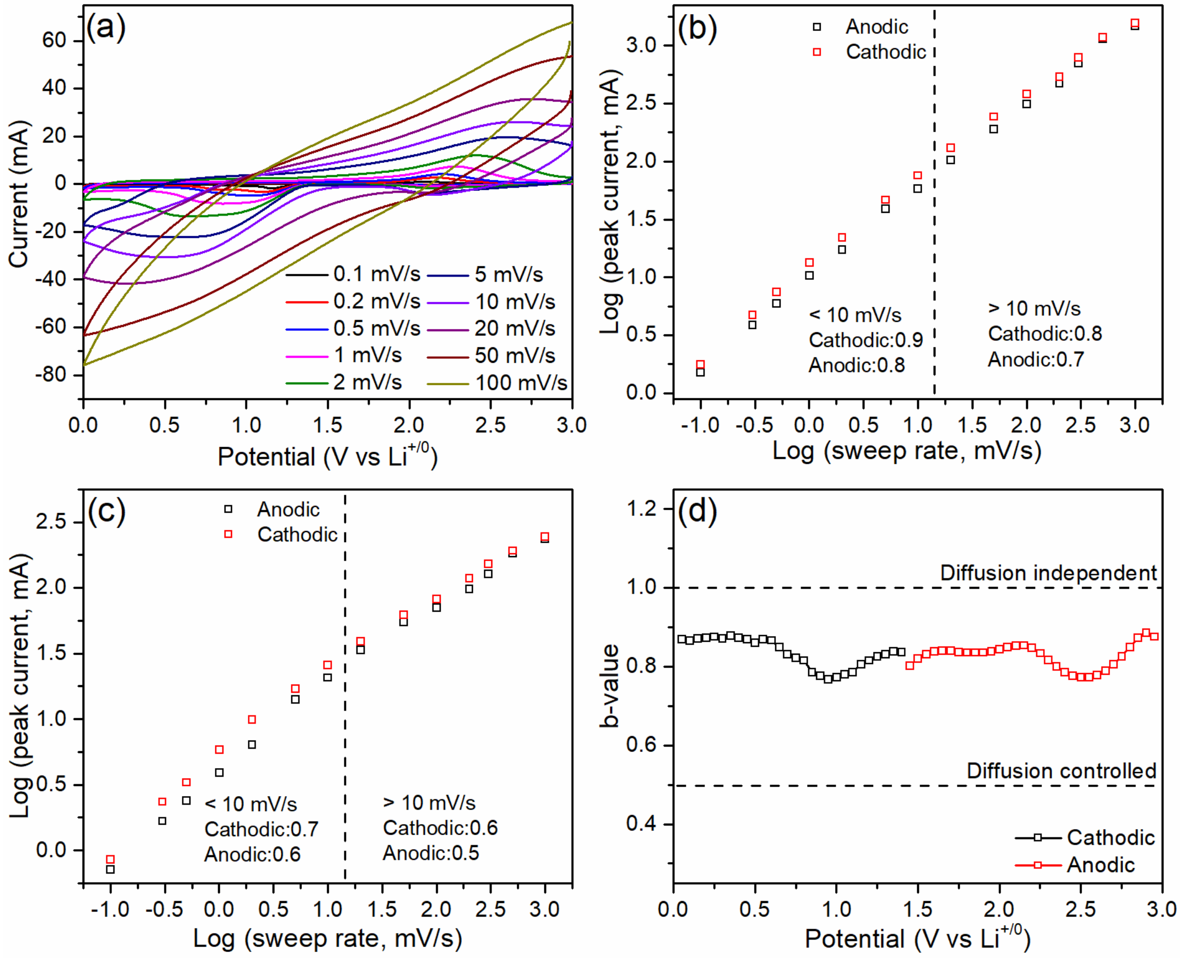

Figure 6.5 (a) Cyclic voltammograms of defect-rich Co_3O_4 nanosheets at different scan rates (0.1-1000 mV s^{-1}). Scan rate dependence of peak current density of (b) defect-rich, and (c) defect-free Co_3O_4 nanosheets. (d) Anodic and cathodic *b*-values of defect-rich Co_3O_4 nanosheets at different state of charge.

Second cathodic signals displayed a reduced intensity peak at 0.83 V signifying the incomplete SEI formation in first cycle due to the increased formation of electronically insulating Li_2O/

particle agglomeration.[47] Broad anodic peak at 2.1 V in first and second cycle of defect-free Co_3O_4 nanosheets represent oxidation of Co. These anodic and cathodic responses are in good agreement with the previous reports of conversion type Co_3O_4 anodes.[48-50]

Further quantitative analysis of pseudocapacitive Li-ion storage is performed by collecting cyclic voltammograms of defect-rich Co_3O_4 nanosheets at various scan rates (Figure 6.5a). Linear dependence of the peak current intensities in this case is a clear indication of the dominant pseudocapacitive type charge storage. Anodic and cathodic process b-value provided further details of potential dependent Li-ion storage mechanism. Variation in the capacitive and diffusion dependent ion storage contribution at different scan rates were represented using power law $i=a\ v^b$, where i is the current (mA), v is the scan rate (mV s^{-1}), a and b are arbitrary constants. As reported in the earlier sections, electrochemical reactions are mainly dominated by semi-infinite linear diffusion processes for b=0.5, and capacitive process predominate as b-value approaches 1.0. Figure 6.5b and c displayed linear dependence of log (i) vs log (v) plot for the defect-rich and defect-free Co_3O_4 nanosheets. Calculated *b*-values for the cathodic and anodic peaks in 0.1-10 mV s^{-1} scan rate for defect-rich Co_3O_4 nanosheets are 0.9 and 0.8 respectively signifying that the current response is surface controlled and thus mostly pseudocapacitive Li-ion storage. On the other hand, defect-free Co_3O_4 nanosheets exhibited b-values < 0.7 and 0.6 respectively in 0.1-1000 mV s^{-1} sweep rates signifying that the current response is limited by sluggish diffusion kinetics. Although b-values decreased to 0.8 and 0.7 respectively in case of defect-rich Co_3O_4 nanosheets with an increase of sweep rates to 10-1000 mV s^{-1}, these values still represent a high degree of pseudocapacitive process. Small drop in b-values can be credited to an increased Ohmic resistance and diffusion constraints at very high sweep rates. Similar phenomena have also been reported for intercalation type and alloying type pseudocapacitive electrodes. [51-54] Cathodic and anodic b-values for defect-rich Co_3O_4 nanosheets provided further insights of potential dependent Li-ion storage (Figure 6.5d). Lithiation (cathodic process) in voltage range 1.5-0 V (conversion reaction and interfacial storage) is mostly dominated by pseudocapacitive process. Delithiation (anodic process) in this case is also more pseudocapacitive in 1.5-3.0 V voltage range. It is thus clear that both conversion reaction and interfacial storage follow a pseudocapacitive diffusion-independent kinetics due to the presence of crystal defects.

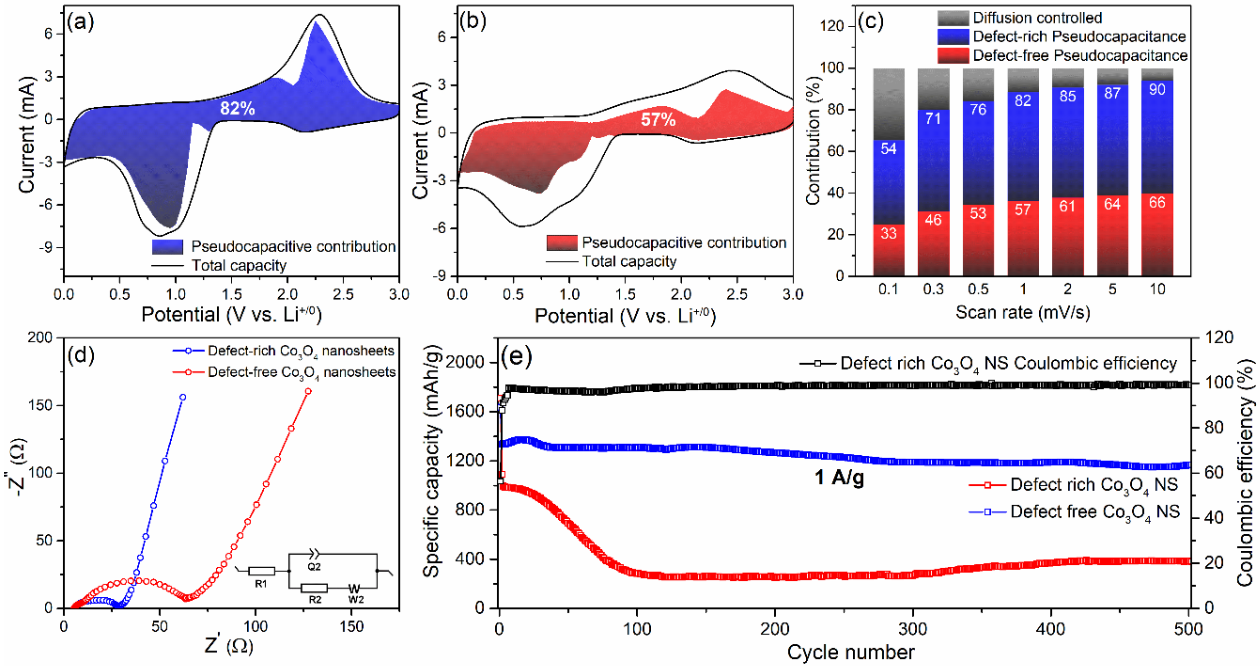

Figure 6.6 Cyclic voltammograms at 1 mV s^{-1} scan rate of (a) defect-rich, and (b) defect-free Co_3O_4 nanosheets. Shaded regions represent pseudocapacitive current contribution. (c) Pseudocapacitive and diffusion-dependent capacity contributions of defect-rich, and defect-free Co_3O_4 nanosheets at different scan rates. (d) Nyquist plots of defect-rich, and defect-free Co_3O_4 nanosheets. Inset: Randles equivalent circuit used for fitting the EIS pattern. (e) Galvanostatic cycling for defect-rich, and defect-free Co_3O_4 nanosheets at a current density of 1 A g^{-1}.

Lithium-ion storage through diffusion-dependent conversion reaction and diffusion independent pseudocapacitance are further distinguished (Figure 6.6a and b) using equation 2.5. Pseudocapacitance lithium-ion storage dominated the entire voltage range of defect-rich Co_3O_4

nanosheet electrodes (Figure 6.6a). A high pseudocapacitive contribution of 82% is exhibited by defect-rich Co_3O_4 nanosheets electrode compared to defect-free Co_3O_4 nanosheets (57%) (Figure 6.6b) at a scan rate of 1 mV s^{-1}, suggesting diffusion-independent Li-ion storage mechanism. Improved pseudocapacitive contribution in case of defect-free Co_3O_4 nanosheets compared to conventional conversion-type anodes can be credited to the 2-D morphology. Gradual increase of pseudocapacitive contribution is observed with an increase of sweep rates from 0.1 to 10 mV s^{-1} (Figure 6.6c) and attained a maximum of 90% at 10 mV s^{-1}. This observation is in line with the slopping discharge profiles at higher current densities that is characteristic of pseudocapacitive Li-ion storage. Reduced diffusion-controlled capacity contribution is observed in case of defect-free Co_3O_4 nanosheets at higher current rates due to the well-known kinetic limitation of conversion reaction.[36] High pseudocapacitive contribution of defect engineered Co_3O_4 nanosheets anode even at slow charge-discharge rates is beneficial to achieve high energy density.

Electrochemical impedance spectroscopic (EIS) measurements are performed to further investigate the Li-ion diffusion kinetics of Co_3O_4 nanosheet based electrodes (Figure 6.6d). Nyquist plots of defect-rich and defect-free Co_3O_4 nanosheets consist of a high frequency semicircle and low frequency sloping line corresponding to charge-transfer resistance (R_{ct}) and solid-state diffusion (Z_w) of Li-ion respectively. Charge transfer resistance of 28 Ω and 64Ω are obtained for defect-rich and defect-free Co_3O_4 nanosheet electrodes respectively by fitting Nyquist plots to the equivalent circuit (Figure 6.6d inset). Lower charge transfer resistance in the case of defect-rich Co_3O_4 nanosheets compared to defect-free Co_3O_4 nanosheets can be related to the presence of defects (such as edge dislocation, vacancies and grain boundaries) and 2D porous microstructure that allows superior contact with electrolyte solution. Lithium-ion diffusion coefficients calculated from Warburg impedance (equation 2.10) are 1×10^{-14} cm^2 s^{-1} and 2.5 x 10^{-}

^{15} cm^{2} s^{-1} for defect-rich and defect-free Co_3O_4 nanosheets respectively. These values endorsed the strong dependence of Li-ion diffusion kinetics with pseudocapacitance, specific capacities and rate-performance. Increased pseudocapacitive lithium storage is also beneficial for achieving fast charging and increased cycling stabilities compared to defect-free Co_3O_4 nanosheets. This is further evidenced from the superior galvanostatic cycling stability of defective Co_3O_4 nanosheet compared to defect-free Co_3O_4 nanosheet anodes. For instance, at a current density of 1 A g^{-1}, defect-rich Co_3O_4 nanosheet electrodes achieved a high reversible specific capacity of 1340 mAh g^{-1} and retained 1160 mAh g^{-1} (87% of the initial capacity) after 500 charge-discharge cycles (Figure 6.6e).

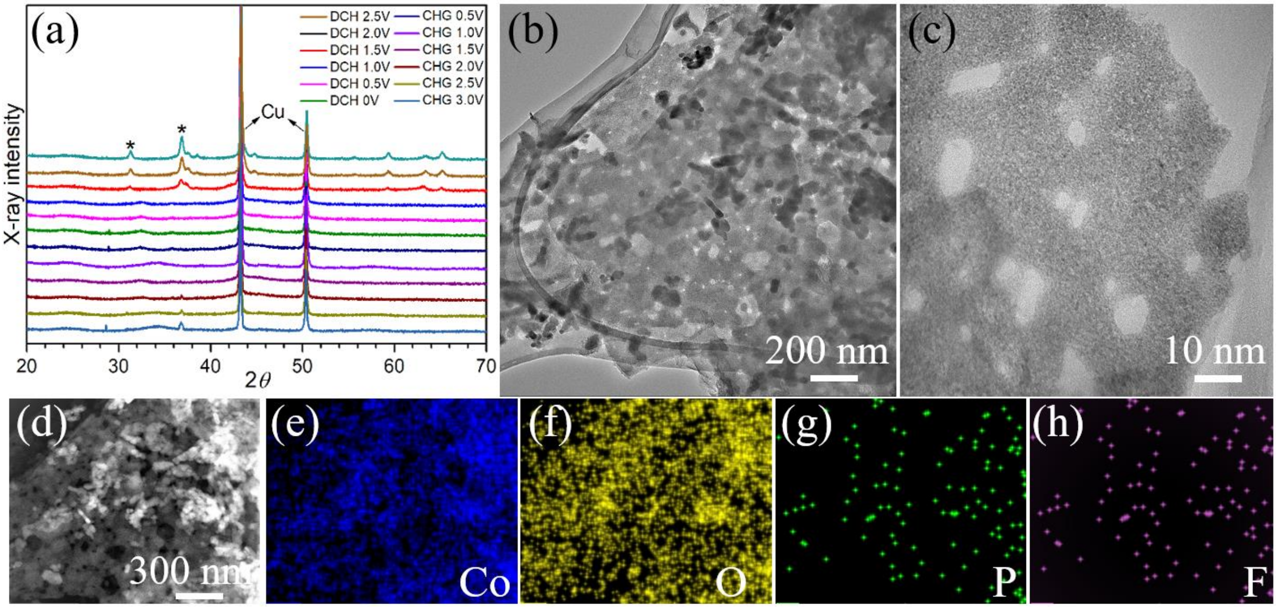

Figure 6.7 (a) *Ex-situ* X-ray diffraction patterns of defect-rich Co_3O_4 nanosheets electrode at different state of charge. (b-c) *Ex-situ* high-resolution TEM images at various magnifications, (d) HAADF image, and (e-h) corresponding EDX elemental mapping of Co_3O_4 nanosheets after 500 charge-discharge cycles at a current density of 1 A g^{-1}.

In contrast, defect-free Co_3O_4 nanosheets exhibited poor cycling stability with only 35% capacity retention after 500 cycles. This should be expected due to the electrode pulverization and formation of electronically insulating Li_2O during lithiation-delithiation process. Moreover, coulombic efficiency on extended cycling is also exceptional, retaining >99.9% even at a high current density of 1 A g^{-1}. It is interesting to note that the commonly used electrolyte additives such as vinylene carbonate (VC) or fluoroethylene carbonate (FEC) are not used for defect-rich Co_3O_4 nanosheet anodes, demonstrating its ability to work in conventional electrolyte solution.

Post-cycling XRD and TEM analysis are performed to investigate the microstructural and morphological changes of defect-rich Co_3O_4 nanosheets at different state of charge to understand its excellent electrochemical performance. X-ray diffraction patterns (Figure 6.7a) of electrodes at various charge-discharge state verified conventional conversion reaction ($Co_3O_4 + 8Li^+ + 8e^- \rightarrow 3Co + 4Li_2O$). Characteristic peaks corresponding to Co_3O_4 disappeared upon initial discharge to 0 V and reappears during charging back to 3 V, signifying the complete reversibility of the process. No metallic Li-peaks are observed in the lithiated Co_3O_4 nanosheet electrodes that rule out the unusual high specific capacity resulting from possible Li-metal deposition. *Ex-situ* HRTEM analysis further verified the excellent structural stability of defect-rich Co_3O_4 nanosheet anodes after 500 discharge/charge cycles (Figure 6.7b and c). EDX elemental mapping (Figure 6.7d-h) of cycled anodes confirmed uniform distribution of Co, O, P and F, which demonstrates compositional homogeneity. Moreover, presence of P and F components designate the existence of a uniform SEI distribution that is crucial for achieving stable electrochemical performance. Retention of 2D- morphology and holey microstructure during lithiation-delithiation process is in line with the outstanding specific capacity, rate performance and cycling stability of defect-rich Co_3O_4 nanosheets.

Exceptional lithium-ion storage performance of defect-rich Co_3O_4 nanosheet anodes can be credited to its 2D-morphology, unique defect-rich (point defects, dislocations and grain boundaries) and holey microstructure. Crystal defects such as edge dislocations, grain boundaries and point defects expedited ultrafast diffusion of Li-ions, which is crucial to achieve improved pseudocapacitance. 2D-morphology facilitated improved contact with the electrolyte solutions, which is necessary for superior Li-ion transport. Holey microstructure enabled the accommodation of volume change during charge-discharge process. Crucial role of these factors on the electrochemical performance is further confirmed by the poor electrochemical performance of commercial Co_3O_4 nanoparticles (Appendix 4). In conclusion, diffusion-independent pseudocapacitive nature of conversion reaction resulted in excellent specific capacity, rate performance and cycling stability of defect-rich Co_3O_4 nanosheets.

6.3 Conclusion

In summary, we demonstrated a high-performance rechargeable Li-ion batteries based on extremely pseudocapacitive defect-rich Co_3O_4 nanosheets anode. This defective electrode exhibited outstanding specific capacities and rate performances compared to any of the transition metal-oxide based anodes reported earlier. Long-term cycling stability and coulombic efficiencies are also excellent. Unusual Li-ion storage performance of Co_3O_4 nanosheets is credited to the pseudocapacitive nature of conversion reaction resulting from ultrafast Li-ion diffusion through various crystal defects. Additionally, 2D morphology improved contact with electrolyte solution, and holey microstructure enabled accommodation of volume changes during charge-discharge process. Remarkable defect induced pseudocapacitance enhanced electrochemical performance of Co_3O_4 nanosheet anodes makes it a potential candidate for the next-generation Li-ion batteries. Demonstrated strategy of defect-induced pseudocapacitance can also be extended to other inexpensive/environmental friendly transition metal oxides (Fe_2O_3, MnO_2 etc.) and battery systems (Na, Mg, Al-ion etc.) for superior energy storage.

6.4 References

1. A. S. Aricò, P. Bruce, B. Scrosati, J. M. Tarascon and W. V. Schalkwijk, *Nat. Mater.*, **2005**, 4, 366-377.
2. P. Poizot, S. Laruelle, S. Grugeon, L. Dupont and J.-M. Tarascon, *Nature*, **2000**, 407, 496-499.
3. S.-H. Yu, S. H. Lee, D. J. Lee, Y.-E. Sung and T. Hyeon, *small*, **2016**, 12, 2146-2172.
4. V. Etacheri, C. Hong, J. Tang and V. G. Pol, *ACS Appl. Mater. Interfaces*, **2018**, 10, 4652-4661.
5. K. Bindumadhavan, M.-H. Yeh, T.-c. Chou, P.-Y. Chang and R. Doong, *ChemistrySelect*, **2016**, 1, 5758-5767.
6. G. Binotto, D. Larcher, A. S. Prakash, R. H. Urbina, M. S. Hegde and J. M. Tarascon, *Chem. Mater.* , **2007**, 19, 3032-3040.
7. Y. Li, B. Tan and Y. Wu, *Nano Lett.*, **2008**, 8, 265-270.
8. W.-Y. Li, L.-N. Xu and J. Chen, *Adv. Funct. Mater.*, **2005**, 15, 851-857.
9. Y. Kim, J.-H. Lee, S. Cho, Y. Kwon, I. In, J. Lee, N.-H. You, E. Reichmanis, H. Ko, K.-T. Lee, H.-K. Kwon, D.-H. Ko, H. Yang and B. Park, *ACS Nano* **2014**, 8, 6701-6712.
10. X. Wang, X.-L. Wu, Y.-G. Guo, Y. Zhong, X. Cao, Y. Ma and J. Yao, *Adv. Funct. Mater.*, **2010**, 20, 1680-1686.
11. Y. Wang and G. Cao, *Adv. Mater.*, **2008**, 20, 2251-2269.
12. X. Li and C. Wang, *J. Mater. Chem. A*, **2013**, 1, 165-182.
13. N. Mahmood, T. Tang and Y. Hou, *Adv. Energy Mater*, **2016**.
14. M. Zheng, H. Tang, L. Li, Q. Hu, L. Zhang, H. Xue and H. Pang, *Adv. Sci.*, **2018**, 5, 1700592.
15. D. Su, X. Xie, P. Munroe, S. Dou and G. Wang, *Sci. Rep.* , **2014**, 4, 06519.
16. X. Wang, H. Guan, S. Chen, H. Li, T. Zhai, D. Tang, Y. Bando and D. Golberg, *Chem. Commun.*, **2011**, 47, 12280-12282.
17. Y. Zheng, L. Qiao, J. Tang, Z. Yang, H. Yue and D. He, *RSC Adv.* , **2015**, 5, 36117-36121.
18. V. Augustyn, P. Simon and B. Dunn, *Energy Environ. Sci.*, **2014**, 7 1597-1614

19. J. Liu, J. Wang, C. Xu, H. Jiang, C. Li, L. Zhang, J. Lin and Z. X. Shen, *Adv. Sci.*, **2017**, 5, 1700322.
20. Y. Xiang, Z. Yang, S. Wang, M. S. A. Hossain, J. Yu, N. A. Kumar and Y. Yamauchi, *Nanoscale*, **2018**, 10, 18010-18018.
21. J. Wang, Q. Deng, M. Li, K. Jiang, Z. Hu and J. Chu, *Nanoscale*, **2018**, 10, 2944-2954.
22. N. Kumar, K. G. Prasad, A. Sena and T.Maiyalagan, *Appl. Surf. Sci.*, **2018**, 449, 492-499.
23. H. Qi, L. Cao, J. Li, J. Huang, Z. Xu, Y. Cheng, X. Kong and K. Yanagisawa, *ACS Appl. Mater. Interfaces*, **2016**, 8, 35253-35263.
24. Y. Zhang, L. Tao, C. Xie, D. Wang, Y. Zou, R. Chen, Y. Wang, C. Jia and S. Wang, *Adv. Mater.*, **2020**, 32, 1905923.
25. Y. Zhao, C. Chang, F. Teng, Y. Zhao, G. Chen, R. Shi, G. I. N. Waterhouse, W. Huang and T. Zhang, *Adv. Energy Mater*, **2017**, 7, 1700005.
26. Z. Lin, B. R. Carvalho, E. Kahn, R. Lv, R. Rao, H. Terrones, M. A. Pimenta and M. Terrones, *2D Mater.*, **2016**, 3, 022002.
27. Y. Jia, L. Zhang, L. Zhuang, H. Liu, X. Yan, X. Wang, J. Liu, J. Wang, Y. Zheng, Z. Xiao, E. Taran, J. Chen, D. Yang, Z. Zhu, S. Wang, L. Dai and X. Yao, *Nat. Catal.*, **2019**, 2, 688-695.
28. J. Li, N. Zhuang, J. Xie, Y. Zhu, H. Lai, W. Qin, M. S. Javed, W. Xie and W. Mai, *ACS Appl. Mater. Interfaces* **2019**, 11, 15581-15590.
29. X.-T. Wang, T. Ouyang, L. Wang, J.-H. Zhong, T. Ma and Z.-Q. Liu, *Angew. Chem., Int. Ed.* , **2019**, 131, 13425-13430.
30. H.-J. Peng, J. Q. Huang, X.-B. Cheng and Q. Zhang, *Adv. Energy Mater.* , **2017**, 7, 1700260.
31. C. Cui, Z. Wei, J. Xu, Y. Zhang, S. Liu, H. Liu, M. Mao, S. Wang, J. Ma and S. Dou, *Energy Storage Mater.*, **2018**, 15, 22-30.
32. Z. Deng, H. Jiang, Y. Hu, Y. Liu, L. Zhang, H. Liu and C. Li, *Adv. Mater.* , **2017**, 29, 1603020.
33. W. Ren, M. Qin, Z. Zhu, M. Yan, Q. Li, L. Zhang, D. Liu and L. Mai, *Nano Lett.* , **2017**, 17, 4713-4718.
34. F. Zheng, Y. Yang and Q. Chen, *Nat. Commun.* , **2014**, 5, 5261.

35. J. Dong, Y. Xue, C. Zhang, Q. Weng, P. Dai, Y. Yang, M. Zhou, C. Li, Q. Cui, X. Kang, C. Tang, Y. Bando, D. Golberg and X. Wang, *Adv. Mater.* , **2017**, 29, 1603692.
36. H. Duan, L. Du, S. Zhang, Z. Chen and S. Wu, *J. Mater. Chem. A*, **2019**, 7, 8327-8334.
37. M. A. Garakani, S. Abouali, B. Zhang, Z.-L. Xu, J. Huang, J.-Q. Huang, E. K. Heidari and J.-K. Kim, *J. Mater. Chem. A*, **2015**, 3, 17827-17836.
38. D. Chen, L. Peng, Y. Yuan, Y. Zhu, Z. Fang, C. Yan, G. Chen, R. Shahbazian-Yassar, J. Lu, K. Amine and G. Yu, *Nano Lett.* , **2017**, 17, 3907-3913.
39. M. A. Garakani, S. Abouali, B. Zhang, C. A. Takagi, Z.-L. Xu, J.-Q. Huang, J. Huang and J.-K. Kim, *ACS Appl. Mater. Interfaces*, **2014**, 5, 400-405.
40. Y. Dou, Y. Wang, D. Tian, J. Xu, Z. Zhang, Q. Liu, B. Ruan, J. Ma, Z. Sun and S. X. Dou, *2D Mater.*, **2017**, 4, 015022.
41. R. Wei, M. Fang, G. Dong, C. Lan, L. Shu, H. Zhang, X. Bu and J. C. Ho, *ACS Appl. Mater. Interfaces* **2018**, 10, 7079-7086.
42. R. Wei, X. Zhou, T. Zhou, J. Hu and J. C. Ho, *J. Phys. Chem. C* **2017**, 121, 19002-19009.
43. C. Hou, Y. Hou, Y. Fan, Y. Zhai, Y. Wang, Z. Sun, R. Fan, F. Dang and J. Wang, *J. Mater. Chem. A*, **2018**, 6, 6967-6976.
44. H. Wang, C. Zhang, Z. Liu, L. Wang, P. Han, H. Xu, K. Zhang, S. Dong, J. Yao and G. Cui, *J. Mater. Chem.*, **2011**, 21, 5430-5434.
45. K. Xie, P. Wu, Y. Zhou, Y. Ye, H. Wang, Y. Tang, Y. Zhou and T. Lu, *ACS Appl. Mater. Interfaces*, **2014**, 6, 10602-10607.
46. C. Yan, G. Chen, J. Sun, C. Lv and J. Pei, *Nano Energy*, **2015**, 15, 558-566.
47. S. Chaudhari and M. Srinivasan, *J. Mater. Chem.*, **2012**, 22, 23049-23056.
48. C. Hou, B. Wang, V. Murugadoss, S. Vupputuri, Y. Chao, Z. Guo, C. Wang and W. Du, *Engineered Science*, **2020**, 11, 19-30.
49. X. Leng, S. Wei, Z. Jiang, J. Lian, G. Wang and Q. Jiang, *Sci. Rep.*, **2015**, 5.
50. G. Patrinoiu, V. Etacheri, S. Somacescu, V. S. Teodorescu, R. Birjega, D. C. Culita, C. N. Hong, J. M. Calderon-Moreno, V. G. Pol and O. Carp, *Electrochim. Acta*, **2018**, 264, 191-202.
51. Y. Jiang, Y. Li, P. Zhou, Z. Lan, Y. Lu, C. Wu and M. Yan, *Adv. Mater.*, **2017**, 29.
52. N. Wang, Y. Wang, X. Xu, T. Liao, Y. Du, Z. Bai and S. Dou, *ACS Appl. Mater. Interfaces*, **2018**, 10, 9353-9361.

53. V. Augustyn, J. Come, M. A. Lowe, J. Kim, P.-L. Taberna, S. H. Tolbert, H. D. Abruña, P. Simon and B. Dunn, *Nat. Mater.*, **2013**, 12, 518-522.

54. S. Lou, X. Cheng, J. Gao, Q. Li, L. Wang, Y. Cao, Y. Ma, P. Zuo, Y. Gao, C. Du, H. Huo and G. Yin, *Energy Storage Materials*, **2018**, 11, 57-66.

Chapter 7

Summary and Future Work

7.1 Summary

High energy and power density lithium-ion batteries developed by implementing novel transition metal oxide-based anodes are discussed in chapters 3 to 6. This study is focused on the development of nanoscale-engineered defective electrodes and understanding the pseudocapacitive charge storage mechanisms of these electrodes. Mechanistic studies including *in-situ* XRD, *ex-situ* HRTEM, EELS, and XPS are also implemented to investigate the unique pseudocapacitive Li-ion storage mechanism. Extreme pseudocapacitance of these electrodes resulted in high-performance lithium-ion batteries with outstanding specific capacities, and rate performances compared to graphite anodes used in state-of-the-art Li-ion batteries. Ultra-long term cycling stability and coulombic efficiencies are also excellent. Lithium-ion full-cells were fabricated with newly developed defect engineered anodes and commercial $LiNiMnCoO_2$ cathodes. These full-cells demonstrated significantly higher energy density, power density and cycle-life compared to current generation commercial Li-ion batteries composed of graphite anodes and $LiNiMnCoO_2$ cathodes. Pseudocapacitance of these electrodes also resulted in the diffusion-independent Li-ion storage behavior of full-cells, which is advantageous in achieving high energy (>350 Wh kg^{-1}) and power densities (≥1 kW kg^{-1}). Hence, synergistic effect of multiple ion-storage mechanisms and microstructural advantages of nanoscale engineered electrodes make them excellent anode materials for next-generation Li-ion batteries.

7.2 Future Work

Although the electrochemical performances of nanoscale defect engineered electrodes are encouraging, there are still few parameters that could be optimised in future to meet the requirements of practical applications. Firstly, cycling stability, energy and power densities of the demonstrated full-cells could be further improved by optimization of electrode weight, thickness, porosity, cell balancing, voltage window, and charge-discharge protocols.[1, 2] It is also worth noting that the energy and power density of full-cells are limited by cathode, emphasizing the need to develop cathode materials with high capacity, and voltage stability.[3, 4] Although these results are competitive with commercial Li-ion full-cells, it can be seen that typical issues associated with electrode/electrolyte interface (unstable SEI, electrolyte depletion, etc.) were not addressed, as this work is mainly focused on electrode architecture.[5, 6] Hence, there is further scope to improve the full-cell stability and performance through optimising the electrolyte composition by using additives like vinylene carbonate (VC) or fluoroethylene carbonate (FEC). Moreover, hybrid solid electrolytes that are an emerging family of solid electrolytes are promising alternatives to liquid electrolytes that can be implemented in batteries containing defect engineered electrodes.[7,8]

Demonstrated strategy of defect engineering to induce pseudocapacitance can also be easily extended to other inexpensive and environmental friendly transition metal oxides. Alternate cost-effective synthesis methods such as solid-state, co-precipitation can be employed for large-scale productions.[9] Additionally, mechanical properties of these defective electrodes can be investigated through various *in-situ* and *ex-situ* techniques.[10, 11] Pseudocapacitance of nanoscale engineered electrodes significantly enhanced the energy storage capacity of Li-ion battery as exhibited in this work. There is further scope for additional research into various systems such as Na-, Al-, Mg-, K- ion based rechargeable batteries.[12, 13] Furthermore, defect engineering of electrode materials at nanoscale opens up new opportunities to explore various high capacity, and voltage cathode materials. Overall, these results constitute a major improvement in the field of nanomaterials for rechargeable batteries, and provides important guidelines for the development of high performance electrodes for next-generation high energy/power density and ultra-long-life rechargeable batteries.

Capítulo 7

Resumen y Trabajo Futuro

7.1. Resumen

En los capítulos 3 a 6 se analizan baterías de iones de litio, de alta densidad energética y de potencia, desarrolladas mediante la aplicación de nuevos ánodos basados en óxidos de metales de transición. Este estudio se centra en el desarrollo de electrodos nanodiseñados, basados en defectos, y en la comprensión de los mecanismos de almacenamiento de carga pseudocapacitiva de estos electrodos. También se han realizado estudios mecanicistas que incluyen *in-situ* XRD, HRTEM *ex-situ*, EELS y XPS para investigar el especial mecanismo de almacenamiento pseudocapacitiva de iones de litio. La extrema pseudocapacitancia de estos electrodos dio lugar a baterías de iones de litio de alto rendimiento, con capacidades específicas y rendimientos extraordinarios en comparación con los ánodos de grafito utilizados en las baterías de iones de litio más modernas. La estabilidad de ciclado a largo plazo y las eficiencias coulómbicas también son excelentes. Se fabricaron baterías completas de iones de litio con ánodos, basados en el diseño de defectos, recientemente desarrollados y cátodos comerciales de $LiNiMnCoO_2$. Estas baterias completas demostraron una densidad de energía, una densidad de potencia y una vida útil significativamente mayores que las baterías de iones de litio comerciales de la generación actual, compuestas por ánodos de grafito y cátodos de $LiNiMnCoO_2$. La pseudocapacitancia de estos electrodos en baterías completas también dio lugar a un comportamiento de almacenamiento de iones de litio no dependiente de la difusión, lo cual es ventajoso para lograr altas densidades de energía (>350 Wh kg^{-1}) y de potencia ($\geq$1 kW kg^{-1}). Por lo tanto, el efecto sinérgico de los múltiples mecanismos de almacenamiento de iones y las ventajas microestructurales de los electrodos diseñados a nanoescala los convierten en excelentes materiales anódicos para las baterías de iones de litio de próxima generación.

7.2. Trabajo Futuro

Aunque el rendimiento electroquímico de los electrodos, con defectos diseñados a nanoescala, es alentador, todavía hay algunos parámetros que podrían optimizarse en el futuro para satisfacer los requisitos de las aplicaciones prácticas. En primer lugar, la estabilidad de ciclado y las densidades de energía y potencia de las baterías completas mostradas podrían mejorarse aún más mediante la optimización del peso, el grosor, la porosidad, el balance del equilibrio electroquímico, la ventana de voltaje y los protocolos de carga/descarga de los electrodos.[1, 2] También cabe destacar que la densidad de energía y potencia de las baterías completas están limitadas por el cátodo, lo que subraya la necesidad de desarrollar materiales catódicos con alta capacidad y estabilidad de voltaje.[3, 4] Aunque estos resultados son competitivos con los de las baterías comerciales de iones de litio, se puede observar que no se han abordado los problemas típicos asociados a la interfaz electrodo/electrolito (SEI inestable, agotamiento del electrolito, etc.), ya que este trabajo se centra principalmente en la arquitectura del electrodo.[5, 6] Por lo tanto, hay más posibilidades de mejorar la estabilidad y el rendimiento de las baterías completas mediante la optimización de la composición del electrolito utilizando aditivos como el carbonato de vinileno (VC) o el carbonato de fluoroetileno (FEC). Además, los electrolitos sólidos híbridos, que son una familia emergente de electrolitos sólidos, son prometedoras alternativas a los electrolitos líquidos que pueden implementarse en baterías que contienen electrodos diseñados mediante defectos.[7,8]

La estrategia demostrada para el diseño de defectos, con el fin de inducir la pseudocapacitancia, también puede extenderse fácilmente a otros óxidos de metales de transición de bajo coste y respetuosos con el medio ambiente. Se pueden emplear métodos alternativos de sintesis rentables, como la coprecipitación en stado sólido, para producciones a gran escala.[9] Además, las propiedades mecánicas de estos electrodos, basados en defectos, pueden investigarse mediante diversas técnicas *in-situ* y *ex-situ*.[10, 11] La pseudocapacitancia de los electrodos diseñados a nanoescala mejoró significativamente la capacidad de almacenamiento de energía de la batería de iones de litio, como se muestra en este trabajo. Hay más posibilidades de investigar en diversos sistemas como las baterías recargables basadas en iones de Na, Al, Mg y K.[12, 13] Además, el diseño de defectos a nanoescala en materiales para electrodos abre nuevas oportunidades para explorar diversos materiales catódicos de alta capacidad y voltaje. En general, estos resultados constituyen un gran avance en el campo de los nanomateriales para baterías recargables, y proporcionan importantes directrices para el desarrollo de electrodos de alto rendimiento para la próxima generación de baterías recargables de alta densidad de energía/potencia y duración ultra larga.

7.3 References

1. J. Liu, Z. Bao, Y. Cui, E. J. Dufek, J. B. Goodenough, P. Khalifah, Q. Li, B. Y. Liaw, P. Liu, A. Manthiram, Y. S. Meng, V. R. Subramanian, M. F. Toney, V. V. Viswanathan, M. S. Whittingham, J. Xiao, W. Xu, J. Yang, X.-Q. Yang and J.-G. Zhang, *Nat. Energy*, **2019**, 4, 180-186.
2. S.-H. Park, P. J. King, R. Tian, C. S. Boland, J. Coelho, C. J. Zhang, P. McBean, N. McEvoy, M. P. Kremer, D. Daly, J. N. Coleman and V. Nicolosi, *Nat. Energy*, **2019**, 4, 560-567.
3. A. Manthiram, *ACS Cent. Sci.*, **2017**, 3, 1063-1069.
4. W. Li, B. Song and A. Manthiram, *Chem. Soc. Rev.*, **2017**, 46, 3006-3059.
5. R. D. Apostolova, E. M. Shembel, B. Markovsky and D. Aurbach, *Surf. Engin. Appl.Electrochem.*, **2020**, 56, 665-674.
6. M. Metzger, P. Walke, S. Solchenbach, G. Salitra, D. Aurbach and H. A. Gasteiger, *J. Electrochem. Soc.*, **2020**, 167, 160522.
7. J. H. K. Pfisterer, M. Baghernejad, G. Giuzio and K. F. Domke, *Nat. Commun.*, **2019**, 10, 5702.
8. S. Müller, M. Lippuner, M. Verezhak, V. D. Andrade, F. D. Carlo and V. Wood, *Adv. Energy Mater*, **2020**, 10, 1904119.
9. D. G. Mackanic, X. Yan, Q. Zhang, N. Matsuhisa, Z. Yu, Y. Jiang, T. Manika, J. Lopez, H. Yan, K. Liu, X. Chen, Y. Cui and Z. Bao, *Nat. Commun.*, **2019**, 10, 5384.
10. G. H. Jeong, S. P. Sasikala, T. Yun, G. Y. Lee, W. J. Lee and S. O. Kim, *Adv. Mater.*, **2020**, 32, 1907006.
11. Y. Liang, H. Dong, D. Aurbach and Y. Yao, *Nat. Energy*, **2020**, 5, 646-656.
12. D. H. S. Tan, A. Banerjee, Z. Chen and Y. S. Meng, *Nat. Nanotechnol.*, **2020**, 15, 170-180.
13. M. B. Dixit, W. Zaman, N. Hortance, S. Vujic, B. Harkey, F. Shen, W.-Y. Tsai, V. D. Andrade, X. C. Chen, N. Balke and K. B. Hatzell, *Joule*, **2020**, 4, 207-221.

Publications by the author

Patents

1. Electrode comprising oxygen-deficient rutile TiO_2 nanowires and uses thereof

V. S. Avvaru, M. Vincent and V. Etacheri

EU Patent Application **2020**, EP20382542.7

Peer reviewed journal publications

1. Extremely pseudocapacitive interface engineered CoO@3D-NRGO hybrid anodes for high energy/ power density and ultralong life lithium-ion batteries, **V.S. Avvaru**, I. J. Fernandez, W. Feng, S. J. Hinder, M. C. Rodriguez and V. Etacheri *Carbon* **2021**, 171, 869-881.

2. Lithium-ion batteries for electric vehicle application, **V.S. Avvaru**, M. Vincent and V. Etacheri *Annals of chemical science research* **2020**, 2, 1-2.

3. High rate hybrid MnO_2@CNT fabric anodes for Li-ion batteries: properties and a lithium storage mechanism study by *in situ* synchrotron X-ray scattering, M. Rana, **V.S. Avvaru**, N. Boaretto, A. Victor, R Marcilla, V. Etacheri and J. J. Vilatela, *J. Mater. Chem. A,* ***2019**,* 7, 26596-26606.

4. High-rate and ultralong-life Mg–Li hybrid batteries based on highly pseudocapacitive dual-phase TiO_2 nanosheet cathodes, M. Vincent, **V.S. Avvaru**, M. C. Rodriguez, M. Haranczyk and V. Etacheri, J. Power Sources, **2021**, 506, 230118.

5. Realization of High Energy Density Sodium-Ion Hybrid Capacitors through Interface Engineering of Pseudocapacitive 3D-CoO-NrGO Hybrid Anodes, W. Feng, **V.S. Avvaru**, S. J. Hinder, M. C. Rodríguez and V. Etacheri, *ACS Appl. Mater. Interfaces* **2021** 13, 24, 27999–28009.

6. Low heat yielding electrospun phosphenanthrene oxide loaded polyacrylonitrile composite separators for safer high energy density lithium-ion batteries, A Yusuf, **VS Avvaru**, M Dirican, S Changchun, and DY Wang, *Appl. Mater. Today* **2020**, 20, 100675.

7. Realization of high energy/power density lithium-ion batteries through nanograin boundary induced pseudocapacitance, **V.S. Avvaru**, I.J. Fernandez, M. Vincent, W. Feng, S. J Hinder, E. Modin, M, C. Rodriguez and V. Etacheri, submitted to *Adv. Energy Mater.* (Under review).

Manuscripts in preparation

1. Oxygen vacancy induced pseudocapacitance of rutile TiO_2 nanowires: Towards superfast charging ultralong life lithium-ion batteries.

V.S. Avvaru, M. Vincent, W. Feng, A. Doñoro and V. Etacheri, To Adv. Energy Mater.

2. Unusual pseudocapacitive lithium-ion storage on defect-rich Co_3O_4 nanosheets.

V.S. Avvaru, M. Vincent, W. Feng, A. Doñoro, S. J. Hinder, M. C. Rodriguez and V. Etacheri to J. Mater. Chem. A.

Book chapters

1. Advanced Lithium-ion batteries for electric vehicles: Promises and challenges of nanostructured electrode materials

V.S. Avvaru, M. Vincent and V. Etacheri, Rechargeable Lithium-ion batteries: Trends and progress in electric vehicles (ISBN: 9781351052702), Published **2020**.

2. Carbon-based integrated devices for efficient photo-energy conversion and storage.

RN Gayen, **V.S. Avvaru** and V. Etacheri, Carbon based nanomaterials for advanced thermal and electrochemical energy storage and conversion (ISBN: 978-0-12-814083-3), Published **2019**.

Presentations by the author

Poster presentations

1. Unusual Pseudocapacitive Lithium-Ion Storage Triggered by Nanograin-Boundaries of Conversion-Type Anodes

V.S. Avvaru and V. Etacheri

Swiss Battery Days 2020/21, 15-17 of February **2021**

Oral presentations

1. Interface engineered CoO@3D-NRGO pseudocapacitive anodes for high energy/ power density lithium-ion batteries

V.S. Avvaru, W. Feng and V. Etacheri.

9th International Edition of Electrochemistry in Nanoscience (Elecnano9), Paris, France, November 23-24, **2020**.

2. High energy/power density lithium-ion batteries through interface engineered CoO@3D-NRGO pseudocapacitive anodes.

V.S. Avvaru and V. Etacheri

4th Erwin Schrödinger Symposium 2021 of the Erwin Schrödinger Society for Nanosciences Advanced Materials, Austria. January 11 - 12, **2021**.

3. Pseudocapacitive Li-ion storage triggered by nanointerfaces in CoO@3D-NRGO anodes for high-energy/power density Li-ion batteries.

V.S. Avvaru, W. Feng and V. Etacheri.

I Congreso Anual de Estudiantes de Doctorado (I-CAED), Miguel Hernández University, February 2, **2021**.

4. Ultrahigh energy and power density batteries enabled by nanograin-boundary induced pseudocapacitive Li-ion storage.

V.S. Avvaru and V. Etacheri

World Nano Congress on Advanced Science and Technology, WNCST (2021), VIT Nano-congress- March 8-13, **2021**.

Appendices

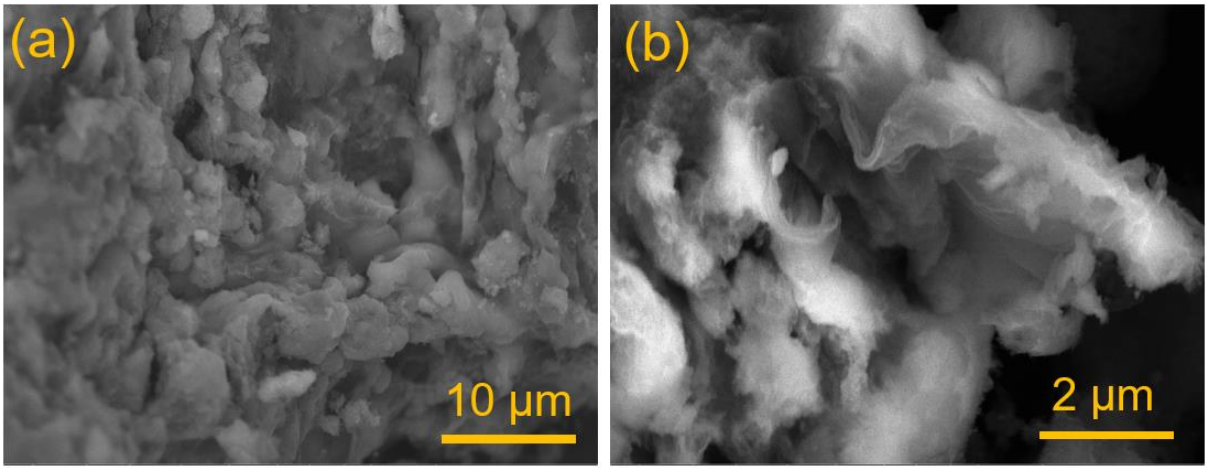

Appendix 1 SEM images of $(NH)_4Co_8(Co_3)_6(OH)_6.4H_2O$@3D-NRGO

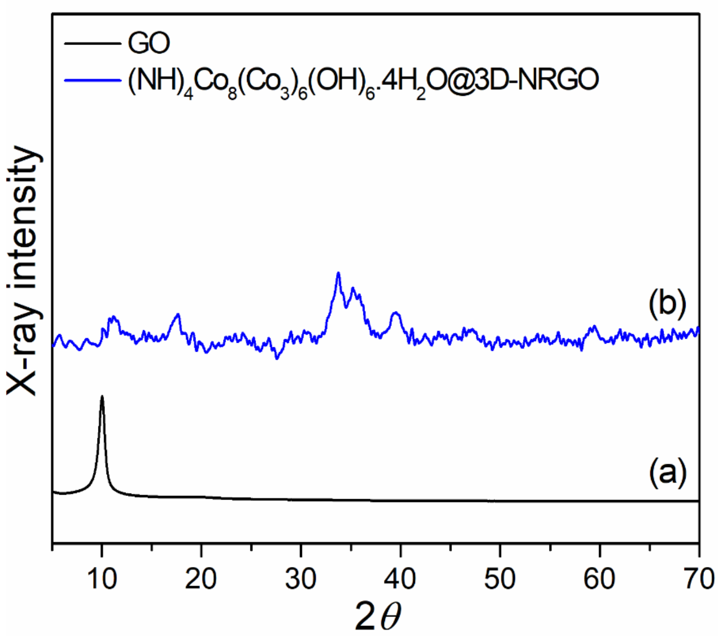

Appendix 2 X-ray diffraction pattern of (a) GO, and (b) $(NH)_4Co_8(Co_3)_6(OH)_6.4H_2O$@3D-NRGO.

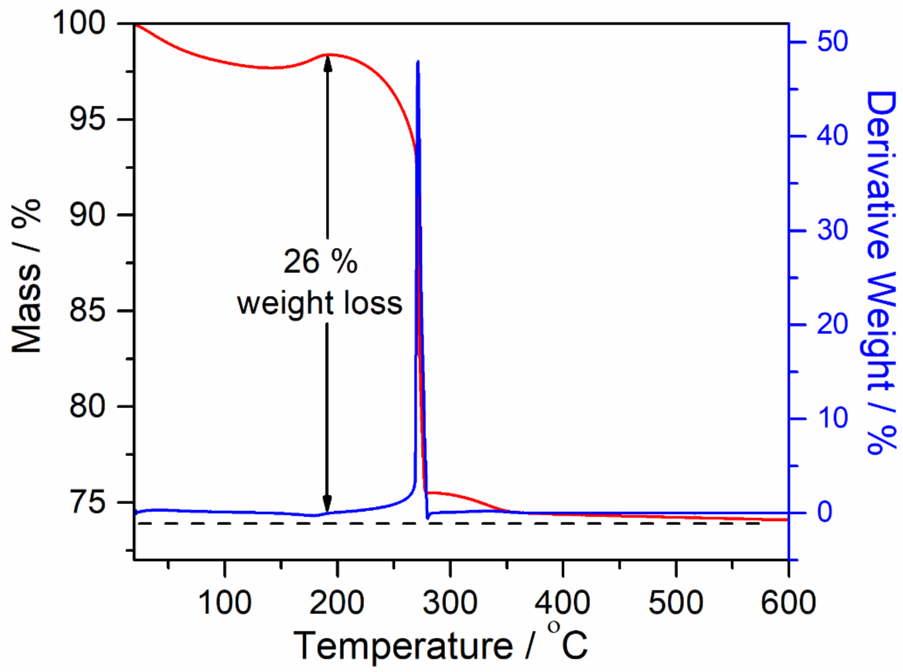

Appendix 3 Thermogravimetric and differential thermal analysis of CoO@3D-NRGO under air atmosphere at a heating rate of 10 °C min^{-1}.

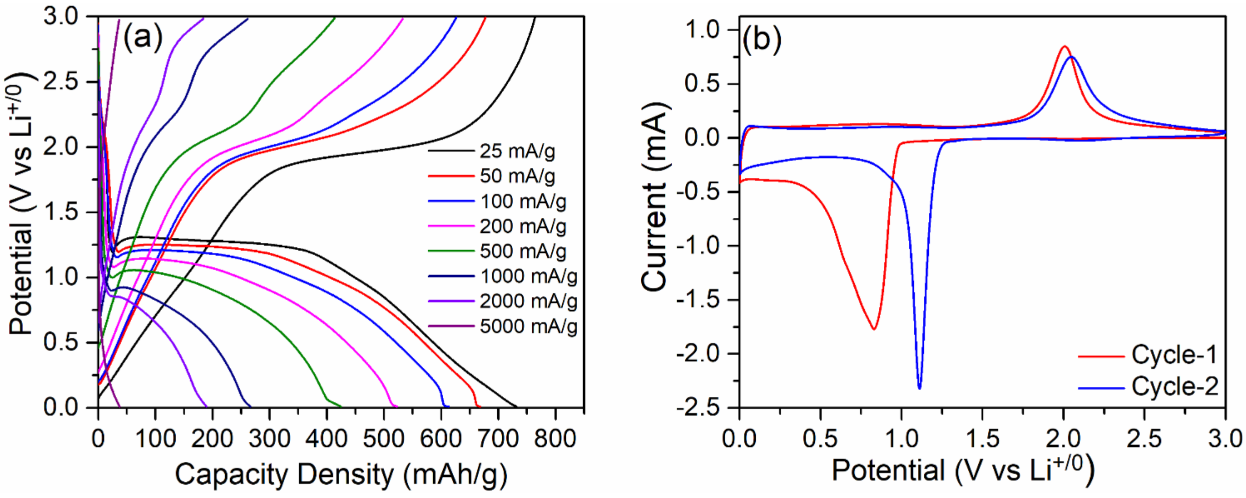

Appendix 4 (a) Galvanostatic voltage profiles at different current densities, and (b) Cyclic voltammograms (at a scan rate of 0.1 mV s^{-1}) of Co_3O_4 nanoparticles (commercial).

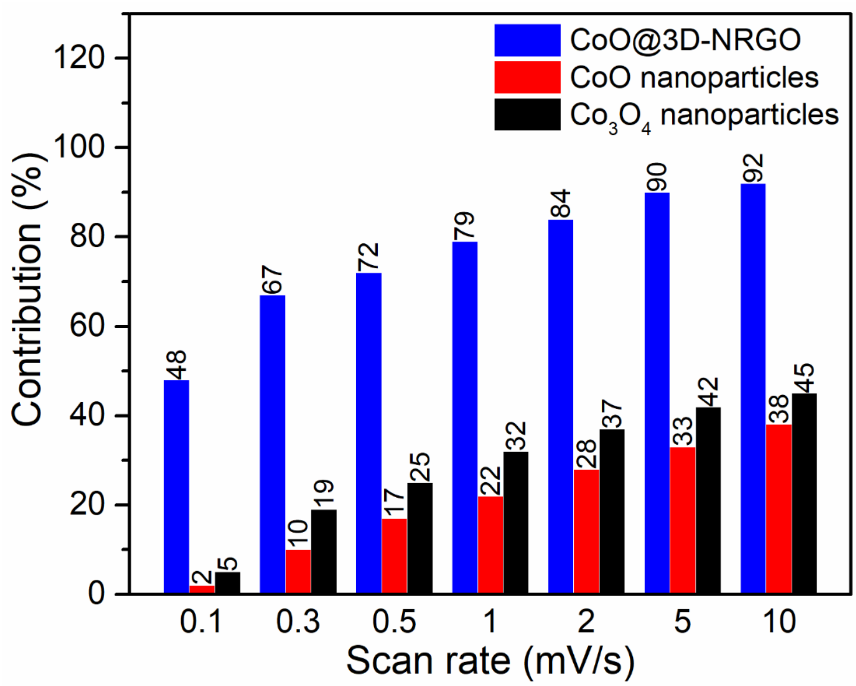

Appendix 5 Capacity contribution at different scan rates of CoO@3D-NRGO, CoO nanoparticles, and commercial Co_3O_4 nanoparticles.

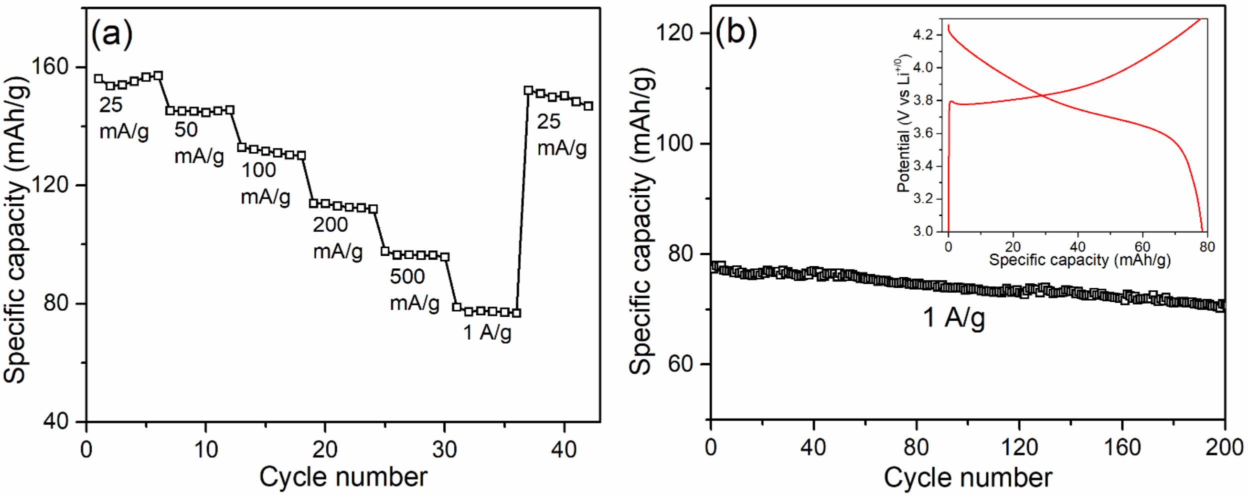

Appendix 6 (a) Galvanostatic rate performance and (b) cycling of $LiNiMnCoO_2$ cathode at a current density of 1 A g^{-1}. (*Inset*- voltage profiles of $LiNiMnCoO_2$ cathode at a current density of 1 A g^{-1}).

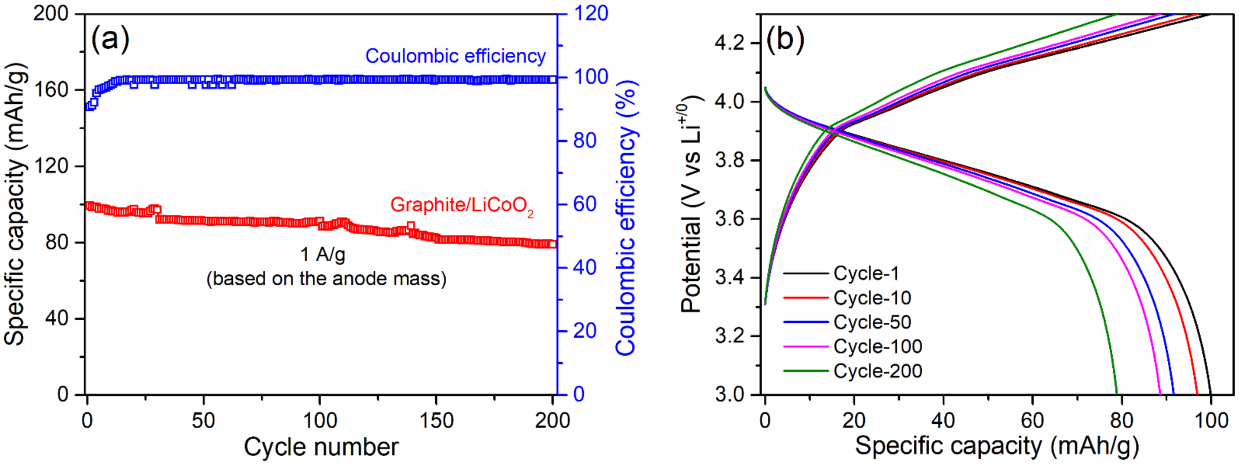

Appendix 7 (a) Galvanostatic cycling and corresponding coulombic efficiency of graphite‖LiNiMnCoO$_2$ full-cell at a current density of 1 A g^{-1} and (b) voltage profiles of graphite‖LiNiMnCoO$_2$ full-cell at a current density of 1 A g^{-1}.

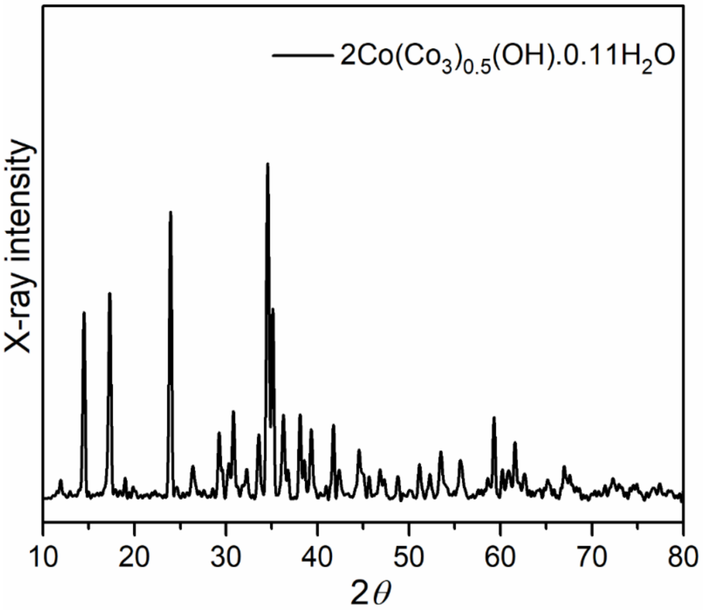

Appendix 8 X-ray diffraction pattern of $2Co(CO_3)_{0.5}(OH).0.11H_2O$.

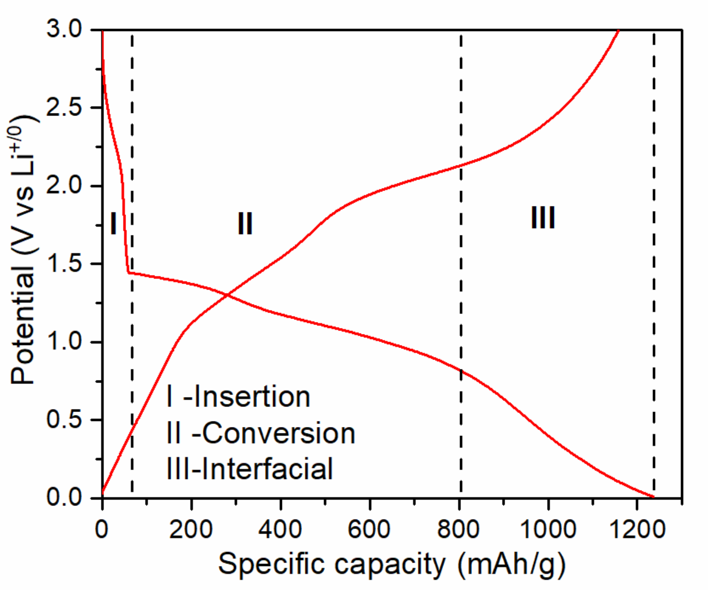

Appendix 9 Galvanostatic charge-discharge profile of Co_3O_4 nanorods at 0.05 A g^{-1} current density.

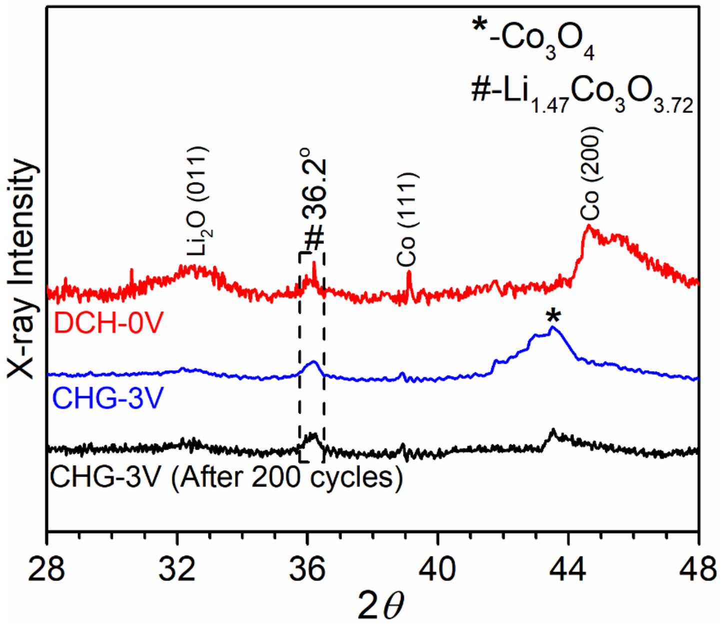

Appendix 10 X-ray diffraction pattern of cycled Co_3O_4 nanorod electrodes at various state of charge.

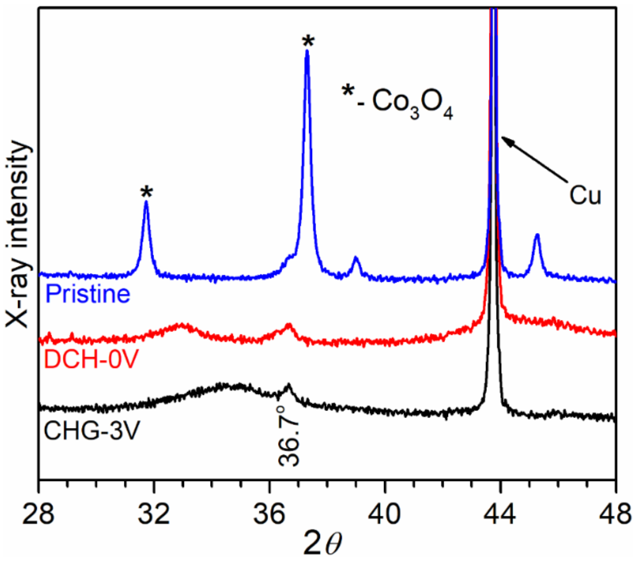

Appendix 11 X-ray diffraction pattern of cycled Co_3O_4 nanoparticle electrodes at various state of charge.

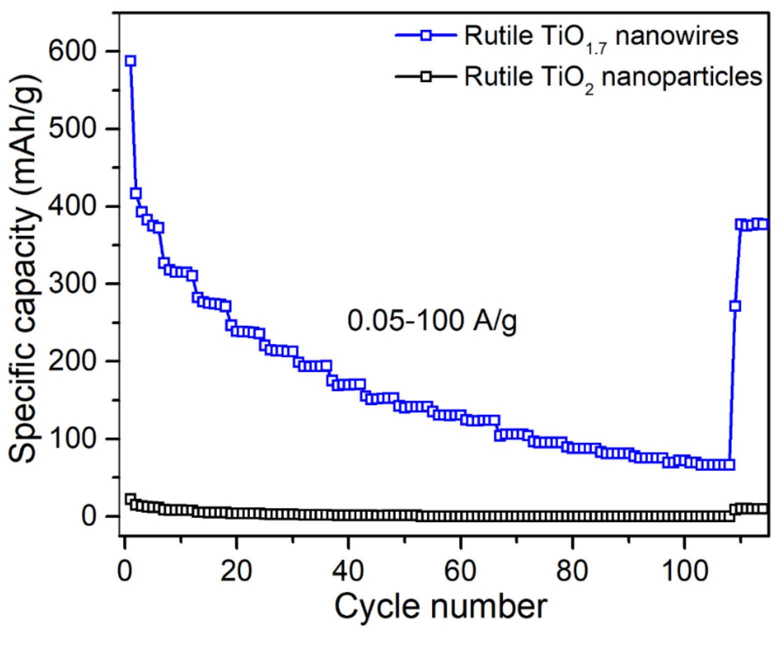

Appendix 12 Galvanostatic rate performance of oxygen vacancy rutile $TiO_{1.7}$ nanowires and rutile TiO_2 nanoparticles (commercial).

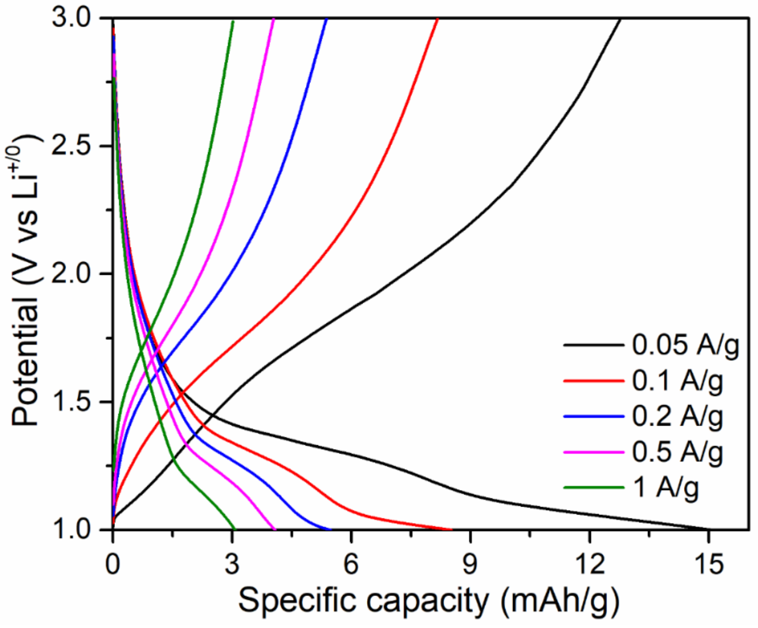

Appendix 13 Galvanostatic charge-discharge profiles of commercial rutile TiO_2 nanoparticles.

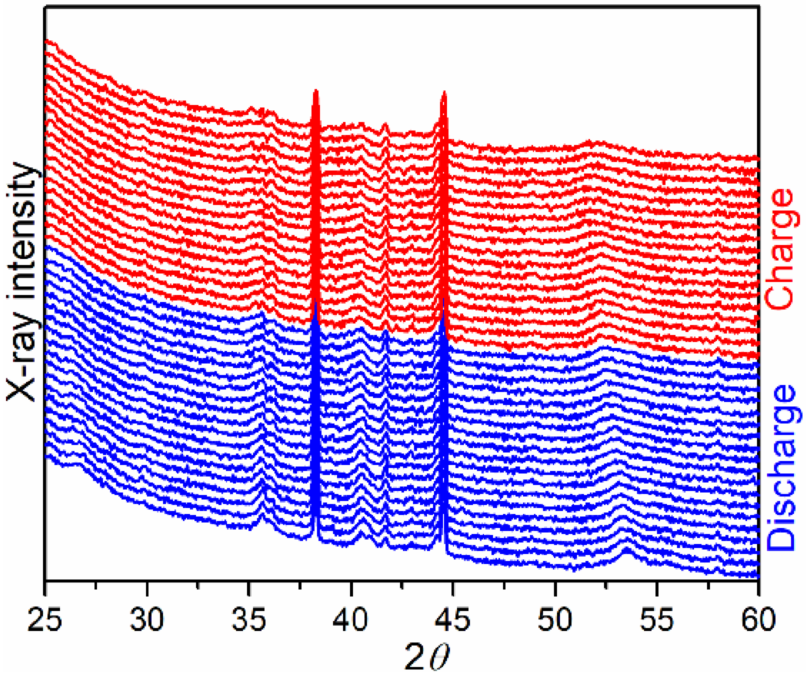

Appendix 14 *In-situ* XRD patterns of oxygen vacancy rutile TiO_2 nanowires after 1st charge-discharge process.

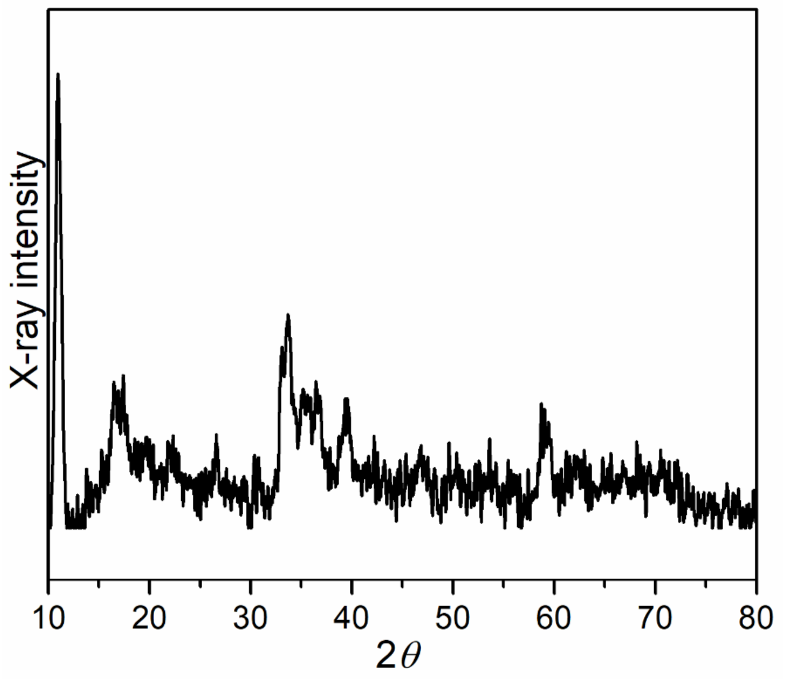

Appendix 15 X-ray diffraction pattern of $(NH)_4Co_8(Co_3)_6(OH)_6.4H_2O$.